



WASHINGTON UNIVERSITY
SEVER INSTITUTE OF TECHNOLOGY
DEPARTMENT OF CHEMICAL ENGINEERING

CHARACTERIZATION OF SINGLE AND MULTIPHASE FLOWS
IN STIRRED TANK REACTORS

by

Aravind R. Rammohan

Prepared under the direction of Professor M. P. Dudukovic' and Dr.V. V.Ranade

A dissertation presented to the Sever Institute of
Washington University in partial fulfillment
of the requirements of the degree of
DOCTOR OF SCIENCE

December ,2002

Saint Louis, Missouri

UMI Number: 3083584

UMI[®]

UMI Microform 3083584

Copyright 2003 by ProQuest Information and Learning Company.
All rights reserved. This microform edition is protected against
unauthorized copying under Title 17, United States Code.

ProQuest Information and Learning Company
300 North Zeeb Road
P.O. Box 1346
Ann Arbor, MI 48106-1346

WASHINGTON UNIVERSITY
SEVER INSTITUTE OF TECHNOLOGY
DEPARTMENT OF CHEMICAL ENGINEERING

ABSTRACT

CHARACTERIZATION OF SINGLE AND MULTIPHASE FLOWS
IN STIRRED TANK REACTORS

by Aravind R. Rammohan

ADVISORS: Professor M. P. Dudukovic'and Dr. V. V. Ranade

December, 2002

St. Louis, Missouri

Stirred tank reactors are used extensively in industry and most often involve multiphase flows. The fluid dynamics in stirred tanks of even single phase flow is extremely complex due to presence of rotating internals and regions of large velocity gradients. In this study, the Computer Automated Radioactive Particle Tracking (CARPT) technique was implemented successfully to characterize such complex flows in a standard baffled tank equipped with the Rushton turbine. CARPT was shown to capture the key features associated with single phase flow like the presence of a radial jet in the impeller region and the recirculating loops above and below the impeller. In addition to providing standard Eulerian fluid dynamic measures, CARPT also provided valuable new "Lagrangian" information to the modeling community, like sojourn time distributions in different zones of the tank, return time distributions to the impeller region, Hurst

exponents, etc. “Dynamic bias” was shown to become significant in the CARPT measured velocities when the flow time scales are 10-50 times lower than the data acquisition time, and a systematic experimental effort enabled the quantification of this effect leading to a needed correction factor. A Monte Carlo based model was developed which allows a priori prediction of this effect in large industrial systems. The issue of “flow followability of the tracer” was also addressed by performing novel numerical experiments which allowed a systematic evaluation of the effect of tracer size and density on their ability to follow the fluid.

The predictive capabilities of two quasi steady computational fluid dynamic (CFD) approaches, the multiple reference frame (MRF) and the Snapshot approach were evaluated. Both of these approaches were shown to predict the single phase flow field reasonably well with no experimental inputs. Both approaches can be extended to simulate multiphase flows and offer promise as valuable design tools.

Gamma ray computed tomography (CT) and Computer Automated Radioactive Particle Tracking (CARPT) were then used to provide detailed local gas holdup profiles and liquid velocity distributions in two phase flows in the same stirred tank. Such data are currently not available and this thesis has initiated the creation of a reliable database, which when extended to include different impeller types and flow conditions, should be useful. CT is shown to capture the internals of the reactor and features of the flow, like gas jets emerging from the sparger etc.

The CARPT technique was shown to identify the regime transitions in stirred tank reactor by capturing the changes in the liquid flow structure. The detailed liquid velocity profiles obtained from CARPT provide valuable inputs to compartmental models, like number of compartments to use, location and size of compartments, residence time distributions of liquid in these compartments, liquid flow rate between compartment to compartment etc. for reactor design of stirred tanks.

Attempts at CFD simulations of gas – liquid flows in stirred tanks revealed that physically based closures for liquid – gas drag, which account for background turbulence, are currently lacking and must be developed. Current drag closures predict unrealistically high values of the slip velocity between the gas and liquid. This limits the ability of the current CFD models to predict gas phase recirculation correctly.

Contents

List of Tables.....	vii
List of Figures.....	ix
Nomenclature.....	xix
Acknowledgements.....	xxii
1. Introduction.....	1
1.1 Motivation for the Research.....	1
1.2 Research Objectives.....	3
1.3 Structure of Thesis.....	3
2. Background.....	4
2.1 Review of Single Phase Flow Measurements in STR.....	4
2.2 Single Phase Flow Modeling.....	22
2.2.1 Numerical Solution of the Navier Stokes Equations...	22
2.2.2 Models for Turbulence.....	30
2.3 Multiphase flows - Experimental Characterization.....	31
2.4 Multiphase flows - Numerical Simulations.....	33
3. A Lagrangian Description of Flows in Stirred Tanks via Computer Automated Radioactive Particle Tracking (CARPT)	39
3.1 Introduction.....	39
3.2 Experimental Set up.....	39
3.2.1 The Stirred Vessel.....	39
3.2.2 The CARPT Set -up.....	40
3.2.3 The CARPT Technique.....	43
3.3 Measurement Errors.....	44
3.3.1 Tracer Ability to Follow the Liquid.....	44
3.3.2 Statistical Nature of Gamma Photons.....	46
3.3.3 Solid Angle Effect.....	47
3.4 Experimental Conditions.....	47
3.5 Results and Discussion.....	48
3.5.1 Validity of Experimental Data.....	48
3.5.2 Location of the Eye of the Recirculating Loops.....	49
3.5.3 Mapping the Dead Zones in the Stirred Tank.....	49
3.5.4 Partial Quantification of Dead Zones Using Sojourn Time Distributions (STDs).....	52
3.6 Summary and Conclusions.....	59
4. Characterization of Single Phase Flows in Stirred Tanks via Computer Automated Radioactive Particle Tracking (CARPT)	60
4.1 Introduction.....	60

4.2	Results and Discussions.....	60
4.2.1	Grid Independence of Computed Mean Quantities.....	61
4.2.2.	Comparison of Radial Pumping Numbers from CARPT with Data in the Literature.....	63
4.2.3	Comparison of Mean Radial Velocity in the Impeller Stream Obtained by CARPT with Data from the Literature.....	65
4.2.4	Comparison of Mean Tangential Velocity in the Impeller Stream from CARPT with Experimental Data in the Literature.....	69
4.2.5	Comparison of Turbulent Kinetic Energies in the Impeller Stream from CARPT with Data from the Literature.....	72
4.2.6.	Reynolds Shear Stress Distributions from CARPT.....	77
4.2.7	Lagrangian Measures of the Fluid Dynamics in STR....	78
	4.2.7.1 Circulation Time Distributions (CTD) and Mean Circulation Times (MCT).....	78
	4.2.7.2 Hurst Exponents from Particle Trajectories.....	79
4.3	CFD simulations.....	80
4.3.1	Comparison of Mean Radial Velocity in the Impeller Stream Obtained by CARPT with CFD Simulations.....	82
4.3.2	Comparison of Mean Tangential Velocity in the Impeller Stream from CARPT with CFD Simulations.....	83
4.3.3	Comparison of Turbulent Kinetic Energies in the Impeller Plane from CARPT with CFD Simulations.....	85
4.4	Summary and Conclusions.....	86
5.	Characterization of Errors in CARPT through Experiments.....	88
5.1	Evaluation of Tracer Position Reconstruction Strategies.....	88
	5.1.1 Introduction.....	88
	5.1.2 Background.....	89
	5.1.3 Results and Discussions.....	93
	5.1.3.1 A Look-up Table Approach.....	93
	5.1.3.2 Full Monte Carlo Approach.....	98
	5.1.3.3 A New Data Acquisition Strategy.....	102
	5.1.4 Conclusions.....	110
5.2	CARPT Dynamic Bias Studies: Evaluation of Accuracy of Position and Velocity Measurements.....	110
	5.2.1 Introduction.....	110
	5.2.2 The Dynamic Bias Issue.....	111
	5.2.3 Experimental Details.....	114
	5.2.4 Details of Numerical Technique.....	115
	5.2.5 Results and Discussions.....	118
	5.2.5.1 Variation of Radial Bias with Data Acquisition Rate	118
	5.2.5.2 Determination of Optimal Data Acquisition Rate	119
	5.2.5.3 Limits on Data Sampling Rates.....	121

	5.2.5.4 Simulated Effect of Sampling Rate.....	123
	5.2.6 Conclusions.....	125
6	Eulerian Flow Field Estimation from Particle Trajectories: Numerical Experiments.....	126
	6.1 Introduction.....	126
	6.2.0 Details of the Simulations.....	127
	6.2.1 Eulerian Flow Field Simulations.....	127
	6.2.1.1 Computational Model.....	128
	6.2.2. Lagrangian Particle Tracking.....	132
	6.2.2.1 Modeling Unsteady Drag Terms.....	133
	6.2.2.2 Modeling Effect of Fluid Turbulence on the Tracer Particle	135
	6.2.2.3 Details of Trajectory Calculation.....	137
	6.2.2.4 Estimating the Eulerian Flow Field from Lagrangian Trajectories Using CARPT Processing Programs.....	138
	6.3.0 Results and Discussions.....	140
	6.3.1 Role of Lift Force.....	142
	6.3.2 Sensitivity to Random Walk Model.....	145
	6.3.3 Effect of CARPT Grid.....	148
	6.3.4 Effect of Particle Density and Size.....	156
	6.3.4.1 Role of Particle Density.....	160
	6.4.0 Summary and Conclusions.....	162
7	Characterization of Gas – Liquid Flow Structures in Stirred Tank Reactors via Computer Automated Radioactive Particle Tracking (CARPT) and Computed Tomography (CT).....	165
	7.1 Introduction.....	165
	7.2 Review of Previous Experimental Measurements.....	166
	7.2.1 Qualitative Characterization of Flow through Photographic Studies.....	166
	7.2.2 Classification of Cavity Structures.....	169
	7.2.3 Power Consumption Measurements.....	173
	7.2.4 Overall Gas Holdup Measurements.....	178
	7.2.5 Local Gas Holdup Measurements.....	179
	7.2.6 Local Bubble Size Measurements.....	182
	7.2.7 Liquid Velocity Measurements.....	184
	7.3 Experimental Studies.....	184
	7.3.1 Details of Computed Tomography (CT).....	184
	7.3.2. Data Analysis Algorithm.....	186
	7.3.3 Details of the CT Scanner at CREL.....	188
	7.3.4 Sources of Errors in CT Measurements.....	192
	7.3.5 Details of the Stirred Tank Set-up.....	193
	7.3.6. Experimental Conditions.....	194
	7.4 Results and Discussions.....	195
	7.4.1 Qualitative Analysis of Gas Holdup and Velocity Distributions.....	197

7.4.1.1	Analysis of Gas Holdup Distributions in the Stirred Tank Reactor.....	197
7.4.1.1.1	Analysis of Contours of Gas Holdups.....	197
7.4.1.1.2	Variation of Average Gas Holdups with Impeller Speeds and Gas Sparging Rates.....	200
7.4.1.2	Analysis of Liquid Velocity Distributions Obtained with CARPT.....	202
7.4.2	Quantitative Characterization of Gas Holdup Distributions and Liquid Velocity Field.....	208
7.4.2.1	Azimuthally Averaged Radial Gas Holdup Distributions.....	208
7.4.2.2	Liquid Velocity Distributions from CARPT.....	211
7.5	Gas Liquid Flow Simulations via Snapshot Approach.....	220
7.5.1	Results and Discussions.....	221
7.6	Conclusions.....	225
8	Summary,Conclusions and Recommendations.....	229
8.1	Recommendations for Future Research.....	233
Appendix A	Grid Independence of Computed Mean Quantities from CARPT.....	236
Appendix B	Dynamic Bias in CT.....	244
B.1	Approach.....	245
B.2	Forward Problem.....	246
B.3	Backward Problem.....	247
B.4	Implementation.....	247
B.5	Results and Discussion of Dynamic Bias Error.....	248
B.5.1	Dynamic Bias in N*N Pixels.....	248
B.6	Conclusions on the Dynamic Bias in CT.....	251
Appendix C	Gas Holdup Variation in STR from Computed Tomography..	253
C.1	Analysis of Contours of Gas Holdup.....	253
References.....		258
Vita		277

LIST OF TABLES

2-1	Evaluation of Single Phase Experimental Techniques.....	7
2-2	Review of Single Phase Measurements in Stirred Tank Reactor...	9
2-2(a)	Parametric Sensitivity of Fluid Dynamic Measurements in Stirred Tanks Reported by Rutherford et al. (1996).....	9
2-2(b)	Parameters of the Systems Used for Validation in this Study.....	10
2-2(c)	Verification of Mass Balance.....	12
2-2(d)	Location of Eye of Circulation Loops.....	18
2-2(e)	Independence of Dimensionless Mean and Turbulent Kinetic Energy with Scale and Re.....	18
2-2(f)	Extent of Periodicity.....	19
2-2(g)	Trailing Vortex Characterization.....	19
2-2(h)	Radial Pumping Number.....	19
2-2(i)	Maximum Mean Velocities and Turbulent Kinetic Energy.....	20
2-2(j)	Data Acquisition Rates and Accuracy of Measurement.....	21
2-3	Summary of Equations Used for the MRF and the SA Models...	25
2-4	Models that Numerically Solve for the Flow in Stirred Tanks....	28
3-1	Location of the Eye of Circulation Loops ($T= D=$ tank diameter).	50
3-2	Different Moments of the STD Curves in Various Axial Zones in a Batch Stirred Tank.....	57
4-1	Details of the Grids Examined in this Study.....	61
4-2	Comparison of Radial Velocities at the Impeller Tip.....	66
4-3	Comparison of recent reports of Radial Velocities at the Impeller Tip from LDA Measurements with CARPT.....	68
4-4	Comparison of Tangential Velocities at the Impeller tip.....	70

4-5	Comparison of Tangential Velocities at the Impeller Tip from LDA Measurements with CARPT.....	71
4-6	Comparison of Radial Turbulent Velocities at the Impeller tip...	73
4-7	Comparison of Tangential Turbulent Velocities at the Impeller tip.....	75
4-8	Comparison of CFD predictions of Radial Velocities at the Impeller Tip.....	83
4-9	Comparison of CFD predictions of Tangential Velocities at the Impeller Tip.....	84
5-1	Calibration Information Organized as a Lookup Table.....	95
5-2(a)	Reconstruction Accuracy Using Model M_1	97
5-2(b)	Reconstruction Accuracy Using Model M_2	98
5-3	Summary of Reconstruction Accuracy of 36 Test Locations (1 Radial Location, 3 Axial Locations and 12 Angular Locations)..	107
5-4	Summary of Reconstruction Accuracy of 36 Test Locations (1 Radial Location, 3 Axial Locations and 12 Angular Locations) After Hiding 8 Detectors.....	107
6-1	Initial Conditions for Particle Tracking Algorithm.....	132
6-2	Gridding Schemes Used for Recovering Eulerian Information from Lagrangian Trajectory Data.....	149
6-3	Comparison of Time Scales of Light and Heavy Tracer.....	160
A-1	Details of the Grids Examined in this Study.....	236
B-1	True Time Averaged Distribution for Input Type 1.....	250
B-2	Reconstructed Time Averged Holdup for Input of Type 1.....	250

List Of Figures

2-1	Classical Flow Structure in Stirred Tank Reactors.....	4
2-2	Details of the Stirred Tank Internals.....	5
2-3	Effect of Blade and Disc Thickness Ratio on Mean Radial Velocity at $r/T=0.17$	11
2-4	Effect of Blade and Disc Thickness Ratio on the Radial Root Mean Squared Velocity at $r/T=0.17$, Rutherford et. al.(1996).....	11
2-5(a)	Schematic Depicting Ensemble Averaged Measurement in STR.....	14
2-5(b)	Schematic Depicting Phase Averaged Measurement in STR.....	15
2-6	Comparison of Predicted Radial Profiles of Axial Mean Velocity (liquid) with Experimental Data at $z/R=0.33$ and $Q_g=8$ l/min.....	34
2-7	Comparison of Predicted Radial Profiles of Tangential Mean Velocity (Liquid) with Experimental Data at $z/R=0.33$ and $Q_g=8$ l/min.....	35
2-8	Comparison of Predicted Radial Profiles of Turbulent Kinetic Energy with Experimental Data at $z/R=0.33$ and $Q_g=8$ l/min.....	36
2-9	Comparison of Predicted Drop in Power Consumption at Different Gas Flow Rates.....	36
2-10	Comparison of Predicted Overall Gas Holdup with Experimental Data	37
3-1	Stirred Tank of the Holland-Chapman Type Used for the CARPT Experimental Study.....	40
3-2(a)	Top View of CARPT Set-up for the Stirred Tank.....	41
3-2(b)	Front View of CARPT Set-up for the Stirred Tank.....	42
3-3	Details of the CARPT Tracer Particle.....	42
3-4	Details of Calibration Procedure.....	44
3-5	Calibration Map for Detector #1.....	45

3-6	Projection of the Particle Trajectory in a Vertical Plane at $N=150$ rpm for 30 s.....	46
3-7	Projection of the Reconstructed Particle Position at $N=150$ rpm (Top View for 1 hr of the 16 hr Run).....	48
3-8	Azimuthally Averaged Velocity Vector plot at $N=150$ rpm.....	50
3-9(a)	Dead zones from Flow Visualization Studies (Kemoun, 1995).....	51
3-9(b)	Map of Dead Zones from CARPT.....	52
3-10	Compartmentalization of the Stirred Tank into Axial Zones.....	53
3-11	Probability Density Functions of the Sojourn Time Distributions in Different Axial Zones of the STR from CARPT Data.....	56
3-12	Axial Variation of the Mean and of the Standard Deviation of the STDs.....	56
3-13	Axial Variation of the Skewness and Kurtosis of the STDs.....	58
4-1(a)	Radial Profile of Radial Velocity at $Z_2= D/3$	62
4-1(b)	Axial Profile of Axial Velocity at $r_1= D/6$	62
4-1(c)	Radial Profile of Tangential Velocity at $Z_2= D/3$	63
4-2	Radial Profile of Radial Pumping Number.....	64
4-3	Radial Velocity Profile in the Impeller Stream.....	66
4-4	Axial Profile of Radial Velocity at the Impeller Tip.....	67
4-5	Radial Profile of Tangential Velocity in the Impeller Stream.....	69
4-6	Axial Variation of the Tangential Velocity in the Impeller Stream at the Impeller Tip.....	71
4-7	Axial Profiles of V_r'/V_{tip} in the Impeller Plane.....	73
4-8	Axial Profile of V_θ'/V_{tip} in the Impeller Plane.....	74
4-9	Profiles of Turbulent Kinetic Energy.....	75
4-10	Fraction of Total Turbulent Energy Associated with a Particular Range of Frequency (0-f).....	76
4-11(a)	Contours of Reynolds Shear Stresses in the Plane Including the Baffles.....	77
4-11(b)	Visualization of Trailing Vortices using Fluorescent Fluid.....	78

4-12	Circulation Time Distribution in the Impeller Region at N=150 rpm....	79
4-13	Hurst Exponents from the Lagrangian Particle Position $r(t)$ in STR.....	80
4-14	View of 3-D grid Used for MRF and Snapshot Simulations.....	81
4-15	Comparison between Predicted and Measured Radial Velocity Profile in the Impeller Stream.....	82
4-16(a)	Comparison between Predicted and Measured Radial Profile of Tangential Velocity.....	84
4-16(b)	Comparison of CFD Predicted Tangential Velocity with LDA Data....	85
4-17	Comparison between Predicted and Measured Radial Profile of Turbulent Kinetic Energy.....	86
5-1	Calibration Map Obtained in a Plexi Glass Stirred Tank Reactor.....	89
5-2	Calibration Map Obtained in the Stainless Steel Reactor.....	91
5-3	Reconstruction of 3528 Known Calibration Points.....	92
5-4	Reconstruction of Unknown Test Points Located at ($r = 0$ cm, $\theta = 0^\circ$, z $= 5.13$ cm).....	93
5-5	Generation of a Fine Grid of Calibration Data Either by Monte Carlo Simulations or through Experiments.....	94
5-6	Reconstruction of 3528 Known Calibration Points.....	96
5-7	Generate a Fine Mesh Around Closest Node.....	96
5-8	Comparison between Measured and Simulated Counts.....	99
5-9(a)	Photo Energy Spectrum Obtained in a Plexiglass Column.....	100
5-9(b)	Photo Energy Spectrum Obtained in a Stainless Steel Reactor.....	100
5-10	Comparison between Measured and Simulated Counts.....	101
5-11	Calibration Curve Obtained in S.S. Column by Acquiring Photopeak Fraction Alone.....	103
5-12	Reconstruction of 396 Known Calibration Points Projected Onto an r - z Plane.....	104
5-13	Details of Reconstructing 12 Test Points ($r=7.2$ cm, $\theta=15^\circ$ - 345° , $z=5.0$ cm) from 3072 Instantaneous Samples Acquired at 50 Hz.....	105
5-14	Variation in σ_r and σ_z with the Sampling Frequency.....	106

5-15	Analyze Effect of Detector Configuration on Reconstruction Accuracy	108
5-16(a)	Variation of Radial and Axial Bias with Number of Detectors Used for Reconstruction.....	109
5-16(b)	Variation of σ_r and σ_z with Number of Detectors Used for Reconstruction.....	109
5-17	Calibration Map for Detector #1.....	112
5-18	Cartoon Illustrating the Concept of ‘Dynamic Bias’	113
5-19	Dimensions of Stirred Tank Reactor.....	114
5-20	Modeling Internals using Monte Carlo Simulation.....	116
5-21	Parity Plot of Predicted vs Measured Calibration Counts Registered by Detector #1.....	117
5-22	Variation of Radial Bias with Data Sampling Rate ($V_{tip} = 0.21 - 2.79$ m/s).....	118
5-23	Variation of Estimated V_θ/V_{tip} vs Data Sampling Rate ($V_{tip} = 1.05 - 2.79$ m/s).....	120
5-24	Errors in CARPT due to Nature of Experimental Technique.....	121
5-25	Simulated Dynamic Distance vs Count Map for Detector #1.....	124
6-1(a)	2-D Domain with Boundary Conditions.....	127
6-1(b)	Details of Grid.....	130
6-2(a)	Grid Dependence of Horizontal Velocities.....	131
6-2(b)	Grid Dependence of Turbulent Kinetic Energy.....	131
6-3	Snapshots of Simulated Particle Trajectories at Different Instants in Time.....	139
6-4(a)	2 –D vector plot from Lagrangian Trajectories.....	140
6-4(b)	2 – D Contour of Turbulent Kinetic Energy from Lagrangian Trajectories.....	141
6-5	Sequence of Numerical Experiments.....	141
6-6(a)	Sensitivity of Lagrangian Estimate of Horizontal Velocity Obtained with Heavy Tracer with Lift Force.....	143

6-6(b)	Sensitivity of Lagrangian Estimate of Vertical Velocity Obtained with Heavy Tracer with Lift Force	143
6-6(c)	Sensitivity of Lagrangian Estimate of Turbulent Kinetic Energy Obtained with Heavy Tracer with Lift Force.....	143
6-7(a)	Sensitivity of Horizontal Velocities Obtained with Neutrally Buoyant Tracer with and without Lift Force.....	144
6-7(b)	Sensitivity of Vertical Velocities Obtained with Neutrally Buoyant Tracer with and without Lift Force.....	144
6-7(c)	Sensitivity of Turbulent Kinetic Energy Obtained with Neutrally Buoyant Tracer with and without Lift Force.....	145
6-8(a)	Velocity Estimates Obtained with DRW and CRW Turbulence Models.....	146
6-8(b)	Turbulent Kinetic Energy Estimates Obtained with DRW and CRW Turbulence Models.....	146
6-9(a)	Sensitivity of Return Time Distributions to Turbulence Model (CRW or DRW).....	147
6-9(b)	Sensitivity of Return Time Distributions to Particle Density.....	147
6-10	Comparison of Eulerian Velocity (Eul) with Lagrangian Estimates Obtained with Half (ha200) and Quarter (q200) Grids.....	150
6-11(a)	Variation of Fractional Occurence with Sampling Frequency for Half Grid	151
6-11(b)	Variation of Fractional Occurence with Sampling Frequency for Original Grid.....	151
6-12(a)	Variation of Horizontal Velocity with Sampling Frequency for Half Grid.....	153
6-12(b)	Variation of Horizontal Velocity with Sampling Frequency for Original Grid.....	154
6-13(a)	Comparison of Horizontal Variation of Turbulent Kinetic Energy Obtained with Quarter (q200) and Half (ha200) Grids at 200Hz.....	155

6-13(b)	Comparison of Vertical Variation of Turbulent Kinetic Energy Obtained with Quarter (q200) and Half (ha200) Grids at 200Hz.....	155
6-14(a)	Horizontal Velocity Estimates Obtained with Dense and Large Particle on Quarter (r3_quart) and Half (r3_half) Grids.....	157
6-14(b)	Vertical Velocity Estimates Obtained with Dense and Large Particle on Quarter (r3_quart) and Half (r3_half) Grids.....	157
6-15(a)	Sensitivity of Lagrangian Estimates to Density of Tracer (r3 = Heavier Tracer).....	158
6-15(b)	Sensitivity of Lagrangian Estimates to Size of Neutrally Buoyant Tracer.....	158
6-16(a)	Effect of Particle Density on Lagrangian Estimate of Horizontal Velocity.....	161
6-16(b)	Effect of Particle Density on Lagrangian Estimate of Vertical Velocity	161
6-16(c)	Effect of Particle Density on Lagrangian Estimate of Turbulent Kinetic Energy.....	162
7-1	Mechanism of Cavity Formation.....	167
7-2	Stable Cavity Formed at Higher Impeller Speeds and Gas Sparging Rates (Reproduced from Bruijn, et. al., 1974).....	168
7-3	Flow Regime Map for CT+CARPT+CFD Data Obtained in Stirred Tank Reactor	172
7-4	Change in RPD with Increasing Gas Sparging Rate at Fixed Impeller Speed.....	174
7-5	Reduction of Power Uptake by Single Impeller in a Gassed STR from Warmoeskerken, 1986 (T=1.2m, D=0.48m, H=T).....	177
7-6	Comparison of Power Uptake Predicted by Cui et. al. Correlation with other Correlations.....	178
7-7(a)	Radial Profile of Gas Holdup at Impeller Plane at Fr=0.29 and Fl=0.05, 0.09 and 0.12.....	180
7-7(b)	Radial Profile of Gas Holdup at Z/T=0.4 at Fr=0.29 and Fl=0.05,0.09 and 0.12.....	181

7-8	Bubble Size and RPD Variation with Fl at Impeller Tip (Lu et. al., 1993)	183
7-9	Schematic of CT Beam Passing through one Pixel.....	186
7-10	Schematic Diagram of the CREL Computer Tomography Scanner with the STR Installation (Front View).....	189
7-11	Schematic Top View of the CREL Computer Tomography (CT) Scanner with the Stirred Tank Installation, at One Specific Location of the Gantry Plate (Note that Dimensions and Angles are not to Scale and have been Exaggerated for Clarity).....	190
7-12	Details of New Collimator Used for Current Study.....	191
7-13	The Adjusted Photoenergy Spectrum of the Radiation Emitted by Cs^{137} Received by the Seven Detectors.....	191
7-14	Details of Sparger Design.....	193
7-15	Details of the Stirred Tank Set-up Used for Gas –Liquid Studies.....	194
7-16	Reconstruction of Internals of the Stirred Tank Reactor.....	195
7-17	CT Scan of the Plane Just Above the Sparger ($Z=5.0$ cm, $Z/T=0.25$)..	196
7-18(a)	Gas Holdup Distribution at $Fl=.112$, $Fr=0.042$ ($N=150$ rpm, $Q=5.0$ l/min) and $Z=5.0$ cm ($Z/T=0.25$).....	198
7-18(b)	Gas Holdup Distribution at $Fl=.112$, $Fr=0.042$ ($N=150$ rpm, $Q=5.0$ l/min) and $Z=10.0$ cm ($Z/T=0.5$).....	198
7-18(c)	Gas Holdup Distribution at $Fl=.112$, $Fr=0.042$ ($N=150$ rpm, $Q=5.0$ l/min) and $Z=15.0$ cm ($Z/T=0.75$).....	199
7-19(a)	Variation of Overall Gas Holdup with Gas Sparging Rate at Different Impeller Speeds.....	200
7-19(b)	Comparison of Overall Holdup from CT with Predictions of Correlations.....	201
7-20	Azimuthally Averaged V_r - V_z Plot at $Fl=0.042$ and $Fr=0.0755$ ($N=200$ rpm, $Q= 2.5$ l/min, S33 Regime).....	202
7-21	Azimuthally Averaged V_r - V_z Plot at $Fl=0.084$ and $Fr=0.0755$ ($N=200$ rpm, $Q= 5.0$ l/min, RC Regime).....	203

7-22	Azimuthally Averaged V_r - V_z Plot at $Fl=.112$ and $Fr=0.042$ ($N=150$ rpm, $Q= 5.0$ l/min, RC Regime).....	204
7-23	Azimuthally Averaged V_r - V_θ Plot at $Fl=0.042$ and $Fr=0.0755$ ($N=200$ rpm, $Q= 2.5$ l/min, S33 Regime) at $Z=0$ cm ($Z/T=0$).....	205
7-24	Azimuthally Averaged V_r - V_θ Plot at $Fl=0.042$ and $Fr=0.0755$ ($N=200$ rpm, $Q= 2.5$ l/min, S33 Regime) at $Z=4.0$ cm ($Z/T=0.2$).....	206
7-25	Azimuthally Averaged V_r - V_θ Plot at $Fl=0.042$ and $Fr=0.0755$ ($N=200$ rpm, $Q= 2.5$ l/min, S33 Regime) at $Z=6.66$ cm ($Z/T=0.33$).....	207
7-26(a)	Influence of Gas Sparging Rates on the Radial Variation of Gas Holdup at $Fr=0.019(N=100$ rpm), $Z/T=0.25$	208
7-26(b)	Influence of Gas Sparging Rates on the Radial Variation of Gas Holdup at $Fr=0.019(N=100$ rpm), $Z/T=0.5$	209
7-26(c)	Influence of Gas Sparging Rates on the Radial Variation of Gas Holdup at $Fr=0.019$ ($N=100$ rpm), $Z/T=0.75$	210
7-27(a)	Radial Profile of Radial Liquid Velocity at Sparger Plane $Z=3.75$ cm	212
7-27(b)	Radial Profile of Radial Liquid Velocity at Impeller Plane $Z=6.75$ cm	213
7-28(a)	Radial Profile of Tangential Liquid Velocity at Sparger Plane $Z=3.75$ cm.....	213
7-28(b)	Radial Profile of Tangential Liquid Velocity at Impeller Plane, $Z=6.75$ cm	214
7-29(a)	Radial Profile of Axial Liquid Velocity at Sparger Plane $Z=3.75$ cm...	215
7-29(b)	Radial Profile of Axial Liquid Velocity at $Z=10.25$ cm.....	216
7-30(a)	Axial Profile of Radial Liquid Velocity at $r=2.0$ cm.....	217
7-30(b)	Axial Profile of Radial Liquid Velocity at $r=3.75$ cm.....	217
7-30(c)	Axial Profile of Radial Liquid Velocity at $r=6.25$ cm.....	218
7-31(a)	Axial Profile of Tangential Liquid Velocity at $r=2.0$ cm.....	218
7-31(b)	Axial Profile of Tangential Liquid Velocity at $r=3.75$ cm.....	219
7-32	Radial Profile of Turbulent Kinetic Energy at the Impeller Plane.....	220
7-33(a)	Predicted Flow Field for N3Q1 Case. Left: Vectors of Liquid Phase; Right: Vectors of Gas Phase.....	222

7-33(b)	Predicted Flow Field for N3Q3 case. Left: Vectors of Liquid Phase; Right: Vectors of Gas Phase.....	222
7-34(a)	Predicted Flow Field at N3Q1. (Left: Contours of Turbulent Kinetic Energy; Right: Contours of Gas Holdup). Ten Uniform Contours of Maximum Value =0.1 (Black) and Minimum Value =0 (Blue).....	223
7-34(b)	Predicted Flow Field at N3Q3. (Left: Contours of Turbulent Kinetic Energy; Right: Contours of Gas Holdup). Ten Uniform Contours of Maximum Value =0.6 (Black) and Minimum Value =0 (Blue).....	223
A-1(a)	Radial Profile of Radial Velocity at $Z_1 = D/5$	237
A-1(b)	Radial Profile of Radial Velocity at $Z_2 = D/3$	237
A-1(c)	Radial Profile of Radial Velocity at $Z_3 = D/2$	238
A-1(d)	Axial Profile of Radial Velocity at $r_1 = D/6$	238
A-1(e)	Axial Profile of Radial Velocity at $r_2 = D/3$	238
A-1(f)	Axial Profile of Radial Velocity at $r_3 = 2D/5$	239
A-2(a)	Radial Profile of Axial Velocity at $Z_1 = D/5$	239
A-2(b)	Radial Profile of Axial Velocity at $Z_2 = D/3$	239
A-2(c)	Radial Profile of Radial Velocity at $Z_3 = D/2$	240
A-2(d)	Axial Profile of Axial Velocity at $r_1 = D/6$	240
A-2(e)	Axial Profile of Axial Velocity at $r_2 = D/3$	240
A-2(f)	Axial Profile of Axial Velocity at $r_3 = 2D/5$	241
A-3(a)	Radial Profile of Tangential Velocity at $Z_1 = D/5$	241
A-3(b)	Radial Profile of Tangential Velocity at $Z_2 = D/3$	241
A-3(c)	Radial Profile of Tangential Velocity at $Z_3 = D/2$	242
A-3(d)	Axial Profile of Tangential Velocity at $r_1 = D/6$	242
A-3(e)	Axial Profile of Tangential Velocity at $r_2 = D/3$	242
A-3(f)	Axial Profile of Tangential Velocity at $r_3 = 2D/5$	243
B-1	Schematic of Radiation Received by Detector Traveling through Column Media.....	245
B-2	Details of Simulated Gas Holdup Fraction.....	247
B-3	The Parameters are $\Delta t = 0.01s$; $\tau = 0.0327s$, $Al_{av} = 1.25$, $N_{sample} = 100$	249

B-4	Comparison of True Time Average with Reconstructed Time Average for Input of Type 1 on a 4 X 4 Pixel.....	249
B-5	The Parameters are $\Delta t=1e-3$ s; $\tau= 0.0327$ s, $Al_{av}=0.125$, $N_{sample}=100$...	251
B-6	The Parameters are $\Delta t=1e-2$ s; $\tau=0.00327$ s, $Al_{av}=0.123$, $N_{sample}=100$...	251
C-1(a)	Gas Holdup Distribution at $Fl = 0.042$ and $Fr = 0.0755$ ($N = 200$ rpm, $Q = 2.5$ l/min) and $Z = 5.0$ cm.....	253
C-1(b)	Gas Holdup Distribution at $Fl = 0.042$ and $Fr = 0.0755$ ($N = 200$ rpm, $Q = 2.5$ l/min) and $Z = 10.0$ cm.....	254
C-1(c)	Gas Holdup Distribution at $Fl = 0.042$ and $Fr = 0.0755$ ($N = 200$ rpm, $Q = 2.5$ l/min) and $Z = 15.0$ cm.....	254
C-2(a)	Gas Holdup Distribution at $Fl = 0.0842$ and $Fr = 0.0755$ ($N = 200$ rpm, $Q = 5.0$ l/min) and $Z = 5.0$ cm.....	255
C-2(b).	Gas Holdup distribution at $Fl = 0.0842$ and $Fr = 0.0755$ ($N = 200$ rpm, $Q = 5.0$ l/min) and $Z = 10.0$ cm.....	255
C-2(c)	Gas Holdup Distribution $Fl = 0.0842$ and $Fr = 0.0755$ ($N = 200$ rpm, $Q = 5.0$ l/min) and $Z = 15.0$ cm.....	256

Nomenclature

Chapter 3

D, T, D_T	Tank Diameter (cm)
D_i	Impeller Diameter (cm)
H_T	Height of Liquid in tank (cm)
N	Rpm
r, R	radial distance (cm)
V_r	mean radial velocity (cm/s)
V_θ	mean tangential velocity (cm/s)
V_z	mean axial velocity (cm/s)
Z	Axial Distance
Re	Reynolds Number
t	time in seconds

Greek symbols

Δ	Incremental change
μ	First moment of the STD
σ^2	Second moment of the STD
γ_1	Third moment of the STD
γ_2	Fourth moment of the STD

Chapter 4

d_p	particle diameter in mm
D	Tank diameter in m
D_I	Impeller diameter in m
C_i	Curies unit of Radioactivity
Re_{imp}	Impeller diameter based Reynolds number
r	Radial distance in m
N	Number of Revolutions made by the impeller in one minute
N_{QP}	Dimensionless Radial Pumping Number
t_b	blade thickness in m
t_{DI}	Impeller disc thickness in m
R_I	Radius of impeller in m
V_r	Eulerian Mean radial velocity in m/s
V_{tip}	Impeller tip speed $-\pi * D_I * N$ (in revolutions per second)
V_θ	Eulerian mean tangential velocity in m/s
w	Blade width in m
V_r'	Radial root mean squared velocity (rms) in m/s
V_θ'	Tangential rms in m/s
TKE	Dimensionless Turbulent Kinetic Energy
H	Hurst Exponent

Chapter 5

C_D	Drag Coefficient
k	Turbulent kinetic energy, $(m/s)^2$
Fl	Radial pumping number
D	Impeller diameter, m
Q_{liq}	Flow rate, m^3/s
$A_{impeller}$	Area of impeller, m^2
X	Horizontal co-ordinate, m

Y	Vertical co-ordinate, m
U	Horizontal velocity, m/s
V	Vertical velocity, m/s
u_p	instantaneous particle velocity, m/s
u	instantaneous fluid velocity, m/s
\bar{U}	Fluctuating horizontal velocity, m/s
\bar{V}	Fluctuating vertical velocity, m/s
V_{reactor}	Volume of reactor, m^3
Δx	grid size in horizontal direction, m
V_{tip}	Velocity at tip of impeller, m/s
r_{impeller}	radius of impeller, m
d_p	particle diameter, m

Greek symbols

ρ_{tracer}	Density of tracer, kg/m^3
ρ_{fluid}	Density of fluid, kg/m^3
ε	Dissipation rate, m^2/s^3
μ	molecular viscosity, $\text{kg}/(\text{m}^2\text{s})$
μ_t	turbulent viscosity, $\text{kg}/(\text{m}^2\text{s})$
τ_{process}	Process time, s
τ_{sample}	Sampling time, s

Acknowledgements

I would like to thank Professor M.P.Dudukovic' my doctoral advisor for his support from the first day of my study at Washington University in St.Louis. Professor Dudukovic has been a source of constant inspiration by the high standards of work he sets both for himself and the standards he expects of his students. This D.Sc experience has been extremely enjoyable due to my interactions with Professor Dudukovic. He has been an excellent teacher in more ways than one. He has provided numerous opportunities to satisfy my desire for learning.

I would like to thank Dr.V.V.Ranade my co-advisor for his constant guidance throughout this thesis. He has been a source of huge support and has been much more than a thesis advisor. It has been a source of great joy to work with Dr.Ranade and learn from him his way of doing research. My early days at National Chemical Laboratory form the most memorable part of my research experience and this is largely due to him.

I would like to thank Dr.Muthanna Al Dahhan who gave me an excellent opportunity to teach his undergraduate laboratory. He was perceptive of my ideas and gave full freedom to try out new things in his lab. He has at different times taken the extra effort to reach out as a friend.

I wish to thank all the members of my committee: Professor Bamin Khomami, Dr. Kevin Myers, Dr. Joshua Sweeney and Dr.Brian Wrenn. I owe special thanks to Professor Bamin Khomami who has been a source of inspiration and guidance during my graduate stay at Washington University. I wish to acknowledge the industrial sponsors of the Chemical Reaction Engineering Laboratory (CREL), the National Science Foundation (NSF) and the Department of Science and Technology (DST, India) whose financial support made this research possible.

I would like to thank Dr. Abdenour Kemoun and Professor Faical Larachi who have been like my advisors on different aspects of my thesis. Dr. Kemoun has been both a close friend and a great advisor to me. From the first day of my research I had a wonderful opportunity to work closely with Dr. Kemoun and learn immensely from his vast experience in a number of different fields. Interacting with Professor Faical Larachi has been another very pleasurable aspect of my thesis experience. Professor Larachi has always been ready to keenly listen to whatever questions I have had and given very sound advice. His enthusiasm for research is simply infectious.

I owe special thanks to Dr. Shantanu Roy, Ms. Booncheng Ong, Dr. Mohan Khadilkar and Mr. Jim Linders. Dr. Shantanu Roy has been a mentor during the initial part of my thesis and then a very close friend with whom I have had a number of useful discussions on different aspects of research. Mr. Jim Linders has done an excellent and efficient job of machining both my single phase setup and multiphase setup for the stirred tank reactor. Mr. Jim Linders due to his vast experience was able to perceive my various needs and constantly come up with suggestions to improve and implement better designs. Dr. Mohan Khadilkar had the foresight to advise me to approach Dr. Kemoun and request him to be my advisor. Ms. Booncheng Ong has been a very close friend and colleague from the first semester of my stay.

The CREL group has provided me a wonderful opportunity to interact with researchers from all over the world. Interacting with the various researchers has been a wonderful learning opportunity. I would like to thank a visiting scholar, Dr. Pascal Fongarland who enriched my learning experience through his unbridled excitement for research. I would like to thank our post doctoral fellow Dr. Peter Spicka for helping in designing and executing some specialized experiments. I would like to thank Peng Chen and Mr. Bekley Shands for their constant help in matters related to the computer.

I owe a huge thanks to my undergraduate fluid mechanics Professor J.B. Joshi who instilled in me a desire to “Close my eyes and open my mind to new ideas” as he often

used to try and drum into our heads. Professor Joshi gave me an opportunity to work on a project under him which convinced me that doing a D.Sc. would be a fun experience. He has also been a source of great inspiration for me to do research at the “forefront” as he likes to emphasize.

I am indebted to my friends from my undergraduate school, Dr.Ganesh Subramanian and Mr.Satish Kadu. Ganesh has been a source of great inspiration all through my thesis. We have constantly discussed our very different research problems and used each other as sounding boards for our ideas. As a friend Ganesh has constantly encouraged my desire for learning in several ways.

I could not have gone through my thesis if it had not been for the unquestioning support from my parents, grandparents, sister, my in-laws and last but not least my wife who has been a source of constant support and inspiration for my thesis.

Aravind R Rammohan
Washington University in S aint Louis
Saint Louis, Missouri
December 2002

Chapter 1

Introduction

1.1 Motivation for the Research

Stirred tank reactors are extensively used in a variety of industries like the paper and pulp, pharmaceutical, fine chemicals, food industry etc. A large number of these applications involve multiphase flows. In designing such reactors, understanding the fluid dynamics is critical particularly when the reaction rates are faster than or comparable to the mixing rates. Characterization of fluid dynamics implies the quantification of velocities and turbulence parameters in every region of the reactor. In this work, we examine the fluid dynamics of both single and multiphase flows in stirred tanks reactors.

Although single phase flows in stirred tanks have been extensively studied using different experimental techniques like Streak Photography (SP) (Cutter, 1967), Hot Wire Anemometry (HWA) (Fort et al., 1982), Laser Doppler Anemometry (LDA) (Schaeffer and Hofken, 1999) and Digital Particle Imaging Velocimetry (DPIV) (Myers et al., 1997), all these techniques provide only Eulerian measurements where, every point or local region is characterized independently. Such measurements do not directly provide the three-dimensional information of large structures, which are responsible for mixing (Lamberto et al., 1996; Roussinova and Kresta, 1999; Hasal et al., 2000). Why is this information important? The phenomenon of mixing, as currently visualized (Ottino, 1989; Baldyga and Bourne, 1984) is one of a cascade of turbulence occurring from the largest scales of the flow to the smallest scales of flow. This occurs through a complex process of continuous evolution and transformation of eddies of larger size to medium size and to ever smaller sizes through vortex stretching and other related phenomena. It is this cascading process that represents the rate limiting step in mixing. Given this, the

Lagrangian nature of the Computer Automated Radioactive Particle Tracking (CARPT) experimental technique, where we follow the tracer particle as it moves around the vessel, makes it well suited for obtaining information on large flow structures. From the CARPT tracer particle trajectories, we hope to quantify the mixing caused by the large structures at least partially.

Characterization of multiphase reactors is further complicated by the presence of the dispersed phase which has its own fluid dynamic characteristics i.e. its own velocities, fluctuations etc. Therefore, the design of multiphase reactors, where reaction rates are faster than mixing or comparable to mixing, requires the fluid dynamic information of both the phases. The existing measurement techniques are restricted to characterizing multiphase flows with very low holdups of the dispersed phase. This is primarily because the non-invasive techniques like LDA and DPIV are optical techniques. With increasing holdup of the dispersed phase the vessel becomes progressively more and more opaque and we can no longer “see” into it with our usual tools. Hence, fluid dynamic characterization of such flows is often restricted to measuring global parameters like the relative power demand, overall gas holdup, critical speed for suspension or for ultimate homogenization (Dohi et al., 1999; Katsanevakis and Smith, 1999). Global parameters tend to conceal the detailed local information, which often contains the clues to the mixing rates (Gosman et al., 1992). Very few papers exist (we have identified a handful which are reviewed in Chapter 2) which provide local fluid dynamic measurements in multiphase flows. Without such local information the rational design and scale-up of multiphase flows in stirred tank reactors is not possible. At CREL and elsewhere CARPT and CT have been successfully applied in a variety of multiphase reactors (Chaouki et al., 1997a, 1997b) viz. bubble columns (Devnathan, 1991; Degaleesan, 1997), Liquid Solid Risers (Roy and Dudukovic, 2001) etc. These are non-optical techniques, which can be used regardless of the magnitude of the dispersed phase holdup. The CARPT technique provides the detailed local fluid dynamic information throughout the entire reactor such as the local velocities, the turbulence parameters. CT provides detailed time averaged local holdup profiles in various planes of the entire reactor and also yields the global

holdup which is the only variable measured with existing experimental techniques. Together CARPT and CT can provide the detailed local fluid dynamic information in the same setup and under identical operating conditions which would increase our understanding of multiphase flows.

The inability of existing measurement techniques to provide Lagrangian information in single-phase flows, and limitations on their use in multiphase flows with high dispersed phase holdup, provide the motivation for the current work and the implementation of CARPT/CT in single phase and multiphase stirred tanks.

1.2 Research Objectives

The specific objectives of this work are:

- To investigate the single phase flow field in stirred tanks with CARPT and provide quantitative estimates of the capabilities of the technique.
- To develop a data base using CARPT – CT in gas – liquid flows in stirred tanks at high gas holdups where other techniques fail.
- To critically evaluate the ability of commercial CFD codes to predict the observed flow fields in single and two phase flows in stirred tanks.

1.3 Structure of Thesis

In Chapter 2 the single phase and multiphase experimental data and CFD predictions of such data available in the literature are discussed. In Chapter 3 and Chapter 4 details of single phase CARPT measurements in the STR are presented. In Chapter 3 qualitative validation of the CARPT results is presented and in Chapter 4 detailed quantitative validation of the CARPT results is given. In Chapter 5 and 6 the efforts to understand and model the different sources of errors typically arising in CARPT measurements are discussed. In Chapter 7 the two phase flow results obtained in the stirred tank reactor via CARPT and CT are outlined. In Chapter 8 the conclusions and recommendations resulting from this study are presented.

Chapter 2

Background

2.1 Review of Single Phase Flow Measurements in STR

Many stirred tanks are equipped with a disk turbine, which is a radial flow impeller that generates the well-known circulatory flow pattern in a baffled cylindrical tank (refer to Figure 2-1). Impeller rotation imparts the radially outward flow through the vertical periphery of the impeller swept volume. This high-speed radial jet entrains the surrounding fluid and slows down as it approaches the tank wall. Near the tank wall, the jet stream splits into two portions, one of which then circulates through the upper and the other through the lower portion of the tank and each is finally drawn back into the impeller region. Many investigators confirm this qualitative picture of the flow (Van Molen and Van Maanen, 1978; Yianneskis et al., 1987; Wu and Patterson, 1989; Ranade and Joshi, 1990). However, a detailed quantitative comparison of the reported data exhibits considerable scatter.

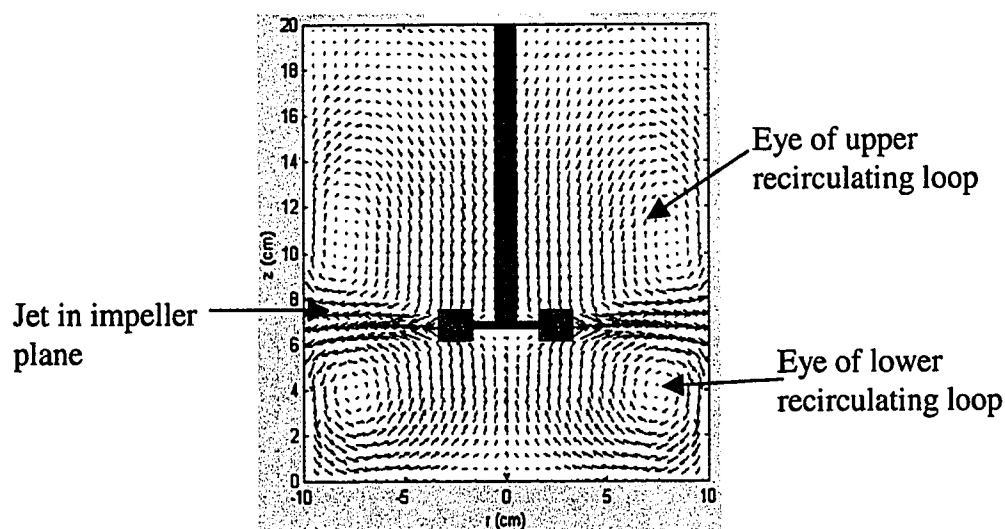


Figure 2-1. Classical Flow Structure in Stirred Tank Reactors

The difference in the performance characteristics of the measurement techniques used is one of the major reasons for the observed scatter in the reported data. A brief description of the different techniques along with the differences between them is briefly summarized in Table 2-1. Apart from the differences in the experimental techniques, the use of non-standard geometry of the experimental set-up is another contribution to the observed scatter. The hub dimensions, disc thickness and blade thickness are not yet standardized and yet all of them have a noticeable effect on the flow (refer to Figure 2-2).

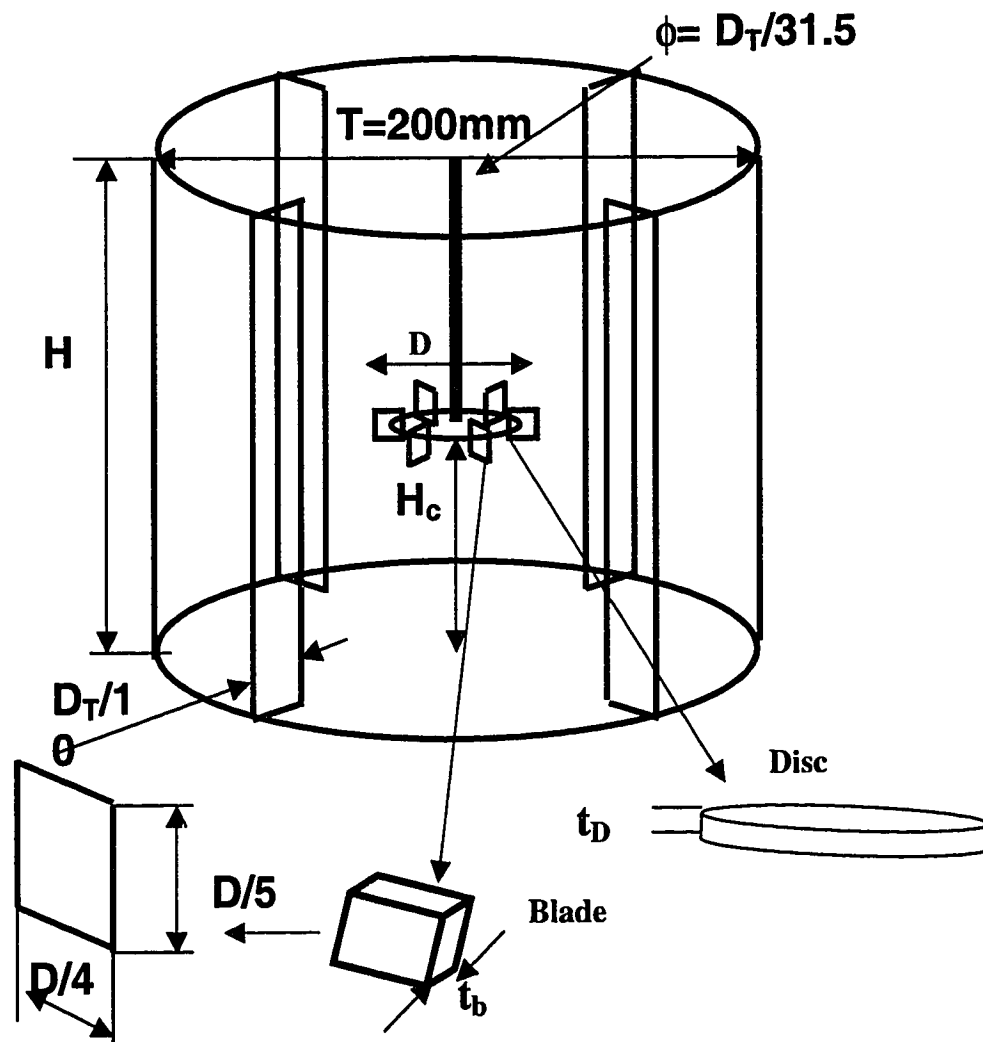


Figure 2-2. Details of the Stirred Tank Internals

Rutherford et al. (1996) examined the sensitivity of the measurements to some of these parameters. Their findings are summarized in Table 2-2(a) and in Figures 2-3 and 2-4. Figure 2-3 shows that a change in the blade thickness and disc thickness to impeller diameter ratio changes the mean radial velocity considerably. For a three fold increase in these ratios the mean radial velocities are reduced by almost 20%. However, it can also be seen that the maximum differences are only at the impeller tip and there are almost no differences away from the impeller. A similar effect on the radial rms velocities is reported in Figure 2-4, which shows that a three-fold increase in the thickness to diameter ratio reduces the radial rms by almost 25%. Table 2-2(b) summarizes the geometry of those studies reported in the literature, the results of which we intend on using here. This brief review summarized in Tables 2-1 and 2-2 and Figures 2-3 and 2-4 is intended to help us in identifying the reason for the differences in the quantitative comparisons reported later in this study.

Table 2-1. Evaluation of Single Phase Experimental Techniques

LDA= Laser Doppler Anemometry, DPIV= Digital Particle Imaging Velocimetry

Criteria	LDA	DPIV	CARPT
Description	Focused laser beams intersect to form measurement volume. Interference pattern of bright and dark stripes is formed. Seed particle moves through the fringes creating alternate dark and bright stripes. Knowing the distance between the two peaks and the time between the two peaks the velocity is calculated and a direction is assigned using a Bragg's cell (Van der Molen and Van Maanen (1978)).	Flow is seeded with particles. A laser beam illuminates a plane. Two images at subsequent time frames of the seeded flow are captured digitally. Flow field is divided into smaller interrogation areas. A cross correlation technique used to obtain the average particle displacements. Fluid velocity is calculated assuming linear displacements over time intervals between successive images.	Motion of a neutrally buoyant radioactive particle followed with time. This Lagrangian information of particle trajectories is used to calculate the Lagrangian velocities and therefore the Eulerian velocities and turbulence quantities.
Data Validation	Data has been validated by comparison with data obtained from HWA and SP and with independent LDA measurements in systems of similar geometry.	No rigorous attempt at validation is reported in the open literature. Some qualitative comparisons with LDA measurement and one quantitative comparison is reported.	Data is validated by comparison with SP, HWA, LDA and DPIV data reported in the literature and qualitative comparisons with visualization studies in same system.
Frequency Response	Up to 30 kHz limitation at high freq: Particle size, concentrations and electronics.	Sampling frequency 10-30 Hz. Digitization speed limits it.	In theory can vary from 50-500 Hz. But practical limitations of particle size and spatial resolution issues limit it to 50-100 Hz.
Size of measurement volume	Typically 50 μ m by 0.25 mm, 5 by 5 μ m possible but requires lens to be placed farther, requires fine particles which require higher energy of light.	Spatial resolution are mm in size. Size is determined by number of particles present per pixel, number of pixels the plane is divided into and size of spatial structures one wishes to capture.	Spatial resolutions are typically of the order of 5mm. These are strong functions of the particle size, the energy of the gamma rays, distance of particle from detector, sensitivity of the detector, solid angle effects etc.
Velocity Range	Wide ranges of velocity are possible. At high velocities difficult to get particles that follow flow, scatter light and have high concentration	Wide ranges of velocity are possible. Problems are similar to those of LDA.	At high velocities the issue of resolution and sampling frequencies can become important and the ability of the particle to follow the flow can also become an

Velocity Component Resolution	Can measure two components simultaneously. Three component LDA's are available in the market but their cost is high, can capture reversal of flow.	Same as LDA i.e. can measure two components simultaneously. But the current stirred tank literature suggests that these two velocities are limited to the radial and tangential velocities. 3D DPIV's available in the market. Can capture flow reversals.	important issue. Measures three dimensional velocities simultaneously. Provides Lagrangian velocity measurements over the entire tank.
Accuracy	Can give high accuracy up to 0.1 %. Errors in refractive index, beam crossing angle make it 1%	Errors from implementation of cross correlation algorithm and errors in the peak finding scheme. Lot of research has been done into the different schemes for these. Accuracy is within 5%.	Main source of errors is from particle reconstruction accuracy, particle's ability to track the fluid and limitations on sampling frequency.
Resolution	Laser pretty good but not as high as HWA. Can go up to 1 in 1000.	Can go as high as 0.6 mm / pixel but this means we will be compromising on the length scales one wishes to capture. In principle closer to 5 mm.	Typically around 5 mm. Recent studies done at CREL suggest possibility of improving resolution upto 2.0 mm.
Ease of Use	Difficult to set up and start getting valid data.	Requires Setting up DPIV, interrogation area, getting a uniform sheet in one plane, adjusting the lens, camera to focus on the interrogation area	Once neutrally buoyant particle is made and calibration is done the actual experiments are very easy.
Ability to capture structure in flow	None directly.	Planar information available.	Complete three dimensional information of the structures in flow.
Use in multiphase flow	Not usable in opaque multiphase flows.	Not usable in opaque multiphase flows.	Can be used in opaque multiphase flows.

Table 2-2. Review of Single Phase Measurements in Stirred Tanks

Table 2-2(a). Parametric sensitivity of fluid dynamic measurements in stirred tanks reported by Rutherford et. al. (1996)

Parameters	Power Number (N_p)	Pumping Number (N_Q)	Dimensionless mean velocity(V/V_{tip})	Dimensionless root mean squared velocity (V^*/V_{tip})
t_b/D	3 fold increase causes 35% reduction in power number	3 fold increase causes 15% reduction. Difference goes down with increasing radial distance from impeller tip	3 fold increase causes 20% reduction in mean velocities. Difference decreases with radial distance from impeller tip	3 fold increase causes 25% reduction in RMS. Difference decreases with increase in radial distance from impeller tip
t_b/D	3 fold increase causes 35% reduction	3 fold increase causes 15% reduction. Difference goes down with increasing radial distance from impeller tip	3 fold increase causes 20% reduction in mean velocities. Difference decreases with radial distance from impeller tip	3 fold increase causes 25% reduction in RMS. Difference decreases with increase in radial distance from impeller tip
D/T	No effect	No effect	No effect	No effect

(refer to Figure 2-2 for the dimensions).

Table 2-2(b). Parameters of the System Used for Validation in This Study

Researcher	T(mm)	D/T	H/T	Hc/T	t_p/D	t_p/D	Re = ND^2/ν	Fluid
Cutter (1967)	290	1/3	1	1/3	_____	_____	34600- 120000	Water
Cooper and Wolf (1968)	380	.27	1	1/3	_____	_____	50000	Water
		& 0.4						
Drobholov et. al. (1978)	1000	1/3	1	1/3	_____	_____	185200 & 288000	Water
Chen et. al. (1988)	89	1/3	1	1/3	_____	_____	1630,3260 & 6520	Water
Wu and Patterson (1989)	270	1/3	1	1/3	_____	_____	30000	Water
Ranade and Joshi (1990)	300	1/3	1	1/2	.008	.027	56000	Water
					.0016	.022		
Yianneskis and Whitelaw (1993)	294	1/3	1	1/3	.03	.03	54000	Water
Zhou and Kresta (1996)	240	1/2	1	1/2	_____	_____	52200	Water
Schaefer et. al. (1996)	150	1/3	1	1/3	.04	.04	800, 1200 & 2000	White oil
Current Work	200	1/3	1	1/3	.008	.015	8200,12300,16400 & 32800	Water

For Dimensions refer to Figure 2-2. $Re = \frac{ND^2}{\nu}$

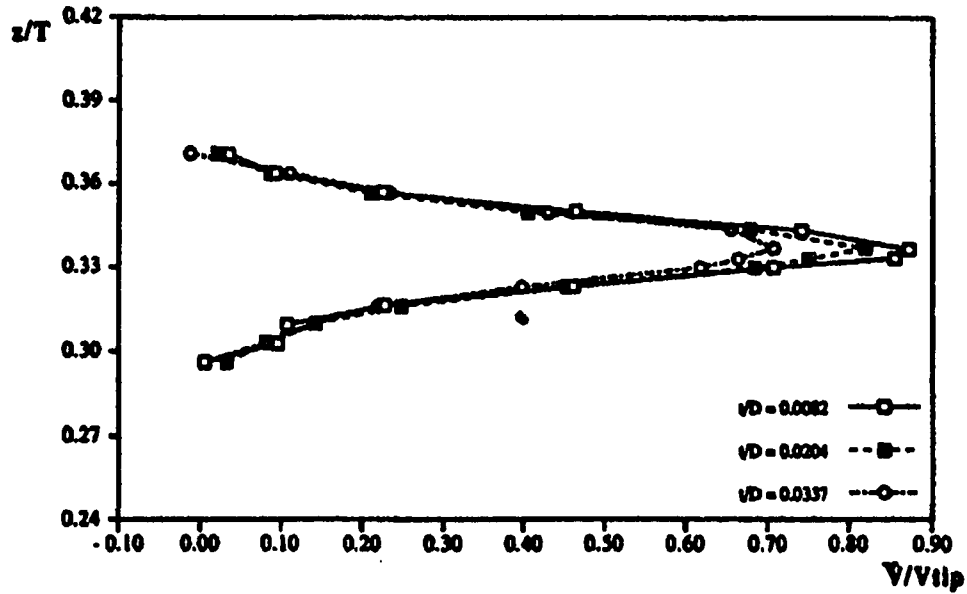


Figure 2-3. Effect of Blade and Disc Thickness Ratio on Mean Radial Velocity at $r/T=0.17$, Rutherford et al. (1996).

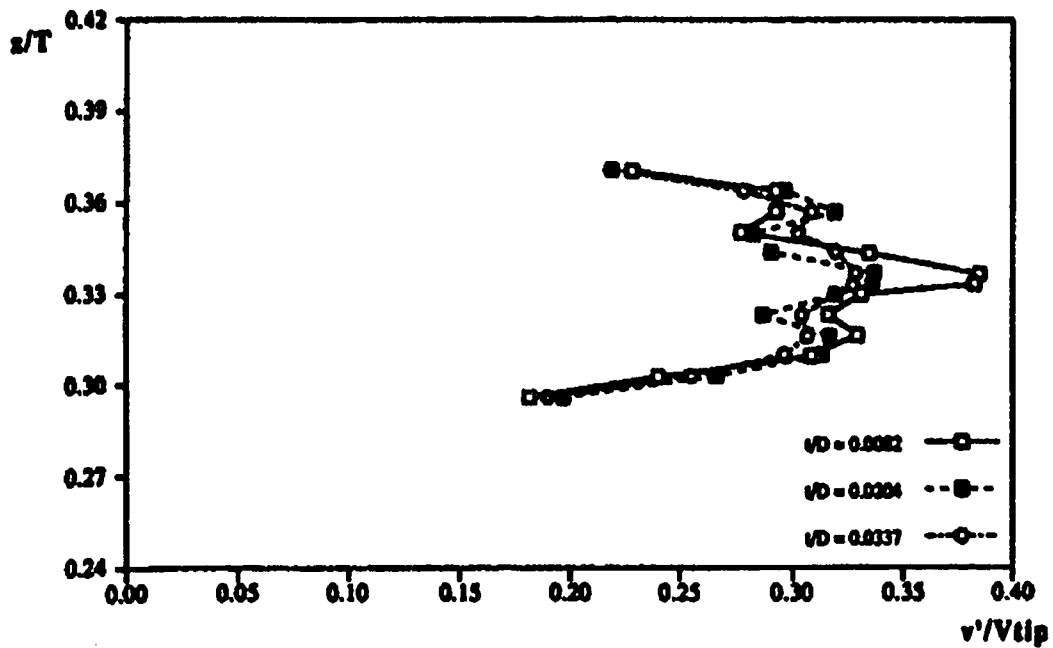


Figure 2-4. Effect of Blade and Disc Thickness Ratio on the Radial Root-Mean-Square Velocity at $r/T=0.17$, Rutherford et al. (1996).

As a first step in establishing the validity of their experimental data many researchers have reported mass balance verifications. The mass balance is usually verified in a control volume containing the impeller. These results have been summarized below in Table 2-2(c). Usually the mass balance is satisfied within 1-10% accuracy.

Table 2-2 (c). Verification of Mass Balance

Researcher	Technique Used	Region Considered	Accuracy
Gunkel and Weber (1975)	HFA	$0 < z/D < .16,$ $0 < r/D < 1$	4%
Yianneskis et al. (1987)	LDA	C.V. around impeller	1%
Wu and Patterson (1989)	LDA	$-.22 < z/D < .22,$ $0 < r/D < 0.55$	1%
Ranade and Joshi (1990)	LDA	C.V. around impeller	5%
Yianneskis and Whitelaw (1993)	LDA	C.V. around impeller	1%
Zhou and Kresta (1996)	LDA	$-.15 < z/D < .23,$ $0 < r/D < .525$	5-10%
This work	CARPT	C.V. around the impeller	7%

As a next step, researchers have identified a number of reproducible physical phenomena that are qualitatively verified. One such phenomenon is the existence of the two ring like vortices one above and the other below the turbine impeller (refer to Figure 2-1). The radial location of the eye of the upper and the lower recirculation loops is reported to be $0.4r/T$, while the axial location of the lower and upper recirculation loop eyes are around $0.2-0.25 z/T$ and $0.4-0.75 z/T$, respectively. The differences in axial location are due to differences in the clearance of the impeller from the tank bottom. These results are summarized in Table 2-2(d). It must be emphasized that while the actual dimensions of the systems are different, a certain geometrical similarity exists between the systems. All the systems use the same type of impeller (Rushton turbine, with the same number of blades (6)), blade width to impeller diameter ratio of $1/5$, blade length to impeller diameter ratio of $1/4$, same impeller diameter to tank diameter ratio of $1/3$ and same height of fluid to tank diameter ratio of one (1). This is summarized in Table 2-2(e). Although the actual dimensions of the different systems are different the dimensionless radial and axial locations of the eye of the loops are comparable. Radial and axial profiles of the dimensionless mean velocities and turbulent velocities (scaled with impeller tip speed) and the radial pumping number are also reported to be independent of the Reynolds numbers (for $Re > 800$) and of the actual dimensions of the system if the above mentioned geometric scaling is maintained. This enables the comparison reported by different researchers.

An overview of the literature suggests that many investigators place emphasis on the impeller discharge stream. Van't Riet and Smith (1975) used stationary HFA and found that the rotation of the blade introduces a periodic flow around the impeller. Lee and Yianneskis (1994) used angle resolved measurements to quantify the extent of this periodicity. Stoots and Calabrese (1995) showed that the dimensionless extent of this region is independent of Reynolds number and scale of the system. These results have been summarized in Table 2-2(f) and provide the basis for the Multiple Reference Frame and Sliding Mesh simulations described later in this Chapter.

Many investigators report the presence of trailing vortices behind the impeller blades. Extensive descriptions of the vortex structures have been provided by Yianneskis et al. (1987). Some of their findings are summarized in Table 2-2(g). The flow in the impeller discharge stream is characterized by the existence of strong radial and tangential components of mean velocity and intense turbulence. This has been quantified by calculating the radial pumping number, the mean radial and tangential velocities, the rms velocities and the turbulent kinetic energy. These are summarized in Tables 2-2(h) and 2-2(i) respectively. The radial pumping numbers at the impeller tip are reported to be in the range of 0.64-0.83 with a mean of 0.75 ± 0.15 . The variation in this value is primarily due to the differences in the size of the control volume. Most of the investigators carry out the integration along the blade height, while some perform the integration up to the point where the radial velocity becomes zero. The latter case results in the higher pumping number (>0.8) while the lower values of 0.65 are due to the differences in the data acquisition technique used for LDA measurements. Conventionally LDA velocities are measured by focussing on a control volume, without accounting for the position of the impeller blade w.r.t. the control volume at the instant of the measurement. Such measurements are referred to as 360° ensemble averaged or time resolved data (refer to Figure 2-5(a)).

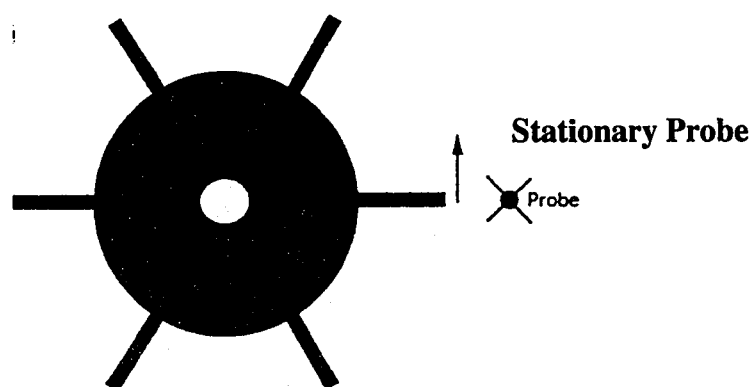


Figure 2-5(a). Schematic Depicting Ensemble Averaged Measurement in STR.

However, such measurements have an inherent data bias towards a higher mean velocity (Rutherford et al., 1996) since more than 50% of the sampled instantaneous velocities are within $1\text{-}20^\circ$ behind the blade. Hence, Rutherford et al. (1996) suggested that a more accurate way of acquiring data would be to ensure that enough samples (500-750) are acquired in every 1° bin behind the impeller. Such data are collected over 60° and are then averaged to yield the “phase averaged” mean (refer to Figure 2-5(b)). The radial pumping number calculated using such measurements are

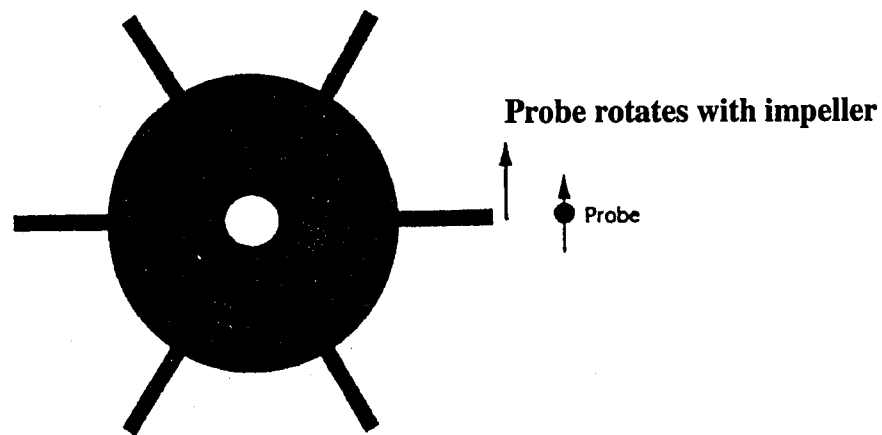


Figure 2-5(b). Schematic Depicting Phase Averaged Measurement in STR.

reported to be 15% lower than the ensemble averaged radial pumping numbers (Stoots and Calabrese, 1995, and Rutherford et al., 1996). However, it is to be expected that even the ensemble averaged measurements should yield comparable values provided the data is sampled at a high enough sampling rate and for a long enough time. This is observed in the measurements of Kemoun (1991) who sampled data at 2048 Hz for 30s. The differences in sampling frequency and sampling time used by the different investigators are summarized in Table 2-2(j).

The observed differences in the reported mean velocities and turbulent kinetic energy are summarized in Table 2-2(i). Reported values of the maximum velocities $V_{\text{rmax}}/V_{\text{tip}}$ vary from 0.58-0.88 and $V_{\theta\text{max}}/V_{\text{tip}}$ values range from 0.61-1.43. The reported rms values range from 0.20-0.41 for V_r'/V_{tip} , 0.2-0.454 for V_θ'/V_{tip} and 0.2 to

$0.33 V_z / V_{tip}$. Reported turbulent kinetic energy $K.E./V_{tip}^2$ is in the range from 0.06 to 0.18. The “Phase averaged” mean velocities are reported to be 15% lower than the ensemble averaged mean velocities, while the phase averaged rms velocities are almost one fourth of the ensemble averaged velocities. Further, the differences in the blade thickness and disc thickness to tank diameter ratios affect the maximum mean velocities. Rutherford et al. (1996) have shown (Refer to Table 2-2(a) and Figures 2-1 & 2.2.) that a threefold increase in blade and disc thickness causes a 15% decrease in the maximum mean velocities and the rms velocities. However, this effect decreases as one moves away from the impeller. Recent DPIV measurements also report mean velocities and turbulent kinetic energies lower than LDA measurements. Fasano and Bakker (1993) reported the maximum axial velocity of $0.046V_{tip}$, which is considerably lower than the LDA value of $0.15 V_{tip}$ (Ranade and Joshi, 1990). The radial velocities from DPIV are 40% lower than reported LDA values. Fasano and Bakker (1993) and Myers et al. (1997) attributed this discrepancy to high out of plane velocities near the impeller region and errors in cross correlation algorithm used (a detailed error analysis is reported by Westerweel in 1994). Deen and Hjertager (1999) reported the maximum radial velocity of $0.55V_{tip}$ which is lower than the LDA determined value of $0.7V_{tip}$, (Wu and Patterson, 1989). The Root Mean Squared (rms) values in the radial direction and axial direction are within 10% of the LDA values. The turbulent kinetic energy values obtained by DPIV are within 15-20% of LDA values. Since this indicates that with the sampling frequency of 10-30 Hz DPIV can capture the turbulent kinetic energies well, then the frequencies below this range contain most of the energy containing eddies. Therefore, the higher frequencies probably contribute a smaller fraction of the total turbulent kinetic energy.

From the above literature review we have identified the different quantities that were measured by different experimental techniques. The range of variation of these parameters has been provided above and the possible reasons for the variations have also been discussed. Further, the literature search suggests that the dimensionless pumping number, mean and turbulent velocities from different studies are

comparable. In this work, we compare some of these quantities (mass balance, location of the circulation loops, radial pumping number, mean and turbulent velocities) computed from the CARPT measurements with similar measures obtained using the experimental techniques reviewed above.

Table 2-2(d). Location of Eye of Circulation Loops

Researcher	Lower loop (r/T)	Lower loop (z/T)	Upper loop (r/T)	Upper loop (z/T)	Clearance (H _c /T)
Yianneskis and Whitelaw (1987)	0.3	.2	0.3	.48	.33
Costes and Couderc (1988)	.4	.25	.4	.75	.5
Schaefer et al. (1997)	.4	.2	.4	.5	.33
Kemoun et al. (1998)	.4	.2	.4	.5	.33

Table 2-2(e). Independence of Dimensionless Mean Velocities and Turbulent Kinetic Energy with Scale and Re

Researcher	T(mm)*	D/T**	H/T ⁺⁺	H _c /T ⁺⁺	Re Range
Cutter (1966)	290	1/3	1	1/3	34600-120000
Van der Molen and Van Maanen (1978)	120, 290 & 900	1/3	1	1.2	8000, 26000 & 120000
Ranade and Joshi (1990)	300 & 500	1/3	1	1.2	37000-130000
Dyster et al. (1993)	150	1/3	1	1.2	2300-37000
Rutherford et al. (1996)	100 & 294	1/3 & 2/5	1	1/3	40000 & 44500
Schaefer et al. (1997)	150	1/3	1	1/3	800, 1200 & 2000

** - T= Tank Diameter, *** - D= Impeller diameter, +’ - H= Height of fluid in tank, ++’ - H_c = Height of Impeller from tank bottom.

Table 2-2(f). Extent of Periodicity

Researcher	Radial Extent $r^*=r/D$	Axial Extent $z^*=z/D/5$
Van der Molen and Van Maanen (1978)	2.0	+(-)1.0
Yianneskis et al. (1987)	1.75	+(-)1.0
Lee and Yianneskis (1994)	2.0	+(-)1.5
Stoos and Calabrese (1995)	1.7	+(-)2.1

$D/5 = W =$ Impeller width.

Table 2-2(g). Trailing Vortex Characterization

Researcher	Axial Location (z/D)	Radial Location	Radius (mm)	Angular Spread
Yianneskis et al. (1987)	1.0	0.47D ($\phi=10^\circ$), 0.55D ($\phi=20^\circ$) and 0.6D ($\phi=30^\circ$)	$30+4.93(\phi)^{1/2}$	20°
Yianneskis and Whitelaw (1993)	1.0	Locus of vortex axis is between Yianneskis et al. (1987) and Van't Reit et al. (1975)	---	20°
Stoos and Calabrese (1995)	1.0	0.51D ($\phi=0-20^\circ$)	---	20°

Table 2-2(h). Radial Pumping Number ($Fl=Q_i/ND^3$)

Researcher	Control Volume $Z^*=z/W$	Fl_{max}	Type of Data
Yianneskis and Whitelaw (1987)	$-1 < z^* < 1$	0.785	360° (e.a.)

Costes and Couderc (1988)		-1<z*<1		0.73	360°(e.a.)
Wu and Patterson (1989)		Z at which V _r =0		0.83	360°(e.a.)
Ranade and Joshi (1990)		-1<z*<1		0.75	360°(e.a.)
Dyster et al. (1993)		-1<z*<1		0.78	360°(e.a.)
Stoos and Calabrese (1995)		-1<z*<1		0.65	60°(p.a.)
		-2.6<z*<2.6		0.75	360°(p.a.)
Rutherford et al. (1996)		Z at which V _r =0		.80	360°(e.a.)
				.64	60°(p.a.)
Kemoun (1991)		-1<z*<1		.69	360°(e.a.)

e.a.-ensemble averaged, p.a.-phase averaged

Table 2-2(i). Maximum Mean Velocities and Turbulent Kinetic Energy

Researcher	r/T	V _{rmax} /V _{tip}	V _{θmax} /V _{tip}	V _r /V _{tip}	V _θ /V _{ti} p	V _z /V _{tip}	KE/V _{tip} ²
Yianneskis and Whitelaw (1987)	—	.70	0.84	—	—	—	.17 0.06 ⁺
Wu and Patterson (1989)	.185	.75	0.70	0.33 0.20 ⁺	0.33 0.20 ⁺	0.33 0.20 ⁺	0.16 0.06 ⁺
Ranade and Joshi (1990)	.17	.69	—	—	—	—	—
Dyster et al. (1993)	.17	.73	—	.454	—	—	—
Stoos and Calabrese (1995)	.17	.87	1.43 (r*=.15)	—	—	—	—

Zhou and Kresta (1996)	0.26	.71	.61	.41	.32	.30	.18
Schaefer et al. (1997)	.17	.85	—	—	—	—	0.08 ⁺

⁺ - Angle Resolved Measurements, * - t= blade or disc thickness.

Table 2-2(j). Data Acquisition Rates and Accuracy of Measurement

Researcher	Sampling Frequency (Hz)	Sampling Time (s)	Type of Data	Accuracy of Mean Velocity	Accuracy of Turbulent Kinetic Energy
Cutter (1966)	600	.07	S.P.(e.a.)	+(-)20%	—
Van der Molen and Van Maanen (1978)	—	200	LDA(e.a.)	—	—
Yianneskis et al. (1987)	1000	300-600	LDA(e.a. & a.r.)	2-3%	5-10%
Wu and Patterson (1989)	7000	1.5	LDA (e.a.)	4%	15%
Ranade and Joshi (1990)	500	20	LDA (e.a.)	+(-)1%	+(-)2%
Lee and Yianneskis (1994)	3000	0.1	LDA (e.a. & a.r.)	2-3%	5-10%
Rutherford et al. (1996)	—	—	LDA (e.a. & a.r.)	2-3%	5-10%
Zhou and Kresta (1996)	1200	5	LDA(e.a.)	—	—
Kemoun (1991)	2048	30	LDA(e.a.)	—	—

e.a.-360° ensemble averaged, a.r.-angle resolved.

Detailed measurements of the flow in stirred tanks using LDA, DPIV etc. have contributed considerably to resolving large as well as small flow structures. Reliable models are needed to verify the information obtained and provide the means for prediction of flow patterns.

There are two basic modeling approaches, the phenomenological models and the numerical solution of the complete Navier Stokes equations. Ambegaonkar et al. (1977) and Fort et al. (1982) used approximate phenomenological models that yield analytical expressions for the mean velocity components in a stirred tank. These models however, tend to oversimplify the complexity of the flow and therefore, can at best represent only the mean velocity profiles. In order to capture the significant three-dimensional nature of the flow, rigorous numerical models are needed.

2.2.1 Numerical Solution of the Navier Stokes Equations

The stirred tank has internals of different shapes some of which (the rotating shaft and the impeller) are in motion. Until recently (Perng and Murthy, 1993) the impeller region was excluded from the solution domain and replaced by the boundary conditions on a control volume or by introducing source terms distributed throughout this volume. The boundary conditions or source terms were assigned using either experimental data or simplified models that ignore the overall geometry of the vessel. In most published papers (refer Table 2-4) the k - ϵ turbulence model has been used which requires boundary conditions for k and ϵ as well.

The applicability of the black box approach is limited by the availability of data. Moreover, this approach cannot be used to screen a large number of alternative mixer configurations. The extension to multiphase flows is not feasible because it is almost impossible to obtain accurate boundary conditions at the impeller. More importantly, this approach cannot capture the details of the flow between the impeller blades, which is

needed for realistic simulations of reactive mixing and multiphase flows in stirred reactors.

To eliminate some of these limitations five different models have since then been developed. Two of these are unsteady approaches: the moving mesh model and the sliding mesh model. Steady state models include the Multiple Reference Frame (MRF), Inner-Outer (IO) and the Snapshot Approach (SA). An introduction to these techniques along with a brief comparison of their predictive capabilities is discussed in Table 2-4. In this work, since both Computer Automated Radioactive Particle Tracking (CARPT) and Computed Tomography (CT) provide only time averaged values of the velocities and holdup it is sufficient at first to examine the steady state approaches of MRF and the SA. The value of the unsteady models lies in their ability to predict the dynamics of the flow particularly near the impeller region which is of interest if tracer run data or mixing time information is available for the system. Also the following considerations make unsteady approaches like the sliding mesh unattractive since at present:

- a) Computational requirements for the solution of full time varying flow in a stirred vessel are greater by an order of magnitude than those required by steady state simulations.
- b) Because of the excessive computational requirements, there are restrictions on the number of computational cells that can be used for these simulations. Such a limitation may make apriori predictions of the desired flow characteristics such as energy dissipation rates, shear rates etc. less accurate
- c) The results obtained using this approach are not yet sufficiently validated for the turbulent regime.

Hence, the two steady approaches alone are reviewed below.

Multiple Reference Frame (MRF) Model

Using sliding mesh simulations, Luo et al. (1994) showed that a cylindrical region enclosing the impeller exists, within which the flow is unsteady and outside which it is

steady. This allows us to assume the flow to consist of multiple “fluid” regions. The

MRF method is a steady state model that simultaneously solves for the flow in a rotating fluid region enclosing the impeller and a stationary fluid region containing the walls, the baffles and the bulk of the tank. The solution from both the reference frames is matched at the interface between the rotating and the stationary fluid region. The effect of rotation is accounted for by the inclusion of the Coriolis acceleration term and the centrifugal force term. Luo et al.’s (1994) comparisons between the predicted axial, radial velocities and LDA data of Yianneskis et al. (1987) were good. There were slight differences between measured and predicted tangential velocities.

Snapshot Approach (SA)

The interaction between the rotating blades and the stationary baffles generates an inherently unsteady flow. Once the flow has developed, the flow pattern becomes cyclic. A snapshot of the flow can therefore describe the flow between the impeller blades at that particular instant. Ranade and Van den Akker (1994) developed this snapshot approach. The flow generated by an impeller is governed mainly by the pressure and centrifugal forces generated by the impeller rotation. The pressure forces cause the suction of the fluid behind the blade and an equivalent ejection in front of the blade. In the SA this suction and ejection is modeled by specifying mass sources on the front side of the blade and sinks on the back side of the blades. The mass source term is the same as the mass sink with an opposite sign. Inward movement does not add any corresponding source to the other variables. The comparisons of computed results using the snapshot approach and data (Ranade and Joshi, 1990) for single phase flow are good qualitatively and quantitatively. The equations used in the MRF and the snapshot approach are summarized below.

The transport equation for a general variable, ϕ , can be written for an incompressible steady flow as:

$$\begin{aligned} & \frac{1}{r} \frac{\partial}{\partial r} (\rho r V_r \phi) + \frac{1}{r} \frac{\partial}{\partial \theta} (\rho V_\theta \phi) + \frac{\partial}{\partial z} (\rho V_z \phi) \\ &= \frac{1}{r} \frac{\partial}{\partial r} \left(\Gamma \phi_{\text{eff}} r \frac{\partial \phi}{\partial r} \right) + \frac{1}{r} \frac{\partial}{\partial \theta} \left(\frac{\Gamma \phi_{\text{eff}}}{r} \frac{\partial \phi}{\partial \theta} \right) + \frac{\partial}{\partial z} \left(\Gamma \phi_{\text{eff}} \frac{\partial \phi}{\partial z} \right) + S_\phi \end{aligned} \quad (2.1)$$

$\Gamma_{\phi_{\text{eff}}}$ denotes an effective turbulent exchange coefficient including the molecular contribution and S_ϕ denotes the volumetric rate of growth or decay in ϕ because of the internal and external sources. The details of the source terms for various ϕ are given below.

Table 2-3. Summary of Equations Used for the MRF and SA models

ϕ	Γ_ϕ	S_ϕ
1	0	0
V_r	μ_{eff}	$\frac{1}{r} \frac{\partial}{\partial r} \left(\mu r \frac{\partial V_r}{\partial r} \right) + \frac{1}{r} \frac{\partial}{\partial \theta} \left(\mu r \frac{\partial}{\partial r} \left(\frac{V_\theta}{r} \right) \right) - \frac{2\mu}{r^2} \frac{\partial V_\theta}{\partial \theta} + \frac{\rho V_\theta^2}{r} + \frac{\partial}{\partial z} \left(\mu \frac{\partial V_z}{\partial r} \right) - \frac{\partial p}{\partial r}$ (2.2)
V_z	μ_{eff}	$\frac{1}{r} \frac{\partial}{\partial r} \left(\mu r \frac{\partial V_r}{\partial z} \right) + \frac{1}{r} \frac{\partial}{\partial \theta} \left(\mu \frac{\partial}{\partial z} (V_\theta) \right) + \frac{\partial}{\partial z} \left(\mu \frac{\partial V_z}{\partial z} \right) - \frac{\partial p}{\partial z}$ (2.3)
V_θ	μ_{eff}	$\mu \frac{\partial}{\partial r} \left(\frac{V_\theta}{r} \right) - \frac{1}{r} \frac{\partial}{\partial r} (\mu V_\theta) - \frac{\rho V_r V_\theta}{r} + \frac{\mu}{r^2} \frac{\partial V_\theta}{\partial \theta} + \frac{1}{r} \frac{\partial}{\partial r} \left(\frac{\mu}{r} \frac{\partial V_\theta}{\partial \theta} \right) + \frac{1}{r} \frac{\partial}{\partial \theta} \left(\frac{2\mu V_r}{r} \right) \frac{\rho V_\theta^2}{r} + \frac{\partial}{\partial z} \left(\frac{\mu}{r} \frac{\partial V_z}{\partial \theta} \right) - \frac{1}{r} \frac{\partial p}{\partial \theta}$ (2.4)
k	$\mu_{\text{eff}}/\sigma_k$	$G - \rho \epsilon$ (2.5)
ϵ	$\mu_{\text{eff}}/\sigma_\epsilon$	$\frac{\epsilon}{k} (C_1 G - C_2 \rho \epsilon)$ (2.6)

And

$$\begin{aligned}
G = & \mu_t \left(2 \left[\left(\frac{\partial V_r}{\partial r} \right)^2 + \left(\frac{1}{r} \frac{\partial V_\theta}{\partial \theta} + \frac{V_r}{r} \right)^2 + \left(\frac{\partial V_z}{\partial z} \right)^2 \right] + \left[r \frac{\partial}{\partial r} \left(\frac{V_\theta}{r} \right) + \frac{1}{r} \frac{\partial V_r}{\partial \theta} \right]^2 \right) \\
& + \mu_t \left(\left[\frac{1}{r} \frac{\partial V_z}{\partial \theta} + \frac{\partial V_\theta}{\partial z} \right]^2 + \left[\frac{\partial V_r}{\partial z} + \frac{\partial V_z}{\partial r} \right]^2 \right)
\end{aligned} \tag{2.7}$$

Where

$$\mu_{eff} = \frac{C_D k^2}{\varepsilon} + \mu \tag{2.8}$$

In the Snapshot approach the source terms ϕ have an additional contribution to account for the impeller rotation. These are given by

$$S = -\rho A_{bc} W \tag{2.9}$$

and the Sink terms for other variables are obtained from

$$S_\phi = S\phi \tag{2.10}$$

Similarly, for the cells in front of the blade a mass source similar to (2.9) but with an opposite sign is specified. The inward motion of the blade does not result in transport of other quantities (like momentum and turbulent kinetic energy). In the MRF model the source terms for momentum contain two additional terms to account for the Coriolis acceleration and the Centrifugal force. These are given below:

$$F_r = \rho(\omega^2 r + 2\omega V_\theta) \tag{2.11}$$

$$F_\theta = \rho(-2\omega V_r) \tag{2.12}$$

It must be mentioned that both the MRF and the computational snapshot approach look promising as design tools since these can be easily extended to any number of impellers and to multiphase flows, without excessive demands on computational resources.

Approximations employed with both MRF and snapshot methods are of the same level and therefore lead to almost the same results

The boundary conditions for both approaches require no empirical inputs unlike the black box approach. For the MRF model the rotating frame is defined to rotate as a solid body with the angular speed of interest. In both Snapshot and MRF approach the impeller disc, the shaft and the blades are all explicitly defined as rotating solid walls. The vessel walls and baffles are defined as impermeable walls with friction. The boundary conditions for velocities at the walls and baffles are set to zero, and the boundary conditions for turbulence are defined using the standard wall function option provided by FLUENT. The top of the liquid is defined as a free surface. The vertical center-line is defined to be the axis of rotation. The angular planes corresponding to the start of the domain and end of the domain are rotationally symmetric.

A summary of the different modeling approaches is provided below in Table 2-4.

Table 2-4. Models that Numerically Solve for the Flow in Stirred Tanks

Type	Reference	Description	Boundary Conditions	Computational Effort	Predictability	Multiphase Capability
Black Box	Harvey and Greaves (1982), Peticleous and Patel (1987), Middleton et al. (1986), Brucato et al. (1989), Ranade and Joshi (1990),	Treats the impeller as a cylindrical region enclosing the impeller. Some define it to be an open cylinder (no top or bottom). The actual shape of the impeller does not matter.	Requires experimental inputs for mean velocities, turbulent kinetic energy and the dissipation rates at the surfaces of the control volumes. Alternatively the impeller also is represented by a series of sources and sinks.	Minimal compared to the other techniques listed in this table.	Comparisons of the mean velocity are good near the impeller but not so good away from the impeller. The turbulent kinetic energy is not predicted well. This approach cannot be used to screen large number of alternative mixer configurations.	Extension to multiphase flows is not feasible because it is virtually impossible to obtain the accurate boundary conditions needed at the impeller.
Moving & Deforming Mesh	Peng and Murthy (1993)	Single mesh and single reference frame used. Grid cells associated with impeller rotate with it causing deformation of mesh. Model is inherently transient.	No experimental inputs needed for the boundary conditions.	Model is computationally very intensive.	In principle this is the right way to model the flow in stirred tanks. However, no qualitative or quantitative comparisons of predictive capabilities exist to date.	Current version of the commercial software FLUENT does not support the Eulerian multiphase model.
Sliding Mesh	Luo et al. (1993), Issa (1993), Bode (1994), Daskopoulos and Harris (1996), Tabor et al. (1996), Ng et al. (1998)	Tank divided into two mesh regions, one attached to the impeller, which slides over the other mesh attached to the stationary boundaries. Model is inherently transient.	No experimental inputs needed. The impeller is modeled as solid wall rotating with a known angular velocity. The turbulent kinetic energy and the dissipation rates	Computational effort is much less than that required for moving meshes but more than the other methods.	Excellent agreement of the mean velocities. However, all researchers report a severe underprediction of turbulent kinetic energy attributed to the use of standard k- ϵ model.	Current version of the commercial software FLUENT does not support the Eulerian multiphase model

Multiple Reference Frame method	Luo et al. (1994),	A steady state model which permits multiple fluid (not grid) to rotate relative to each other. Choice of the location of the interface is critical.	No experimental input needed except for the location of interface. The other boundary conditions are as defined as above.	The computation time is much lower than both moving mesh and sliding mesh simulations but more than the Snapshot approach.	Mean velocity predictions are reasonably good. Turbulent kinetic energy is underpredicted.	Current version of the commercial software FLUENT supports the Eulerian multiphase model
Inner Outer Method	Brucato et al. (1994)	A steady-state model, which divides the whole tank into two partly overlapping regions and solves for the flow in each region iteratively.	No experimental inputs needed. The solution of one region serves as the boundary condition for the other region.	Faster than moving and sliding mesh simulations but slower than MRF and SA.	Predictions of mean velocities are good while turbulent kinetic energy is underpredicted.	Current version of FLUENT does not offer this modeling option.
Snapshot Approach	Ranade and Van den Akker (1994),	A steady state model where flow between blades is assumed to be developed. The action of the blades is explicitly accounted by introducing source and sink terms behind and in front of the blades.	No empirical inputs are needed. Other boundary conditions same as above.	Requires least time.	Mean velocity predictions are good while turbulence predictions are not.	Directly amenable for multiphase simulations since procedure same as for single phase model..

2.2.2 Models for Turbulence

In the stirred tank literature the most commonly used model for turbulence is the standard k - ϵ model. This model has been reviewed extensively (Ranade and Joshi, 1990). Hence, in this section we summarize the use of other turbulence models. Placek et al. (1986) used a modified k - ϵ model. They introduced an alternate balance equation for the turbulent kinetic energy of large-scale vortices. They solved the transport equations for the turbulent kinetic energy of production scale vortices (k_T) and the inertial range vortices (k_P) along with the rate of dissipation (ϵ) and the momentum equations. The agreement between predicted and measured mean velocities was not satisfactory. They have not reported quantitative comparisons of the turbulent kinetic energy.

Jenne and Reuss (1999) selected two modified versions of the k - ϵ model which account for the non-equilibrium process, one was Chen and Kim's model (CK, 1987) and the other the renormalization group theory (RNG) proposed by Yakhot and Orszag (1986). Their results suggest that the standard k - ϵ model predicted the mean velocities within 10% of experimental data and the turbulent kinetic energies within 24%. This was in better agreement than achieved by the other two models for which the mean velocity deviations were about 25% for CK and 40% for RNG model, while the deviations in the kinetic energy were 30%(CK) and 50%(RNG). Jenne and Reuss (1999) do not attempt to explain this discrepancy. Moreover, they used the black box approach to model the impeller region. Therefore, it is unclear whether the deviations are entirely due to the different turbulence models or if they are somewhat caused by the black box method. Oshinowo and Marshall (1999) compared the effects of using different turbulence models in the MRF approach, and concluded that not much difference could be seen in the mean velocity and turbulence predictions. Ng et al (1998), who reported sliding mesh simulations with the standard k - ϵ model, suggested that a different turbulence model like the Reynolds Stress Model (RSM) might do a better job. On the contrary, Revstedt et al. (1998) reported that the RSM model parameters are not universal, cannot handle fully

developed turbulence nor mixed laminar/turbulent flows and that moreover RSM, which requires solving an enlarged system of seven additional PDE's, has difficulty in convergence.

Large Eddy simulations in stirred tanks have been reported by Revstedt et al. (1998), Derksen et al.(1998) and Derksen and Van den Akker, (1999). Revstedt et al. (1998) overpredict the azimuthal and radial velocities, pumping numbers and the rms values when compared with experimental data of Wu and Patterson, (1989). Derksen and Van den Akker's (1999) comparisons of the radial velocities with Wu and Patterson, (1989) and Derksen et al's (1998) LDA data are good. The tangential velocities are overestimated with maximum deviations of 15%. The computed turbulent kinetic energy shows broader peaks and larger magnitude near impeller than the data. The deviations from data are attributed to the lack of adequate spatial resolution (currently they use six million nodes) and not accounting for the solid wall in the sub grid scale model. While the LES models resolve more scales of turbulence than the standard turbulence models, both LES simulations discussed above overestimate the experimental values. The price at which this extra information is obtained i.e. long integration times, huge grids, higher order discretization schemes etc. currently does not justify the use of this scheme.

2.3 Multiphase Flows – Experimental Characterization

Unlike the extensive characterization of single phase flows in stirred tanks, the study of multiphase flows has been restricted to determination of global parameters like power consumption, relative power demand, overall holdup measurements, mixing time measurements and critical impeller speed required for complete homogenization or suspension. Only a few studies such as those of Lu and Ju (1987), Morud and Hjertager (1996), and Deen and Hjertager (1999), report the local quantities. We review each of these studies below.

Lu and Ju (1987) used HWA to simultaneously measure the local gas (air) holdup (accuracy is within 20%), the resultant mean liquid velocity (within 5% accuracy) and the root mean square (rms) fluctuating velocity of the liquid which was filtered tap water. They used a standard tank (28.8 cm diameter) with a disc turbine and a perforated ring sparger of 8 cm diameter. Measurements were made in the impeller discharge stream, confined to a vertical plane midway between the two baffles. The holdup, mean liquid velocity and turbulent intensities' variations with impeller speed and gas sparging rate at different radial and axial locations are reported. They report holdups in the range of 5-25 %T. They have performed experiments from 400 to 720 rpm. These quantities can also be obtained using CT and CARPT as discussed later on in this work (Chapter 7).

Morud and Hjertager (1996) measured the mean and turbulent gas velocities using LDA. They used a tank of standard dimensions (0.222m in diameter), with a dished bottom, a Rushton turbine, with length of blade = width of blade = 1/4 impeller diameter, and with a clearance from the bottom of the tank of 0.47T. Gas (air) was introduced through an inlet pipe and entered through a porous sparger below the impeller. The vessel was operated at 360, 400, 560 and 720 RPM and gas flow rates $Q = 0.49, 0.75, 1$ and 1.33 volumes of gas per volume of liquid per minute (vvm). Their overall gas holdup varied from 1-8 %. They reported the gas phase radial velocity variations with RPM and the gas velocities at three different heights ($h = 0.23D, 0.47D$ and $0.72D$) using Phase Doppler anemometry. Gas phase turbulence seems to be isotropic. The radial velocities were measured every 5 mm in the radial direction and at an angle of 5 degrees relative to the baffles. Overall gas holdup variation with impeller rotation speed was reported. This work is very systematic and provides information that can be compared to data to be obtained from CT studies. Deen and Hjertager (1999) used DPIV to study the liquid phase properties for the same system as used by Morud and Hjertager (1996). Together they provide a relatively complete characterization of the gas-liquid system in the stirred tank at low to modest gas holdups (1-7%). Deen and Hjertager (1999) performed measurements at impeller speed of 360 rpm and gas flow rate of 0.5 vvm. They compared the axial profiles of their radial and axial velocity, both with and without gas, with LDA data of Wu and Patterson

(1989) obtained without gas. The maximum radial velocity without gas was 23% lower and with gas was 80% lower than indicated by Wu and Patterson's (1989) liquid phase data. They did not measure the tangential velocities.

In summary, while Morud and Hjertager (1996) and Deen and Hjertager (1999) reported detailed measurements of gas phase and liquid phase velocities, both studies are restricted to low gas holdup fractions in the range of 0.01-0.07. Only Lu and Ju (1987) measured simultaneously liquid phase velocity, turbulence parameters and gas holdup fractions. Unfortunately, Lu and Ju (1987) reported only the resultant liquid velocities (not individual components) and their gas holdup measurements are not accurate, with errors as high as 20%. Hence, for gas-liquid systems there is a clear need for accurate and reliable information on the fluid dynamics of the liquid and gas phase, especially at higher gas holdup fractions. Given this, we would like to initiate the creation of a reliable database for the estimation of important fluid dynamic parameters for gas-liquid flows in stirred tanks using CARPT and CT.

2.4 Multiphase Flows – Numerical Simulations

Pericleous and Patel (1987) modeled gas-liquid flows in stirred vessels using an algebraic slip model. Momentum equations were solved using mixture properties. The presence of bubbles was accounted for by solving a convection diffusion equation with a constant slip velocity. The bubble concentrations were used to update the mixture density. Gosman et al. (1992) reported 3-D simulations of gas-liquid and liquid-solid flow in a stirred vessel using the black box approach. They used a two-fluid model with a k - ϵ turbulence model extended for two-phase flow (with consistent definitions for k and ϵ in the Favre averaged sense). Their gas-liquid simulations underestimated the measured gas holdup by 10-50 % according to the data of Revill and Irvine (1987), and the slip velocities predicted by their liquid-solid simulations are around 0.04m/s which is of the order of their particle settling velocities. The gas holdup underestimation is attributed to not modeling the coalescence and redispersion phenomena. Daskopoulos and Harris (1996)

suggested that Gosman et al.'s (1992) solid concentrations may be too dilute to draw any meaningful conclusion from their work.

Ranade and Van den Akker (1994) extended the snapshot approach (SA) to three dimensional multiphase simulations. They used a two-fluid model like Gosman et al. (1992) but employed a Reynolds averaging approach unlike Gosman et al. (1992) who used the Favre averaging. Although Favre averaging leads to fewer terms requiring closure, the experimental techniques, provide us with Reynolds averaged information. The SA model, unlike Gosman's, requires no experimental input for the impeller region. Ranade and Van den Akker (1994) compared their results with the experimental data of Rousar and Van den Akker (1994). The comparison between the predicted and experimental axial velocities is shown below in Figure 2-6. The axial velocity is over estimated near the impeller (maximum deviation within 35-40%) and underestimated near the wall.

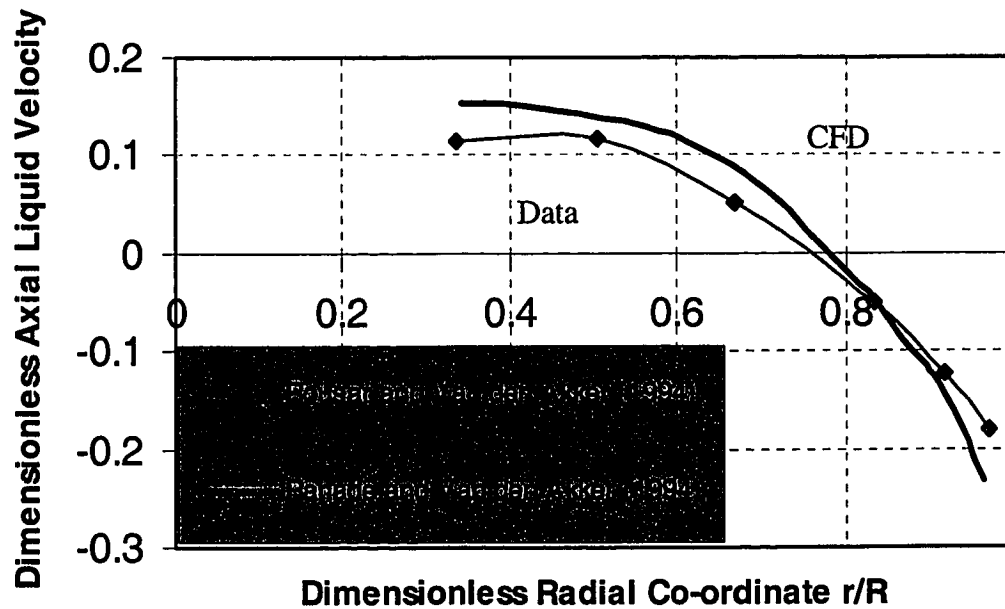


Figure 2-6. Comparison of Predicted Radial Profiles of Axial Mean Velocity (Liquid) with Experimental Data at $z/R=0.33$ and $Q_g= 8$ l/min

The comparison between the experimental and the predicted tangential velocities is shown in Figure 2-7. The tangential velocities are underestimated near the impeller region (maximum deviation within 21%) while the velocities are considerably overestimated near the wall (around 40% deviation from the data). Lack of adequate spatial resolution is cited as a reason for this difference.

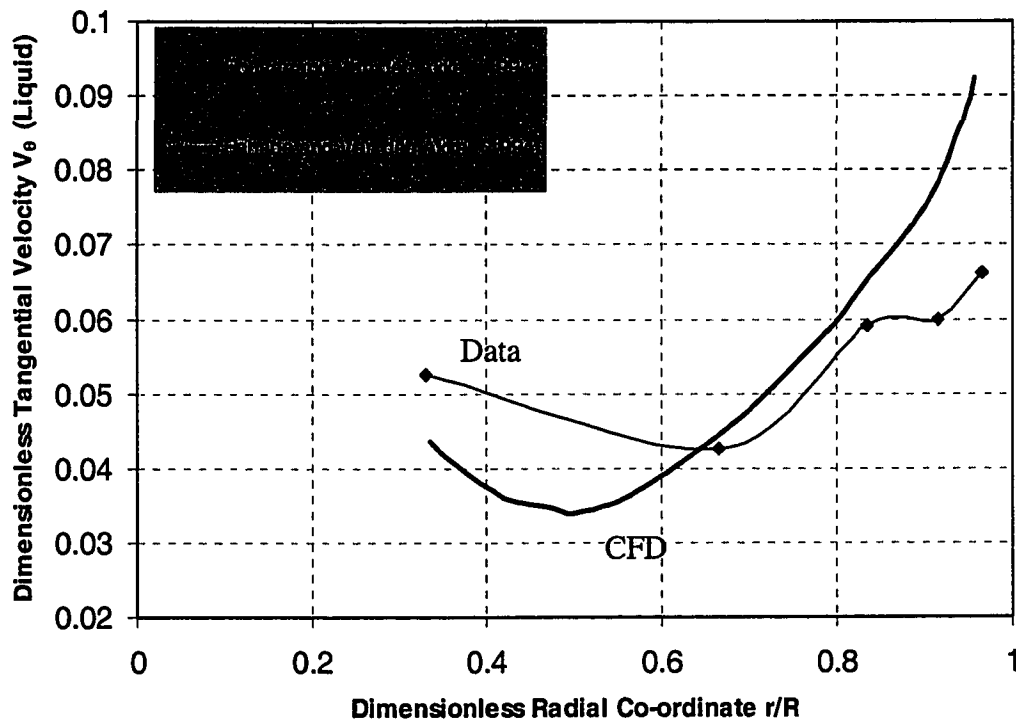


Figure 2-7. Comparison of Predicted Radial Profiles of Tangential Mean Velocity (Liquid) with Experimental Data at $z/R=0.33$ and $Q_g=8$ l/min

The comparison between the experimental and predicted turbulent kinetic energy is shown below in Figure 2-8. Rousar and Van den Akker (1994) have reported only the axial and tangential fluctuating velocities. Hence the kinetic energy is calculated assuming isotropy. The kinetic energy is underestimated by almost 90% near the impeller tip while it is overestimated by 53% near the wall.

The predicted and experimental relative power demand is compared below in Figure 2-9. The predictions underestimate the reduction in power demand (maximum deviation is 67%). Inadequate grid resolution is cited as the reason for the quantitative differences. However, the model is seen to predict the right qualitative trend.

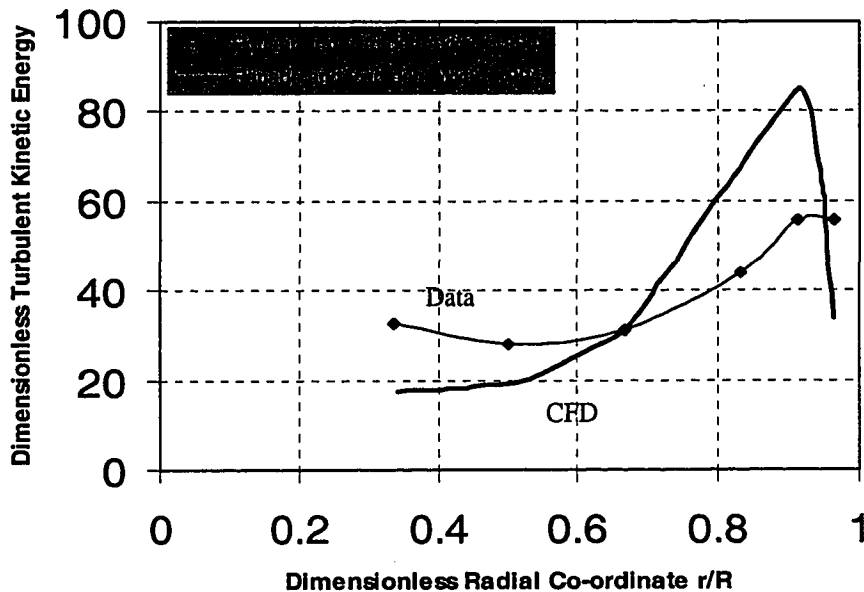


Figure 2-8. Comparison of Predicted Radial Profiles of Turbulent Kinetic Energy with Experimental Data at $z/R=0.33$ and $Q_g= 8$ l/min

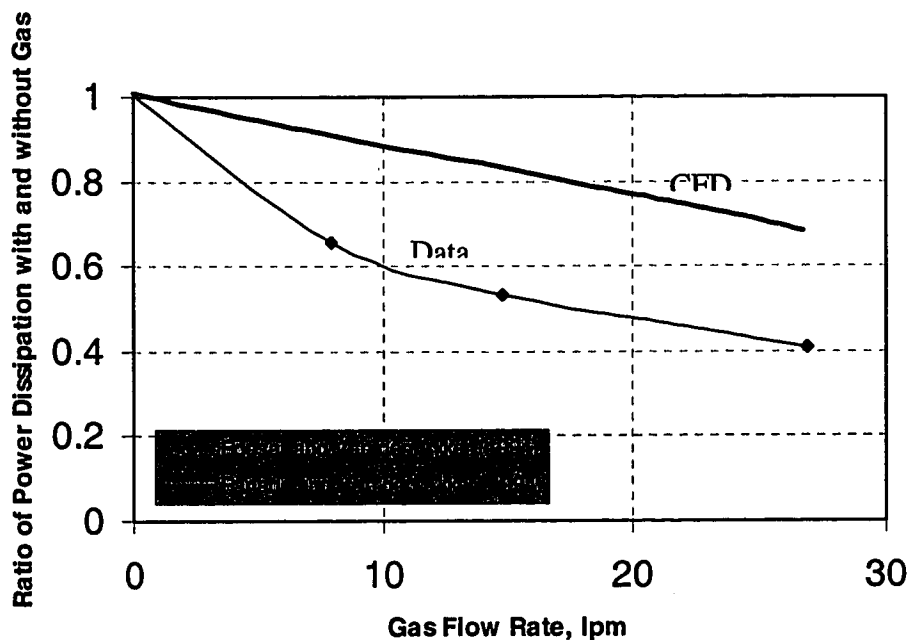


Figure 2-9. Comparison of Predicted Drop in Power Consumption at Different Gas Flow Rates

The comparison between predicted and measured overall gas holdup is shown below in Figure 2-10. The predicted gas holdup profiles compare very well with the measured holdup values (maximum deviation is around 5%). However, the maximum holdup studied was 5%.

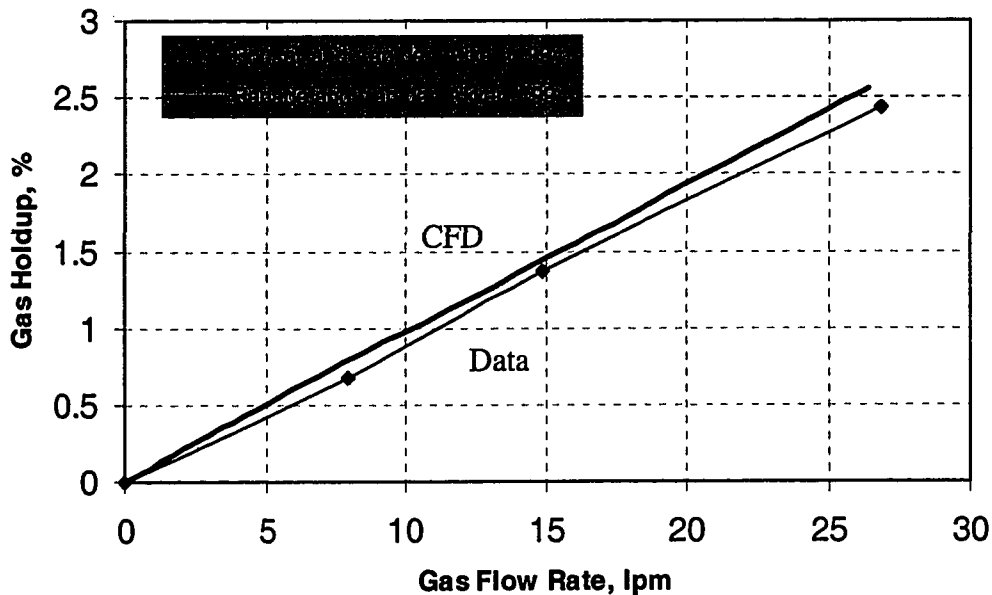


Figure 2-10. Comparison of Predicted Overall Gas Holdup with Experimental Data.

Thus, the Snapshot approach is seen to predict the qualitative trends well and the quantitative agreement is reasonable given that the model requires no experimental input (other than the bubble diameter for the two fluid model). The model is also reported to capture the right trend for other phenomena like accumulation of gas behind the impeller, pressure distributions in the impeller region, angular variations of gas and liquid velocity around the impeller tip, etc. Clearly with additional improvement (like adequate spatial resolution, customized drag formulations etc.) the model has potential to be validated with two phase data.

Morud and Hjertager (1996) reported a two-dimensional, two-fluid simulation with the standard $k-\epsilon$ model. They modeled the impellers and baffles with source and sink terms (like Pericleous and Patel, (1987)). Comparisons between the measured and the simulated overall gas holdup and of the relative power demand variation with gas flow rate are

reasonable (predictions within 20-40% of data). The mean velocity predictions of the gas phase near the impeller compare well with the data but the velocities are overestimated in the bulk. Qualitative profiles of the tangential velocities compare well with measured data. The conditions used by Morud and Hjertager (1996) are different and one reports liquid phase velocities while the other reports gas phase velocities. Hence there is little scope for comparing the two studies.

The above review suggests that multiphase flow modeling in stirred tanks is still in a nascent stage. Given the unavailability of a detailed experimental database for multiphase flows in stirred tanks, methods like the Snapshot approach, MRF and sliding mesh approach which require no experimental inputs are preferred over the black box approaches. Out of the above three methods we propose to examine the predictive capabilities of the SA to simulate gas–liquid flows in stirred tanks.

Chapter 3

A Lagrangian Description of Flows in Stirred Tanks Via Computer Automated Radioactive Particle Tracking (CARPT)

3.1 Introduction

In this chapter Computer Automated Radioactive Particle Tracking (CARPT) is implemented for the first time in characterization of flows in stirred tanks. Both the experimental technique and the experimental set up are discussed. A qualitative assessment of the CARPT results obtained in a STR using water as the fluid is provided. The objective of this study is to establish the type of information that CARPT can provide in single phase flows in stirred tanks. This is followed by quantitative comparison with data obtained by established techniques like LDA and DPIV (Chapter 4). The ultimate objective is to use CARPT in opaque multiphase flows in stirred tanks at conditions inaccessible to other measurement techniques.

3.2 Experimental Setup

3.2.1 The Stirred Vessel

The stirred vessel used is of the standard Holland and Chapman type (1966) consisting of a cylindrical tank with four baffles and a stirrer (Figure 3-1). All the parts are made of a transparent material (clear plexi glass). The diameter of the vessel is $D=0.2\text{m}$. The baffles are $D/10$ in width and $D/125$ in thickness, vertical and flush with the wall. The agitator is a Rushton turbine composed of a disc of $D_f= D/3$ overall diameter with six rectangular

radial blades of $w=D/15$ height and thickness $D/125$. The turbine is located at a distance D_1 from the bottom of the tank which is filled with water to a height equal to the tank diameter. The shaft diameter is $D/31.5$ and the disc thickness is $D/67$.

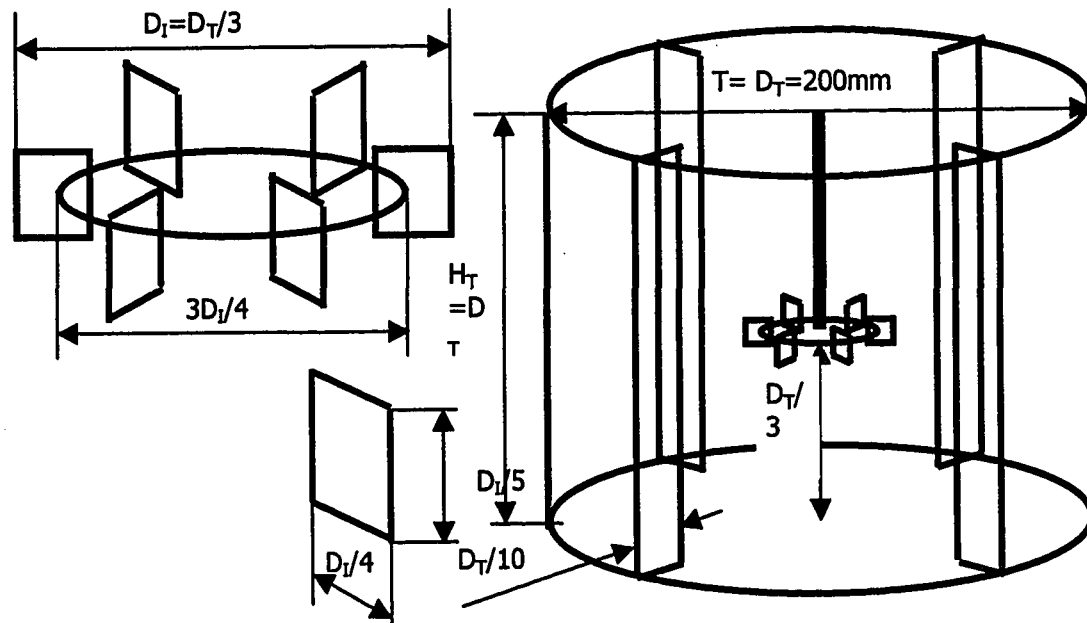


Figure 3-1. Stirred Tank of the Holland-Chapman type Used for the CARPT Experimental Study

3.2.2 The CARPT Setup

The CARPT set up consists of 16 scintillation detectors (Figure 3-2) mounted on aluminum supports, which are arranged on an octagonal base. There are eight aluminum supports placed around the tank at 45 degrees to each other. Each support has two holes of diameter 2.2'' (5.6 cms). The axial location of the center of the holes from the octagonal base plate is as follows: The lowest hole is at a distance of $Z_1=2.86$ cms, then $Z_2=7.72$ cms, $Z_3=12.59$ cms and $Z_4=17.45$ cms. Every aluminum support has the holes placed, either at Z_1 and Z_4 or at Z_2 and Z_3 . Every consecutive support has alternate locations of the holes. This configuration optimizes the extent to which the particle can be seen by each detector in the tank (Degaleesan, 1997). Each detector unit is a cylinder

2.125'' (5.4 cms) in diameter and 10.25'' (26.0 cms) long, and contains an active cylindrical Sodium Iodide crystal (2'' X 2'' i.e. 5.08 cms X 5.08 cms). Every axial level has four detectors each at right angles with the others. These detectors are placed at the above mentioned four different axial levels. The detectors at each axial level are staggered by 45 degrees with respect to the previous level.

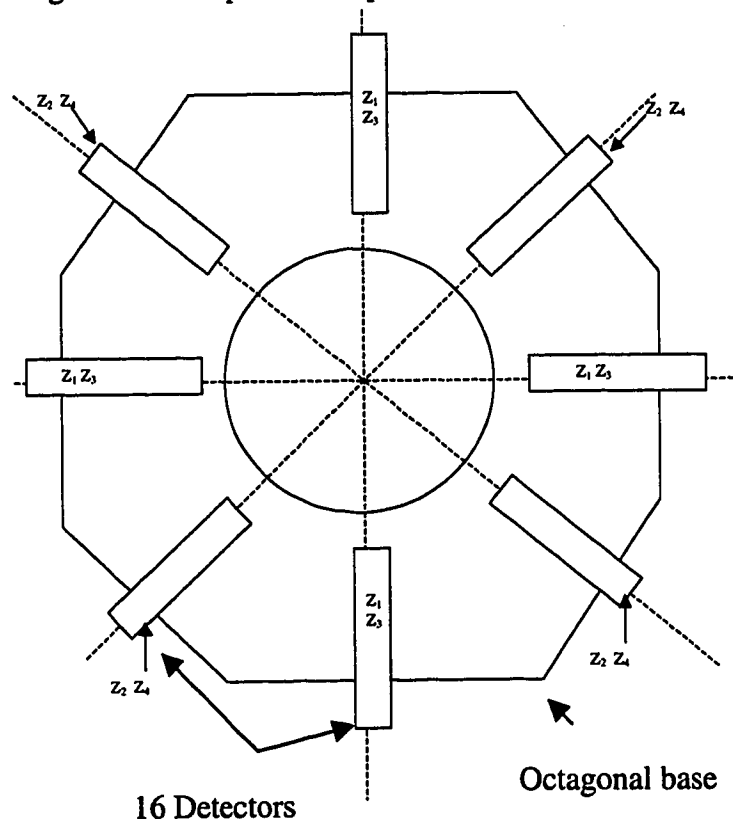


Figure 3-2(a). Top View of CARPT Setup for the Stirred Tank

The radioactive particle (Figure 3-3), the position of which is tracked, is about 2.3 mm in diameter, made of polypropylene with radioactive Scandium embedded in it (Sc-46, 80 μCi) and with an air pocket so that the effective density of the particle is equal to that of water (or the fluid tracked). In spite of the fact that the tracer particle is neutrally buoyant, its size is too large to enable it to follow all the energy containing eddies in the flow. This particle was chosen because it was readily available to test the CARPT technique in stirred tanks. Once feasibility is established one can search for a more suitable tracer size

to reach a compromise between size and density mismatch. We discuss the limitations of the current tracer particle in the subsequent section.

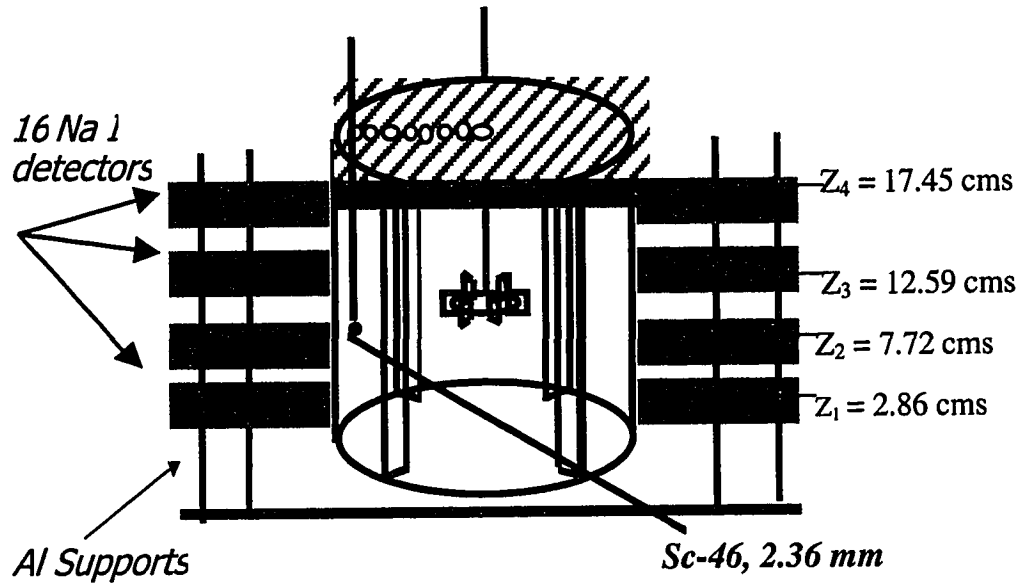


Figure 3-2(b). Front View of CARPT Setup for the Stirred Tank

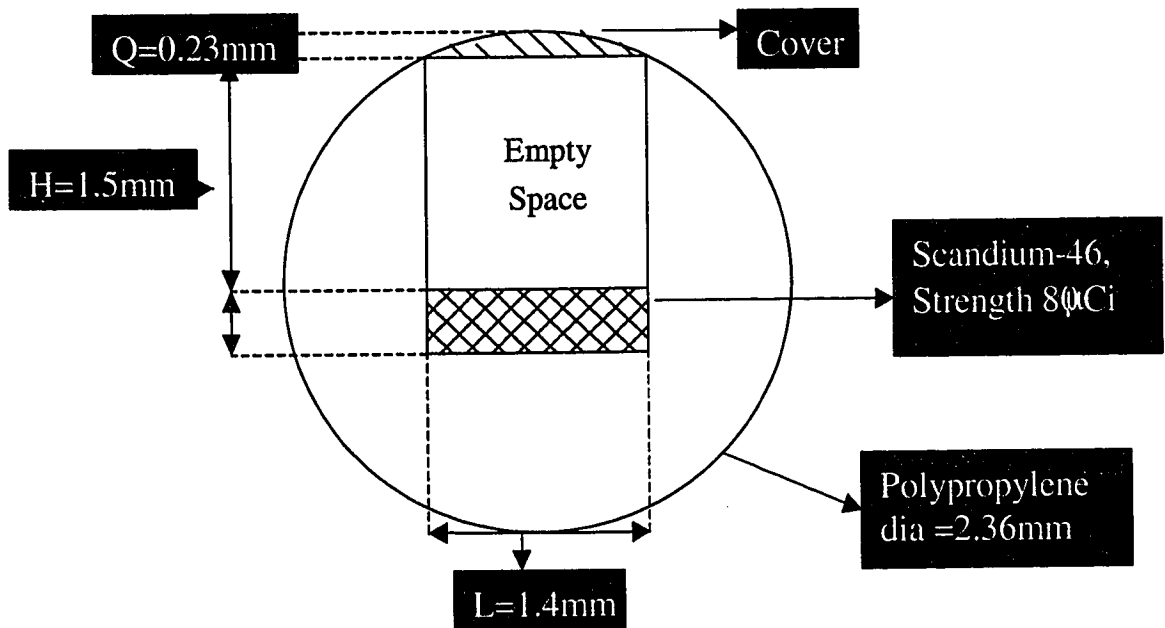


Figure 3-3. Details of the CARPT Tracer Particle

3.2.3 The CARPT Technique

Devanathan (1991) adapted the Computer Automated Radioactive Particle Tracking (CARPT) technique to study the motion of the liquid phase in bubble columns. A single radioactive particle, that is neutrally buoyant with respect to the liquid being tracked, was used with radioactive Scandium, Sc-46, emitting γ radiation employed as the isotope. During an experiment, as the particle moves about in the vessel tracking the liquid phase, the position of the particle is determined by an array of scintillation detectors that monitor the γ radiation emitted by the particle. The radiation intensity recorded at each detector decreases exponentially with increasing distance between the particle and the detector. In order to estimate the position of the particle from the radiation intensities, calibration is performed prior to a CARPT experiment by placing the particle at various known locations and monitoring the radiation recorded by each detector (Figure 3-4). Using the information acquired, calibration curves are established that relate the intensity received at a detector to the distance between the particle and the detector (Figure 3-5). Once the distance of the particle from the set of detectors is evaluated, a weighted regression scheme is used to estimate the position of the particle at a given sampling instant in time. Thereby a sequence of instantaneous position data is obtained that yields the position of the particle at successive sampling instants (Figure 3-6). In our experiments the sampling frequency was 50 Hz, i.e. particle position is identified at 0.02 seconds intervals. Time differentiation of the successive particle positions yields the instantaneous Lagrangian velocities of the particle, i.e., velocities as a function of time and position of the particle. Ensemble averaging of the Lagrangian particle velocities, detected in each of the compartments into which the tank has been subdivided to, is performed to calculate the average velocities and the various "turbulence" parameters of the liquid. Clearly, due to finite size of the particle, we are not capturing the true and fine scale liquid turbulence but rather various cross correlations of particle velocity fluctuations around the mean.

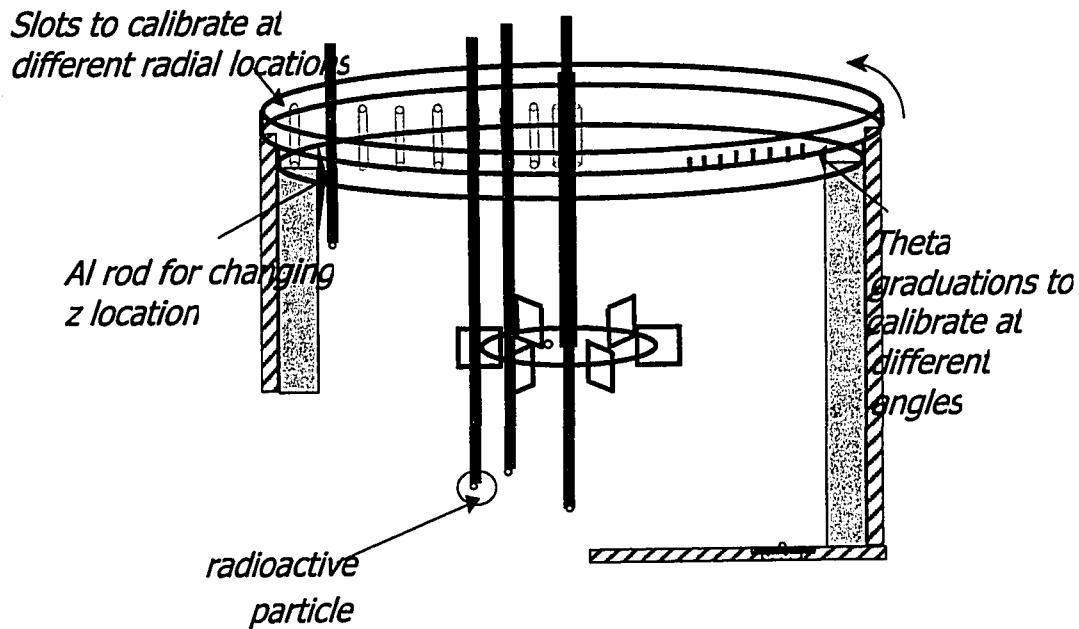


Figure 3-4. Details of the CARPT Calibration Procedure.

3.3 Measurement Errors

A preliminary identification of the different sources of errors in CARPT measurements is discussed here. A more detailed quantitative analysis of the various errors is discussed in Chapter 5.

3.3.1 Tracer Ability to Follow the Liquid

The accuracy of determining the liquid velocity using the particle tracking technique depends in part on the ability of the tracer particle to follow the liquid. Close matching of the density of the particle with that of the liquid ensures that the particle is neutrally buoyant. However, the finite size of the particle makes it differ from a liquid element, unable to sample the small scale eddies. Devanathan (1991) showed that for a particle of size 2.36 mm, and a difference of 0.01 gm/cm^3 in density between the particle and the liquid, the maximum difference in the velocities (between particle and liquid) is 1cm/s.

Degaleesan (1997) estimated that the maximum frequency at which the 2.36 mm particle can be taken to follow up to 99.0% of the liquid velocity is 30Hz. She also showed that for frequencies smaller than 30 Hz, which represent the large scale eddies, the particle is able to closely follow the liquid phase, and the measured particle fluctuating velocities can be considered to be those of the liquid phase. Higher frequency eddies cannot be followed by the current particle (for further analysis refer to Chapter 5, section 5.3.4.4).

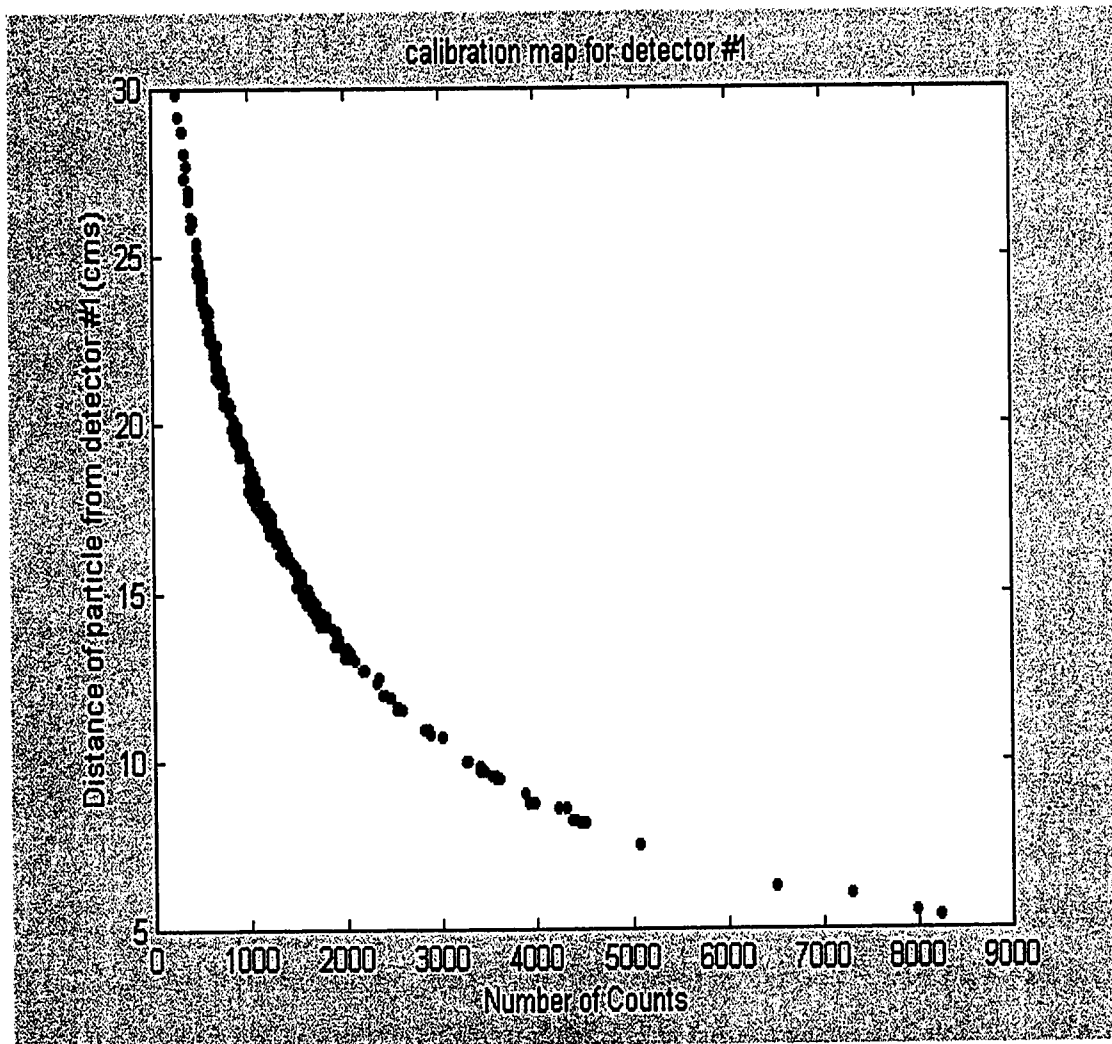


Figure 3-5. Calibration Map for Detector #1

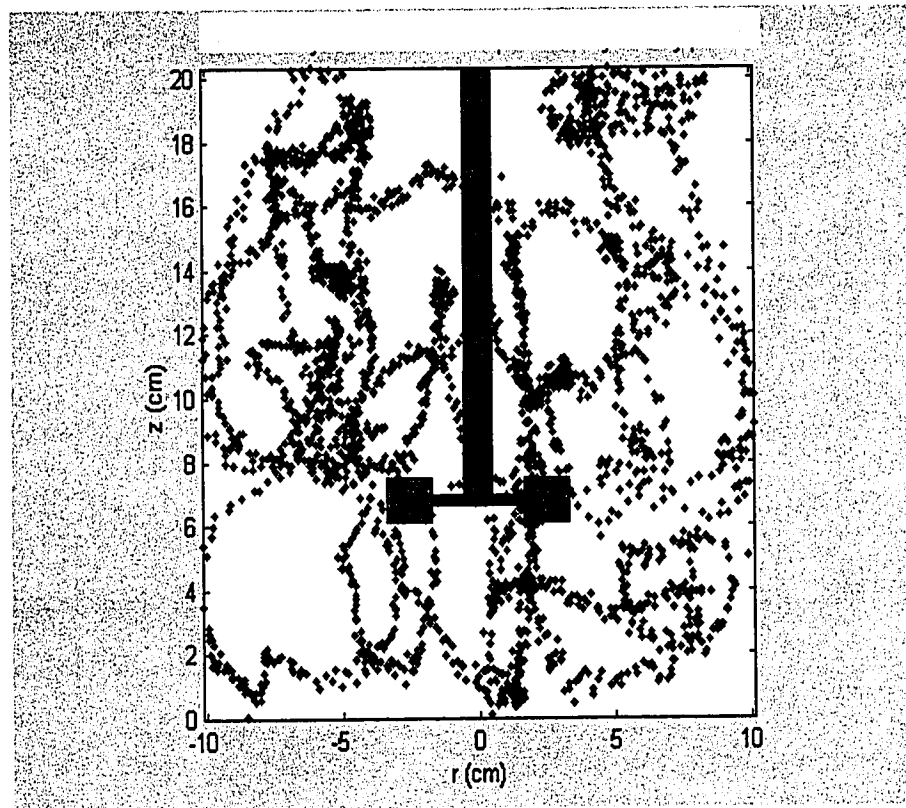


Figure 3-6. Projection of the Particle Trajectory in a Vertical Plane at $N = 150$ rpm for 30 s

3.3.2 Statistical Nature of Gamma Photons

The emission of gamma photons from a radioactive source follows a Poisson distribution (Tsoulfanidis, 1983). Therefore every mean count reported in the calibration curve is associated with a distribution of counts. When reconstructing the particle position from the instantaneous counts registered by each detector only the mean values are used, while in reality the counts measured will be but one value from the distribution seen around the mean. Hence, the reconstructed particle position will not be the exact instantaneous position. The error in reconstructing the particle position along a known trajectory (a

circular one when particle is placed in the impeller disc at $r=6.0$ cms, $Z=6.67$ cms) is found to be less than 3mm (for more details refer to Chapter 5 section 5.2).

3.3.3 Solid Angle Effect

Devanathan (1991) showed that the solid angle has a significant effect on the detected radiation intensity and that the side face of the detector composed of Sodium Iodide (NaI) cylindrical crystal is more effective than the front face from the standpoint of detection. If many detectors see the particle, each with a different solid angle, then the errors introduced by some detectors are partially compensated for by the other detectors resulting in better accuracy. To obtain higher accuracy in tracer location, solid angle effects have to be considered in the calibration. To some extent this has been implemented by Degaleesan (1997), by using a two step method in reconstructing the particle position. In the second step solid angle effects are taken into account. Further improvements can be accomplished by modeling the various interactions of the radiation with the medium and the detector crystal. Modeling of the gamma ray interactions using Monte Carlo simulations has been successfully performed by Larachi et al. (1994) who has used radioactive particle tracking to study the behavior of solids in ebullated beds.

Given the above possible sources of errors in reconstructing the particle position in a stirred tank, and considering the estimates of their maximum magnitudes, we find the accuracy in reconstructing particle position to be reasonably good. This can be seen from the fact that the reconstructed particle positions are hardly ever located in the region of the baffles which are about 1.5 mm thick (Figure 3-7).

3.4 Experimental Conditions

Water is used as the fluid whose motion is tracked by the radioactive particle. Experiments were conducted at 150 rpm ($Re_{imp}=12,345$) at room temperature. The height of the liquid in the tank was 20.0 cm (equal to tank diameter).

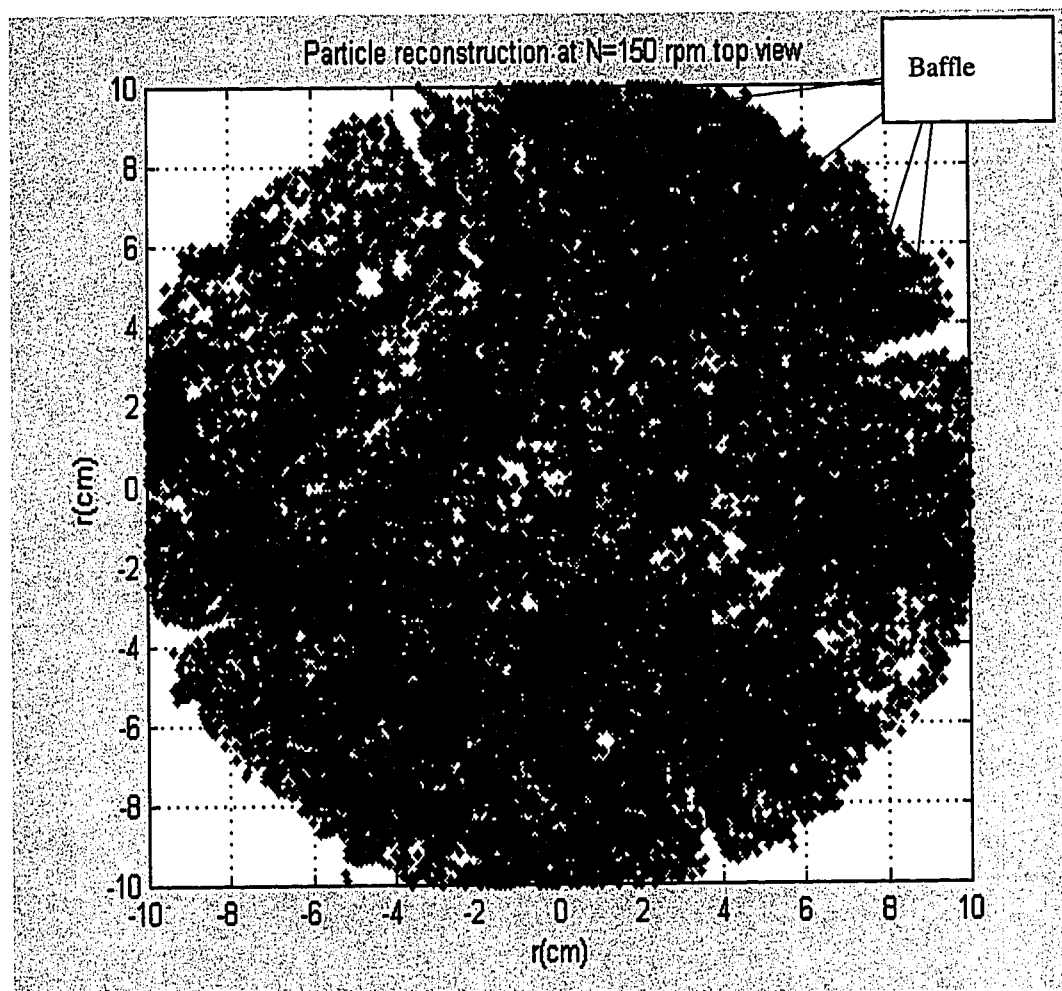


Figure 3-7. Projection of the Reconstructed Particle Position at N = 150 rpm (Top View for 1 hr of the 16 hr Run)

3.5 Results and Discussion

3.5.1 Validity of Experimental Data

As a first step in establishing the validity of their experimental data, different researchers have reported mass balance verifications. The balance is usually verified in a control

volume containing the impeller. These results have already been summarized in Table 2-2(c) which shows that the mass balance is usually satisfied within 1-10% accuracy. Table 2-2(c) suggests that CARPT's accuracy in closing the mass balance within 7% is comparable to other techniques.

3.5.2 Location of the Eye of the Recirculating Loops

The azimuthally averaged velocity in the r-z plane is displayed in Figure 3-8. The velocity vector plot captures the key qualitative features expected in this stirred tank configuration (Van Molen and Van Maanen, 1978; Yianneskis et. al., 1987; Costes and Couderc, 1988; Wu and Patterson, 1989; and Ranade and Joshi, 1990). There is a radial jet in the plane of the impeller, which goes right to the walls. This high-speed radial jet entrains the surrounding fluid and slows down as it approaches the tank wall. Near the tank wall, the jet stream splits into two portions, one of which then circulates through the upper and the other through the lower portion of the tank and both are finally drawn back into the impeller region. These two streams result in the two recirculation loops seen in Figure 3-8. One loop is above the impeller and the other below the impeller. Both circulation loops exhibit what is conventionally called the eye of the loop. The vertical position of the eye of the upper loop is found to be around $D/2$ and the eye of the bottom loop is at an elevation around $D/5$ (where D is tank diameter) with the radial location of both loops at $2D/5$. This compares well with the dimensionless locations reported by other researchers as evident from Table 3-1.

3.5.3 Mapping the Dead Zones in the Stirred Tank

At the bottom of the stirred tank the influence of the impeller is not as pronounced as in the rest of the tank. This results in regions of very low velocities at the bottom of the tank where fluid elements (or dispersed phase like solid particles) tend to spend much longer time than in other portions of the tank. The presence of such regions can lower the mixing

efficiency. The existence of such zones has been identified by flow visualization studies (Kemoun, 1995). Kemoun introduced a number of polypropylene beads (of $d_p=0.3$ mm and $\rho_p = 0.8$ gm/cc.) into the water flow in the same tank configuration as used in this work and illuminated the bottom of the tank with a laser sheet.

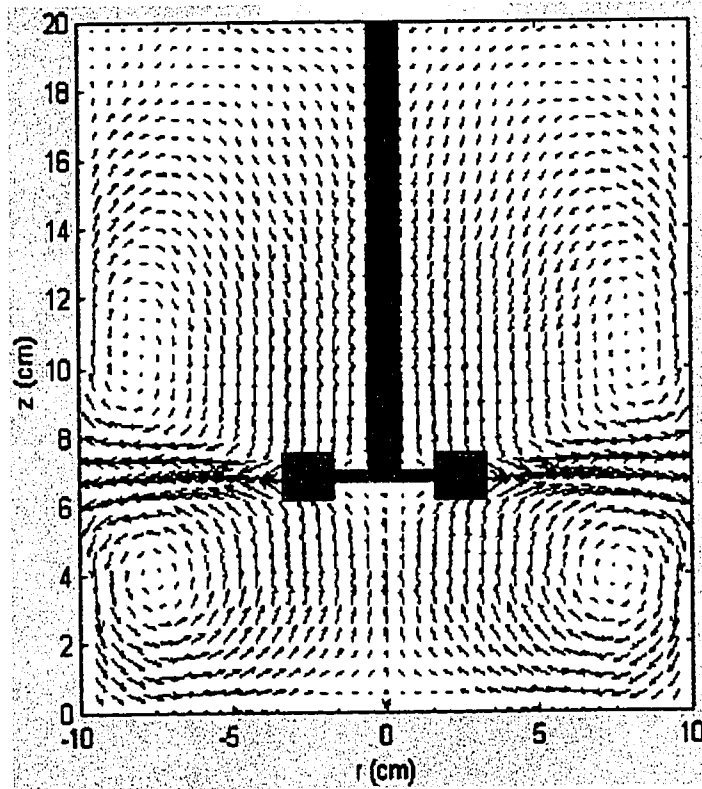


Figure 3-8. Azimuthally Averaged Velocity Vector plot at $N = 150$ rpm

Table 3-1. Location of the Eye of Circulation Loops ($T = D =$ tank diameter)

Researcher	Lower r/T	Lower z/T	Upper r/T	Upper z/T	Clearance H_c/T
Yianneskis et. al. (1987)	0.3	0.20	0.30	0.48	0.33
Costes and Couderc (1988)	0.4	0.25	0.4	0.75	0.50
Schaefer et. al. (1997)	0.4	0.20	0.4	0.5	0.33
Kemoun, et. al. (1998)	0.4	0.20	0.4	0.5	0.33
Current work	0.4	0.20	0.4	0.5	0.33

The regions with higher number of particles reflect more light and appear as the bright regions in the photograph. We reproduce here one such snapshot taken by Kemoun (1995) in Figure 3-9a where the bright spots can be seen to be in the form of a starfish like pattern. These bright regions correspond to the dead zones where particle velocities are low causing more particles to accumulate and settle. A similar plot has been generated from the CARPT data where the vector plot of the resultant of the radial and the tangential velocity at the bottom of the tank is shown in Figure 3-9b. The plot is colored with the contours of the total velocity vector in this plane. The blue regions show the regions of very low velocity. The yellow regions show the regions of high velocity. At the bottom the dead zone can be seen clearly and it seems to resemble a starfish. The interesting thing is that these dead zones seem to be due to a swirling tornado like structure, which starts just below the impeller plane and is entirely three dimensional in nature. The instability seems to begin at the baffles and slowly propagates downward until the starfish like pattern is observed at the bottom. This comparison of CARPT obtained results with direct flow visualisation illustrates CARPT's potential for capturing important flow phenomena.

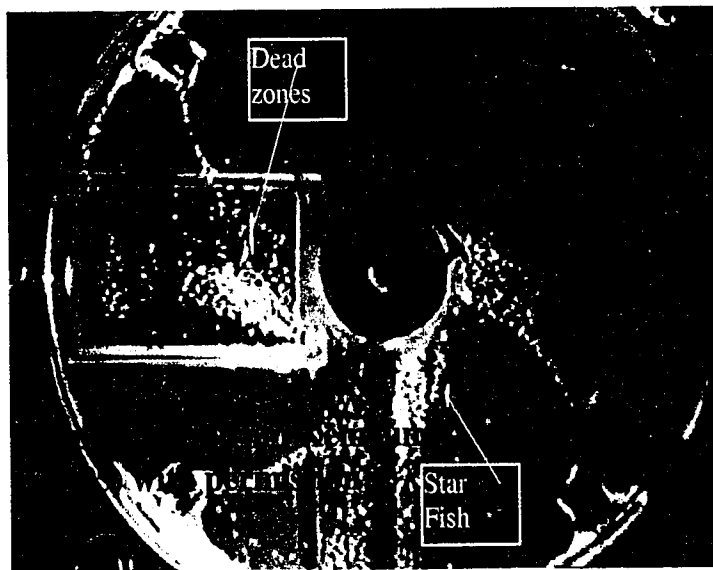


Figure 3-9a. Dead Zones from Flow Visualization Studies (Kemoun, 1995)

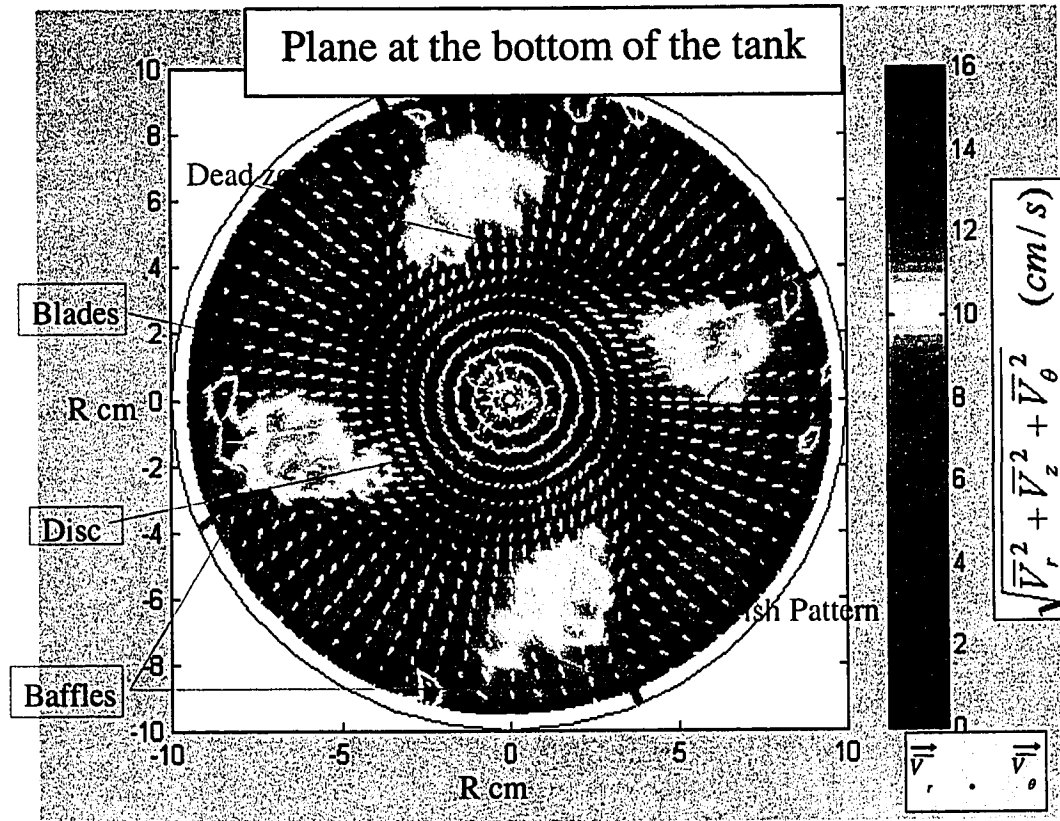


Figure 3-9b. Map of Dead Zones from CARPT

3.5.4 Partial Quantification of Dead Zones Using Sojourn Time Distributions (STDs)

In this study we extract the Sojourn Time Distribution (STD), i.e. strictly speaking the probability density function of Sojourn times for different regions in the tank, from the CARPT experiment. For illustrative purposes we have divided the tank only in the axial (vertical) direction into ten regions, each 2cms in height as shown in Figure 3-10. For each of these zones we compute the STD, as illustrated below, and we display the STDs in Figure 3-11. It is important to note that any desired additional compartmentalization in the angular (θ) and radial (r) direction is possible. Thus, STDs can be calculated from the experimental CARPT data for any region of interest in the stirred tank.

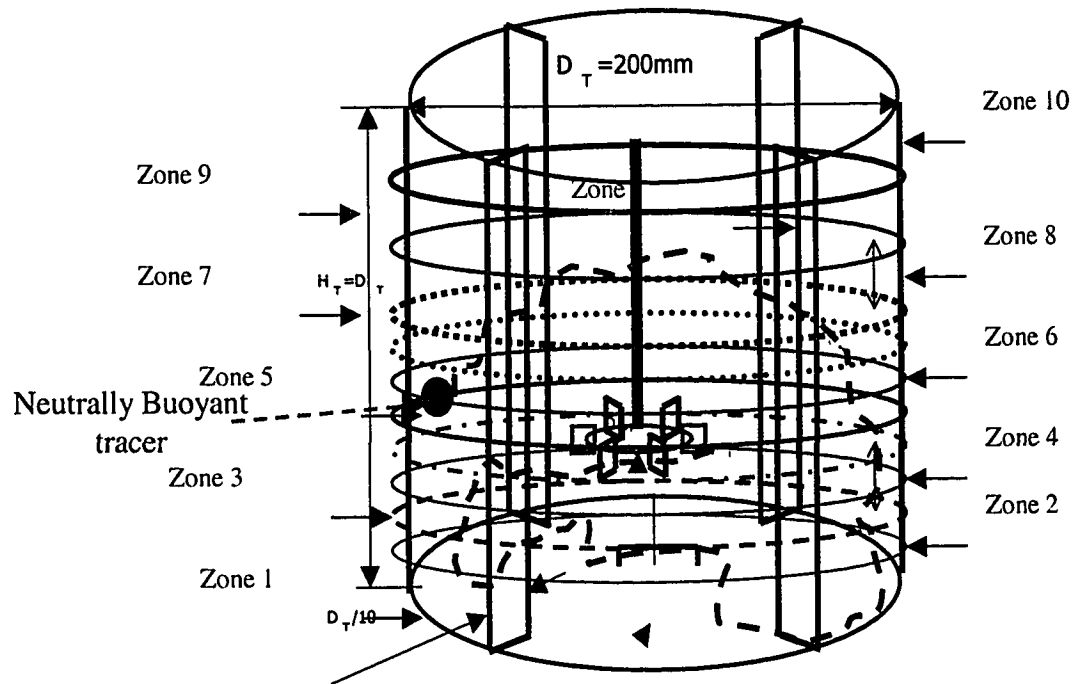


Figure 3-10. Compartmentalization of the Stirred Tank into Axial Zones

We obtain the STD for an axial slice of the tank, defined above in Figure 3-10, as follows. From the CARPT experiment the record of the particle trajectory as a function of time is available with the time starting at zero and with every subsequent particle location recorded at intervals of $\Delta t = 0.02$ seconds (corresponding to $f_{\text{sample}} = 50\text{Hz}$). Hence, the N^{th} particle position corresponds to the time of $N\Delta t$ seconds since the start of the experiment. To generate the STD curve for each zone, the records of the particle positions are scanned until the particle is found in the zone of interest (i.e. the axial co-ordinate of the tracer is between Z_{lower} and Z_{upper} of that zone). Now the particle position is tracked until the tracer leaves the zone of interest. The number of consecutive occurrences (say N) from the time the tracer particle entered the zone until the time the tracer particle leaves the zone of interest is noted. From this the sojourn time of the tracer particle during that pass through the zone of interest can be calculated as

$$t_{\text{resl}} = N \cdot \Delta t \quad (3-1)$$

This procedure is repeated every time the particle enters and leaves the zone of interest. For a typical CARPT run of 16 hours the particle enters and leaves the bottom most zone ($Z=0-2\text{cms}$) more than 20,000 times and each of those visits contributes to the STD curve. The above procedure is repeated for all the other zones. All STDs are then calculated. In addition, the STD, like any other probability density function, can be characterized in terms of its moments like the mean value, standard deviation, skewness and kurtosis and this is also done. The definition of each of these statistical quantities is reviewed below.

The mean of the STD in the i^{th} zone is denoted by μ_i and is defined by

$$\mu_i = \sum_{j=1}^{N_{\text{tot}}} t_{\text{res}j} E_i(t_{\text{res}j}) \Delta t \quad (3-2)$$

Here N_{tot} corresponds to the number of particle occurrences in zone i (20000 for the bottom zone), $t_{\text{res}j}$ is the sojourn time of the tracer particle during the j^{th} trip to zone i of interest, as given by (3.1) and $E_i(t_{\text{res}j})$ is the probability density function p.d.f. of the STD for that zone. The first moment (μ_i) provides an insight as to whether the region experiences low or high through flow. A region where the mean residence times are higher can be thought of as a region of lower velocities and ultimately as dead zones.

The variance of the STD in the i^{th} zone is denoted by σ_i^2 and is defined by

$$\sigma_i^2 = \sum_{j=1}^{N_{\text{tot}}} (t_{\text{res}j} - \mu_i)^2 E_i(t_{\text{res}j}) \Delta t \quad (3-3)$$

The positive square root of the variance is the standard deviation denoted by σ_i . σ_i^2 is also referred to as the second moment about the mean value and it indicates how “spread out” the STD is.

Skewness is the third moment about the mean, and is defined for the STD of the i^{th} zone as

$$\gamma_{1i} = \sum_{j=1}^{N_{\text{tot}}} \left(\frac{t_{\text{res}j} - \mu_i}{\sigma_i} \right)^3 E_i(t_{\text{res}j}) \Delta t \quad (3-4)$$

It is a measure of asymmetry of the distribution. If $\gamma_{1i} > 0$, the distribution is said to be skewed to the right and if $\gamma_{1i} < 0$, the distribution is said to be skewed to the left. If the p.d.f. of the variable is symmetric about the mean then $\gamma_{1i} = 0$.

The fourth moment about the mean is called kurtosis, and is defined for the STD of the i^{th} zone as

$$\gamma_{2i} = \sum_{j=1}^{N_{tot}} \left(\frac{t_{resj} - \mu_i}{\sigma_i} \right)^4 E_i(t_{resj}) \Delta t - 3 \quad (3-5)$$

It reflects the degree to which the population is distributed in the tail of the distribution. $\gamma_{2i} > 0$ means that the data is concentrated around the mean (it is leptokurtic); $\gamma_{2i} < 0$ means that the data is concentrated in the tails of the distribution (it is platykurtic).

The CARPT data in the stirred tank has been processed as discussed above to generate the STD curves shown in Figure 3-11. Inspection of the STD's in various zones reveals that there is a definite similarity in the shape of the STDs in the zones above (eg. E_5 and E_6 etc.) and below the impeller (eg. E_2 , E_3). It is also evident from Figure 3-11 that the STD in the very bottom region (E_1) is very similar to that in the top most region (E_{10}). Moreover, the mean residence times and the standard deviations (variances) are the largest in these zones, as shown in Figure 3-12. As discussed earlier, flow visualisation with polystyrene particles revealed stagnant zones in the bottom zones which were confirmed by CARPT. CARPT data interpreted in terms of STDs and their moments reveal that the stagnant zones can then also be expected in the top region in the tank where the standard deviation of the STD is even somewhat higher than in the zone at the bottom of the tank (see Figure 3-12). Further compartmentalization of the tank for CARPT data processing can identify the precise location of such dead zones. Clearly, compartmentalization in the θ and r direction would allow examination of the regions around the baffles etc.

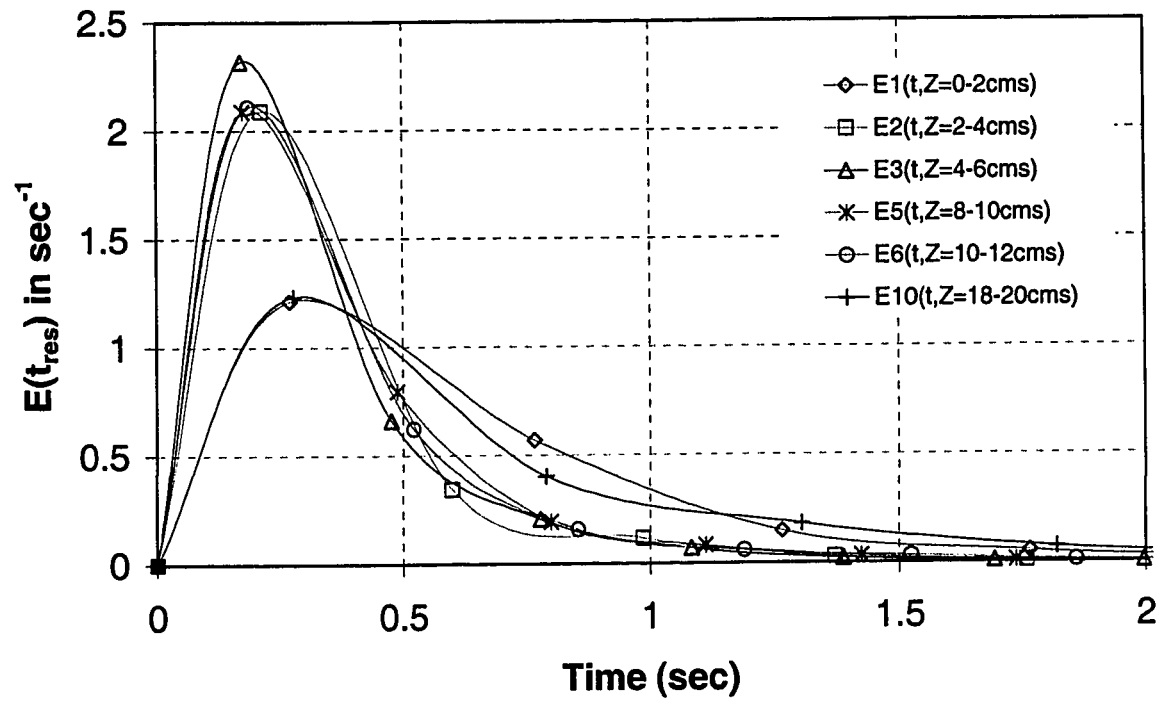


Figure 3-11. Probability Density Functions of the Sojourn Time Distributions in Different Axial Zones of the STR from CARPT Data.

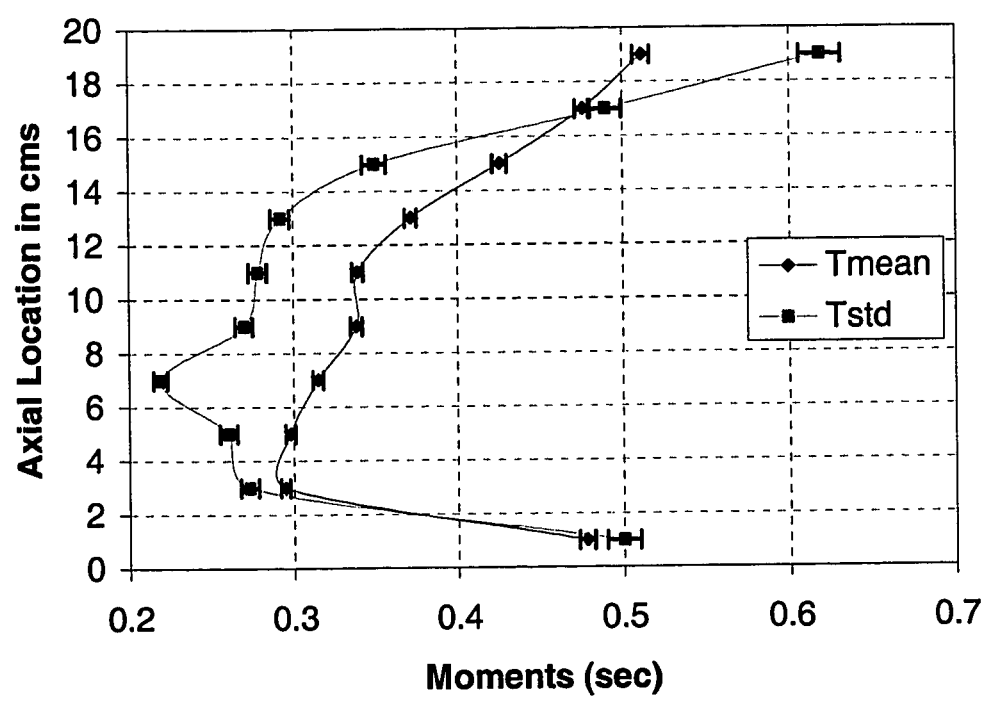


Figure 3-12. Axial Variation of the Mean and of the Standard Deviation of the STDs

From the STD curves the different moments were extracted as per equations (3-2)-(3-5) and are summarized in Table 3-2.

Table 3-2. Different Moments of the STD Curves in Various Axial Zones in a Batch Stirred Tank

Zone	Z (cm)	Tmean (sec)	Tstd (sec)	Skewness	Kurtosis
1	0-2	0.478	0.5	1.94	6.62
2	2-4	0.295	0.278	2.41	10.0
3	4-6	0.298	0.26	2.40	9.76
4	6-8	0.315	0.219	1.30	3.91
5	8-10	0.338	0.269	2.61	10.8
6	10-12	0.339	0.278	2.91	13.1
7	12-14	0.371	0.293	2.64	13.3
8	14-16	0.426	0.349	1.90	6.05
9	16-18	0.476	0.489	2.02	6.86
10	18-20	0.511	0.618	1.94	5.15

In Figure 3-12 the axial variation of the mean and the standard deviation of the STD curves for the axially distributed compartments are shown. This figure indicates that the mean residence time is the highest at the top and the bottom of the tank which was also evident from Figure 3-11. This trend is as expected since both at the top and the bottom of the tank the velocities are very low and, hence, once the particle enters these regions it tends to remain longer in these regions than in the impeller plane where the velocities are the highest. The mean residence time reaches a minimum in zone 2 ($Z=2-4$ cms) and then increases progressively until it reaches its maximum value in the topmost zone. The axial variation of the standard deviation of the sojourn times reaches a minimum in the zone containing the impeller (Zone 4) and then increases exhibiting the same trend as the mean sojourn times. The lowest standard deviation in the impeller plane would seem to suggest

that the flow in this region is the closest to plug flow with the deviation from plug flow increasing as we move away from this zone. This confirms the presence of an almost unidirectional radial jet in the impeller zone and regions of lower velocity near the bottom and top of the tank. The axial variation of the third and the fourth moment of the STD's are shown in Figure 3-13. The skewness (third moment) is seen to be greater than zero in the entire tank which indicates that the distribution is skewed to the right throughout the tank. This skewness to the right is seen to be the smallest in the zone containing the impeller and at the bottom and the top portion of the tank. The kurtosis in the entire tank is greater than zero which suggests that the sojourn times are concentrated around the mean (i.e. it is leptokurtic) as evident from Figure 3-11.

It should be reemphasized that we have compartmentalized the stirred tank into equal segments in the axial direction without partitioning in radial or azimuthal direction only as a matter of convenience and to illustrate the STD concept and demonstrate how CARPT data can be used to obtain STDs. The stirred tank could readily be divided into a two dimensional or three dimensional compartmental sections as demonstrated by Mann and coworkers (Mann et. al., 1997) and CARPT data can be used to provide STDs of such compartments and to provide "connectiveness" i.e. flow exchange parameters between the compartments which are needed for mixer and reactor performance calculations.

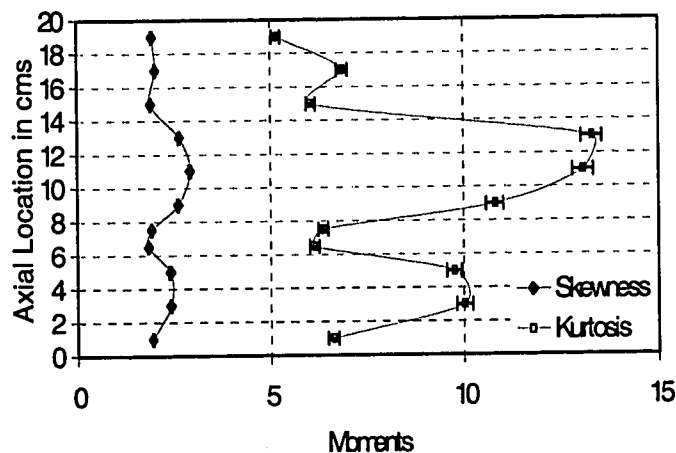


Figure 3-13. Axial Variation of the Skewness and the Kurtosis of the STDs

3.6 Summary and Conclusions

In this work CARPT has been introduced as a technique for measuring the flow field in a stirred tank with single-phase flow. The striking feature of CARPT is that upon calibration, data that take months to collect with conventional laser based techniques can be obtained in 16-20 hours! It has been shown that the CARPT technique can qualitatively capture many of the important flow structures observed in stirred tanks. The full three dimensional Lagrangian measurements obtained by CARPT also provide both better flow visualization and quantitative measures of the specific features of the flow pattern, like the location of the eye of the recirculating loops and the shapes of the dead zones at the bottom of the tank. CARPT allows direct assessment of the sojourn time distributions in different parts of the stirred tank. A partial quantification of the dead zones and active zones was achieved by examining the obtained STD curves. A more detailed quantitative comparison of the mean velocity and turbulent velocity profiles obtained in different regions of the tank by CARPT to the values reported by conventional LDA and DPIV techniques is presented in the following chapter (refer to chapter 4). Such a comparison will enable us to ascertain the limitations and the accuracy of the CARPT measurements in single phase flows before we embark on multiphase flow studies in stirred tanks.

Chapter 4

Characterization of Single Phase Flows in Stirred Tanks Via Computer Automated Radioactive Particle Tracking (CARPT)

4.1 Introduction

In this chapter a detailed quantitative assessment of the accuracy of the CARPT technique is provided. Comparison of the complete three dimensional mean velocity profiles from CARPT with similar PIV, LDA and other data is made. Further, comparisons of the fluctuating velocity components, like the root mean squared (rms) velocity and the turbulent kinetic energy are also reported in this chapter. In addition, the three dimensional profiles of the components of the Reynolds stress tensor are reported and discussed. Some Lagrangian measures of the fluid dynamics like Circulation time distributions (CTDs) and Hurst exponents are evaluated from the collected CARPT data.

4.2 Results and Discussions

The CARPT technique's ability to capture some of the key qualitative features of the flow in stirred tanks has already been described in detail (Chapter 3 and Rammohan et. al., 2001). The validity of the acquired velocity data was established by showing that it satisfies the mass balance. The technique's ability to capture the three dimensional recirculating loops above and below the impeller has been confirmed both qualitatively and quantitatively. Further, CARPT's ability to capture some of the other important characteristics of the flow in STR have been discussed in Chapter 3 and by Rammohan et. al. (2001).

In this chapter detailed quantitative comparisons of the velocity and turbulence measurements are provided. Further based on the findings (in Chapter 2) related to scaling of velocities and turbulent kinetic all velocities in this chapter have been non-dimensionalized by the impeller tip speed, the turbulent kinetic energy by V_{tip}^2 and the spatial co-ordinates with the tank diameter.

4.2.1 Grid Independence of Computed Mean Quantities:

Three different grids summarized in Table 4-1 were examined in this study.

Table 4-1. Details of the Grids Examined in This Study.

Grid Parameters	Grid I (GI)	Grid II (GII)	Grid III (GIII)
N_I	36	72	72
N_J	10	40	20
N_K	20	80	40
Δr (cm)	1.0	0.25	0.5
Δz (cm)	1.0	0.25	0.5
$\Delta\theta$ (degrees)	10°	5°	5°

N_I is the number of compartments in the angular direction, N_J is the number of compartments in the radial direction and N_K is the number of compartments in the axial direction. For each grid used the radial and the axial variation of the radial velocity, the tangential velocity and the axial velocity were examined. The radial variation of the velocities were examined at three different axial planes ($Z_1=D/5$, $Z_2=D/3$ and $Z_3=D/2$, where D is the tank diameter). The first and the third axial planes correspond to the axial locations of the eye of the lower and the upper recirculation loops, respectively (Rammohan et al., 2001). The second axial plane corresponds to the impeller midplane. Similarly, the axial variation of the velocities was examined at three different radial

locations ($r_1=D/6$, $r_2=D/3$ and $r_3=2D/5$). The first radial location lies at the impeller tip and the third radial location corresponds to the radial co-ordinate of the eye of the two recirculation loops. The results at a few select conditions are reported below in Figure 4-1 (For more detailed comparisons refer to Appendix A and Rammohan et. al., 2001b). The velocities reported in these figures have been non-dimensionalized with impeller tip speed.

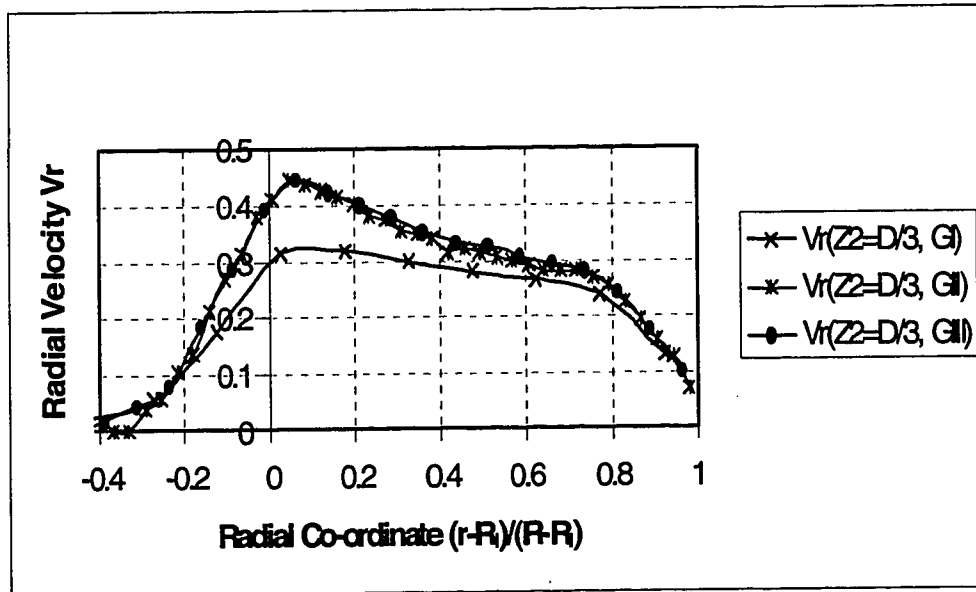


Figure 4-1(a). Radial Profile of Radial Velocity at $Z_2= D/3$

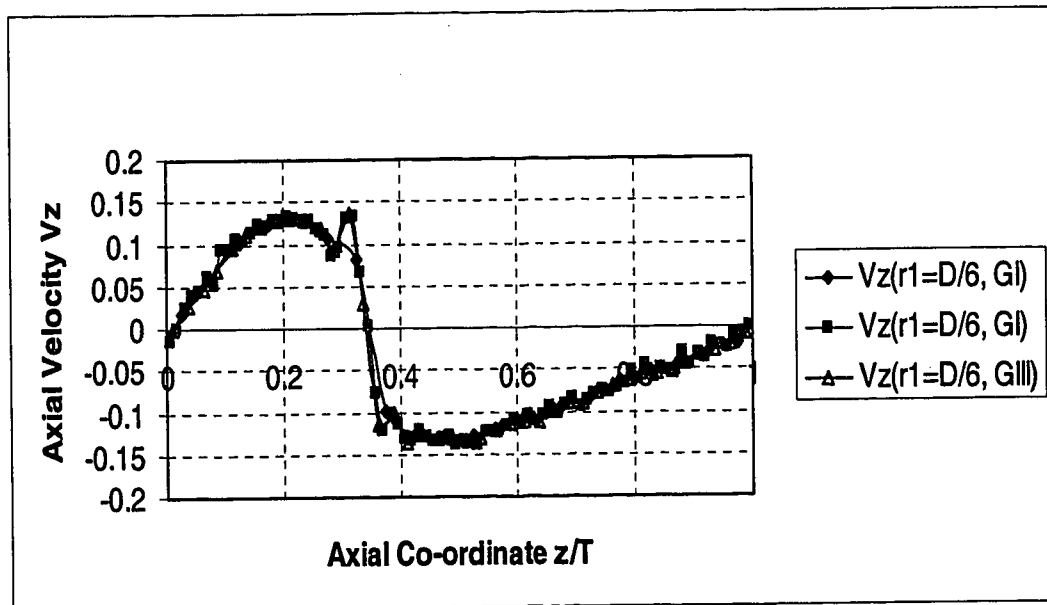


Figure 4-1(b). Axial Profile of Axial Velocity at $r_1= D/6$

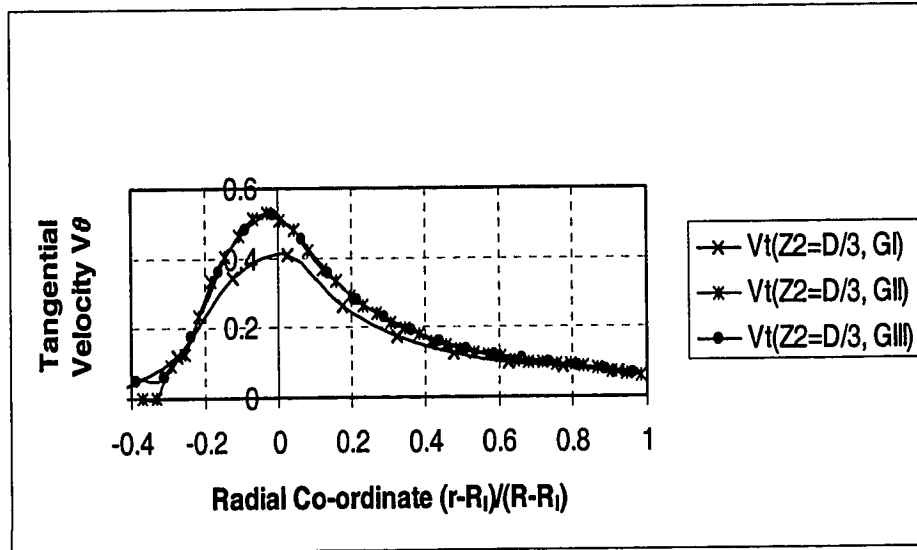


Figure 4-1(c). Radial Profile of Tangential Velocity at $Z_2 = D/3$

Due to current limited duration of CARPT runs there are inadequate statistics when one uses very fine grids (i.e. insufficient number of particle visits) and, therefore, at present we cannot tell whether current CARPT results are completely grid independent. However, the results presented so far are encouraging since for a number of variables the finer grids II and III produced results that are very close. Therefore we will use grid III for further interpretation of all data.

4.2.2 Comparison of Radial Pumping Numbers from CARPT with Data in the Literature

An important feature of the radial discharge flow is the outlet velocity profile across the blade height. A measure of the amount of fluid pumped by the impeller can be obtained from this profile, and is typically defined by the relationship:

$$Q_p(r) = \int_0^{2\pi/b} \int_{-b/2}^{b/2} \overline{V_r}(r, \theta, z) r d\theta dz \quad (4-1)$$

where D_1 = Impeller Diameter, b = blade height. It must be mentioned here that not all researchers use the same vertical limits for integrating the radial velocity profile. Some researchers like Wu and Patterson (1989) integrate up to the point where the radial

velocities become zero (which may not correspond to the ends of the impeller blade).

The impeller radial flow number (Fl), or the pumping number, can be defined as:

$$N_{Q_r} = \frac{Q_p}{ND_1^3} \quad (4-2)$$

The radial pumping number calculated from CARPT data by equation (4.1) has been compared with other values for N_{Q_r} in the literature. The CARPT determined values are seen to be within the reported band of results, as shown in Figure 4-2. In this figure the

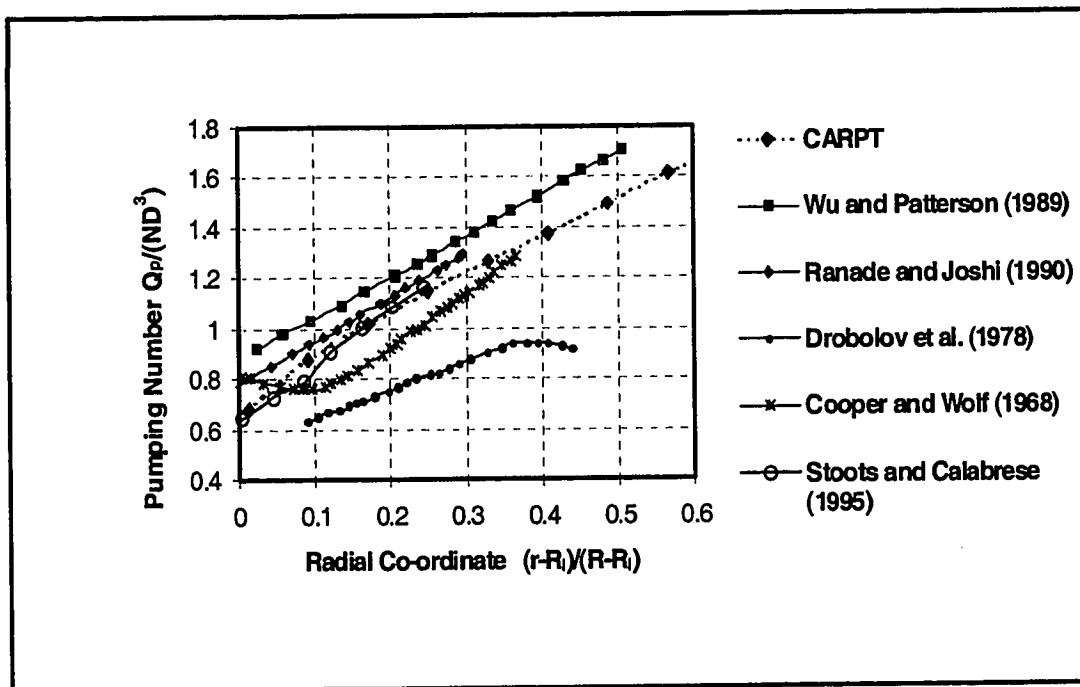


Figure 4-2. Radial Profile of Radial Pumping Number

CARPT results are compared with LDA data obtained by Wu and Patterson (1989), Ranade and Joshi (1990), Stoots and Calabrese (1995) and with HFA data of Drobolov et al. (1978) and HWA data of Cooper and Wolf (1967). The pumping number at the impeller tip from CARPT measurements is 0.67. This compares very well with the value of 0.64 reported by Stoots and Calabrese (1995) but is lower than the standard value of 0.75 reported in the literature. It is clear from Figure 4-2 that Wu and Patterson's (1989) pumping numbers are higher than all the other reported values. However, Wu and Patterson (1989) carry out their integration up to the point where the radial velocity

becomes zero. Hence, their integration covers a larger control volume which is responsible for their larger radial pumping numbers. This difference in the domain of integration accounts also for the difference between Ranade and Joshi's (1990) and Wu and Patterson's (1989) radial pumping numbers though both are obtained using LDA measurements. The radial pumping numbers obtained by Ranade and Joshi (1990) are higher than those of Stoots and Calabrese (1995) because the former account for time resolved, or 360° ensemble averaged data, while the latter are based on phase averaged velocities. Phase averaged measurements (refer to Figure 2-5(b), Chapter 2) account for the relative location of blade w.r.t measurement point and collect samples in bins of $1^\circ - 5^\circ$ while ensemble averaged measurements don't account for the relative location of the blade w.r.t measurement point. Rutherford et al. (1996) report that phase averaged velocity measurements result in 15% lower pumping numbers than the ensemble averaged pumping numbers. The ratio of blade and disc thickness to impeller diameter (t_b/D_1 and t_D/D_1) for the above two studies of Ranade and Joshi (1990) and Stoots and Calabrese (1995) is 0.020 and 0.030, respectively. Therefore, the higher blade thickness to impeller diameter ratio of Stoots and Calabrese (1995) could also be the reason for the lower radial pumping numbers. The values of Stoots and Calabrese (1995) seem to be comparable with the CARPT values. Only Cooper and Wolf's (1968) and Drobholov et al.'s (1978) values are lower than CARPT. Cooper and Wolf (1968) used pitot tube to measure their radial velocities, while Drobholov et al. (1978) used HFA. The accuracy of their results is poor. In conclusion, CARPT predicts the right trend but the radial pumping numbers from CARPT are somewhat lower (up to 10%) than what one would get if one were to do phase averaged LDA measurement in the same tank.

4.2.3 Comparison of the Mean Radial Velocity in the Impeller Stream Obtained by CARPT with Data from the Literature

We compare CARPT data with the data of Chen et al. (1988), Ranade and Joshi (1990), both obtained by LDA, Cooper and Wolf (1967), obtained by HWA, and Cutter (1967)

obtained by Streak Photography. The data were obtained in the midplane between the baffles. The comparisons are shown in Figure 4-3,

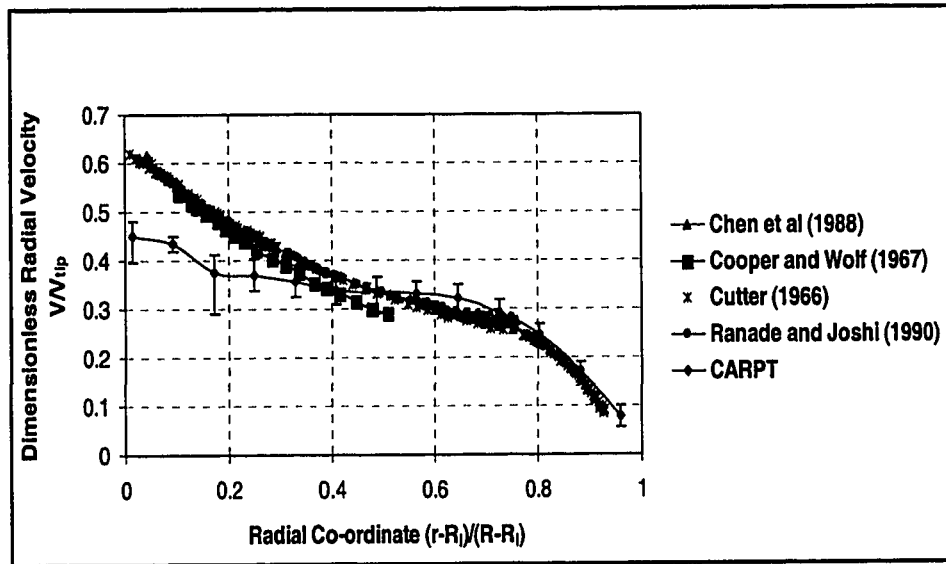


Figure 4-3. Radial Velocity Profile in the Impeller Stream

The bars indicated on the CARPT data correspond to the maximum and minimum values observed in the different mid-planes between the baffles ($\theta = 45^\circ, 135^\circ, 225^\circ$ and 315°). The differences between the measured radial velocity at the impeller tip are summarized below in Table 4-2. This table suggests that the CARPT measurements are lower than the other measurements by about 10-25 %. Figure 4-3, however, suggests that CARPT captures the right qualitative trend. The quantitative comparison in the regions away from the impeller is good (within 10%). It must also be noted that some of these measurements are not very accurate (for eg. Cutter (1966)).

Table 4-2. Comparison of Radial Velocities at the Impeller Tip

Researcher	V_{rmax}/V_{tip} (accuracy of data)	% Deviation from CARPT
Cutter (1966)	0.62 (+(-) 20%)	23%
Cooper and Wolf (1967)	0.54	11%
Chen et al. (1988)	0.615 (+(-) 5%)	23%
CARPT (2000)	0.48	N.A.

Therefore, comparisons with more recent reports in the literature are provided below in Figure 4-4.

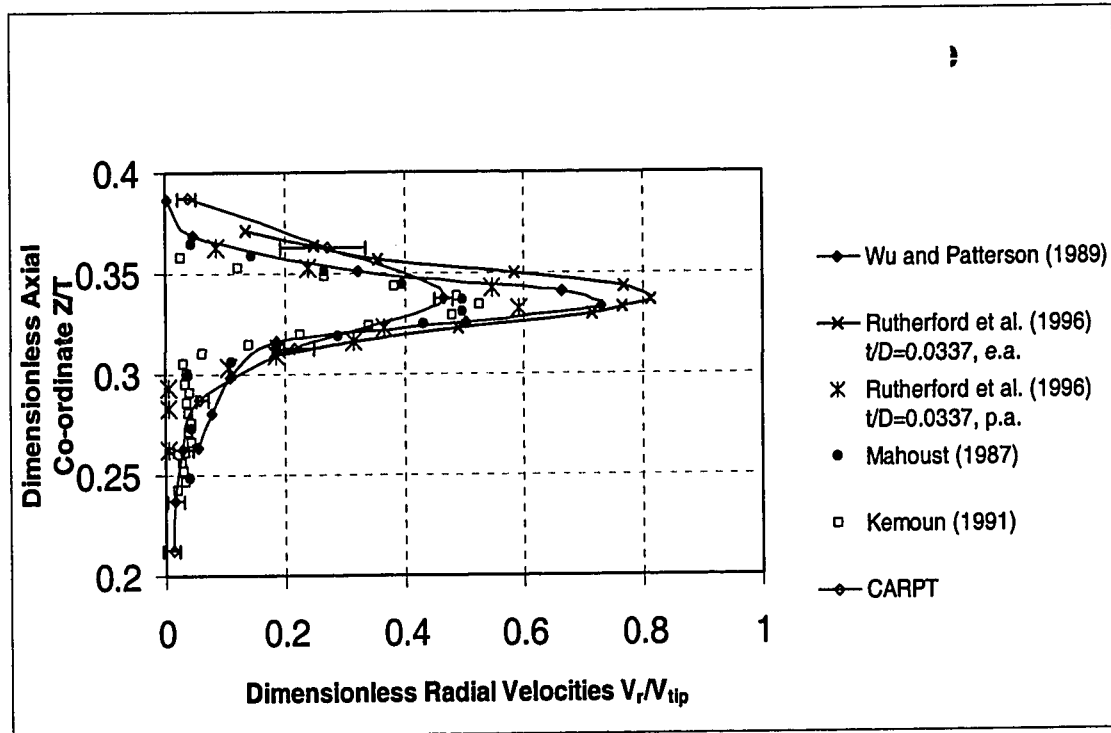


Figure 4-4. Axial Profile of Radial Velocity at the Impeller Tip

Here the comparison of CARPT is restricted to LDA data alone since the accuracy of LDA is reported to be higher than that of the other techniques. The differences between the different LDA data and the CARPT measurement are summarized below in Table 4-3. From Table 4-3 the differences between CARPT measurements and those of the other researchers is seen to vary between 4-51%. The wide scatter in the data is mainly due to two factors. One is the difference in the blade thickness to impeller diameter ratio (Rutherford et al., 1996) and the other is due to data rate bias in the LDA data. The difference between CARPT and Mahouast's (1987) and Kemoun's (1991) data is less than 10%. This comparison is very good considering the fact that the current geometry is exactly the same as that used by Mahouast (1987) and Kemoun (1991). Rutherford et al.

(1996) have reported both ensemble averaged and “phase averaged” velocities for blade thickness to impeller diameter ratio of 0.0337.

Table 4-3 Comparison of Recent Reports of Radial Velocities at the Impeller Tip from LDA Measurements with CARPT

Researcher	V_{rmax}/V_{tip}	% Deviation from CARPT
Mahouast (1987)	0.50	4%
Wu and Patterson (1989, e.a.)	0.73	34%
Wu and Patterson (1989, p.a.)	0.51	6%
Kemoun (1991)	0.525	8.6%
Rutherford et al. (1996) $t/D_1=0.008$ (e.a.)	0.98	51%
Rutherford et al. (1996) $t/D_1=0.008$ (p.a.)	0.72	33%
Rutherford et al. (1996) $t/D_1=0.0337$ (e.a.)	0.81	41%
Rutherford et al. (1996) $t/D_1=0.0337$ (p.a.)	0.59	11%
CARPT (2000) $t/D_1=0.045$	0.48	—

Their “phase averaged” mean is 27% lower than their ensemble averaged mean. Assuming that this difference can be generalized, we have computed the “phase averaged velocities” for the other ensemble averaged data. Based on this assumption, Wu and Patterson’s (1989) data shows a difference of 6% from CARPT and Rutherford et al.’s (1996) data for $t/D_1=0.008$ shows a 33% difference. Based on the above discussion we conclude that CARPT definitely captures the right qualitative trend and the right order of magnitude. But the CARPT measured velocities seem to be lower (10-20%) than the other data reported in the literature. Given that the current CARPT data was shown to be

relatively grid independent for the grid used, there would seem to be a loss of information of the velocities elsewhere. Based on the analysis of the possible sources of error in the CARPT measurements (Rammohan et al., 2001) one concludes that the size of the CARPT particle may be the principal contributor to the differences observed (this issue is discussed in greater detail in Chapter 5). The size of the CARPT particle determines the rate at which the data can be sampled (Degaleesan (1997)) and more importantly its flow following capability. This suggests a need to perform CARPT experiments with a smaller particle and subsequently acquire data at higher sampling frequency.

4.2.4 Comparison of the Mean Tangential Velocity in the Impeller Stream from CARPT with Experimental Data in the Literature

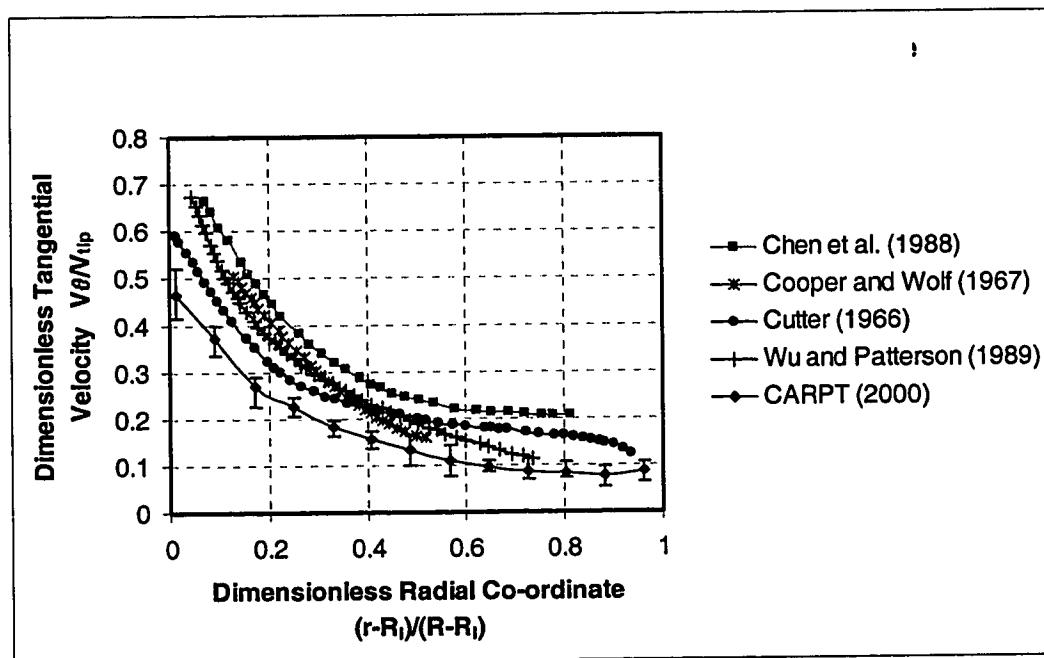


Figure 4-5. Radial Profile of Tangential Velocity in the Impeller Stream

In Figure 4-5 and Table 4-4 the tangential velocities from CARPT are compared with experimental data reported in the literature. All the comparisons are made at the impeller plane and the angular location corresponding to the mid-plane between the

baffles. Since there are four midplanes (corresponding to $\theta = 45^\circ, 135^\circ, 225^\circ$ and 315°) between the four baffles the CARPT data is averaged over these four planes.

The bars on the CARPT data represent the maximum and minimum values at these angular locations. It is not clear if the other reported experimental data are based on such an average, or if it corresponds to a single midplane between the baffles.

Table 4-4. Comparison of Tangential Velocities at the Impeller Tip

Researcher	$V_{\theta_{max}}/V_{tip}$	% Deviation from CARPT
Cutter (1966)	0.59	12%
Chen et al. (1988)	0.66	21%
Wu and Patterson (1989)	0.66	21%
CARPT (2000)	0.52	—

From Figure 4-5 it can be seen that CARPT is able to capture the right qualitative trend of the tangential velocity. Table 4-4 summarizes the comparison of the tangential velocities at the impeller tip. The deviations from LDA and other data are seen to be within 10-21%. As mentioned earlier the accuracy of Cutter's (1966) data is low (+/- 20%). The differences between CARPT and Wu and Patterson's (1989) data become progressively lower away from the impeller, while Chen et al.'s (1988) velocities near the wall are 40% and 58% higher than Wu and Patterson's (1989) and CARPT, respectively. The tank diameter in Chen et al. (1988) experiments was one – third that of Wu and Patterson (1989) and around one half of CARPT's. It is not clear if this difference in tank diameter is responsible for the observed differences. The comparison of the tangential velocities measured by CARPT with LDA results is shown in Figure 4-6 and Table 4-5. The differences between the LDA data and CARPT at the impeller tip are seen to be within 15-25%. The axial profiles from CARPT are seen to be broader than the LDA measured values. This is due to the fact that the CARPT velocities are cell centered velocities while the LDA data are point measurements. Therefore, in principle with a finer CARPT grid

one would expect to see a sharper velocity gradient (as seen with LDA data). If the CARPT data were sampled at higher sampling frequencies then such high gradients in velocities could be captured in principle (this has been shown through simulations in Chapter 6).

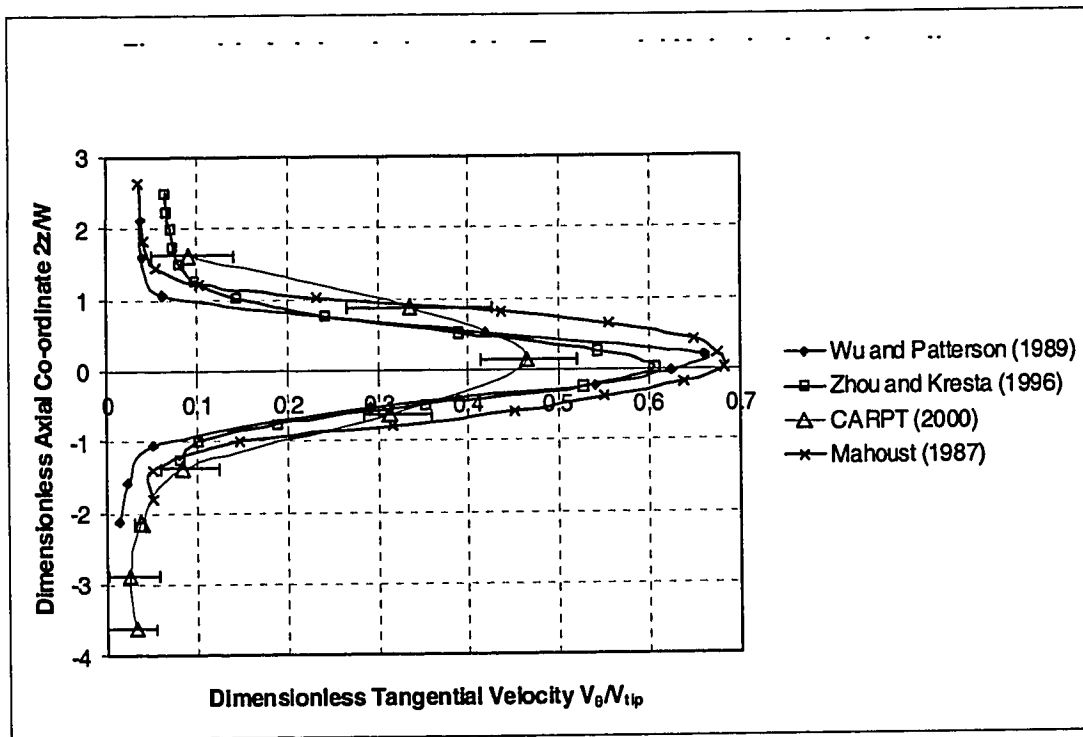


Figure 4-6. Axial Variation of the Tangential Velocity in the Impeller Stream at the Impeller Tip

Table 4-5. Comparison of Tangential Velocities at the Impeller Tip from LDA Measurements with CARPT.

Researcher	$V_{\theta\max}/V_{tip}$	% Deviation from CARPT
Mahaoust (1987)	0.68	24%
Wu and Patterson (1989)	0.66	21%
Zhou and Kresta (1996)	0.61	15%
CARPT (2000)	0.52	—

However, for the set of data presented here the sampling frequencies were limited to 50-60 Hz by the particle size (Degaleesan, 1997). Hence, CARPT experiments with a smaller particle size, with data sampled at higher frequencies and by acquiring data over longer durations (current CARPT runs acquire data over 20 hours) would provide more accurate measurements of the velocities. The longer duration of CARPT runs would ensure greater number of particle occurrences in the entire vessel allowing the use of finer grids. If these limitations are overcome one would finally still be limited by the resolution of the CARPT system. Recent studies in CREL (Roy et al. (1999)) have shown that changes in the detector configurations, type of crystal used, source strength can bring about reasonable improvements in the resolution of the system. To conclude, the CARPT measured tangential velocities seem to capture the right qualitative trend and the right order of magnitude of the tangential velocities.

4.2.5 Comparison of the Turbulent Kinetic Energies in the Impeller Stream from CARPT with Data from the Literature

The axial profiles of dimensionless radial turbulent velocities are compared in Figure 4-7. Table 4-6 summarizes the differences at the impeller tip. Wu and Patterson (1989) report both the total turbulent and the fluctuating component calculated after removing the deterministic contribution to the fluctuating velocities. Dyster et al. (1993), Zhou and Kresta (1996) and CARPT (2000) report only the total fluctuating velocity. The differences between these measurements and CARPT are seen to vary from -14% to 45%. While the total turbulent velocities from Dyster et al. (1993) and Wu and Patterson (1989) show one peak at the impeller midplane, the CARPT measurements and Wu and Patterson's (1989) random components show twin peaks. The location of Wu and Patterson's (1989) twin peaks are near the impeller center while those from CARPT are near the blade tip. The above comparisons seem to suggest that CARPT is missing some information on the fluctuating velocities. Similar comparison of the turbulent tangential velocities are shown in Figure 4-8 and Table 4-7. These comparisons also suggest that

CARPT loses information in capturing the fluctuating velocities. Interestingly the difference between the radial and the tangential components of the fluctuating velocities from the different reports is within 0-13%.

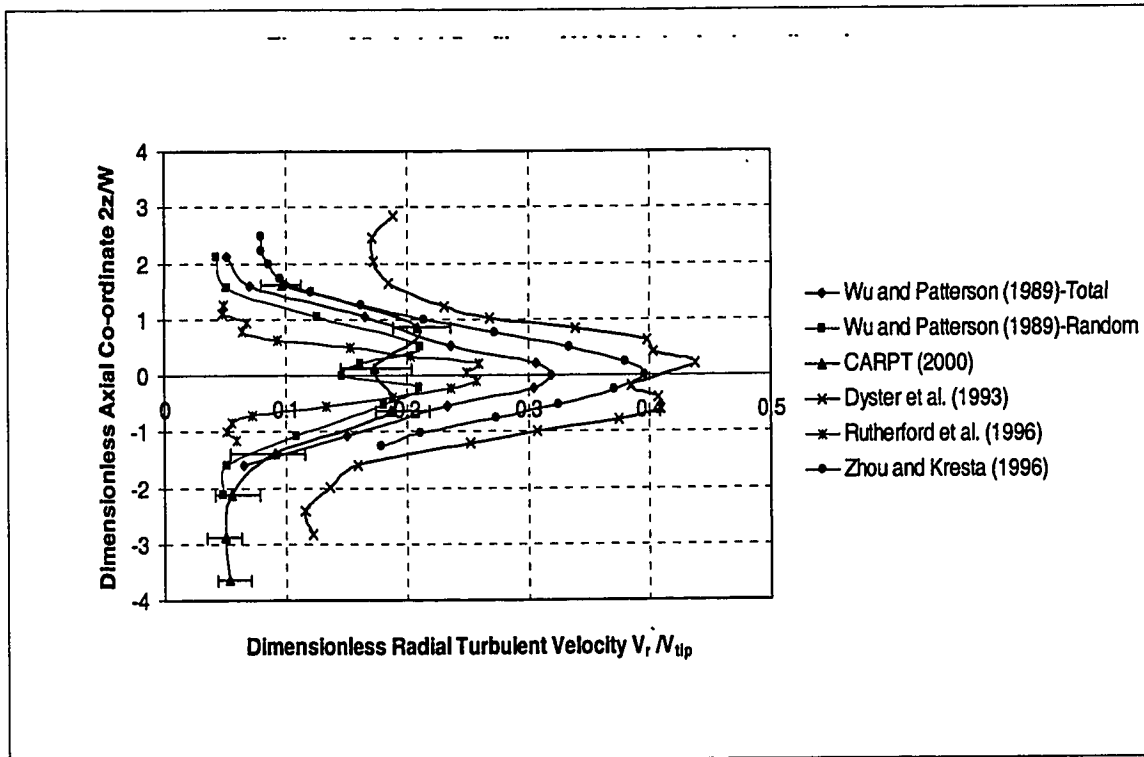


Figure 4-7. Axial Profiles of V_r'/V_{tip} in the Impeller Plane

Table 4-6. Comparison of Radial Turbulent Velocities at the Impeller Tip

Researcher	V_r'/V_{tip}	% Deviation from CARPT
Wu and Patterson (1989) -Total Fluctuating Velocity.	0.32	25%
Wu and Patterson (1989) - Random Component	0.21	-14%
Dyster et al. (1993)	0.44	45%
Rutherford et al. (1996)	0.26	8%
Zhou and Kresta (1996)	0.40	40%
CARPT(2000)	0.24	—

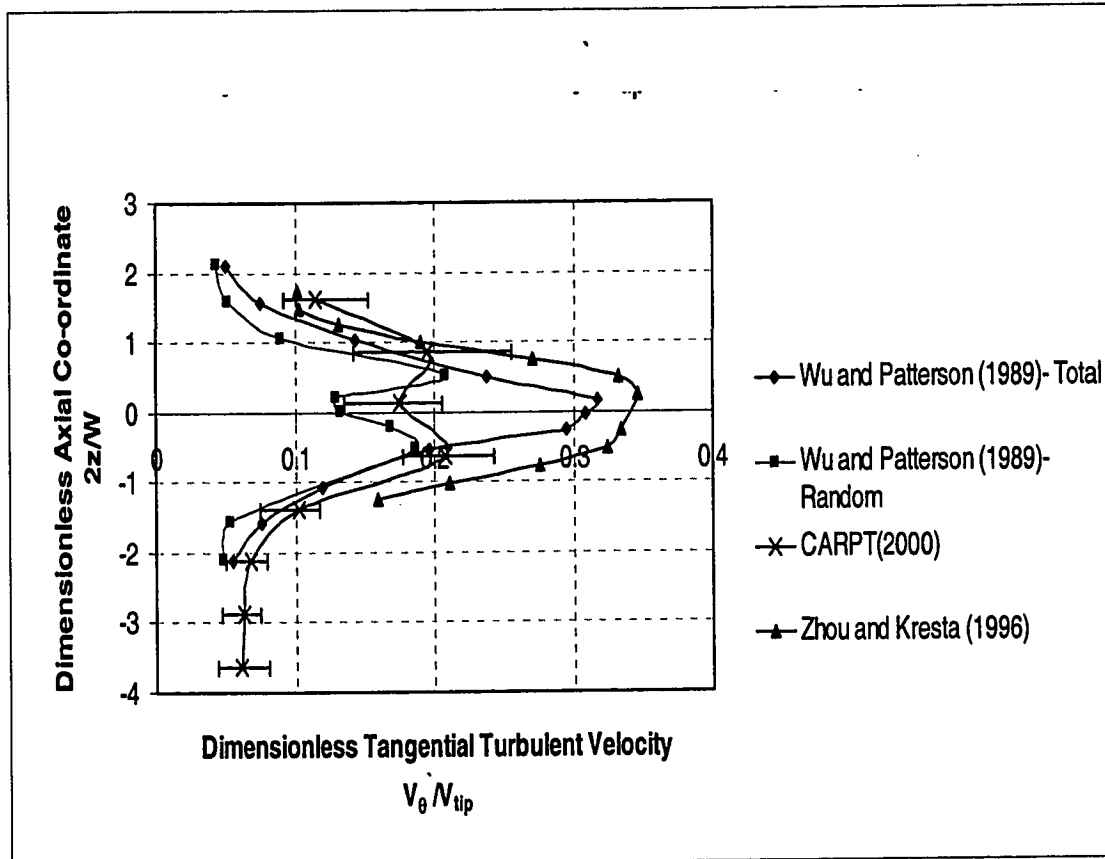


Figure 4-8. Axial Profile of V_{θ}'/V_{tip} in the Impeller Plane

The turbulent kinetic energies computed from CARPT data do contain the contributions from periodic fluctuations or pseudo turbulence (Yianneskis et. al., 1987) since these are not angle resolved measurements. The comparison of the profiles of turbulent kinetic energy is shown in Figure 4-9. Differences between CARPT and Wu and Patterson (1989) seem to be as high as 30-50% near the impeller region. The overall CARPT values at different radial locations are also lower than the values reported by Wu and Patterson (1989), Ranade and Joshi (1990) and Costes and Couderc (1988). It was initially thought that this under-prediction might be due to the low sampling frequency (50 Hz) used in CARPT. To confirm this a Fast Fourier Transform of the instantaneous LDA data of

Kemoun (1995) was performed and found that for points near the impeller most of the energy is contained within frequencies corresponding to the impeller rotation frequency.

Table 4-7. Comparison of Tangential Turbulent Velocities at the Impeller Tip

Researcher	V_{θ}/V_{tip}	% Deviation from CARPT
Wu and Patterson (1989) – Total Fluctuating Velocity	0.32	19%
Wu and Patterson (1989) – Random Component	0.21	-24%
Zhou and Kresta (1996)	0.35	26%
CARPT (2000)	0.26	—

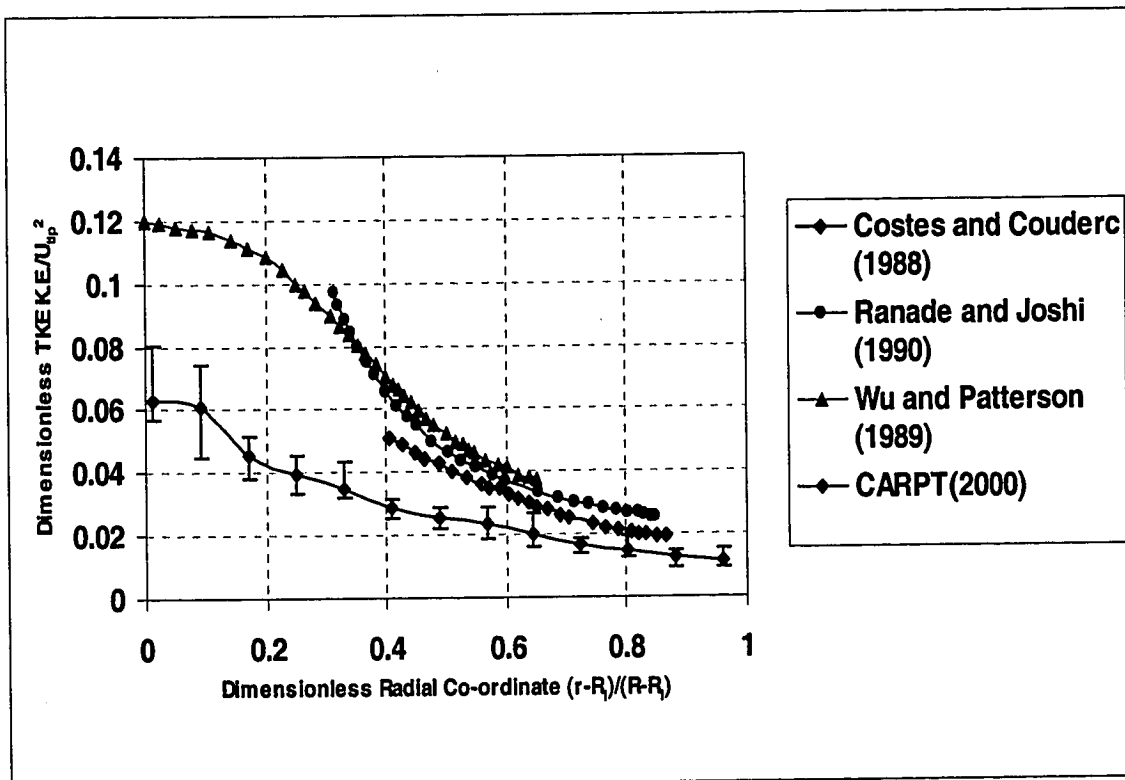


Figure 4-9. Profiles of Turbulent Kinetic Energy

Mujumdar et al. (1970) and Kemoun (1995) have shown this. It turns out that with those frequencies we should be able to capture 70-80% of the turbulent kinetic energy (this

includes the pseudo turbulence). We analyzed one such instantaneous data set from Kemoun's thesis (1995) at 420 RPM. The FFT of the data showed a clear peak at 42 Hz corresponding to the first harmonic of the blade rotation frequency ($= 420/60 \times 6$ (number of blades)). We calculated the area under the power spectral density curve and this quantity corresponds to the total turbulent energy associated with the signal at that point (Batchelor, 1953). From this curve we computed the fraction of the total energy associated with different ranges of frequency say 0-10 Hz, 0-20 Hz, 0-30 Hz and so on. We show this below in Figure 4-10:

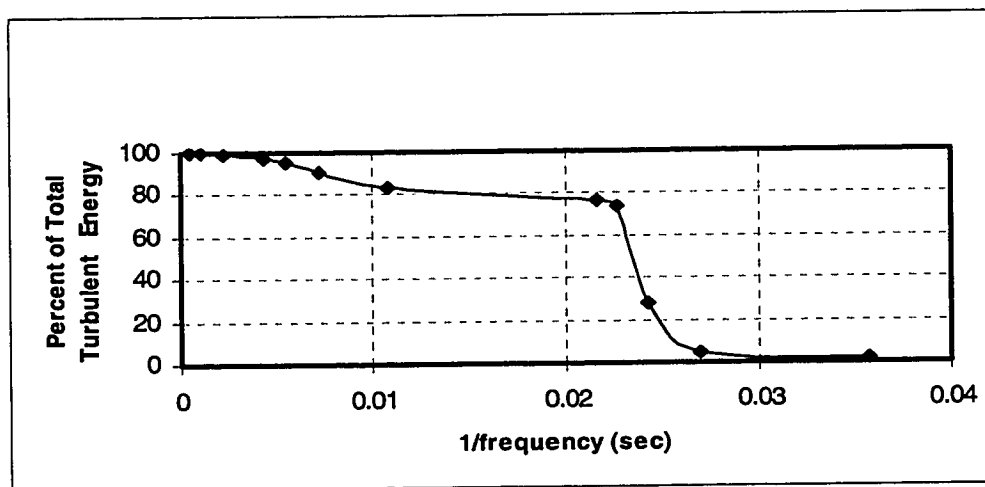


Figure 4-10. Fraction of Total Turbulent Energy Associated with a Particular Range of Frequency (0-f)

This plot implies that at 420 RPM by capturing frequencies in the range 0-50 Hz ($f_{\text{sample}} \sim 100$ Hz) we should be able to capture around 70-80% of the total turbulent energy. Based on the same argument at 150 RPM (first harmonic would be at $150/60 \times 6 = 15$ Hz) we would expect that by capturing frequencies between 0-15 Hz ($f_{\text{sample}} \sim 30$ Hz) we should be able to capture a similar fraction of the total energy. This clearly indicates that in CARPT we are losing turbulence information elsewhere. The next suspect was the

effect of particle size. Degaleesan (1997) showed that with a particle of 2.3 mm diameter we should be able to capture at least frequencies up to 30 Hz. The conclusions of Degaleesan (1997) were based on a simplistic model. No experiments have been done to verify the validity of this. Hence, a definite need exists to systematically quantify the flow following capabilities of the tracer particle of a finite size. At the end of this discussion we conclude that given the current size of the tracer particle ($d_p = 2.36$ mm) we might 'actually' be missing out some information for the turbulence parameters (refer Chapter 5 for a more detailed discussion of this issue).

4.2.6 Reynolds Shear Stress Distributions from CARPT

These instantaneous velocities obtained by CARPT in various compartments are ensemble averaged to generate the components of the Reynolds' stress tensor. The normal components of this tensor have been reported above as the root mean squared velocities the sum of which is equal to the turbulent kinetic energy. The off-diagonal elements, or the shear stress components are reported in Figure 4-11(a) at one angular location including the baffles. The contours indicate the counter rotating trailing vortices behind the blades. These counter rotating vortices are seen to emerge from the impeller and die out near the walls. In the visualization studies (Figure 4-11(b)) a fluorescent dye was introduced in the impeller region. The dye is seen to follow the counter rotating vortices, which emerge from behind the impeller and die out as they approach the wall. This suggests that the Reynolds like shear stress measurements contain some valuable information regarding the flow structures in the stirred tank reactor. A quantitative comparison of the Reynolds Shear stress distribution is not reported due to the lack of such data in the literature.

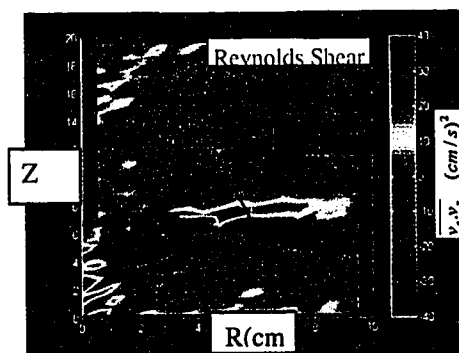


Figure 4-11(a). Contours of Reynolds Shear Stresses in the Plane Including the Baffles

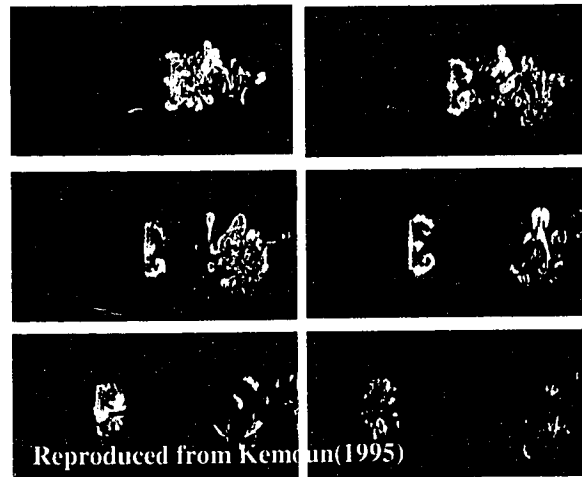


Figure 4-11(b). Visualization of Trailing Vortices using Fluorescent Fluid

4.2.7 Lagrangian Measures of the Fluid Dynamics in STR

4.2.7.1 Circulation Time Distributions (CTD) and Mean Circulation Times (MCT)

Owing to the Lagrangian nature of the flow field the information about the circulation time distributions can be obtained. Here a control volume containing the impeller of radius $D/3$ and height of twice the blade height ($2D/15$) was considered. From the CARPT particle trajectories the time differences between two subsequent visits of the tracer to the control volume were recorded. A frequency distribution of return times to the impeller zone has been plotted in Figure 4-12. The mean of the CTD (of 16330 samples) was found to be 3.53 seconds and the standard deviation was found to be 2.96 seconds. The mean was found to converge with 5000 samples. The bi-modal CTD obtained from CARPT is comparable to the bi-modal CTD's reported by Roberts et al. (1995). However, for the dimensions of the current tank the Mean Circulation Time from CARPT seems to be higher than the MCT reported by Roberts et al. (1995) but they measured the return times to the plane containing the impeller and not just a small control volume enclosing the impeller. The MCT is found to be sensitive to the size of the control volume and is expected to be lower for larger control volumes. This might explain the higher MCT's from CARPT.

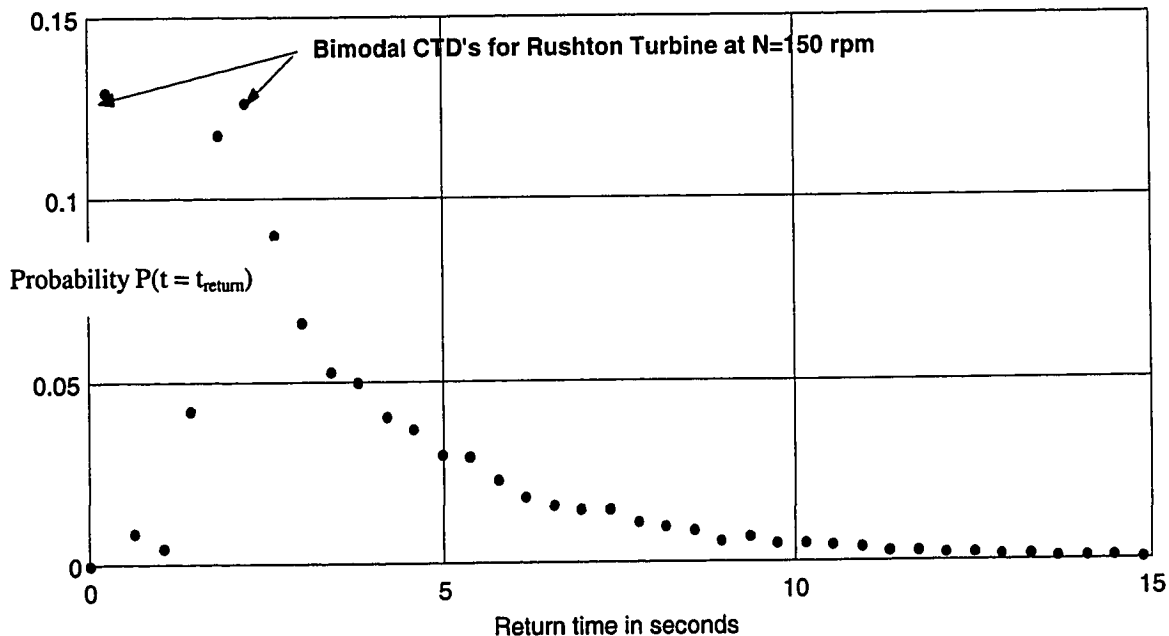


Figure 4-12. Circulation Time Distribution in the Impeller Region at $N = 150$ rpm

4.2.7.2 Hurst Exponents from Particle Trajectories

Hurst's (1956) rescaled R/S analysis, as modified by Mandelbrot and Wallis (1969), was applied to the instantaneous Lagrangian particle position ($r(t)$). The random variable under consideration is the Lagrangian tracer position $r(t)$. Several bins (N), each containing τ consecutive positions, are selected at random from the entire position data set. For each bin the Range (R) and the standard deviation (S) of the random variable is evaluated as shown by Yang et al. (1992). The mean R/S is then evaluated for a particular bin size τ . The number of bins ($N \sim 25$) are selected such that the mean R/S converges. This procedure is repeated for several τ ranging from 1-10000. The slope of $\ln(R/S)$ vs $\ln(\tau)$ yields the Hurst exponent which is seen to be 0.8 from the graph shown in Figure 4-13.

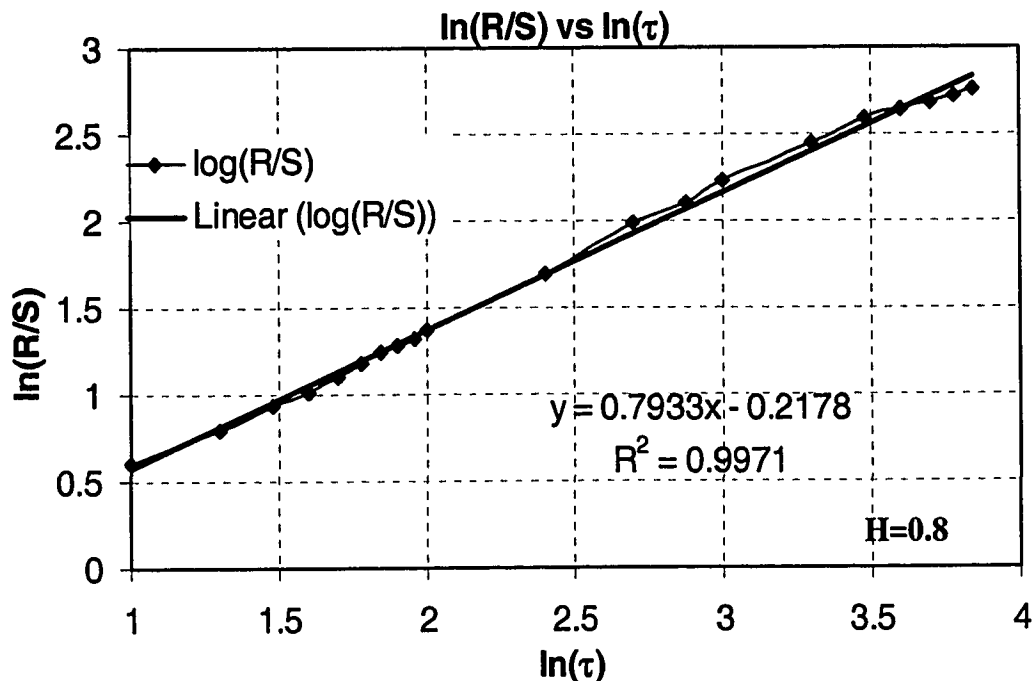


Figure 4-13. Hurst Exponent from the Lagrangian Particle Position $r(t)$ in STR

A H-value of 0.5 indicates a mixing mechanism similar to Brownian motion and a diffusion type mixing model can adequately describe the process. $H > 0.5$ indicates the persistence of long term non-cyclical effects due to turbulent dispersion. A compensatory effect, or possible cyclic motion, results in H values less than 0.5. The analysis based on the instantaneous particle position suggests that long term or persistent effects are significant in stirred tanks. Some other Lagrangian measures of the fluid dynamics like Sojourn time distributions (Rammohan et al., 2001) have also been extracted from the CARPT data in stirred tank reactors (Refer to chapter 3).

4.3 CFD Simulations

In this section we briefly outline the details of the numerical simulations performed. We have already outlined the details behind the two approaches which we use here (the Snapshot Approach (SA) and the Multiple Reference Frames (MRF) model). We have simulated exactly the same geometry as the experimental setup. The computational

domain is only half the tank since a plane of symmetry can be found. The cylindrical co-ordinate system was used with the center of the bottom of the tank taken as the origin of the co-ordinate system. For both types of simulations exactly the same grid is used. A non-uniform grid has been generated in the framework of FLUENT 4.51 containing 94 cells in the angular direction, 57 cells in the radial direction and 78 cells in the axial direction. The selection of grid size was based on simulations reported in the literature (Ng et al., 1998) which showed that simulations were not grid sensitive if over 70,000 cells were used. Based on the reported simulations a grid size of around 450,000 was chosen. It is assumed that this grid is sufficiently large to provide grid independent solutions. We show a sample grid for each type of simulation below:

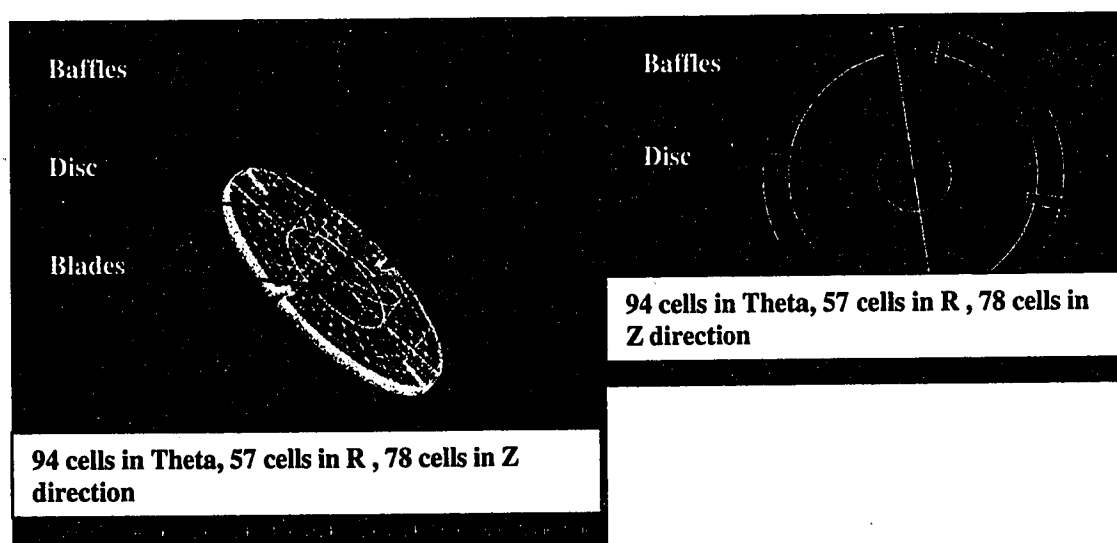


Figure 4-14 . View of 3-D Grid Used for MRF and Snapshot Simulations

The momentum transport equations were solved in the cylindrical co-ordinate system along with the standard k - ϵ model of turbulence. The relevant equations and boundary conditions for the two approaches have been discussed earlier (Chapter 2). The details of the solver and numerical technique used are available in the FLUENT manual. The simulations were solved for the identical conditions at which our experimental results were obtained. The Fluent velocities were non-dimensionalized by defining the impeller

tip speed as 1m/s. In this section we briefly discuss the quantitative comparisons of the CFD simulations with the CARPT results.

4.3.1 Comparison of Mean Radial Velocity in the Impeller Stream Obtained by CARPT with CFD Simulations

The azimuthally averaged radial velocity vectors in the impeller mid plane from simulations are compared with such values obtained from CARPT results. These comparisons are shown below in Figure 4-15.

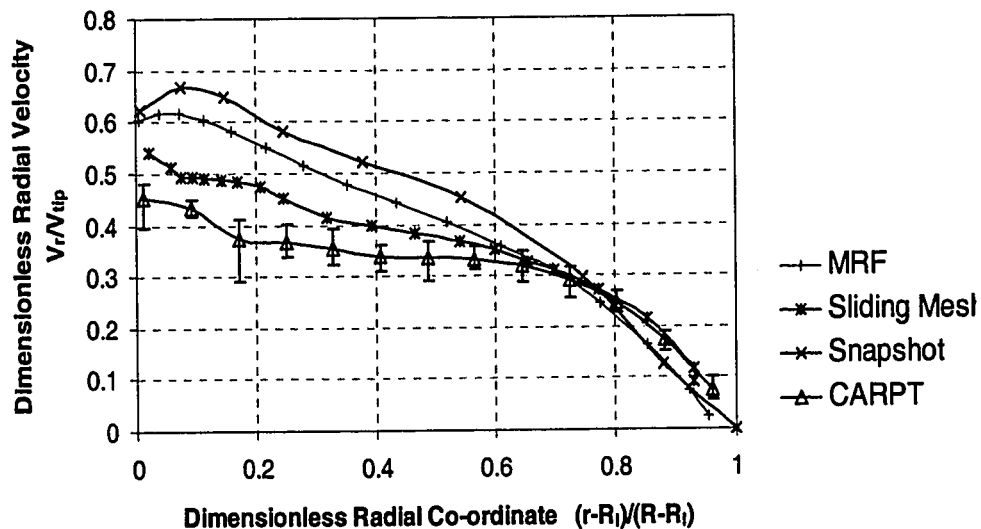


Figure 4-15. Comparison between Predicted and Measured Radial Velocity Profile in the Impeller Stream

The radial velocity profiles in the impeller stream predicted by the two CFD approaches (SA and MRF) are compared with those computed from CARPT in figure 4-15(a). The differences between CARPT and CFD results for the radial velocity at the impeller tip are summarized in Table 4-8. The differences are seen to vary from 7-30% with the

difference between the sliding mesh computation (of Ng et al. (1998)) and CARPT being the lowest.

Table 4-8. Comparison of CFD Predictions of Radial Velocities at the Impeller Tip

Technique	V_r/V_{tip}	% Deviation from CARPT
CARPT	0.48	—
MRF	0.62	23%
S.A.	0.68	29%
Sliding Mesh	0.54	7%

The predictions of the MRF technique are qualitatively comparable with the S.A. but the quantitative values are 5-10% lower than the SA predictions.

To summarize, CARPT radial velocity profiles are lower than the predictions of the two different CFD simulations as expected. However, considering the fact that the two independent CFD simulations require no empirical inputs and that the comparisons between them seem reasonably good are an indication that the CFD simulations predict the right magnitude of the maximum radial velocity. This is also confirmed by the fact that LDA and other techniques (see Table 4-6) measured higher values than CARPT.

4.3.2. Comparison of Mean Tangential Velocity in the Impeller Stream from CARPT with CFD Simulations

In Figure 4-16(a) we compare the tangential velocity profiles predicted by SA and MRF with the values computed from CARPT. The qualitative profiles from CARPT match very well with those predicted by CFD. The differences in the predictions at the impeller tip are summarized in Table 4-9. The magnitudes of tangential velocity predicted by SA

and MRF compare very well with each other except near the impeller where MRF predictions are 17% lower than the Snapshot predictions.

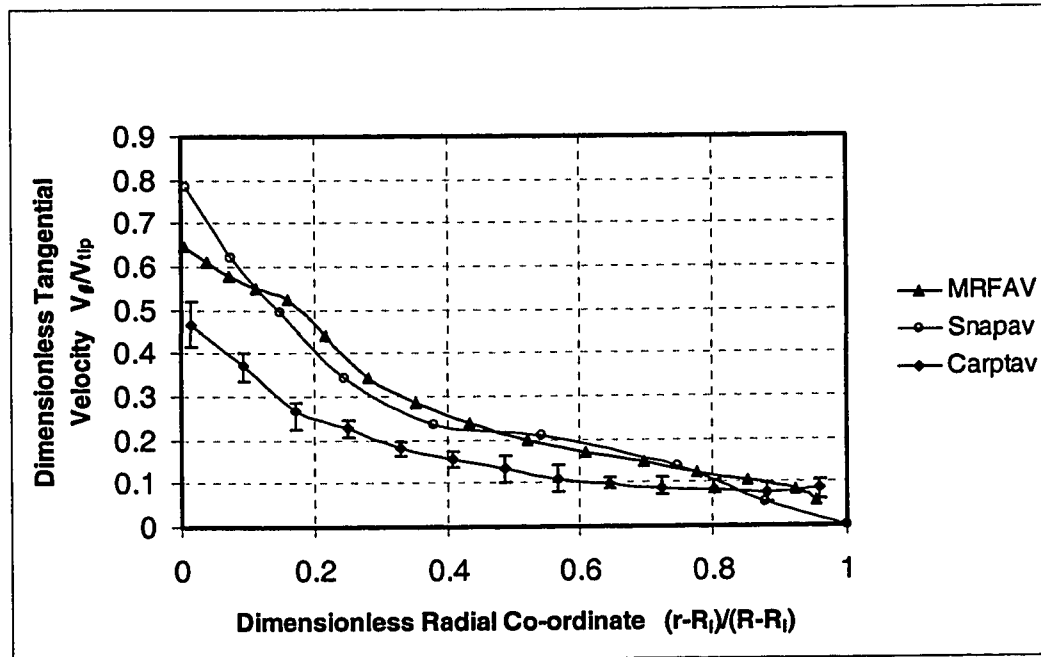


Figure 4-16(a). Comparison between Predicted and Measured Radial Profile of Tangential Velocity

Table 4-9. Comparison of CFD Predictions of Tangential Velocities at the Impeller Tip

Technique	V_θ/V_{tip}	% Deviation from CARPT
CARPT	0.52	—
MRF	0.65	20%
S.A.	0.78	33%

At the impeller tip the CARPT values are almost 30% lower than those predicted by SA and 20% lower than those predicted by MRF. Away from the impeller the CARPT values compare reasonably with both SA and MRF (differences are lower than 20%). Figure 4-16(b) suggests that the CFD predictions compare reasonably well with the LDA data of Chen et. al. (1987) and Wu and Patterson (1989).

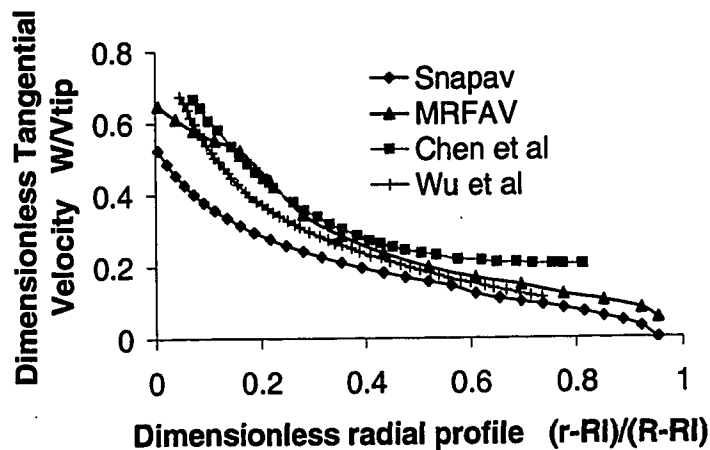


Figure 4-16(b). Comparison of CFD Predicted Tangential Velocity with LDA Data

The match between the two CFD predictions is good since neither simulation requires empirical input. Considering the fact that other experimental techniques measure values higher than those detected by CARPT it is fair to assume that the simulations do predict close to the correct values.

4.3.3 Comparison of Turbulent Kinetic Energies in the Impeller Plane from CARPT with CFD Simulations

The comparison between the predicted and measured profiles of turbulent kinetic energy is shown in Figure 4-17. Except near the impeller region, where the CARPT values are higher in the rest of the tank the Snapshot predictions are about 30% higher than both the MRF and the CARPT values. All three values are much lower than the turbulent kinetic profiles reported by other experimental techniques. The underestimation of the turbulent kinetic energies by CARPT have been discussed earlier (Section 2.2.2). The fact that the CARPT values fall right on top of the MRF predictions in the region away from the impeller may be more of a coincidence than actually providing any information on the model's ability to predict the turbulence. This under-estimation of turbulence by CFD models is a much lamented affair in the stirred tank literature. The cause for this is

attributed to the use of the isotropic turbulence model, which causes greater dissipation to be predicted than is actually present. But currently there is no clear evidence recommending the use of other nonisotropic turbulence models. Only LES simulations (Chapter 2) seem to be able to capture the right magnitude of the turbulence.

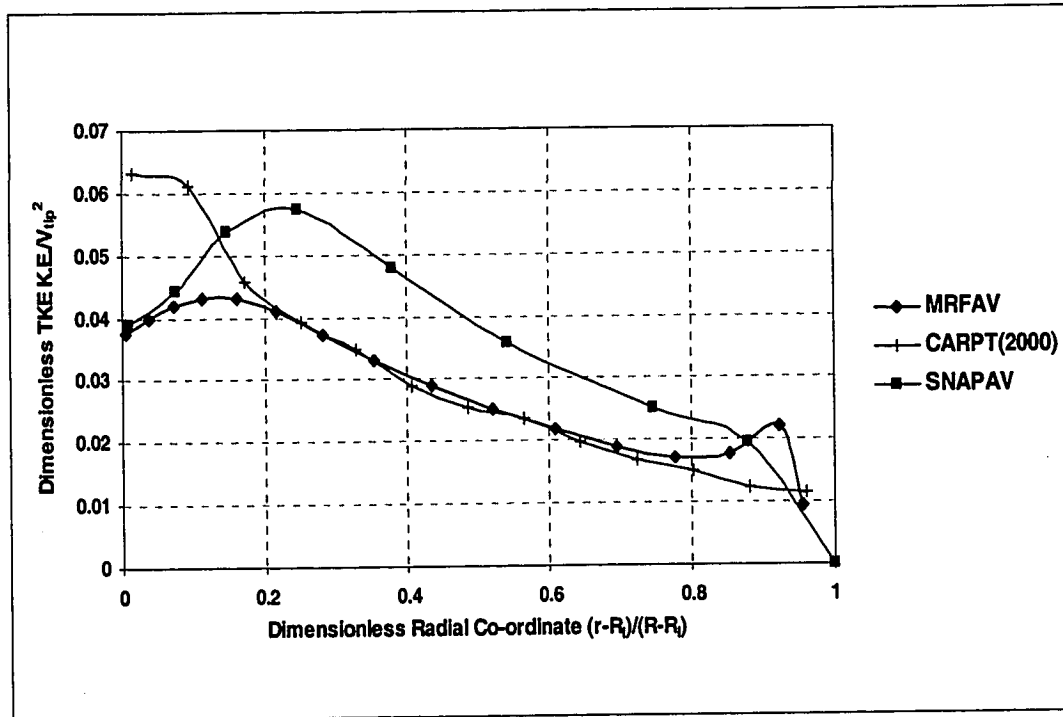


Figure 4-17. Comparison between Predicted and Measured Radial Profile of Turbulent Kinetic Energy

We feel that currently matching of the mean itself is a good sign of the predictive capability of a model simulation. A match of turbulence using such models is not a realistic expectation.

4.4 Summary and Conclusions

An extensive validation of the single phase CARPT measurements in stirred tank reactor has been provided. Various Eulerian measures of flow like the Radial pumping number,

mean radial velocity, mean tangential velocity, turbulent kinetic energy, diagonal elements of the Reynolds shear stress tensor, etc. were extracted from CARPT. These measures were compared extensively with similar quantities obtained with other experimental techniques like LDA, DPIV, HWA, HFA, Pitot tube etc. A detailed analysis of the differences in these measures from different experimental techniques has been provided. The study revealed that the flow measures are very sensitive to a number of parameters like ratio of blade thickness to impeller diameter, disc thickness to impeller diameter, accuracy of experimental technique, mode of data acquisition - ensemble averaged/ phase averaged, data acquisition rate, angular plane in which data has been obtained, etc. especially in the near impeller region. The current work also discusses CARPT's potential to provide information about the three dimensional Reynolds like shear stress distribution in the entire tank. Information of this kind will be of considerable interest in the design and scale-up of bioreactors. Further, the technique's ability to provide some Lagrangian measures of the fluid dynamics is also explored. In this study detailed comparisons of the mean velocities and turbulent parameters from CARPT with similar data in the literature has been provided. The analysis indicates that CARPT results in general seem to capture most of the relevant physics of the flow and the quantitative comparisons show values whose order of magnitude is definitely comparable to the existing data in the literature. In all the cases the right order of magnitude is captured. In this study we have also identified some of the sources of error in the CARPT technique and in what direction the efforts towards improving CARPT should be made. The size of the current CARPT tracer ($d_p=2.3$ mm) has been identified to be one of the major sources of the loss in information. Hence, work has been done to evaluate the flow following capability of tracers of smaller diameters in the same tank and under similar operating conditions. It is expected that this study will enable us to select an appropriate tracer size for further explorations in two-phase flows in stirred tank reactors. Providing explanations for the differences between CARPT measurements and other techniques forms the basis for Chapter 5 where we look into the different sources of errors in greater detail.

Chapter 5

Characterization of Errors in CARPT through Experiments

The data obtained from the CARPT technique are susceptible to three broad classes of errors. These are 1) errors in reconstructing the trajectories from detector signals, 2) errors in estimating the Eulerian information from the reconstructed trajectories, and 3) errors due to tracer particle not following the flow faithfully. The errors of type (1) result from the inaccuracy of the tracer position reconstruction algorithm or could be due to a phenomenon called the “dynamic bias”. The two different errors of type (1) have been discussed and quantified experimentally in this chapter.

5.1 Evaluation of Tracer Position Reconstruction Strategies

5.1.1 Introduction

Calibration experiments originally performed in the high pressure stainless steel bubble column reactor in air revealed a considerable spread, exceeding that encountered previously in plexiglass columns, in the calibration curve. Hence, reconstructing the known calibration points, using the existing reconstruction algorithm, resulted in considerable error. To improve the reconstruction accuracy a two pronged approach is adopted: i) a new tracer reconstruction procedure, which does not use the spline fit/weighted regression technique, is sought, and ii) a new tracer data acquisition strategy, which helps in containing the spread in the calibration curve is considered. This new data acquisition protocol has been successfully implemented in identifying the unknown tracer locations in a stainless steel reactor.

5.1.2 Background

The first step in a CARPT experiment is to obtain a calibration map of the count registered by each detector for several hundred known locations of the tracer. A typical calibration curve obtained in a plexiglass column is shown below in Figure 5-1.

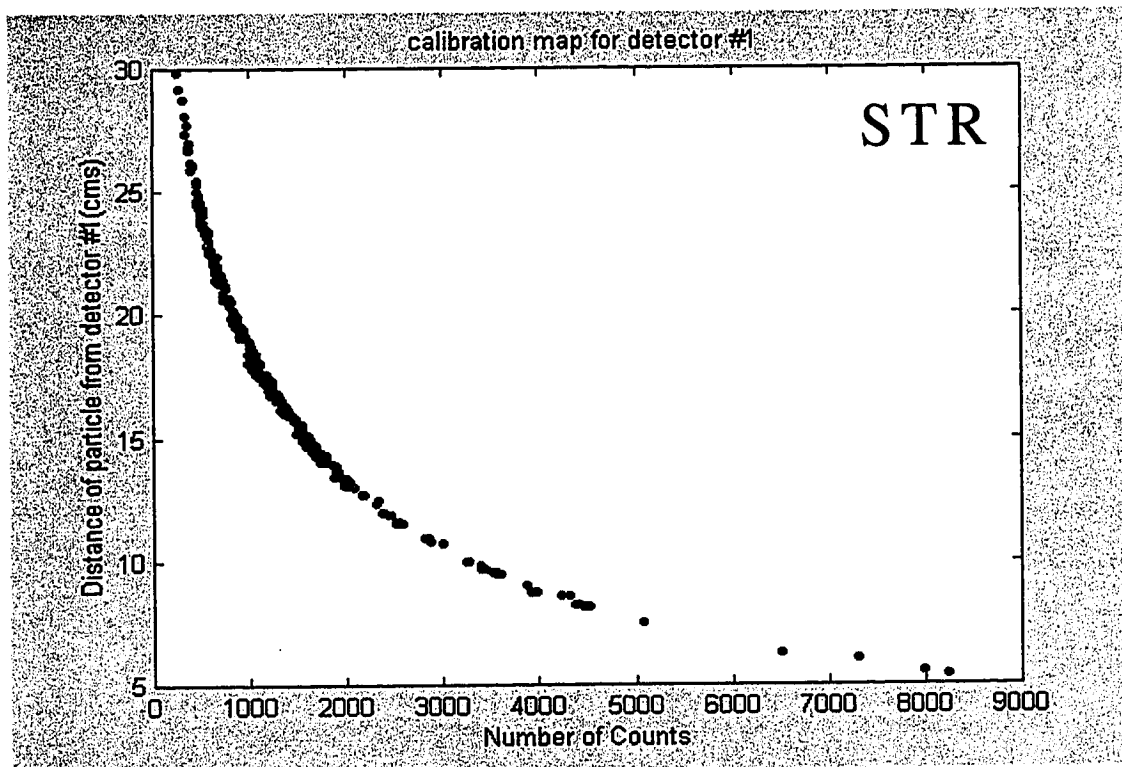


Figure 5-1. Calibration Map Obtained in a Plexiglass Stirred Tank Reactor

From Figure 5-1 it is clear that for a fixed distance between detector and the radioactive tracer a unique mean count is registered by that detector. It is this existence of a unique mean count which allows us to use this radioactive technique for reconstructing the tracer location. It must be mentioned that when a particle is placed in front of a detector at a given distance, the instantaneous counts received by the detector follows a random distribution which is best characterized by a Poisson distribution. This variation in the instantaneous counts is due to several factors like quantum nature of the emission of photons by radioactive decay of unstable Sc^{46} , unstable dispersed phase holdup

fluctuations and tracer particle location during the sampling interval (dynamic bias). These differences in the instantaneous counts, and the errors introduced by it, are analyzed in greater detail in Section 5.2.2 (refer to Figure 5 –24). It must be emphasized here that in reconstructing the tracer position while in motion, the instantaneous counts are used which then can be expected to be associated with a distribution of distances. But the error associated with this is minimized by ensuring that the tracer particle either has a high radioactive strength or by setting a low threshold for the detector. This ensures that a large number of photons is collected by the detector and the associated normalized standard deviation scales inversely with the number of counts collected by the detector. Hence this uncertainty in counts results in uncertainties in distance of the order ~0.1 cm.

Referring to the calibration plot of detector 1, Figure 5-1 suggests that if detector#1 registers 3000 counts then the tracer particle is 10.0 cm (+/- 0.5 cm) from detector#1. Hence, this calibration curve can be expected to provide an accurate reconstruction of the distance of the tracer from each detector which can then be used to obtain the exact tracer co-ordinates by solving a system of linear equations (Devanathan, 1991). However, when calibration experiments were performed in air in a stainless steel column the calibration curve obtained looked very different as shown in Figure5-2. With a curve of this form the conventional approach of generating a spline of the form:

$$d_{10} = f_{10}(C_{10}) \quad (5-1)$$

where d_{10} is the tracer distance from detector 10 and C_{10} is the count recorded at detector 10, will not work well, for if we feed a count of $C_{10} = 100$ to equation (5.1) then the predicted distance d_{10} is 36 cm while Figure5-2 suggests that the distance of the tracer from detector 10, d_{10} , can be anywhere between 30-42 cm. This clearly indicates that the spline based approach to fitting the count vs distance data of Figure5-2 would result in considerable error in estimating the distances accurately. Further, it has been observed that even small errors in the reconstructed distances (~1-2mm) can get amplified considerably when solving for the exact tracer co-ordinates using the weighted least-squares regression technique (Devanathan,1991).

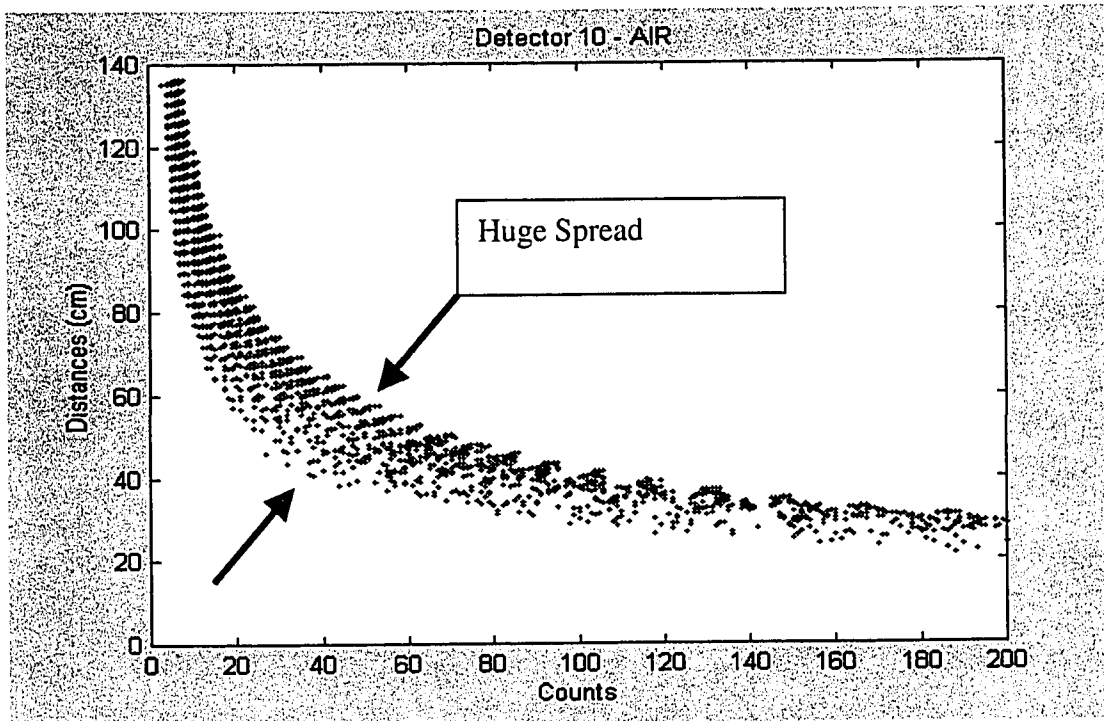


Figure 5-2. Calibration Map Obtained in the Stainless Steel Reactor

Hence, for systems where the calibration curve is like Figure 5-2 the existing approach cannot be used to reconstruct even the known calibration points as illustrated clearly by Figure 5-3. Figure 5-3 shows a comparison between the actual calibration points shown by the blue points (3528 in all, corresponding to 49 points per axial plane and around 72 axial planes) and the reconstructed points (the red dots). Ideally the red dots should have fallen right on top of the blue dots (implying exact reconstruction of calibration points). The spread of the red dots around each blue dot corresponds to the reconstructed location at each axial plane. This illustrates that the existing spline based reconstruction approach cannot be used to reconstruct even the known calibration points.

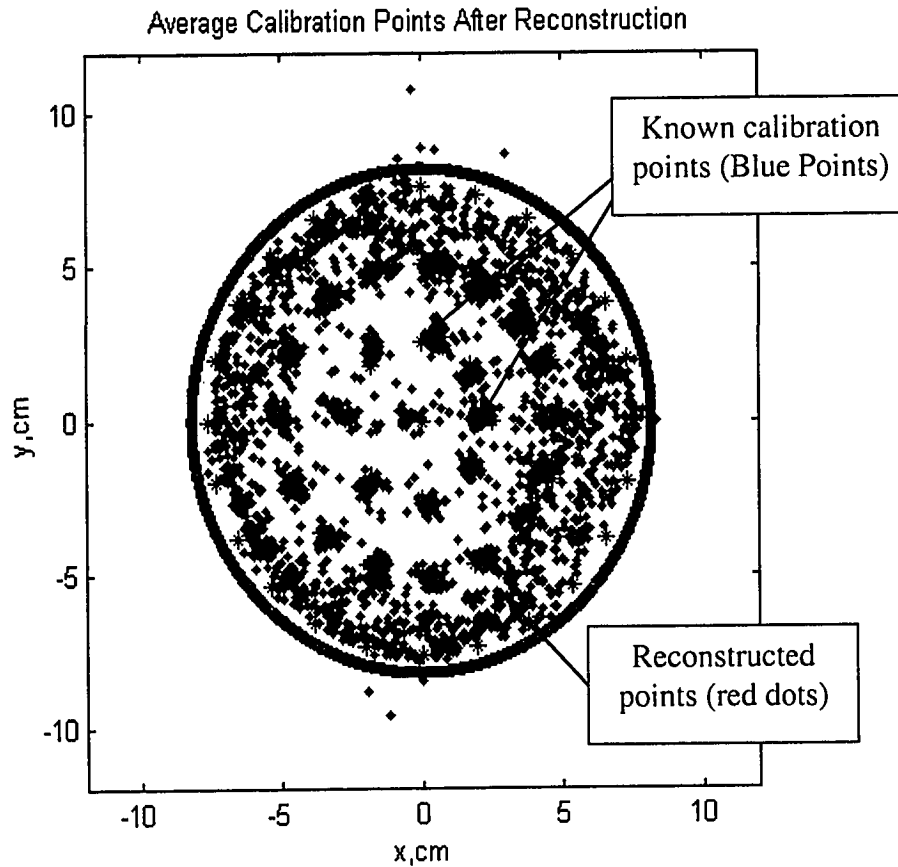


Figure 5-3. Reconstruction of 3528 Known Calibration Points

As expected the errors in reconstructing other tracer locations are larger as shown below in Figure5-4. Hence, the problem was identified to be the use of the existing spline based reconstruction approach for systems whose calibration curve looks like that shown in Figure5-2 and the further amplification of this error by the use of the existing weighted least squares regression technique in identifying the exact tracer co-ordinates (x,y,z) .

To remedy this situation a two pronged solution approach has been adopted. In one, the spline based reconstruction approach and the weighted least squares regression technique are replaced by different approaches, and in the second a new data acquisition strategy is outlined which confines the spread in the calibration curve allowing the usage of the

existing reconstruction algorithms. Both are expected to provide better reconstructions of both the calibration as well as the unknown test points.

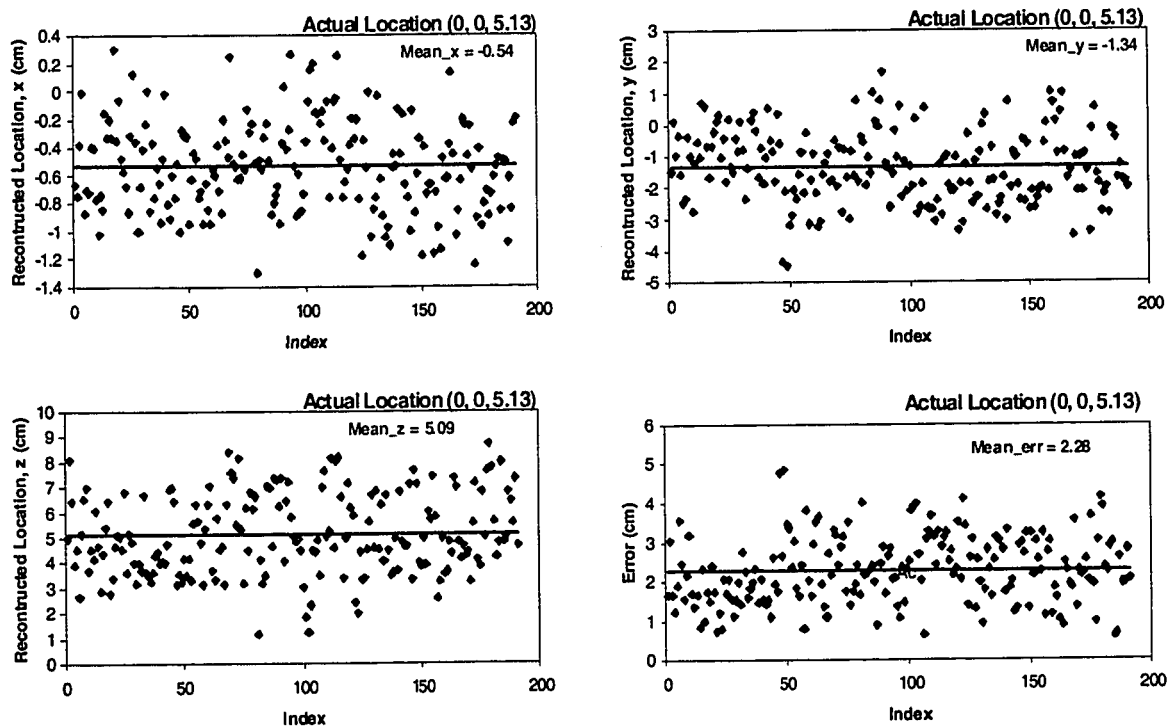


Figure 5-4. Reconstruction of Unknown Test Points Located at ($r = 0$ cm, $\theta = 0^\circ$, $z = 5.13$ cm)

5.1.3 Results and Discussion:

5.1.3.1 A Look-up Table Approach:

Larachi et al. (1994) used a two - step approach to reconstruct the unknown tracer position. In the first step they use the calibration data spread on a coarse grid (implying smaller number of calibration data, say a few hundreds as against 3528) to generate the system constants like: detector dead times (τ_d), detector gains (R) and attenuation coefficients of the medium (μ_l , μ_g , etc.). They use these constants in a model which then generates an estimate of the counts for any particular position of the tracer with respect to a detector given by:

$$C_{est} = \frac{T\nu R\phi\epsilon}{1 + \tau\nu R\phi\epsilon} \quad (5-2)$$

where T is the sampling period(sec), ν is number of gamma ray photons emitted per disintegration of Sc^{46} ($\nu = 2$), ϕ is the photopeak efficiency and ϵ (function of distance of tracer from detector) is the total intrinsic detection efficiency of the detector (Tsoulfanidis, 1983). The notations used are exactly the same as in Larachi et al. (1994). This model is then used to generate a finer grid of calibration data which is then stored in the form of a lookup table. This is schematically outlined below in Figure5-5:

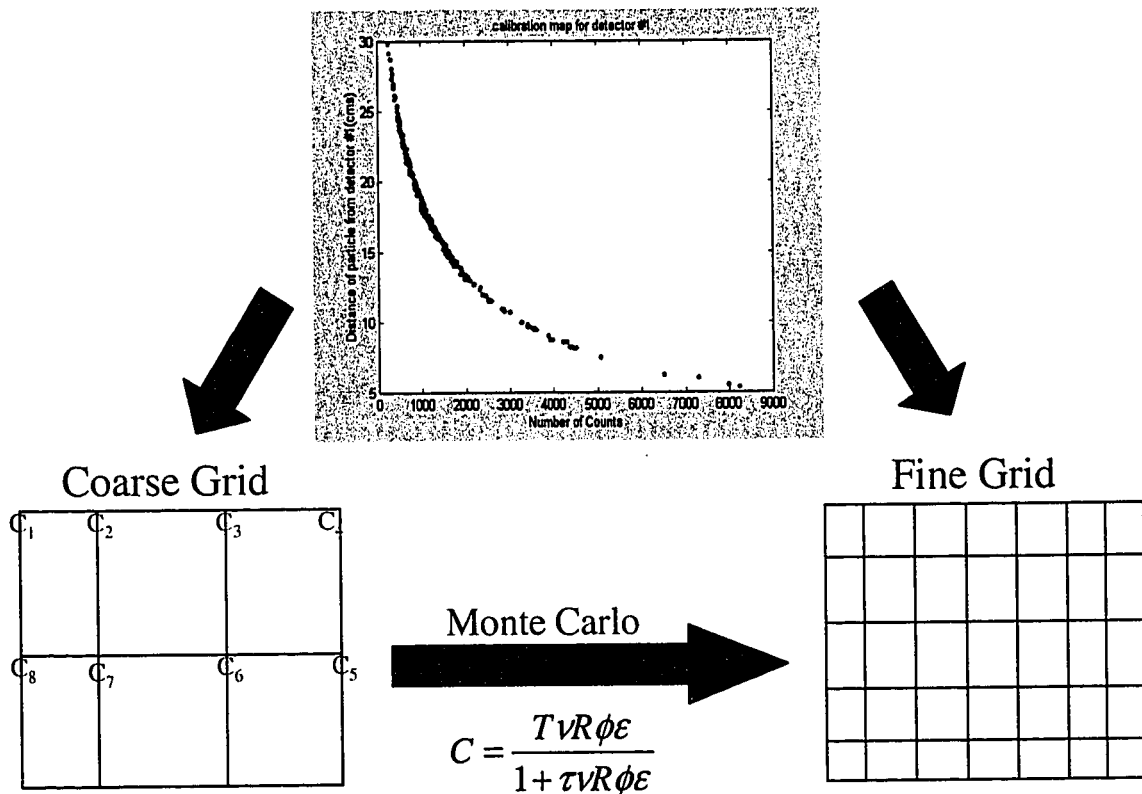


Figure 5-5. Generation of a Fine Grid of Calibration Data Either by Monte Carlo Simulations or through Experiments

This first step of Larachi et al. (1994) is redundant when calibration experiments have been performed on a dense grid like in the stainless steel reactor (3528 points). Hence the calibration data can be organized into a lookup table as shown below in Table 5-1:

Table 5-1. Calibration Information Organized as a Lookup Table

X	Y	Z	C ₁	C ₂	C ₃	C ₄	C ₅	C ₆	C ₇	C ₈
0	0	0	39	42	12	37	45	89	12	5
0	0.2	0	--	---	---	---	---	---	---	
..	..									

The lookup table stores the co-ordinates of each calibration point and the corresponding time averaged count registered by each detector. To reconstruct an unknown tracer location a quantity χ^2 is computed at each node via equation (5.3):

$$\chi^2(j) = \sum_{i=1}^{N_n=16} \frac{(C_i - M_i)^2}{\sigma_i^2} \quad (5-3)$$

where j is the j^{th} calibration node, C_i is the count (calibration) registered by the i^{th} detector for the tracer at the j^{th} node (obtained from the lookup table), M_i is the count measured by the i^{th} detector when the particle is kept at an unknown location and $\sigma_i^2 = C_i$. This χ^2 is computed for all the known calibration points (i.e $j=1-3528$). The node which minimizes χ^2 is identified as the node closest to the unknown point. The time averaged counts corresponding to the known calibration points in the stainless steel column were then fed into this algorithm. This approach was found to yield perfect reconstruction of the calibration points as shown below in Figure 5-6. While this new algorithm, which does not use the spline fitting technique, clearly does an excellent job of reconstructing the known calibration points, its performance in reconstructing the unknown tracer location has to be evaluated. Exact reconstruction is possible (as seen from Figure5-6) provided the unknown point lies on the calibration nodes. But if the unknown point lies in between the nodes then the algorithm in its existing form cannot be expected to do a good job unless the calibration grid is extremely fine ($\Delta x, \Delta y, \Delta z \sim 0.05-0.1\text{mm}$). Hence, a second iteration has to be performed to identify the exact location of the unknown point. This is done by following the ideas outlined in Larachi et al. (1994). They generate a fine grid around the closest node identified in the first iteration as shown below in Figure5-7.

χ^2 Approach

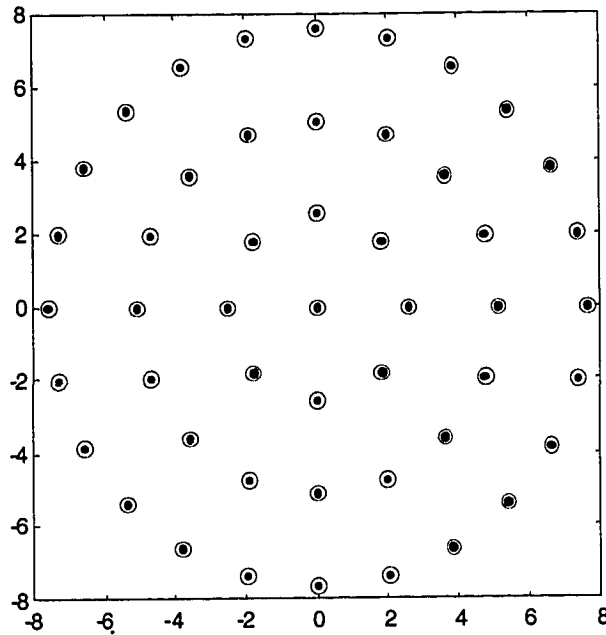


Figure 5-6. Reconstruction of 3528 Known Calibration Points

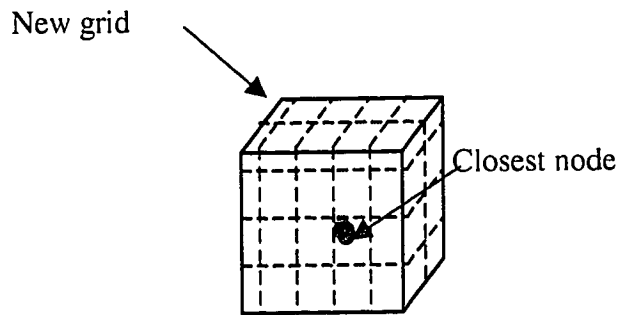


Figure 5-7. Generate a Fine Mesh Around Closest Node

The new grid can be generated by an approximate formula given below:

$$C = \frac{TC_{ref} \left(\frac{r_{ref}}{r}\right)^2 \exp(\mu_R(\delta_{ref} - \delta))}{T - \tau C_{ref} + \tau \left(\frac{r_{ref}}{r}\right)^2 C_{ref} \exp(\mu_R(\delta_{ref} - \delta))} \quad (5.4)$$

Count at new node $\rightarrow C$
 Sampling Time $\rightarrow T$
 Detector dead-time $\rightarrow \tau$
 Distance traveled by photon before striking detector $\rightarrow \delta$
 Tsoufanidis (1983)
 Count at closest node $\rightarrow C_{ref}$

Where r_{ref} is the distance between detector and the closest node and r is the distance between detector and the new node. The information corresponding to the new grid is organized as a lookup table similar to Table 5-1. The same criterion of χ^2 is then used to identify the exact location of the unknown test location. Equation (5.4) permits the evaluation of the contribution of the detector response time (τ_d), attenuation coefficient of the medium and attenuation coefficient of the stainless steel wall (μ_R). Three different approximations of (5.4) were used to evaluate various contributions to total counts. The first model (M_1) ignored the attenuation coefficients and the detector dead times (i.e. μ_R and τ_d were set to zero) and the second model (M_2) accounts for the wall attenuation and the detector dead times. The ability of models M_1 and M_2 to reconstruct ten unknown test points is tabulated below. The ability of models is quantified in terms of a standard deviation, minimum (E_{min}) and maximum (E_{max}) relative errors in estimating the radial and axial co-ordinates.

Table 5-2(a). Reconstruction Accuracy using Model M_1

S.N.	$\sigma_r(cm)$	$\sigma_z(cm)$	$E_{r_{min}}(cm)$	$E_{r_{max}}(cm)$	$E_{z_{min}}(cm)$	$E_{z_{max}}(cm)$
1	.64	.31	-.65	1.14	-.07	.87
2	.78	.20	-.78	1.38	-.07	.57
3	.74	.40	-1.19	1.32	-.77	.67
4	.72	.21	-.54	1.26	-.27	.47
5	.56	.16	-.62	.91	-.17	.37
6	.57	.18	-.72	.85	-.07	.47
7	.60	.26	-.50	1.05	-.17	.67
8	.66	.18	-.64	1.02	-.27	.47
9	.77	.25	-.84	1.4	-.17	.47
10	.57	.18	-.77	1.07		.27

From Table 5-2(a) and 5-2(b) it is clear that the model which accounts for the attenuation coefficient of the column wall does a better job than model M_1 (which ignores μ_R).

Calculations revealed that attenuation caused by the presence of the stainless steel column wall was sometimes as high as that encountered by a photon beam traveling ten times the distance in water (i.e. $\delta_{ss}=10\delta_{water}$). Also a comparison of the errors in reconstruction using M_3 are seen to be much lower than the mean errors seen in Figure 5-4. Thus, it can be concluded that the new reconstruction approach yields a definite improvement in reconstruction of both the calibration points as well as the unknown tracer locations.

Table 5-2(b). Reconstruction Accuracy using Model M_2

S.N.	$\sigma_r(cm)$	$\sigma_z(cm)$	$E_{r\ min}(cm)$	$E_{r\ max}(cm)$	$E_{z\ min}(cm)$	$E_{z\ max}(cm)$
1	.55	.20	-.70	1.31	-.57	.17
2	.67	.06	-.77	1.12	-.07	.07
3	.77	.31	-1.13	1.14	-.37	.77
4	.66	.09	-.56	1.06	-.07	.17
5	.61	.11	-.30	1.25	-.17	.27
6	.69	.06	-.56	1.25	-.07	.07
7	.59	.12	-.35	1.22	-.07	.27
8	.59	.18	-.18	1.23	-.07	.47
9	.60	.20	-.42	1.15	-.07	.47
10	.61	.18	-.40	1.13	-.27	0.27

5.1.3.2 Full Monte Carlo Approach:

The above comparisons between the two different models M_1 and M_2 suggested that modeling the 'physics' of the different phenomenon may improve the reconstruction accuracy. Hence, a full Monte Carlo model was developed where the first step is similar to Larachi et al. (1994), i.e. a Monte Carlo simulation is done to generate a calibration like data on a finer grid (refer to Figure 5-5). However, a full Monte Carlo simulation with the stainless steel column calibration data revealed that Monte Carlo simulations do often predict counts which are higher than the measured counts, as shown below in Figure 5-8.

This seemed to indicate that the presence of “Stainless Steel” wall may be causing the phenomenon of build-up to occur (Tsoulfanidis, 1983). Build-up is the phenomenon of registering counts coming directly from the source as well as the scattered photons. Under these conditions the Beer – Lambert like expression for attenuation in intensity of counts must be corrected by a premultiplicative factor called the “Build-up factor”. The equation used to generate a Monte Carlo estimate of the count does not account for the phenomenon of build-up which might explain the observed over-prediction in counts. Hence, a Monte Carlo simulation done with data containing the full energy spectrum will need to account for the phenomenon of build-up which is a non-trivial matter.

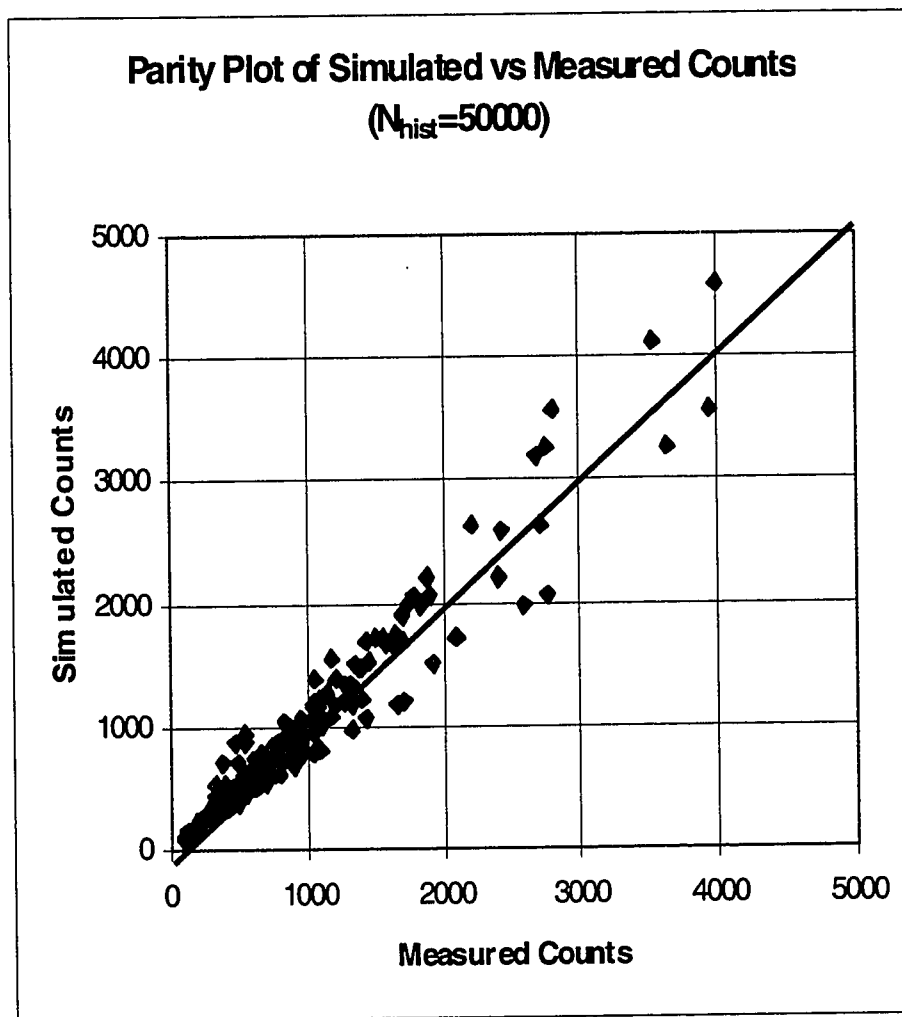


Figure 5-8. Comparison between Measured and Simulated Counts

The presence of build-up was confirmed by comparing the spectrum measured with and without stainless steel wall (Figures 5.9a and 5.9b). Some preliminary attempts were made to model the phenomenon of build-up by developing an iterative neural network based algorithm. The iterative scheme was not robust and did not yield converged results for the build-up function.

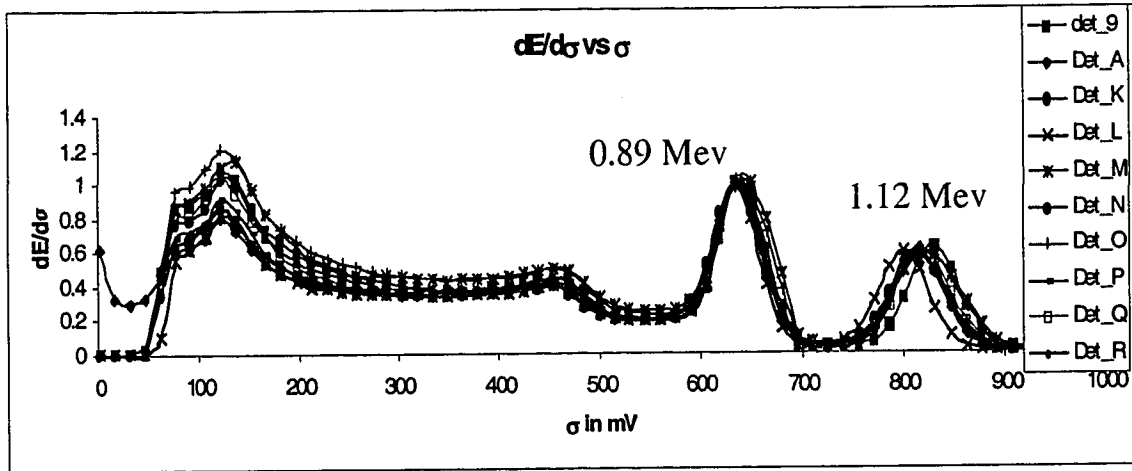


Figure 5-9a. Photo Energy Spectrum Obtained in a Plexi-Glass Column

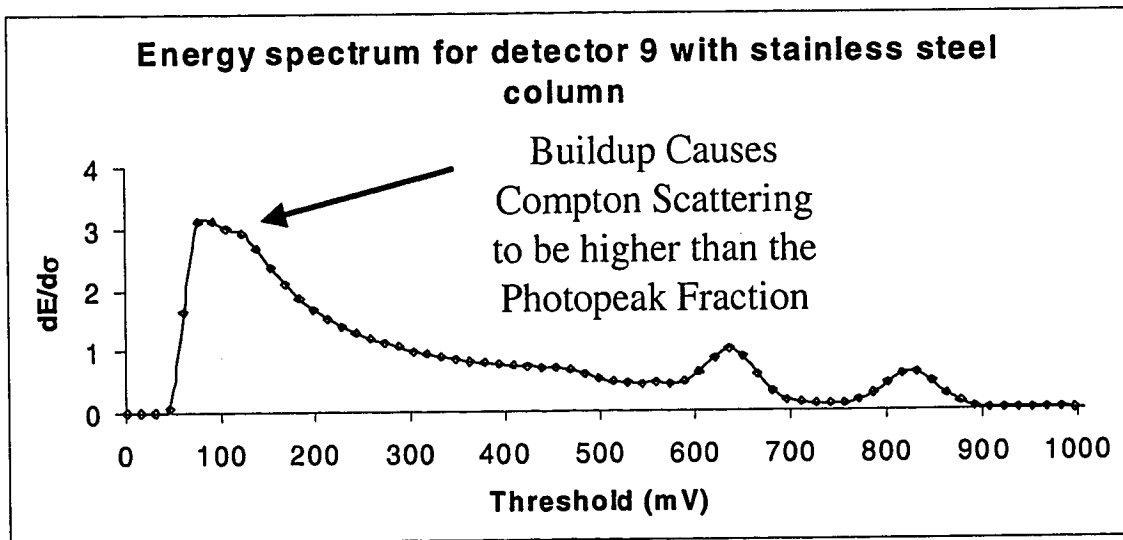


Figure 5-9b. Photo Energy Spectrum Obtained in a Stainless Steel Reactor

Therefore, this approach was not further pursued. The only way to avoid modeling build-up is to constrain the detectors to acquire only the photopeak fraction of the photon energy spectrum, i.e. in Figure 5-9a and 5-9b if the detectors can be constrained to collect only those photons with energy greater than 600mV then one can be certain that the data will not be corrupted by the build-up phenomenon. Some preliminary Monte Carlo simulations were done by acquiring data with a threshold of 560mV to register only the photopeak fraction. Monte Carlo simulations were done with 1,000 photon histories. A fine grid of calibration data was generated using Monte Carlo simulations. The parity plots of the simulated vs measured counts for the new data set are shown below in Figure 5-10 and indicate that the simulated counts compare very well with the measured counts.

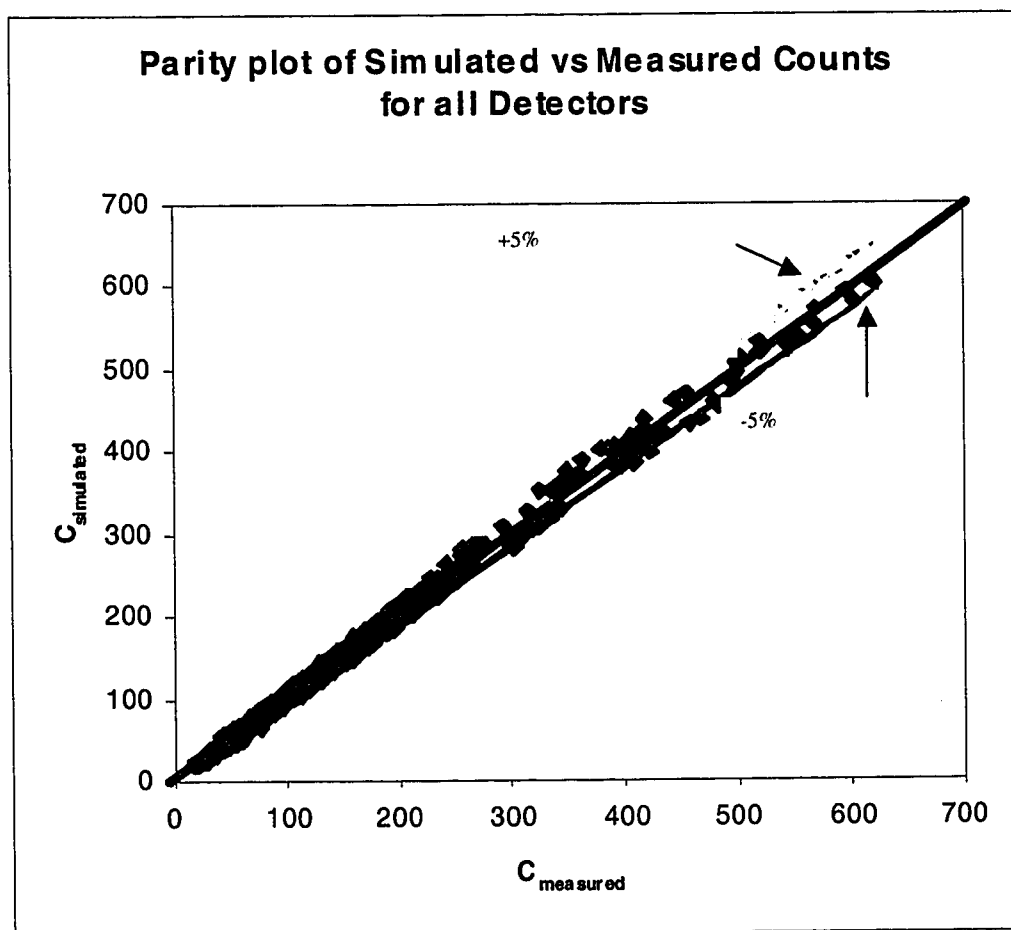


Figure 5-10. Comparison between Measured and Simulated Counts

In Sections 5.1.3.1 and 5.1.3.2 two new reconstruction approaches have been outlined, both of which are based on modeling the physics of the photon emission phenomenon. Both these approaches seem to give a reasonably good reconstruction of the tracer location. The second approach 5.1.3.2 also suggests that the phenomenon of build-up, due to the presence of stainless steel column walls, might be the cause of the large spread in the calibration curve (refer to Figure 5-2). This suggestion led us to explore a new data acquisition strategy as outlined below.

5.1.3.3. A New Data Acquisition Strategy:

From the above analysis it is clear that the earlier data acquisition strategy of setting a low threshold does not really work well for the stainless steel reactors. This is mainly due to the fact that a large fraction of the collected photons come from the scattered photons and not the photopeak photons (refer to Figure 5-9(b)). The presence of a large fraction of scattered or 'Compton' photons causes the instantaneous counts to be distributed in a random manner which does not follow the Poisson distribution. The normalized standard deviation for this new distribution does not necessarily scale inversely with the number of counts, this implies that, it does not really help to set a low threshold for the data collection. Hence, the new data-acquisition strategy is based on the assumption that the observed scatter in the calibration curve is caused by build-up at the stainless steel column wall. Through Figures 5.9a and 5.9b we also established that presence of build-up affects only the Compton scattering portion of the energy spectrum and not the photopeak fraction of the spectrum. Therefore, the new data acquisition strategy is to acquire only the photopeak fraction of the energy spectrum and then examine the appearance of the calibration curve. These calibration experiments were performed in a stainless steel column (O.D.= 10.4 in (26.4 cm) and thickness = 0.24 in (0.6 cm)) surrounding an 8.5 in (21.6 cm) stirred tank reactor with the impeller rotating at 400 rpm (corresponding to tip speed of $V_{tip}=1.4$ m/s) with gas being sparged at 10.0 Scfh. The resulting calibration curve is shown below in Figure 5-11. The above calibration curve suggests that acquiring only the photopeak fraction of the energy spectrum results in a calibration curve which is

very similar to the calibration curve obtained in plexiglass column (refer to Figure5-1) with the only difference being the gradient of the calibration curve which depends on the attenuation coefficient of the intervening media. In stainless steel columns the gradient of the calibration curves are steeper than those in plexiglass column due to the higher attenuation coefficient of the stainless steel column wall.

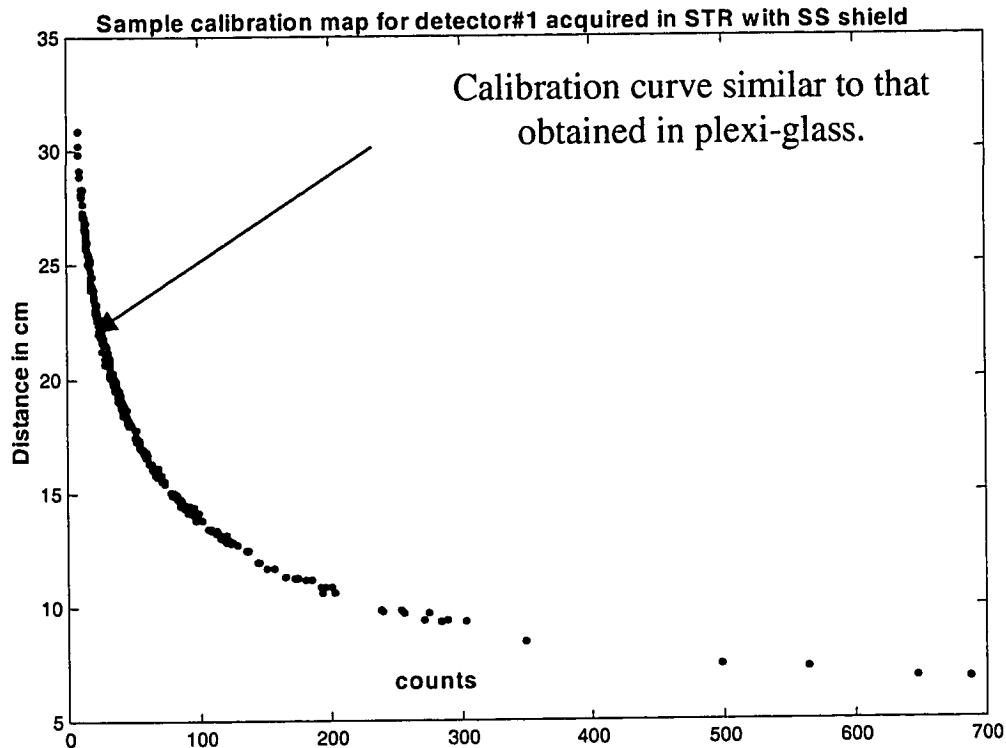


Figure 5-11. Calibration Curve Obtained in S.S. Column by Acquiring Photopeak Fraction Alone

The above calibration curve suggests that with this new data acquisition strategy particle reconstruction should be reasonably accurate with the existing spline/weighted least squares regression approach. Hence, the time averaged counts registered by each detector corresponding to the known calibration points were fed to the existing spline based reconstruction approach. The details of reconstructing the 396 known calibration points is shown below in Figures 5-12. The figure suggest that the existing spline based approach can reconstruct the known calibration points faithfully except for the calibration points

near the bottom, top and walls of the column. The reconstruction is definitely much better than seen earlier (Figure 5.3). In the figure the blue circles represent the known calibration points while the red dots represent the reconstructed point. Further, the spline based approach was used for reconstructing 36 test locations (corresponding to 3 radial locations 3.8, 5.7 and 9.5 cm, $\theta=0-360^\circ$, $z=0-20$ cm, $\Delta\theta=30^\circ$ and $\Delta z=2.0$ cm).

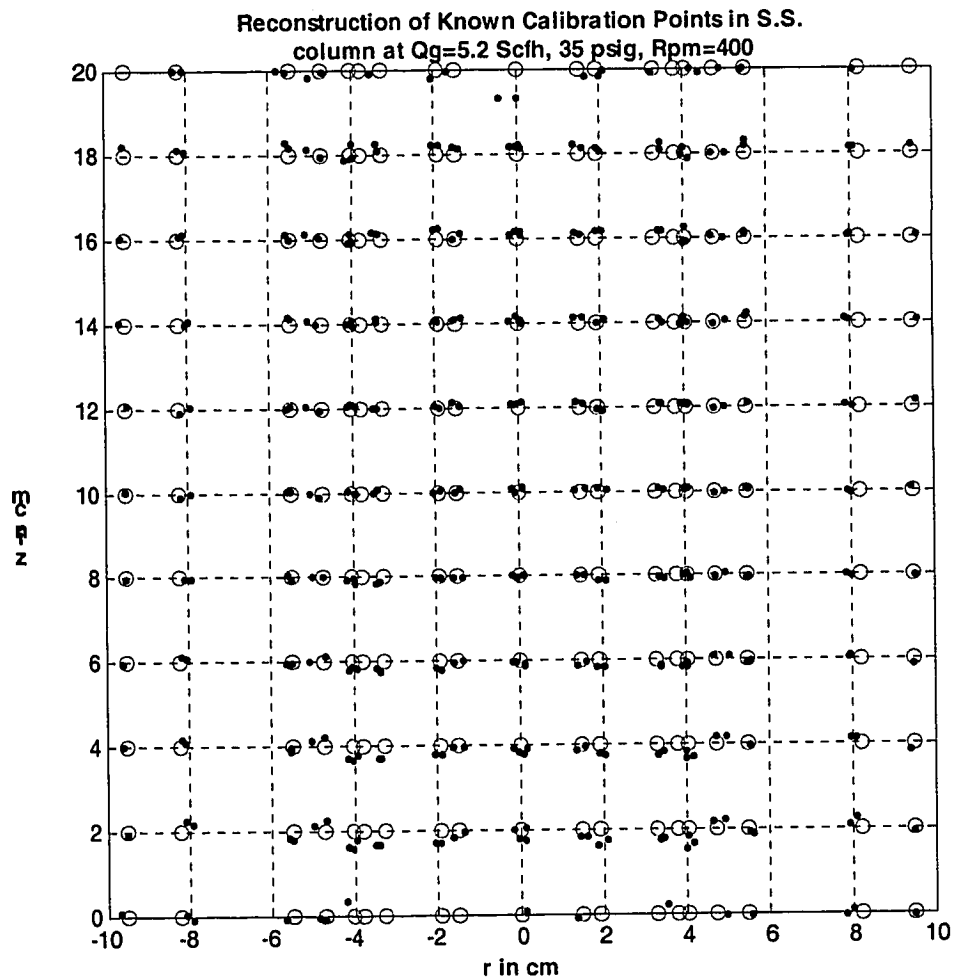


Figure 5-12. Reconstruction of 396 Known Calibration Points Projected Onto an r-z Plane

The details of reconstructing a set of 12 test points corresponding to one axial plane are shown below in Figure 5-13.

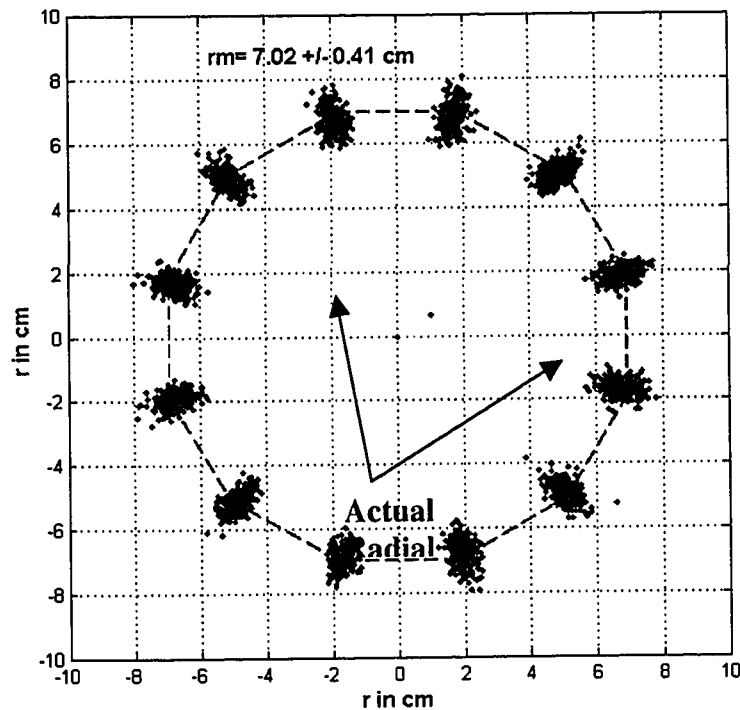


Figure 5-13. Details of Reconstructing 12 Test Points ($r = 7.2$ cm, $\theta = 15^\circ$ - 345° , $z = 5.0$ cm) from 3072 Instantaneous Samples Acquired at 50 Hz

Hence, the variances were computed around the reconstructed radial location. This, σ_r , is of the order of 4.0 mm which is comparable to σ_r reported by Larachi et al. (1994) of 2.5-3.0 mm when they acquired data at 33 Hz. They have also shown that the radial variance and the axial variance decrease with a decrease in sampling frequency and increase with an increase in sampling frequency. This result from Larachi et. al.'s work (1994) is reproduced below in Figure 5-14. It has to be mentioned, however, that while the variation in Figure 5-14 was obtained with 8 detectors the current study used 16 detectors. But Larachi et al.'s (1994) experiments were done in a plexiglass column while the current experiments were done in a stainless steel column. Further Larachi et al.'s column diameter was 4 inches while the current set-up is 10.4 inches in diameter.

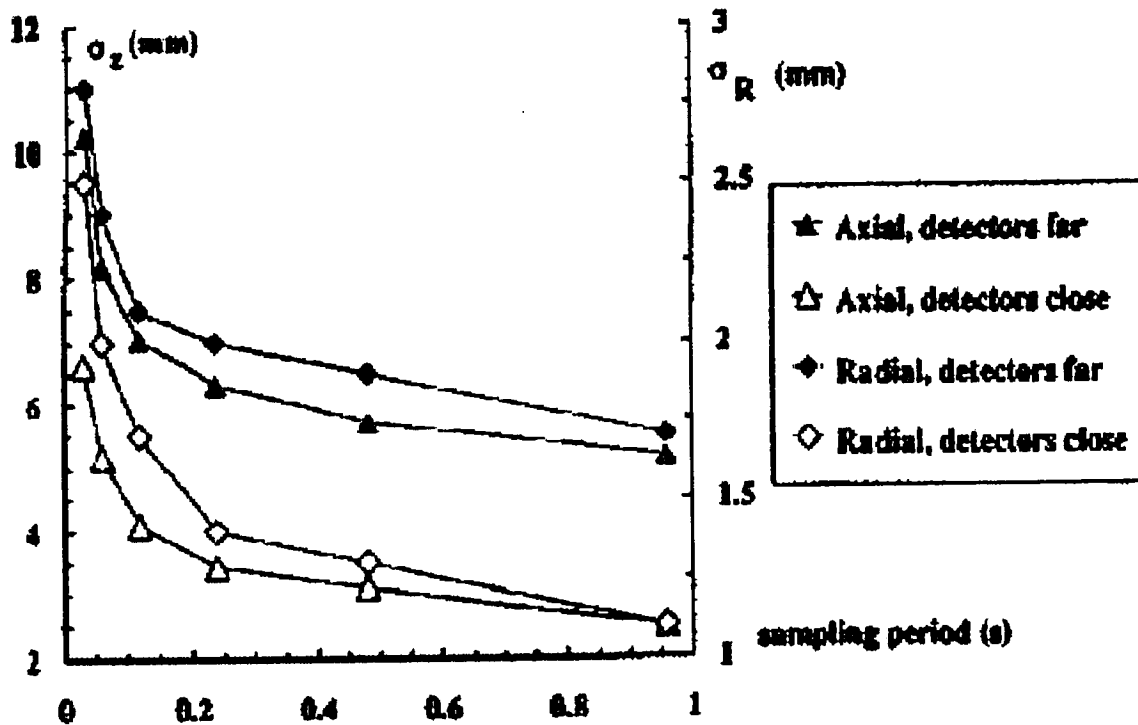


Figure 5-14. Variation in σ_r and σ_z with the Sampling Frequency

Given all these differences, the radial σ_r obtained in the current study seems reasonable. The accuracy in reconstructing all the 36 test locations are summarized below in the form of Table 5-3.

Table 5-3 suggests that both the estimate of the mean radial location as well as the mean axial location are biased. The radial estimate is always negatively biased while the axial estimate is positively biased in the center of the column but towards the top is negatively biased. The σ_r and σ_z are all comparable and are between 4.0-4.5 mm. These numbers are comparable to similar values reported by Larachi et al. (1994). On the face of it the σ_z (4.0-4.5 mm) from the current study may seem to be better than those of Larachi et al.

(9.5 –11.0 mm). But it must be kept in mind that Larachi et al.'s study used only 8 detectors while in current study 16 detectors were used.

Table 5-3. Summary of Reconstruction Accuracy of 36 Test Locations (1 Radial Location, 3 Axial Locations and 12 Angular Locations)

Location	R_{actual} (cm)	R_{recon} +/- σ_r (cm)	Z_{actual} (cm)	Z_{recon} +/- σ_z (cm)
1	7.2	7.02 +/- 0.41	5.0	5.1 +/- 0.45
2	7.2	6.93 +/- 0.38	10.0	10.0 +/- 0.40
3	7.2	6.96 +/- 0.40	15.0	14.9 +/- 0.46

In order to analyze the effect of detector configuration and number of detectors the above analysis was repeated for two different detector configurations. In the first detector configuration only 8 detectors were used as shown below in Figure 5-15: The accuracy in reconstructing the 36 test points after hiding 8 detectors is reported below in Table 5-4.

Table 5-4. Summary of Reconstruction Accuracy of 36 Test Locations (1 Radial Location, 3 Axial Locations and 12 Angular Locations) After Hiding 8 Detectors

Location	R_{actual} (cm)	R_{recon} +/- σ_r (cm)	Z_{actual} (cm)	Z_{recon} +/- σ_z (cm)
1	7.2	7.08 +/- 0.69	5.0	5.31 +/- 1.29
2	7.2	7.05 +/- 0.65	10.0	9.92 +/- 1.11
3	7.2	7.00 +/- 0.73	15.0	14.22 +/- 1.44

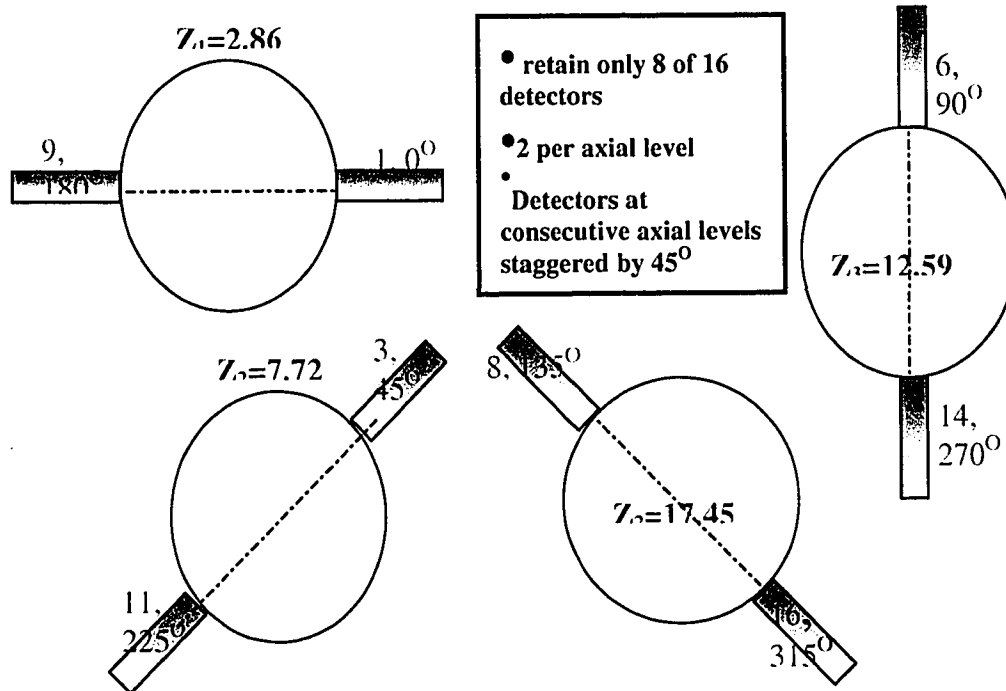


Figure 5-15. Analyze Effect of Detector Configuration on Reconstruction Accuracy

Table 5-4 suggests that by hiding 8 detectors the error in the estimate of the mean axial location has gone up. The σ_r and σ_z have also gone up with $\sigma_r(8)/\sigma_r(16) \sim 1.75$ and $\sigma_z(8)/\sigma_z(16) \sim 3.0$. The σ_z , which appears to be large (11-14 mm), is comparable to the values reported by Larachi et. al. with 8 detectors. Hence, Table 5-4 suggests that the number of detectors used for reconstruction definitely affects the reconstruction accuracy. This was also seen to be the case when only 4 detectors were used for reconstruction. These results have been summarized below in the Figures 5.16a and 5.16b respectively. Figure 5-16a suggests that the bias in the radial estimate is not affected much by the number of detectors used for reconstruction, while the bias in the axial estimate goes down with the increase in the number of detectors (4.0 mm to 0.5 mm).

Figure 5-16b suggests that σ_z is comparable to σ_r for large number of detectors, and σ_z and σ_r progressively increase as the number of detectors decreases. The rate at which σ_z increases is higher than the rate at which σ_r increases.

E_r and E_z vs N_D used for reconstruction

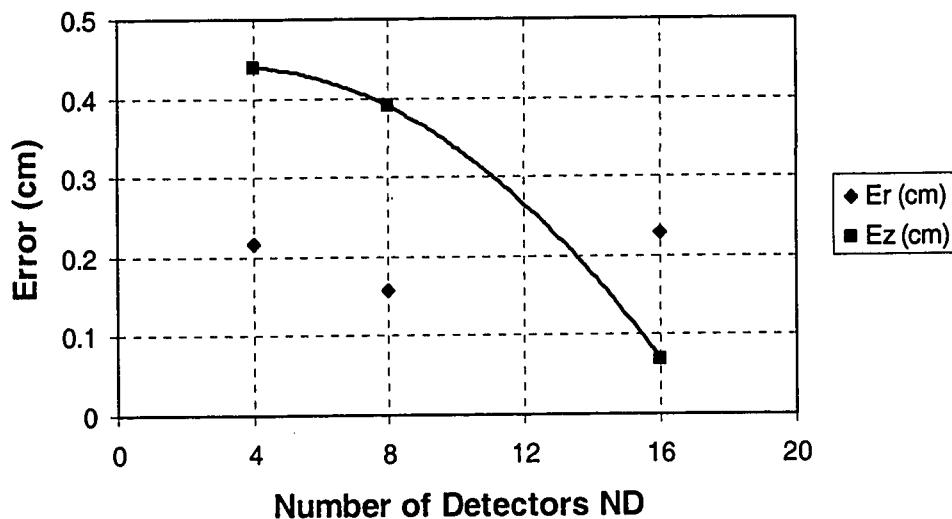


Figure 5-16a. Variation of Radial and Axial Bias with Number of Detectors used for Reconstruction

σ_r and σ_z vs N_D used for reconstruction

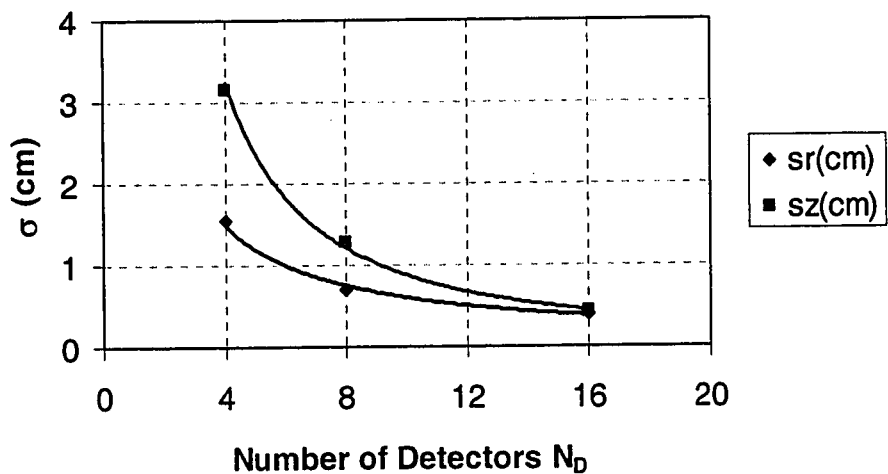


Figure 5-16b. Variation of σ_r and σ_z with Number of Detectors used for Reconstruction

This suggests that the error boundaries associated with the particle position reconstruction change from a sphere (when N is large) to an ellipsoid (when N is small). To generalize these results one would need to look at the variation of σ_r and σ_z with detector density (defined as $N_D/(\text{Active volume of interest in reactor})$). The above analysis suggests that with the new data acquisition strategy even the existing spline based/weighted regression technique can be used to obtain reasonably good estimates of the tracer location in the stainless steel column.

5.1.4 Conclusions

In this section we have shown that depending on the material of construction of the reactor wall (or internals) different reconstruction strategies can introduce very little to considerable errors in identifying the particle location. In the presence of dense walls it has been shown that the use of a physics based model (like the Monte Carlo model developed by Larachi et. al., 1994) is likely to give better results than the conventional spline based algorithm. But the use of this algorithm in two-phase flow situations requires experimental inputs of the dispersed phase holdup distributions. Hence, an alternative is to use the new data acquisition strategy proposed in this section which allows us to continue using the conventional spline based approach by collecting only the photopeak photons. Hence, the data which we report in chapter 7 has been collected using this new data acquisition strategy. In the following section 5.2 we introduce the concept of 'dynamic bias' and quantify the errors introduced by it both experimentally as well as numerically.

5.2 CARPT Dynamic Bias Studies: Evaluation of Accuracy of Position and Velocity Measurements

5.2.1 Introduction

In this section the accuracy of the velocity measurements obtained from CARPT as a function of the *sampling frequency* is evaluated. For the purpose of illustration, CARPT

experiments have been performed in a stirred tank by placing the radioactive tracer particle at the impeller tip. Particle trajectory information was obtained over a range of rotational speeds (60-800 rpm corresponding to Impeller tip speeds ranging from 21 cm/s to 2.80 m/s) at different sampling frequencies (ranging from 10-200 Hz). From the trajectory information the particle velocities were obtained by multiplying the difference in two subsequent positions with the sampling frequency and assigning the velocity vector to the midpoint of that cell. For each rpm, plots of reconstructed velocity vs. sampling frequency were made. These enable us to establish the proper *de-biasing* procedures by selecting the appropriate data sampling rate for a particular velocity. A Monte-Carlo based model has been developed, which permits an *a priori* evaluation of the extent of dynamic bias, thus providing guidance in setting the appropriate data sampling rate for different velocities. This study is expected to be of considerable use when implementing the CARPT technique in industrial systems where such detailed experimental analysis of technique's accuracy will be both cumbersome and time consuming.

5.2.2 The Dynamic Bias Issue

In the CARPT technique two kinds of measurements are performed. The first kind called 'static measurement' is performed for calibrating the data acquisition process. During calibration the radioactive tracer is placed at several hundred known locations and the NaI (TI) scintillation detectors register a certain number of sample counts (typically 256 samples acquired @50 Hz). A calibration map for each detector is then generated by plotting the mean of these 256 samples at each point against the distance of that point from that detector. A typical calibration curve is shown below in Figure 5-17. Once the calibration map has been generated for each detector then the 'dynamic measurement' is performed by introducing the tracer particle into the flow field whose fluid dynamics is to be characterized. As the tracer starts moving with the fluid, the photons emitted by the radioactive tracer are registered by each detector for τ seconds (corresponding to a data

acquisition rate of $f_{sample} = \frac{1}{\tau}$).

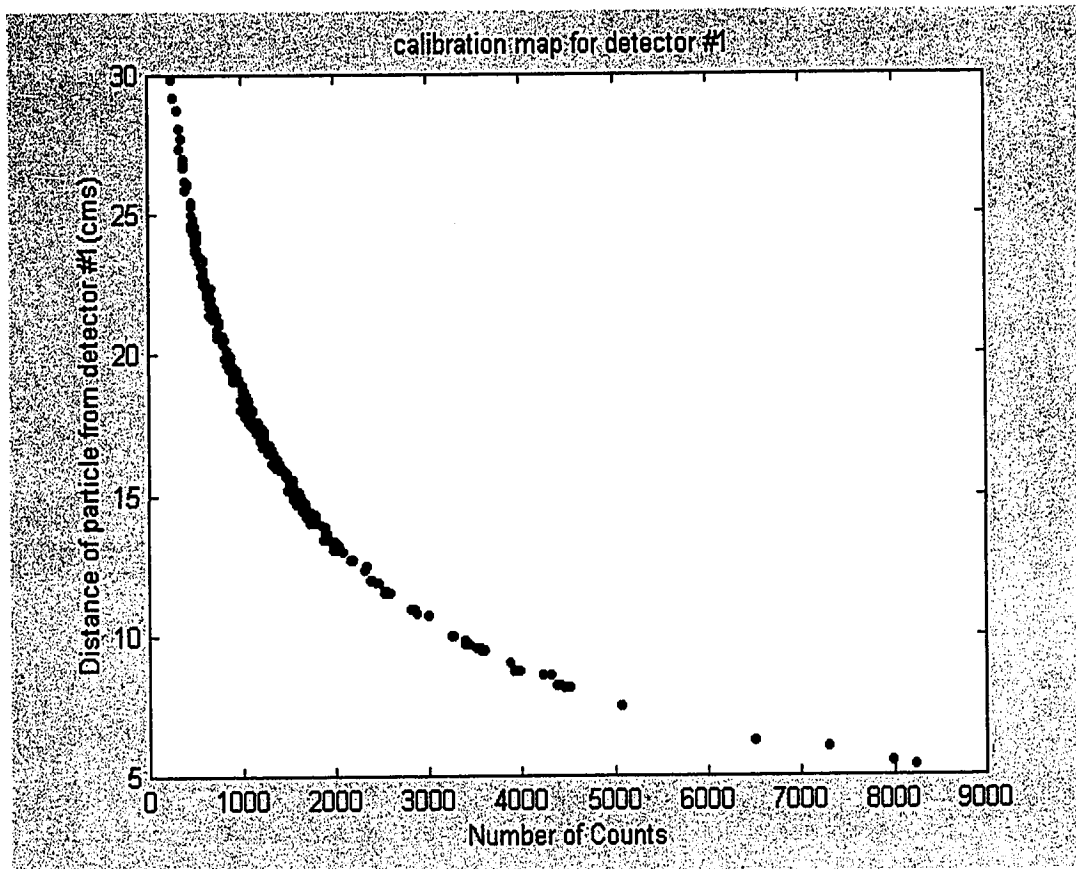


Figure 5-17. Calibration Map for Detector #1

This vector of counts acquired at each sampling instant is then fed into the calibration curve for that detector to find out the corresponding distance of the tracer from that detector given below by equation (5.5).

$$d_{\text{tracer}}^{i^{\text{th}} \text{ detector}} = f(C_{i^{\text{th}} \text{ detector}}) \quad (5-5)$$

Knowing the distance of the tracer from each detector, the tracer co-ordinates can be computed (Degaleesan, 1997). The dynamic bias issue arises due to the fact that when the tracer particle is in motion the count registered by the i^{th} detector at a certain location $(x_p(t, t_0), y_p(t, t_0), z_p(t, t_0))$ in the reactor will strongly depend on the past particle trajectory, the fluid velocity along the particle path and the rate at which the photon counts are registered by that detector. Hence, the mean count registered by the i^{th} detector when particle is kept stationary $C_{\text{stationary}}^{i^{\text{th}} \text{ detector}}(x_p, y_p, z_p)$ will be different from the

instantaneous count $C_{dynamic}^{i^{th} \text{ detector}}(x_p(t, t_o), y_p(t, t_o), z_p(t, t_o))$ registered by the i^{th} detector as the particle moves to the point $(x_p(t, t_o), y_p(t, t_o), z_p(t, t_o))$. Hence, when the particle is in motion the distance between tracer and detector estimated from the static calibration measurements (5.5) will be different from the real distance of the tracer from detector. This concept is illustrated below in Figure 5-18.

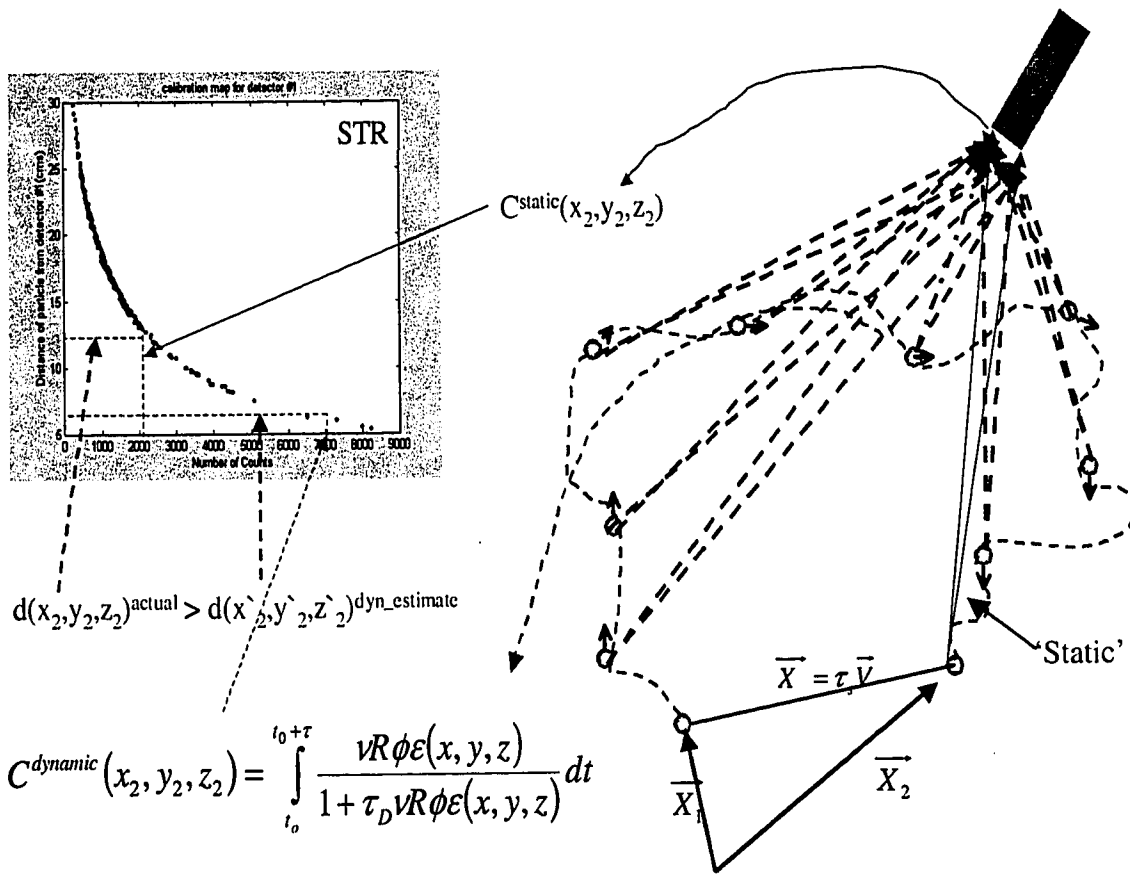


Figure 5-18. Cartoon Illustrating the Concept of 'Dynamic Bias'

From Figure 5-18 it can be seen that, as the fluid velocity increases for a fixed sampling rate, or as the sampling rate decreases for a fixed fluid velocity, the greater will be the deviation of the dynamic measurement from the static measurement. In this work we have quantified the error introduced in the reconstructed particle position and the particle velocity for different sampling rates and fluid velocities experimentally using the following approach.

5.2.3 Experimental Details

To quantify the error due to the dynamic bias effect the errors introduced due to the flow following capability of the tracer must be decoupled from the CARPT measurements. Further, the tracer must follow a known trajectory with a known velocity to be able to compare the experimental results and quantify the error. Hence, the radioactive tracer was placed at the tip of a 6-bladed Rushton turbine in the stirred tank (details of the tank dimensions are provided below in Figure 5-19). The impeller speed was varied from 60 – 800 rpm corresponding to tangential velocities of 21 cm/s to 2.79 m/s. At each impeller speed photon count data was registered by each of 16 detectors surrounding the stirred tank (details of detector configuration provided in Rammohan et. al., 2001a). Data was acquired at the rate of 200 Hz. The dynamic measurements were preceded by static calibration experiments that resulted in calibration curves like the one shown in Figure 5-17.

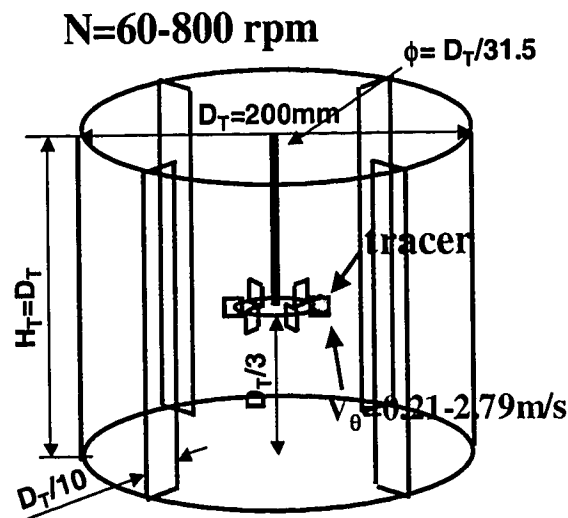


Figure 5-19. Dimensions of Stirred Tank Reactor

The impeller speeds were monitored with a high precision magnetic tachometer and the variations in the speed were within 1%. The raw count data generated from these experiments were then reprocessed to generate raw count data corresponding to experiments where the data acquisition rates are 25, 50 and 100 Hz acquired over a time

period of five minutes. These raw data corresponding to the different sampling frequencies were then fed into the CARPT reconstruction algorithm (Chaouki et. al., 1997) to estimate the particle trajectories at different sampling rates and different impeller speeds. In the following section the details of the numerical technique used to quantify the dynamic bias is outlined.

5.2.4. Details of Numerical Technique

A Monte Carlo based phenomenological model developed earlier (Larachi et. al., 1994) has been further extended to simulate the dynamic bias CARPT experiments. Theoretically, the number of photopeak counts C recorded by a detector during a sampling interval T from a point radioactive source of strength R placed at a location (x,y,z) inside a dense medium, the tank to be studied, can be expressed by the following relationship (Tsoulafanidis, 1983; and Moens et. al., 1981):

$$C = \frac{TvR\phi\varepsilon}{1 + \tau vR\phi\varepsilon} \quad (5-6)$$

where

$$\varepsilon = \iint_{\Omega} \frac{r \cdot n}{r^3} \exp(-\mu_R(e_R - e_{shaft}) - \mu_{shaft}e_{shaft} - \mu_w e_w) (1 - \exp(-\mu_D d)) d\Sigma \quad (5-7)$$

where ν is the number of γ rays emitted per disintegration (for example $\nu=2$ for Sc^{46}); ε is the total efficiency, i.e. the probability that γ rays will emerge from the reactor without scattering and will interact with the detector; τ is the dead time per recorded pulse, and ϕ is the photopeak energy to total energy (or photopeak) ratio. 'r' is the distance between the source and a point P on the outer surface of the detector crystal, e_R the path length traveled by the γ - ray in the reactor, e_{shaft} is the length of the ray traveling through the shaft (Figure 5-20.), e_w is the path length through the reactor wall and d is the crystal thickness in the direction given by the vector \vec{r} . Ω is the solid angle subtended by the detector surface at the source and \vec{n} is an external unit vector locally

perpendicular to $d\Sigma$. μ_R , μ_{shaft} , μ_W and μ_D are the total linear attenuation coefficients of the reactor inventory, stainless steel shaft (onto which impeller is mounted), the reactor wall and the detector material, respectively. Each of the above attenuation coefficients depend on the γ - ray energy.

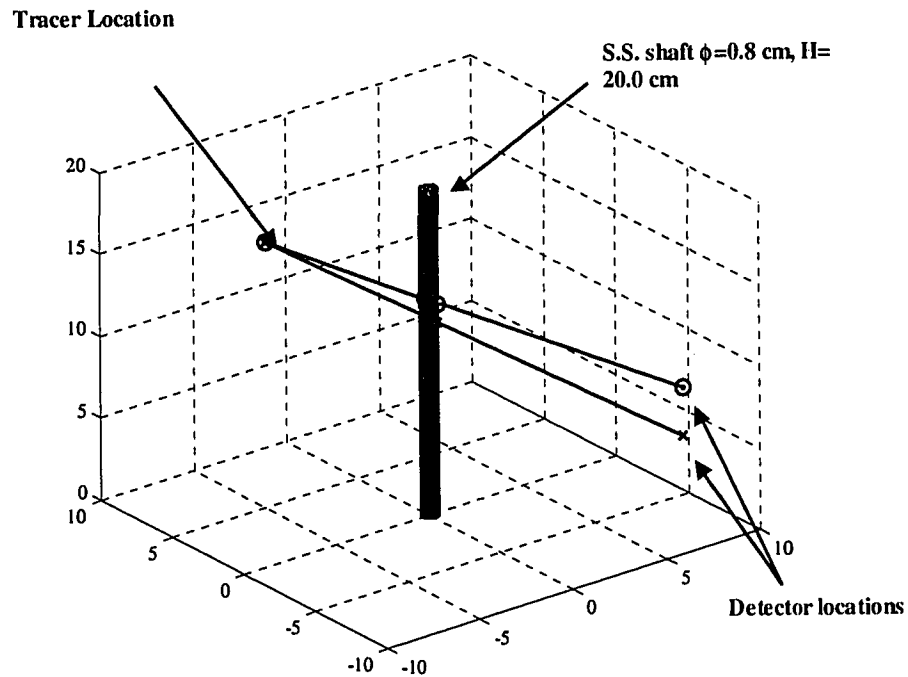


Figure 5-20. Modeling Internals using Monte Carlo Simulation

It is in the computation of the intrinsic efficiency ε that the Monte Carlo procedure is used. Out of N photons emitted by the tracer only a certain fraction of the photons will intersect the detector crystal. The direction of each photon is picked at random, using a rectangular random number generator (corresponding to a Monte Carlo random sample), and depending on the direction cosines of the photons it can be checked if a particular photon will intersect the detector or not. This fraction of the total photons that do intersect the detector surface, by definition is the solid angle subtended by the detector at the location of the tracer. The advantage of using a Monte Carlo integration is that the

error decreases with the increase in number of photon histories tracked as $\frac{1}{\sqrt{N_{history}}}$. 117

It has been found previously (Larachi et. al., 1994) that tracking 1000 photon histories provides a reasonably accurate estimate of the intrinsic detection efficiency ε . The first step in the Monte Carlo simulation is to estimate the parameters of the model equation (5.6), i.e. R, τ, μ , using the calibration data or the static measurements discussed earlier (section 5.2.4). Then the next step is to verify that the model can then be used to simulate the counts registered by the detectors corresponding to each known calibration point. A sample parity plot of the simulated versus measured calibration counts for detector #1 (Figure 5-21) suggests reasonably good predictions by the model.

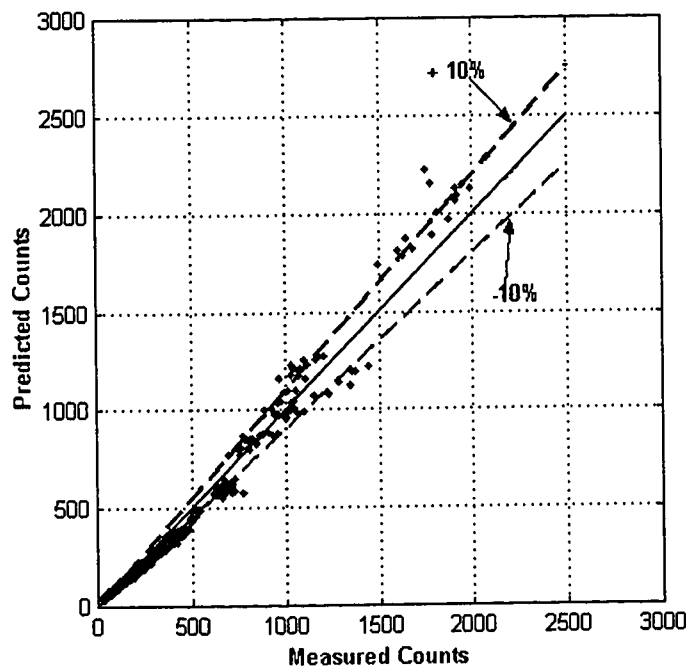


Figure 5-21. Parity Plot of Predicted vs Measured Calibration Counts Registered by Detector #1

The next step in using the model is to feed the known circular particle trajectory (corresponding to a certain impeller speed) $\bar{X}(t)$ sampled at a certain sampling frequency

$f_{sample} = \frac{1}{\tau}$ to equation (5.6) to generate a dynamic estimate of the count registered by

the i^{th} detector i.e. $C_{dynamic}^{i^{th} detector}(x_p(t, t_0), y_p(t, t_0), z_p(t, t_0))$ as :

$$C_{dynamic}(\vec{X}(t_0 + \tau), i) = \int_{t_0}^{t_0 + \tau} \frac{vR\phi\epsilon(x, y, z)}{1 + \tau_D vR\phi\epsilon(x, y, z)} dt \tag{5-8}$$

This equation is handled numerically as:

$$C_{dynamic}(\vec{X}(t_0 + \tau), i) = \sum_{k=1}^{N_{small}} C_k\left(\vec{X}\left(t_0 + \frac{k}{N_{small}}\tau\right), i\right) \tag{5-9}$$

The value of the integral does not change for values of $N_{small} > 20$. Thus, equations (5.8) and (5.9) are used to numerically generate a raw count file corresponding to the dynamic CARPT measurements. These are then fed into a Monte Carlo based particle rendition algorithm (Chaouki et. al., 1997) to estimate the particle trajectory and particle velocity for different sampling rates and impeller speeds. In the following sections the experimental results are discussed in detail and some preliminary results from the simulations are outlined.

5.2.5 Results and Discussions

5.2.5.1 Variation of Radial Bias with Data Acquisition Rate

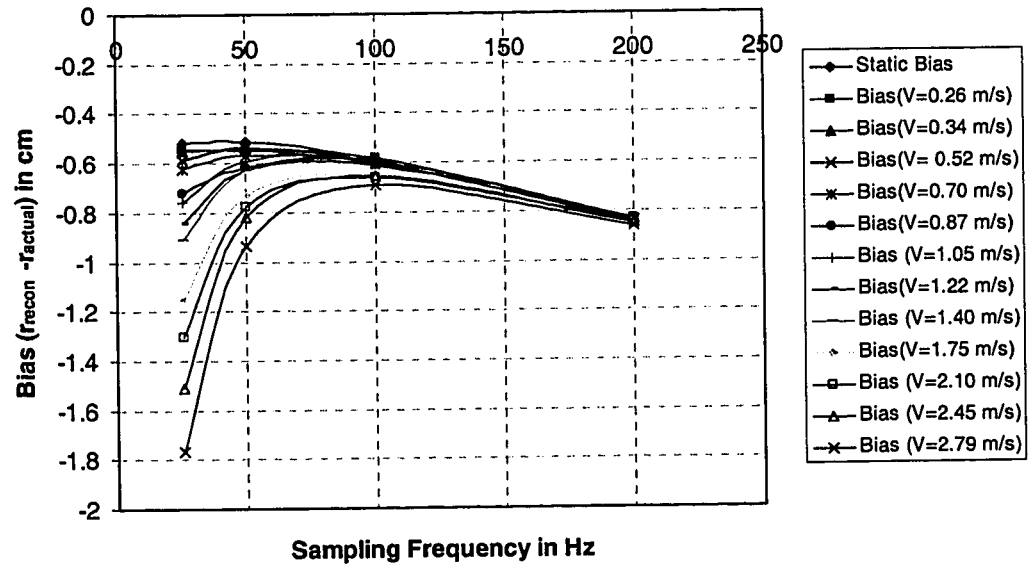


Figure 5-22. Variation of Radial Bias with Data Sampling Rate ($V_{tip}=0.21 - 2.79$ m/s)

In Figure 5-22 the variation of the radial bias ($r_{reconstructed} - r_{actual}$) with the data sampling rate at different impeller speeds is shown. It can be seen that for all impeller speeds and sampling frequencies the bias is always negative, i.e. the reconstructed radial particle position is always underestimated. Further, for a given impeller speed it can be seen that the radial bias is at the minimum within a certain optimal data sampling rate window. The window shifts to the right with increasing velocities, i.e. at lower impeller speeds (26 –52 cm/s) the bias seems to be the smallest between 25 –50 Hz while for higher velocities (1.05 – 2.79 m/s) the minimum in the bias seems to be found between 75 – 125 Hz. For all speeds the bias becomes independent of the sampling rate beyond 200 Hz. However, as the data acquisition rate increases, the number of photon counts registered by a detector decreases and therefore the resolving capability of the detector deteriorates. Hence, there seems to be an inherent upper limit on the data sampling rates fixed by the resolving capability of the detectors. Given that, the lower limit on the sampling frequency seen from Figure 5-22 would seem to correspond to the desired minimum frequency below which the dynamic bias effects become important. That one should anticipate such limits is shown later theoretically.

5.2.5.2 Determination of Optimal Data Acquisition Rate

Based on the reconstructed particle trajectories the azimuthal velocity of the particle has been computed using the existing CARPT algorithms (Degaleesan, 1997). The variation of the nondimensional azimuthal velocity (V_{θ}/V_{tip}) with sampling frequencies, for different impeller tip speeds, is shown below in Figure 5-23 and is similar in nature to Figure 5-22. Ideally, the estimated nondimensional velocities must be equal to 1. The figure suggests that at all data acquisition rates and for all impeller speeds the velocity is underestimated. The bias in the velocity is found to be minimum in a certain optimal sampling window. The bias at lower sampling rates is found to become higher with the increase in impeller speeds. Beyond a certain sampling rate (200 Hz) the bias seems to be independent of the sampling rate.

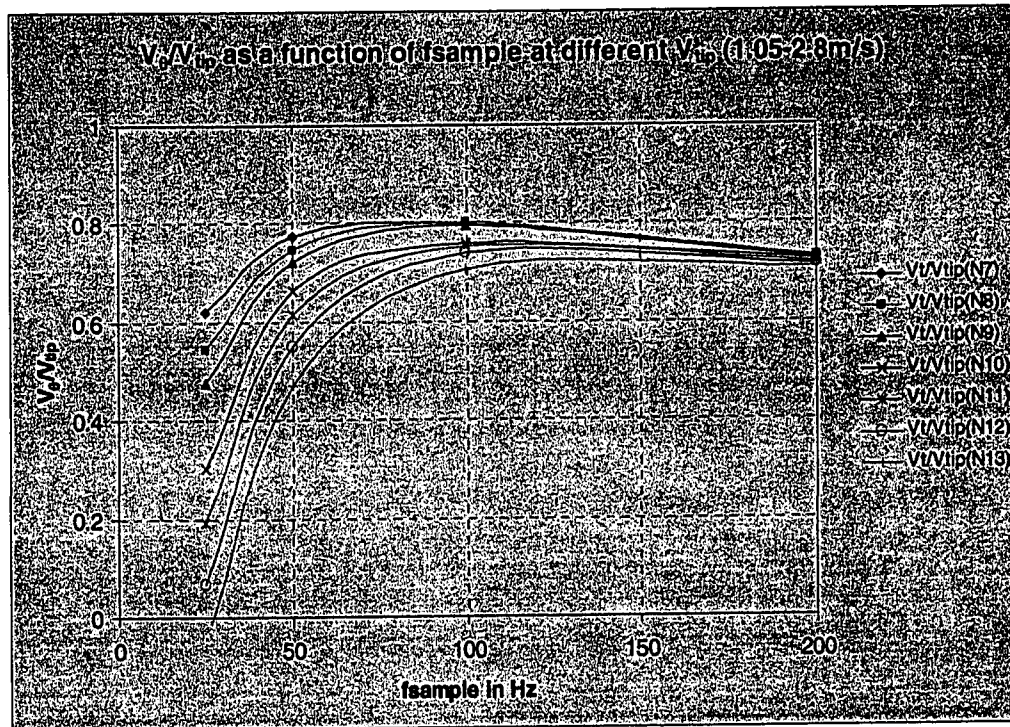


Figure 5-23. Variation of Estimated V_e/V_{tip} vs Data Sampling Rate ($V_{tip} = 1.05 - 2.79$ m/s)

The estimates of the bias shown above incorporate the contribution from the statistical fluctuations due to the nature of the photon emission process. The different contributions to the bias observed can be thought of as shown below in Figure 5-24. In the current experiment the medium was quiescent and hence the final data are corrupted only by the static bias and the dynamic bias. Subtracting the static bias contribution from the velocity estimates suggests that the dynamic bias is of the order of 14 – 30 % (with increasing velocities). This would seem to be a considerable loss of information due to the dynamic bias effects.

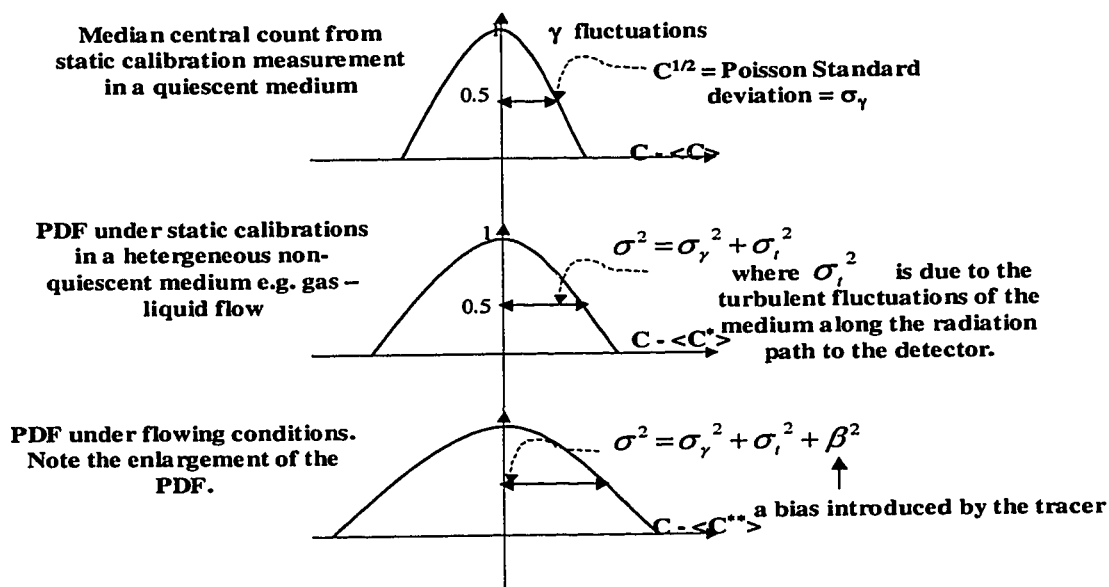


Figure 5-24. Errors in CARPT due to Nature of Experimental Technique

5.2.5.3 Limits on Data Sampling Rates

The optimum sampling frequency to capture a certain velocity is seen to be bounded between a f_{\min} and a f_{\max} . The f_{\min} is the smallest frequency with which one needs to sample the data to ensure that the dynamic count at a certain location is as close as possible to the static count registered at that point. This criterion will ensure that the fluid velocities will be captured reasonably accurately. This minimum frequency is therefore determined by the following relationship:

$$\frac{\text{abs}(C^{\text{dynamic}}(x_2, y_2, z_2) - C^{\text{static}}(x_2, y_2, z_2))}{\sqrt{C^{\text{static}}(x_2, y_2, z_2)}} \ll 1 \quad (5-10)$$

The f_{\max} is the maximum frequency with which one can sample the data beyond which the statistical nature of the emission process makes it meaningless to acquire photons. An estimate of this maximum frequency can be obtained as follows:

$$V_x = \frac{\Delta x}{\Delta t} \quad (5-11)$$

$$1/\Delta t = \frac{V_x}{\Delta x} \quad (5-12)$$

Now the LHS will be maximum when V_x is maximum and Δx is minimum. The maximum V_x is the maximum velocity one is expecting in the system. The smallest displacement one can measure is the resolution of the system in that direction. Now an estimate of Δx is given in (Chaouki et. al., 1997) as:

$$\Delta x = \frac{1}{(S\sqrt{C})} \quad (5-13)$$

$$C = \frac{\Gamma_D R_{source}}{f_s} \quad (5-14)$$

where R_{source} is the source strength in disintegrations per second, $\Gamma_D = v\phi\epsilon T$ and S is the sensitivity of the system. From the above we get:

$$f_{s\ max} = V_x S \sqrt{\frac{\Gamma_D R_{source}}{f_{s\ max}}} \quad (5-15)$$

Therefore we estimate the maximum sampling frequency as:

$$f_{s\ max} = (\Gamma_D R_{source})^{1/3} (V_x S)^{2/3} \quad (5-16)$$

Now, V_x is the maximum velocity we wish to be able to capture, R_{source} is known and S is a complex function of the detector arrangement (Γ_D), relative location of the tracer in the column with respect to the detector arrangement and several other factors (Roy, 2000). An estimate of S is obtainable from Roy (2000) where the distributions of S for different detector configurations and locations of tracers are given. The maximum mean sensitivities seem to be of the order of 3.39 %/mm. The fact that S and V_x are functions of position i.e. (x, y, z) suggests that the appropriate sampling frequency f_s would also be a function of (x, y, z) . But estimates of the maximum allowable sampling frequency can be made by using the sensitivity calculated at the point where the maximum velocities are expected for a particular detector and tracer arrangement. For the stirred tank set-up this maximum velocity is expected at the impeller tip which is near the column center. These calculations predict a maximum sampling frequency of 600 Hz whose order of magnitude is comparable to the maximum sampling rate observed experimentally.

At lower frequencies error due to the statistical nature of the photon emission process would be lower than at higher frequencies. Hence, the lower estimate obtained experimentally can be thought of as a reasonable estimate of the desired frequency for data acquisition. The above analysis allows us to anticipate that there would be an upper limit on the sampling frequency as we see from the experimental results reported in Sections 5.2.5.1 and 5.2.5.2 where beyond 120 Hz the velocities start deviating from the plateau..

5.2.5.4 Simulated Effect of Sampling Rate

Based on the details of the numerical scheme outlined in Section 5.2.4 some preliminary simulations are reported below in Figure 5-25. A circular trajectory similar to the experimental trajectory was fed into the Monte Carlo simulations. The particle was assumed to be moving at 1.0 m/s along this circular trajectory. A raw count file was generated from the Monte Carlo simulation corresponding to different sampling rates. A plot of this counts vs distance of tracer from detector #1 is shown below in Figure 5-25. It is seen that as the data sampling rate is increased more and more points are picked up by the detector. With the increase in the data sampling rate the calibration map looks closer and closer to the one with a single curve similar to the static calibration map (Figure 5-17). These results are encouraging given that the simulations shown below were performed without accounting for the statistical fluctuations of the photon emission process.

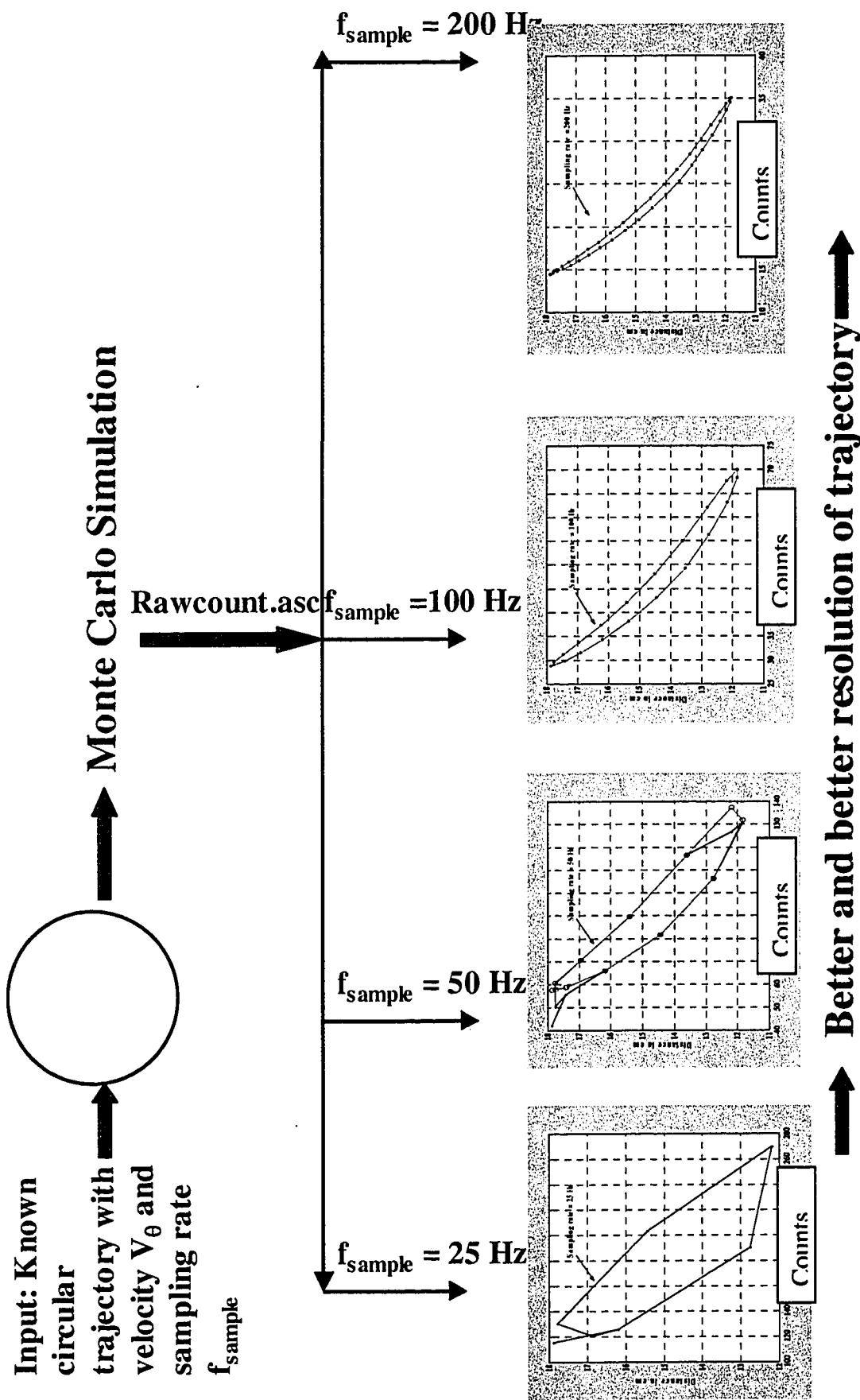


Figure 5-25. Simulated Dynamic Distance vs Count Map for Detector #1

The dynamic bias effect has been quantified experimentally. The experimental results suggest that an optimal sampling frequency window exists. Further the appropriate sampling frequency would seem to differ from region to region in the reactor depending on local flow conditions. This would suggest that CARPT data should be acquired at the highest experimentally possible sampling frequency. Then the data must be reprocessed at different optimal frequencies in different zones based on a physical understanding of the flow being investigated. The preliminary results obtained from the numerical simulations are very encouraging. This will enable us to develop the ability to estimate f_{optimal} “*a priori*” for any reactor configuration to capture V_{desired} accurately. This will be of considerable use when the CARPT technique has to be implemented in large industrial reactors where performing such experimental studies is both cumbersome as well as time consuming. In the following section the errors in estimating the Eulerian information from the reconstructed trajectories and errors due to tracer not following the flow faithfully (refer section 5.1) are discussed in detail.

Chapter 6

Eulerian Flow Field Estimation from Particle Trajectories: Numerical Experiments

6.1 Introduction

In this chapter we investigate in detail the errors in estimating the Eulerian information from the reconstructed trajectories (error of type 2), and errors due to tracer particle not following the flow faithfully (error of type 3) using simulations. Errors in reconstructing trajectories from detector signals have been studied extensively (Larchi et. al., 1997; Roy et. al., 2001; Chapter 5, Sections 5.1, 5.2, Rammohan, 2000b and Rammohan et. al., 2001c). On the other hand little work has been performed in quantifying the errors of type (2) and (3) mentioned above. Several factors such as tracer size, data sampling rate, Eulerian grid used for the recovery process, etc. may affect the magnitude of errors of type (2) and (3). It is very difficult to perform a controlled CARPT experiment where each of these parameters is systematically varied and its influence on the recovered Eulerian information is studied. As an alternative, in this work, a CARPT experiment is numerically simulated to evaluate the parametric sensitivity of the Eulerian recovery process. This study attempts to provide an estimate of the magnitude of the error of type (2) and of type (3) through some numerical experiments with the focus on stirred tank type flow.

The approach adopted in this chapter is based on simulation of the Eulerian flow field in the system of interest. A single particle is then introduced in such a stationary flow field and particle motion (trajectory) within the domain is simulated numerically. The simulated particle trajectory data is then fed into CARPT processing programs (Devanathan et. al., 1990), which extract the Eulerian mean velocities and the turbulent kinetic energy. The error of type 2, i.e. the error introduced by the CARPT processing programs, is then quantified by comparing the original Eulerian mean velocities and turbulent kinetic energy with the corresponding Eulerian quantities estimated from the

Lagrangian trajectories by the CARPT processing programs. A preliminary quantification of the error of type (3), i.e. the inability of the tracer particle to follow the flow, is attempted by estimating the flow following capability of a large and heavy tracer and of neutrally buoyant tracers ranging in diameter from $150\mu\text{m}$ to $2,300\mu\text{m}$.

6.2.0 Details of the Simulations

6.2.1 Eulerian Flow Field Simulations

In a stirred tank reactor very large velocity gradients exist in the axial direction near the impeller blades (Rammohan et. al., 2001b). Hence, in these regions the flow following capability of the tracers of finite size will be severely tested. Further, in this region the CARPT processing issues like the size of the grid used, the sampling frequency of the trajectory data and particle occurrence statistics are critical. It is therefore important to select an appropriate model problem, which retains these key features but still allows fast evaluation of the desired parameters.

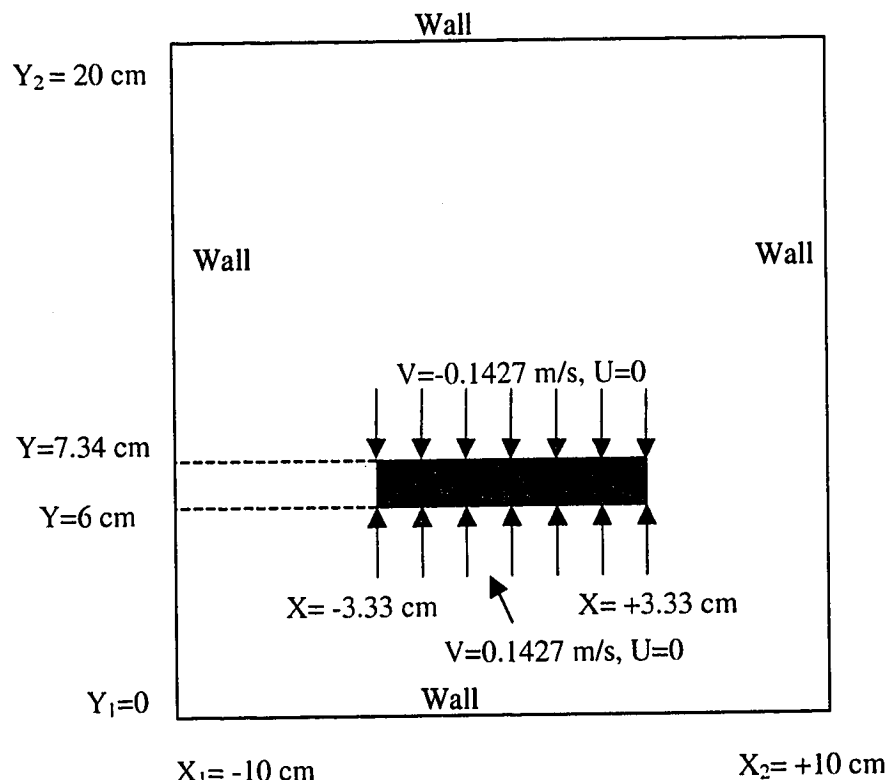


Figure 6-1(a). 2-D Domain with Boundary Conditions

A two – dimensional geometry shown in Figure 6-1(a) was therefore chosen as it enables a quick evaluation of the sensitivity of the numerical simulations to a whole range of numerical parameters like: the grid used for the Eulerian simulations, the grid used for converting the Lagrangian information to the Eulerian information (Rammohan, 2000a) and turbulence model used for the random walk of the tracer particle (Discrete Random walk (DRW) or Continuous Random Walk (CRW)) model.

6.2.1.1 Computational Model

The geometry studied was a 2-D square of width 20.0 cm (from –10.0 cm to 10.0 cm) and height 20.0 cm (refer to Figure 6-1(a)). This geometry and the dimensions were selected to closely mimic the experimental system of Rammohan et. al. (2001a). A Cartesian grid was used and the velocities were solved for in the Cartesian co-ordinate system. A standard k - ε turbulence model was used. The following equations were solved using the commercial CFD code FLUENT4.5:

$$\frac{\partial}{\partial x_i}(\rho u_i \phi) = \frac{\partial}{\partial x_i} \left[\Gamma_\phi \frac{\partial \phi}{\partial x_i} \right] + S_\phi \quad (6-1)$$

where $\phi=1, U$ and V yields the equations of continuity and momentum transport in the x direction and y direction, respectively. In equation (6.1) S_ϕ is the source term, which is zero for the continuity equation and contains the contributions from the pressure term and the viscous terms for the momentum transport equations. Thus the term Γ_ϕ $\phi=U$ and V it is equal to:

$$\Gamma_\phi = \mu_{eff} = \frac{C_D k^2}{\varepsilon} + \mu \quad (6-2)$$

where k is the turbulent kinetic energy and ε is the rate of dissipation. The transport equations for the turbulent kinetic energy and the dissipation rate are as follows:

$$\frac{\partial}{\partial x_i}(\rho u_i k) = \frac{\partial}{\partial x_i} \frac{\mu_t}{\sigma_k} \frac{\partial k}{\partial x_i} + G_k - \rho \varepsilon \quad (6-3)$$

and

$$\frac{\partial}{\partial x_i}(\rho u_i \varepsilon) = \frac{\partial}{\partial x_i} \frac{\mu_t}{\sigma_\varepsilon} \frac{\partial \varepsilon}{\partial x_i} + C_{1\varepsilon} \frac{\varepsilon}{k} G_k - C_{2\varepsilon} \rho \frac{\varepsilon^2}{k} \quad (6-4)$$

where G_k is the generation of k and is given by

$$G_k = \mu_t \left(\frac{\partial u_j}{\partial x_i} + \frac{\partial u_i}{\partial x_j} \right) \frac{\partial u_j}{\partial x_i} \quad (6-5)$$

The turbulent viscosity is related to k and ε by the expression

$$\mu_t = \rho C_\mu \frac{k^2}{\varepsilon} \quad (6-6)$$

The coefficients $C_{1\varepsilon}$, $C_{2\varepsilon}$, C_μ , σ_k and σ_ε are empirical constants which are taken to have the following values (Launder and Spalding, 1974):

$$C_{1\varepsilon} = 1.44, C_{2\varepsilon} = 1.92, C_\mu = 0.09, \sigma_k = 1.0 \text{ and } \sigma_\varepsilon = 1.3 \quad (6-7)$$

The top, bottom and sides of the column were modeled as no slip boundaries with standard wall functions (Launder and Spalding, 1974) used for the turbulent kinetic energy and dissipation rate.

The flow generated by the Rushton turbine was simulated by fixing the liquid velocities in the live cells (that is the flow was not solved for in these cells) in the domain corresponding to the location of the top and bottom surface of the impeller. Simulations were carried out to simulate the flow generated with impeller tip speed of 1.0 m/s. The knowledge of the pumping number and impeller dimensions may be used to estimate the liquid velocity at the top and bottom horizontal surfaces of the impeller swept volume as:

$$V_y = \frac{2}{\pi} (Fl) ND \quad (6-8)$$

where Fl is the pumping number of the Rushton turbine, N is impeller rotation speed and D is the impeller diameter.

The “stirred tank” was divided into three blocks in the horizontal direction and three blocks in the vertical direction. The details of a typical grid (G_3) used in the simulation are shown in Figure 6-1(b). A higher order discretization scheme, QUICK was used for the simulation to capture the circulating flow structure accurately. A convergence criterion of $1e-4$ (ratio of current residuals to residual after first iteration) was set for each variable (i.e. pressure, velocities etc.). The convergence of the simulations was further ensured by verifying the mass balance (within 0.1%) in

various control volumes in the tank. Four different grids were examined for the Eulerian simulations: 42 X 42 (G_1), 82 X 82 (G_2 , $N_{impeller} = 12$, $\Delta y_{impeller} = 1.0$ mm), 82 X 82 (G_3 , $N_{impeller} = 24$, $\Delta y_{impeller} = 0.5$ mm), and 162 X 162 (G_4 , $N_{impeller} = 72$, $\Delta y_{impeller} \sim 0.15$ mm). The grids differ not only in the total number of cells but also the distribution of cells in certain regions of the system. For instance $N_{impeller} = 12$ implies there are 12 cells in the impeller zone and $\Delta y_{impeller} =$ grid spacing in the vertical direction in the impeller zone.

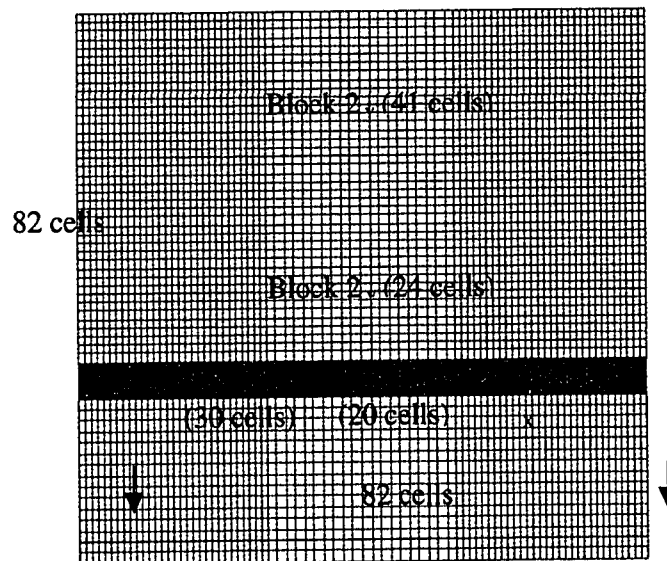


Figure 6-1(b). Details of Grid

Detailed comparisons of the mean velocities and the turbulent kinetic energies (obtained with the different grids) were made at selected locations in the stirred tank ($X_1 = -4.5$ cm, $X_2 = 4.5$ cm, $Y_1 = 4.5$ cm and $Y_2 = 11.5$ cm). Some of these comparisons are shown in Figure 6-2. Figure 6-2(a) compares the horizontal velocity at the vertical plane $X = -4.5$ cm obtained with the grids G_2 , G_3 and G_4 . The results obtained with G_3 and G_4 are seen to compare very well (within 1%) right from the bottom to the top of the tank, while the comparison of the velocities computed with G_3 and G_4 with those obtained with G_2 is good (within 1%) in the bottom portion of the tank and in the impeller zone but not in the top portion of the tank where the differences can be up to 10%. Figure 6-2(b) reveals that in the impeller region there is a difference in the computed turbulent kinetic energies of nearly 10% between grids G_3 and G_4 (with G_2 underestimating the kinetic energy by almost 50%). It has been

reported earlier (Ranade et. al., 2001, Bartels et. al., 2000) that obtaining grid independence for the turbulent kinetic energy with the standard $k - \epsilon$ turbulence model is very difficult. Hence, for these simulations the observed difference of upto 10% will be regarded as acceptable. Therefore the results obtained with grids G_3 and G_4 can be considered acceptable for our purposes. It must be emphasized that a fine grid in the impeller region is essential to obtain grid independent results. The results obtained with G_3 are used for all subsequent simulations.

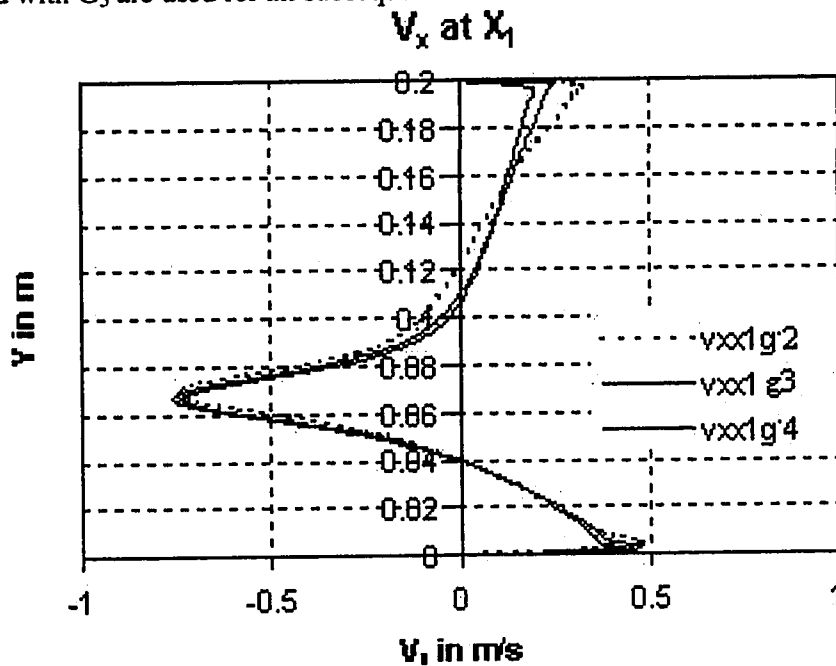


Figure 6-2(a). Grid Dependence of Horizontal Velocities

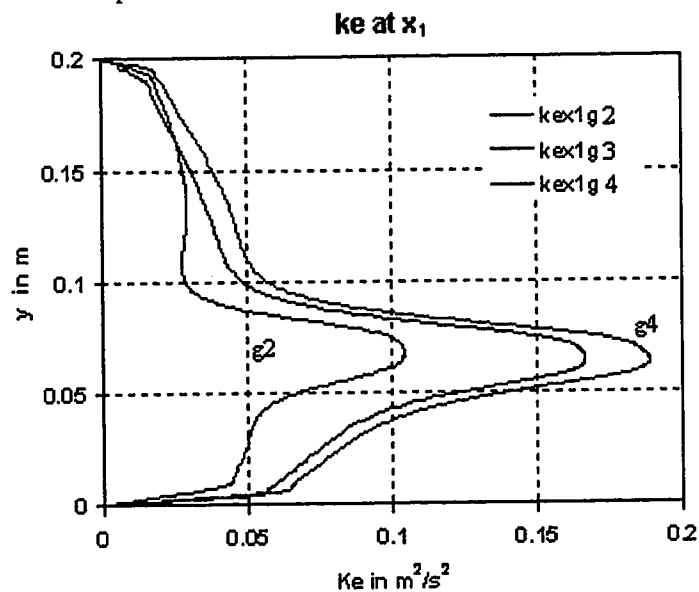


Figure 6-2(b). Grid Dependence of Turbulent Kinetic Energy

6.2.2 Lagrangian Particle Tracking

Once the grid independent Eulerian flow field was computed, the Lagrangian particle tracking was initiated. The particle tracking simulations were decoupled from the Eulerian fluid velocity calculations. A tracer particle of size 10 μm and the same density as the liquid (1,000 kg/m^3) was chosen for the simulations to quantify the error of type 2, i.e. to determine the inaccuracies involved in inferring the flow field from Lagrangian trajectories. For each condition ten independent particle injections were made. The initial conditions for these ten injections are listed in Table 6-1.

Table 6-1. Initial Conditions for Particle Tracking Algorithm

S.N.	X_{particle} (m)	Y_{particle} (m)	V_x (m/s)	V_y (m/s)
1	-0.057	.078	-.448	.105
2	.0522	.078	.457	.090
3	-0.07	.034	.0226	-.175
4	.0017	.134	-.003	-.328
5	.0856	.026	-0.067	-.216
6	-0.081	.068	-.2713	.0178
7	.074	.165	-.128	.148
8	-0.005	0.073	-0.095	-.143
9	-0.037	.068	-.854	-.001
10	-0.092	.014	.107	-.164

For each injection 1 million particle occurrences were obtained. Hence, for each condition ten million particle occurrences were obtained in all. The resulting particle trajectories covered the whole space. The equations used for computing the particle trajectory are:

$$\frac{du_p}{dt} = F_D(u - u_p) + g_x(\rho_p - \rho)/\rho_p + F_x \quad (6-9)$$

where $F_D(u - u_p)$ is the drag force per unit particle mass and F_D is given by:

$$F_D = \frac{18\mu C_D Re}{\rho_p d_p^2 24} \quad (6-10)$$

Here, u is the fluid phase instantaneous velocity at the particle location, u_p is the particle velocity, μ is the molecular viscosity of the fluid, ρ is the fluid density, ρ_p is the density of the particle, and d_p is the particle diameter. Re stands for the relative particle Reynolds number, which is defined as:

$$Re = \frac{\rho d_p |u_p - u|}{\mu} \quad (6-11)$$

The drag coefficient, C_D , is a function of the relative particle Reynolds number of the following general form:

$$C_D = a_1 + a_2/Re + a_3/Re^2 \quad (6-12)$$

where the a 's are constants specified over a wide range of Reynolds number by Morsi and Alexander (1972).

6.2.2.1 Modeling Unsteady Drag Terms

It should be mentioned that the above equations account only for the steady state drag forces and do not currently account for the unsteady drag terms like the added mass, pressure gradient, the Basset memory integral term, lift force etc. This added mass or virtual mass force is given by:

$$F_{VM} = \frac{1}{2} \frac{\rho}{\rho_p} \left(\frac{Du}{Dt} - \frac{du_p}{dt} \right) \quad (6-13a)$$

where

$$\frac{D}{Dt} = \frac{\partial}{\partial t} + \vec{u} \cdot \vec{\nabla} \quad (6-13b)$$

$$\frac{d}{dt} = \frac{\partial}{\partial t} + \vec{u}_p \cdot \vec{\nabla} \quad (6-13c)$$

The added mass term, pressure gradient term and the Basset force term are negligible for the neutrally buoyant tracer and for the heavy tracer (Sangani et. al., 1991; Michaelidis, 1997; Lovalenti and Brady, 1995; Mei et. al., 1995). Another important force, which acts on the tracer particle, is the lift force or the lateral migration force.

All these forces like the virtual mass force, pressure gradient force, Basset force and lift force; originate from one single integral (Patankar et. al., 2001) which represents the hydrodynamic surface force exerted by the background fluid on a particle immersed in the fluid. This integral is represented as follows:

$$F_{hydrodynamic} = \oint [-PI + T] \bullet ndT \quad (6-14)$$

where P is the pressure field, T is the shear stress tensor and n is the unit normal to the surface of the particle. For simple linear flows this integral can be regarded as a superposition of the different forces listed above. For complex non-linear flows this linear superposition is not necessarily valid (Gavze, 1990) and the rigorous approach to account for the hydrodynamic forces requires the solution of this integral over the particle surface (given by equation (5.30)). To compute this integral rigorously, one would need to know the velocity gradients along the surface of the particle, which requires the base flow field information at very small length scales, like those obtained from direct numerical simulations by Patankar et. al. (2001). In the absence of such detailed computations most of the researchers performing Euler – Lagrange simulations assume, as done in this work as well, that the linearity assumption holds and account separately for each of the different components of the hydrodynamic force by models developed through analytical calculations for simpler flows.

Formulation of the lift force has been studied by a number of researchers like Saffman (1965), Rubinow and Keller (1961), Ho and Leal (1974), Mclaughlin (1991) and Mei (1992). In the current study the lift force was not accounted for in the calculations with the neutrally buoyant tracer (except for studies with $d_p=250\mu\text{m}$). It is expected that neglecting the lift force will introduce errors in the computed trajectories especially for finite tracer sizes ($> 800\mu\text{m}$, Sommerfeld, 1990). Hence, the errors predicted by the current study must be interpreted as a conservative estimate. For the non-neutrally buoyant tracers, both the modified Saffman lift force (Mei, 1992) and Rubinow and Kellers' (1961) rotational lift force have been accounted for. The formulation used for these forces is given below:

$$\frac{F_{saffman}}{m_p} = \frac{9.67}{\pi d_p} \frac{\sqrt{\mu_c \rho}}{\rho_p} [iV_{ry} - jV_{rx}] \frac{\omega_{cz}}{\sqrt{|\omega_{cz}|}} \quad (6-15a)$$

where V_r is the relative velocity between the fluid (u_f) and the particle (u_p) given by:

$$V_r = (u_{fx} - u_{px})\mathbf{i} + (u_{fy} - u_{py})\mathbf{j} \quad (6-15b)$$

and ω_c is the vorticity of the continuous phase, which for a 2-D flow will have only the component perpendicular to the x - y plane:

$$\omega_c = \omega_{cx}\mathbf{i} + \omega_{cy}\mathbf{j} + \omega_{cz}\mathbf{k} = \nabla \times \bar{u}_c \quad (6-15c)$$

$$m_p = \frac{\pi}{6} d_p^3 \rho_p \quad (6-15d)$$

Mei, 1992 proposed a correction factor to the Saffman force to extend its validity to a larger range of shear Reynolds numbers. This correction factor, obtained empirically, is given by:

$$\begin{aligned} F_{modified} / F_{saffman} &= \left(1 - 0.3314 \beta^{1/2}\right) \exp\left(\frac{-Re_p}{10}\right) + 0.3314 \beta^{1/2} \quad Re_p \leq 40 \\ &= 0.0524 (\beta Re_p)^{1/2} \quad Re_p > 40 \end{aligned} \quad (6-15e)$$

$$\beta = \frac{d_p}{2|u - u_p|} |\omega_c|, \quad 0.005 < \beta < 0.4$$

where β is a measure of the local shear. The Rubinow and Keller's correction to Saffman's lift force is given by:

$$\frac{F_{R-K}}{m_p} = \frac{3\rho}{4\rho_p} (-iV_{ry} + jV_{rx}) \omega_z \quad (6-16)$$

All of the above additional forces were incorporated through user-defined subroutines in FLUENT 4.5.

6.2.2.2 Modeling Effect of Fluid Turbulence on the Tracer Particle

In the current work, since the fluid turbulence is modeled for by the $k-\varepsilon$ model, and not solved for exactly, its effect on the particle also has to be modeled. It is reported (Crowe et. al., 1998) that only for particles much smaller than the Kolmogorov length scale (i.e. $d_p/\eta \ll 1$) of the base flow the fluid turbulence will have a direct impact on the particle. For larger particles the turbulence effect will be through the macroscopic base flow. For the impeller tip speed in the current work the smallest

$d_p/\eta \sim O(1)$. Hence, in the current work the effect of turbulence is modeled by two different random walk models: the discrete random walk model (Gosman and Ionnides, 1981) and the continuous random walk model (Thompson, 1988). Both of these models assume that the fluid velocity consists of two components, the mean and the fluctuation:

$$u_f = \overline{u_f} + u'_f \quad (6-17)$$

a) **Discrete Random Walk Model:** In the discrete random walk (DRW) model, or “eddy lifetime” model, the interaction of a particle with a succession of discrete fluid phase turbulent eddies is simulated. Each eddy is assumed to be characterized by: a) Gaussian distributed random velocity fluctuation and b) a time scale τ_e . The values of the fluctuating velocity component, which prevail during the lifetime of the turbulent eddy, are sampled by assuming that they obey a Gaussian probability distribution function, so that

$$u'_f = \zeta \sqrt{u'^2} \quad (6-18)$$

where ζ is a normally distributed random number, and the remainder of the R.H.S. is the local root mean squared velocity (r.m.s) of the velocity fluctuations. Since the turbulent kinetic energy is known at each point in the flow, these values of the r.m.s fluctuating components can be obtained (assuming isotropy) as:

$$\sqrt{u_f'^2} = \sqrt{v_f'^2} = \sqrt{w_f'^2} = \sqrt{2k/3} (3-D) = \sqrt{3k/4} (2-D) \quad (6-19)$$

The characteristic life time of an eddy is defined as either a constant:

$$\tau_e = 2T_L \quad (6-20a)$$

or as a random variation about T_L :

$$\tau_e = -T_L \log(r) \quad (6-20b)$$

where r is a uniform random number between 0 and 1 and T_L is the Lagrangian eddy time scale given by $T_L = 0.15 \frac{k}{\varepsilon}$. The option of random calculation of τ_e yields a more realistic exponential decay of the correlation function unlike the constant eddy lifetime model, which yields a linear decay. The particle is assumed to interact with the fluid phase eddy over this eddy lifetime. When the eddy lifetime is reached, a new

value of the instantaneous velocity is obtained by applying a new value of ζ . In the current studies the DRW model is used with the variable eddy lifetime model.

b) Continuous Random Walk (CRW) Model:

In the CRW model, the instantaneous fluid phase velocity is obtained through the solution of the Langevin equation (Thompson, 1988; Pope, 1994):

$$dU_f^{instantaneous}(x_p(t), y_p(t)) = -\frac{1}{\rho_f} \frac{\partial \langle p \rangle}{\partial x_i} dt - \left(\frac{1}{2} + \frac{3}{4} C_o \right) \frac{\langle \epsilon \rangle}{k} (U_f^{instantaneous} - \overline{U_f}) dt + \left(\frac{2U_f U_f'}{T} \right)^{\frac{1}{2}} dw \quad (6-21)$$

Here the first two terms on the R.H.S. of the equation (6-21) are the deterministic force acting on the fluid particle and the third term is the random or Brownian force acting on the fluid particle. dw is a Weiner random process with zero mean and variance $\langle dw^2 \rangle = dt$. The use of the Langevin equation for modeling the fluid turbulence is expected to give a more realistic representation of the fluid correlation function. The CRW model is however computationally more demanding. In the current study both DRW and CRW are evaluated.

6.2.2.3 Details of Trajectory Calculation

Once the particle velocities are obtained, the particle locations can be obtained by integrating the following equation:

$$\frac{dx}{dt} = u_p \quad (6-22)$$

The integration can be done by either simple Euler's method or by a fourth order Runge Kutta scheme. The Euler's integration technique was used to obtain the particle locations from their velocities. The time step for integration was specified through a step length factor (λ). This factor is roughly equivalent to the number of time steps required to traverse the current continuous phase control volume. For the current calculations a step length factor of twenty was specified for each cell. A larger step length factor would mean a more accurate calculation of the trajectory but at the cost of obtaining trajectory information over shorter time periods. When solving the force balance equations on the particle, the fluid velocities were obtained at the tracer location by interpolating the fluid velocities in that computational cell. Using cell

centered fluid velocities was avoided, as this could introduce considerable error if the computational cell were large enough to expect gradients in the fluid velocity within that cell. For each tracer injection a maximum of one million time steps were specified.

6.2.2.4 Estimating the Eulerian Flow Field from Lagrangian Trajectories Using CARPT Processing Programs

The Lagrangian simulations yield the Lagrangian history of the particle's motion in the entire domain. Some snapshots of typical particle trajectories are shown in Figures 6-3(a) – 6-3(d). Figure 6-3(a) shows the evolution of the particle trajectory over the first three seconds of its motion. The particle was introduced just above the impeller tip ($X = -5.66$ cm, $Y = 7.8$ cm) with the fluid velocity at that point. The radial flow coming out of the Rushton turbine is seen to drag the particle radially for a short distance (~ 2 cm) before lifting the particle upwards. The particle is then seen to follow the different vortices in the upper half of the tank and lands up near the impeller tip at the R.H.S. of the tank after 3 seconds ($X \sim 3$ cm, $Y \sim 8.0$ cm). The snapshots of the particle motion over the next few intervals of time are shown in Figures 6-3(b) – 6-3(d) where the particle is seen to follow both the upper and lower recirculating structures. The particle trajectory when plotted over a period of 200 seconds (corresponding to 1 million particle occurrences) was observed to cover the entire space of the tank. Once the particle trajectories are obtained from the Lagrangian simulations they are fed into the CARPT processing programs. The CARPT program then divides the entire tank into a number of voxels (3-D) or pixels (2-D). The division of the tank into compartments can be uniform or non-uniform. Non-uniform division follows the multi-zone philosophy used in FLUENT4.5 (refer to Figure 6-1(b)). Here the whole tank is divided into a certain number of blocks in the horizontal and the vertical direction. The starting co-ordinate and ending co-ordinate for each of these blocks need to be specified and the number of cells in each of these blocks has to be input to the CARPT processing programs. The particle velocities are computed from the instantaneous positions, and the velocity is assigned to the midpoint of the two successive instantaneous positions.

$$U\left(\frac{X_1 + X_2}{2}, \frac{Y_1 + Y_2}{2}\right) = \frac{(X_2 - X_1)}{\Delta t} \quad (6-23)$$

$$V\left(\frac{X_1 + X_2}{2}, \frac{Y_1 + Y_2}{2}\right) = \frac{(Y_2 - Y_1)}{\Delta t} \quad (6-24)$$

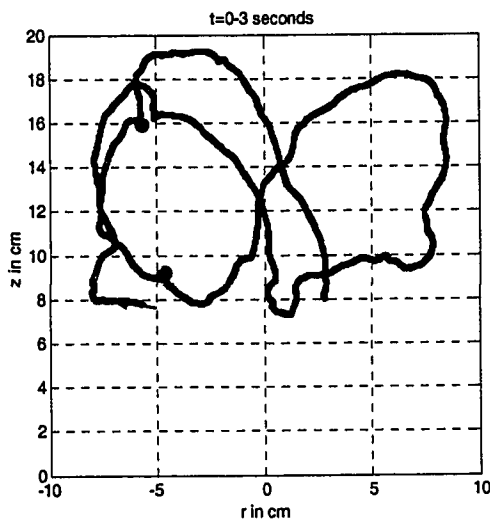


Figure 6-3(a)

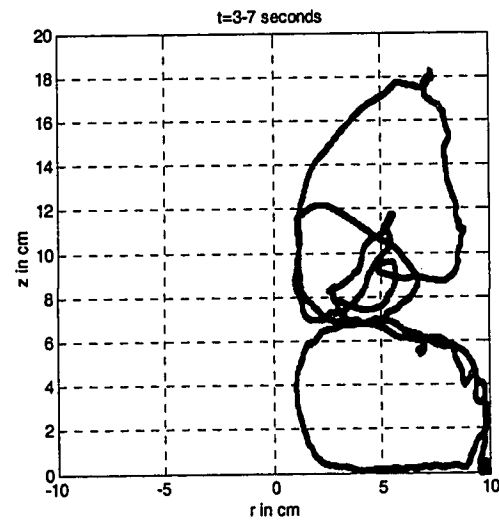


Figure 6-3(b)

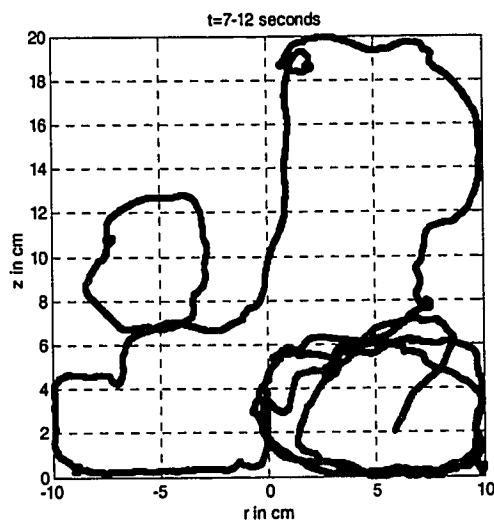


Figure 6-3(c)

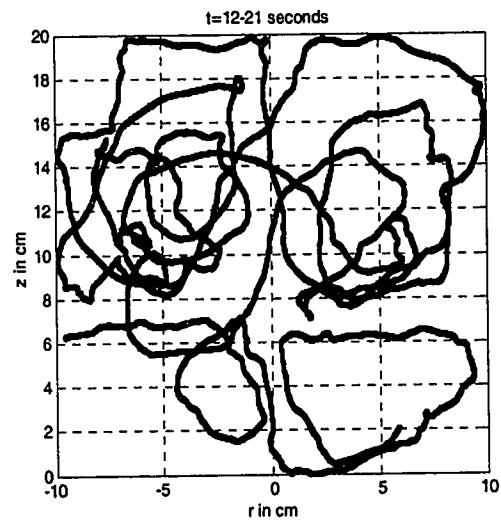


Figure 6-3(d)

Figure 6-3. Snapshots of Simulated Particle Trajectories at Different Instants in Time

The voxel/pixel to which this midpoint belongs is identified and the computed instantaneous velocity is assigned to that cell. This procedure is repeated for each of the ten million occurrences and the corresponding velocities are assigned to the different cells. Using the instantaneous velocities associated with each cell, the

corresponding ensemble averaged velocities and turbulent kinetic energies are computed for each cell (Rammohan, 2000a).

$$\langle U(x, y) \rangle = \frac{1}{N} \sum_{n=1}^N U_n(x, y) \quad (6-25)$$

$$U'(x, y) = U(x, y) - \langle U(x, y) \rangle \quad (6-26)$$

$$\langle U'(x, y) V'(x, y) \rangle = \frac{1}{N} \sum_{n=1}^N U'_n(x, y) V'_n(x, y) \quad (6-27)$$

These ensemble averaged quantities, which are assumed equivalent to the time averaged quantities (flow field assumed to be stationary and ergodic), were then compared with the Eulerian velocities obtained in Section 6.2.1.1.

6.3.0 Results and Discussion

In Figure 6-4(a) the ensemble averaged velocity vector plot in the entire tank is shown. It can be seen that the Eulerian estimates from the Lagrangian trajectories can capture the classic flow structure reported in stirred tanks equipped with Rushton turbines. Further the contours of the turbulent kinetic energy distribution are shown in Figure 6-4(b). The steps in simulating a typical CARPT experiment are summarized in Figure 6-5. The sensitivity to the different numerical parameters in a particle tracking simulation is discussed in the following sections.

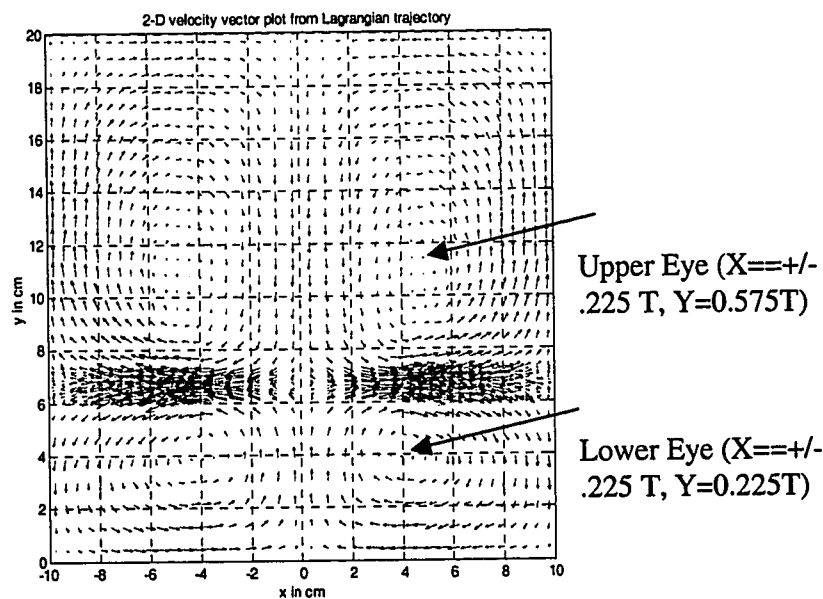


Figure 6-4(a). 2 -D Vector Plot from Lagrangian Trajectories

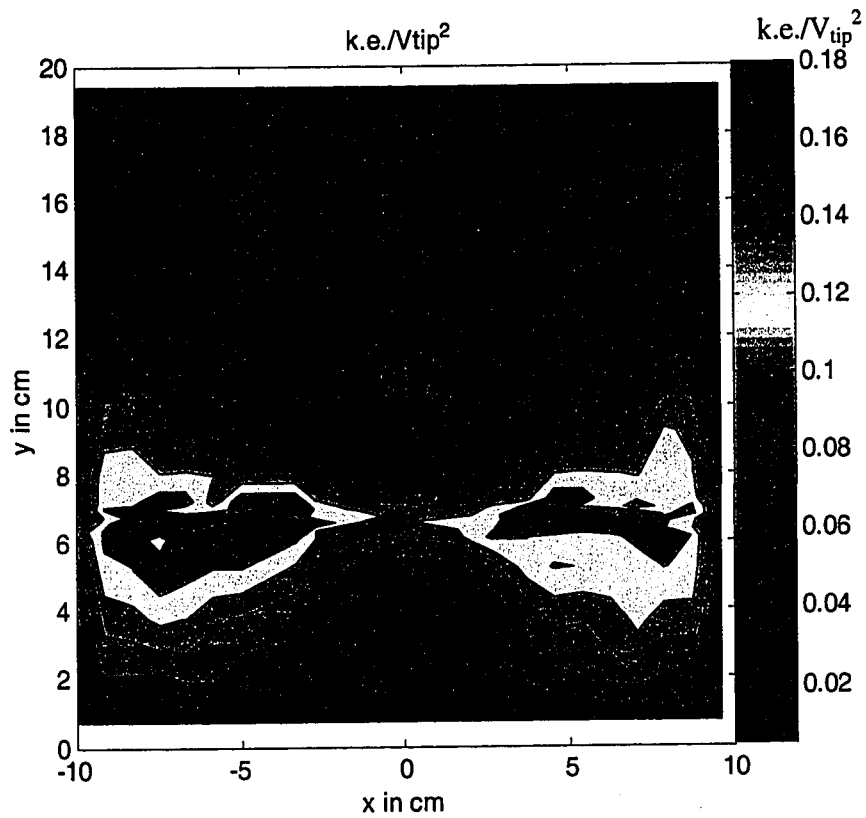


Figure 6-4(b). 2 – D Contour of Turbulent Kinetic Energy from Lagrangian Trajectories

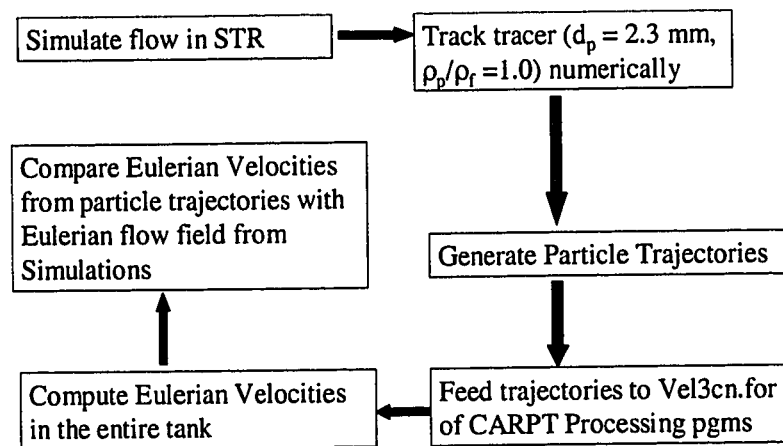


Figure 6-5. Sequence of Numerical Experiments

6.3.1 Role of Lift Force

The role of the lift force was examined by implementing the modified Saffman shear lift force (6.15a) and the Rubinow – Keller’s rotational lift force (6.16). The Saffman shear lift force introduces a lateral force component, which is one order of magnitude larger than the Rubinow – Keller’s rotational lift force. In this section the influence of the lift force on Eulerian estimates, obtained from a large, heavy and from a large neutrally buoyant tracer, is examined. The effect of the lift force on the large and heavy tracer is shown in Figure 6-6. It can be seen from Figure 6-6(a) and Figure 6-6(b) that in the regions of large base flow velocities the horizontal velocities obtained with the lift force are higher (10%) than without the lift force, while the vertical velocities obtained with the lift forces are lower (36%) than those obtained without the lift forces. The differences in velocities with and without lift forces ($E^{rel} = 6-11\%$) are higher for the heavier particle than for the neutrally buoyant tracer. From Figure 6-6(c) it can be seen that the estimate of the turbulent kinetic energy obtained in the impeller region with the lift force is higher than the estimate obtained without the lift force ($E^{max} = 100\%$, $E^{rel} = -11\%$) and is closer to the original Eulerian values.

The estimates for velocities and turbulent kinetic energies obtained with and without lift forces for the neutrally buoyant tracer are shown in Figure 6-7. It must be emphasized that the current lift force models are expected to underestimate the lateral force component (as explained in Section 6.2.1). Hence, it can be seen (Figures 6-7(a) and 6-7(b)) that the velocities remain almost unchanged with/without lift forces ($E^{rel} = -0.75\%$ to 3% , $E^{max} = 37 - 44\%$). The estimates of the turbulent kinetic energies are also seen (Figure 6-7(c)) to remain relatively unchanged with/without lift forces ($E^{rel} = 3.7\%$, $E^{max} = 33\%$). Hence, the errors predicted by the current study for the neutrally buoyant particle must be interpreted as underpredicting the true error.

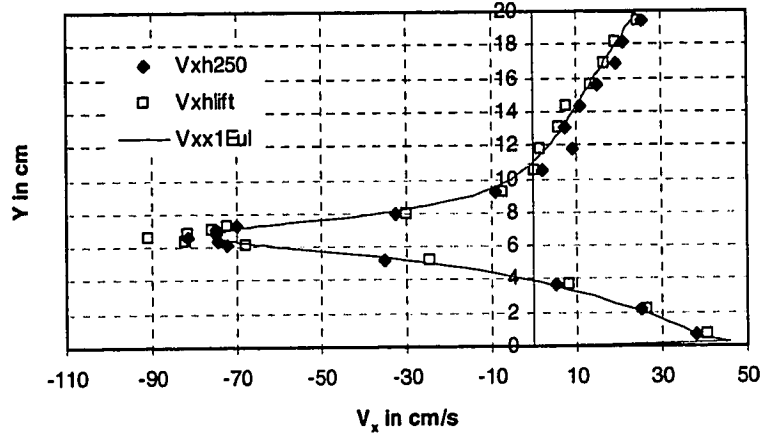


Figure 6-6(a). Sensitivity of Lagrangian Estimate of Horizontal Velocity Obtained with Heavy Tracer with Lift Force

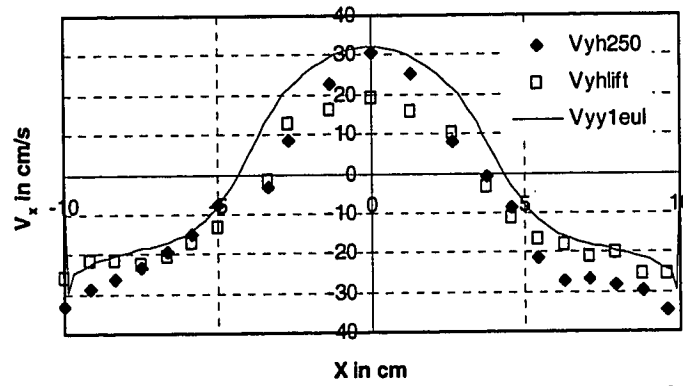


Figure 6-6(b). Sensitivity of Lagrangian Estimate of Vertical Velocity Obtained with Heavy Tracer with Lift Force

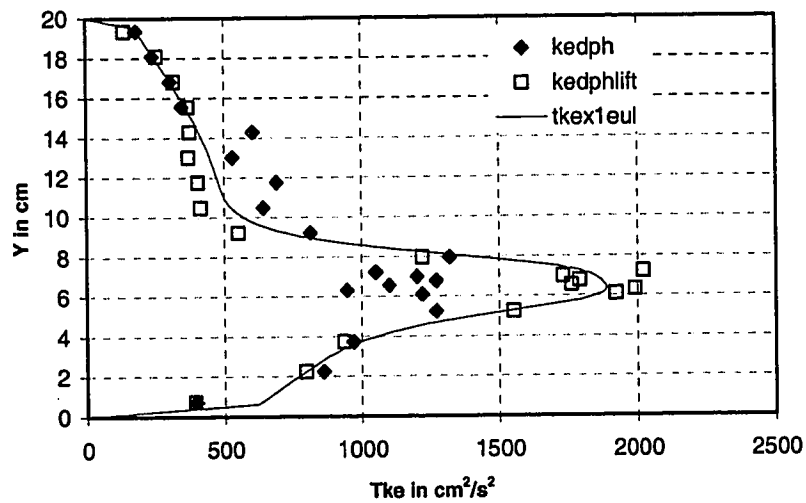


Figure 6-6(c). Sensitivity of Lagrangian Estimate of Turbulent Kinetic Energy Obtained with Heavy Tracer with Lift Force

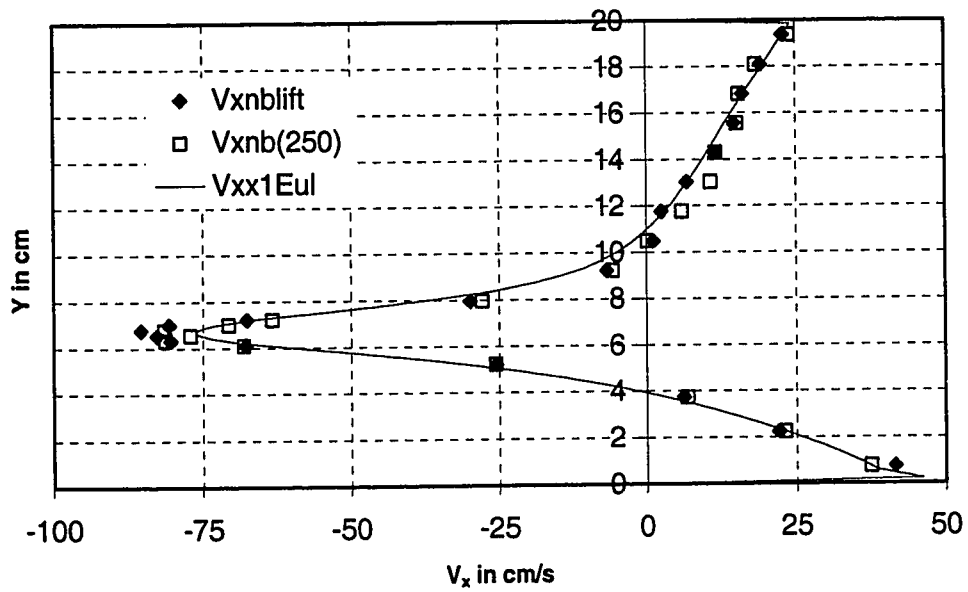


Figure 6-7(a). Sensitivity of Horizontal Velocities Obtained with Neutrally Buoyant Tracer with and without Lift Force

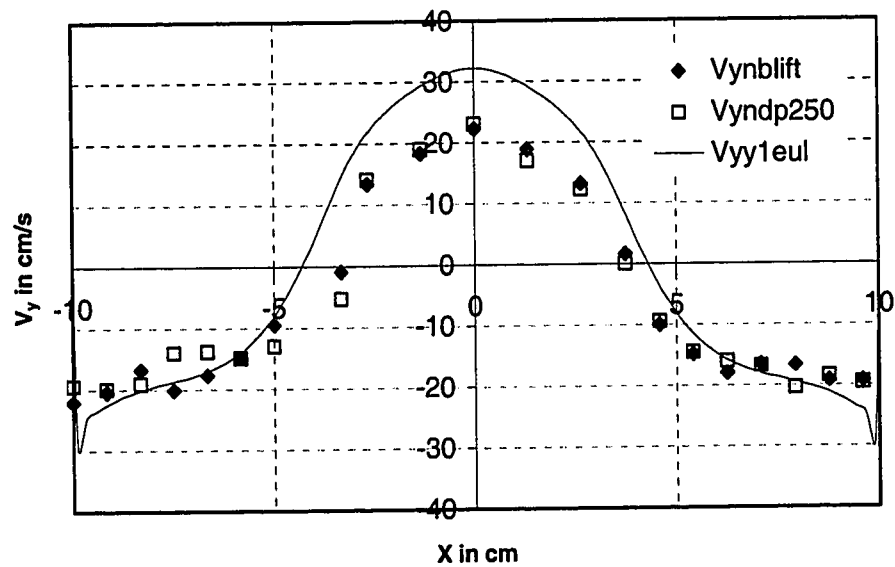


Figure 6-7(b). Sensitivity of Vertical Velocities Obtained with Neutrally Buoyant Tracer with and without Lift Force

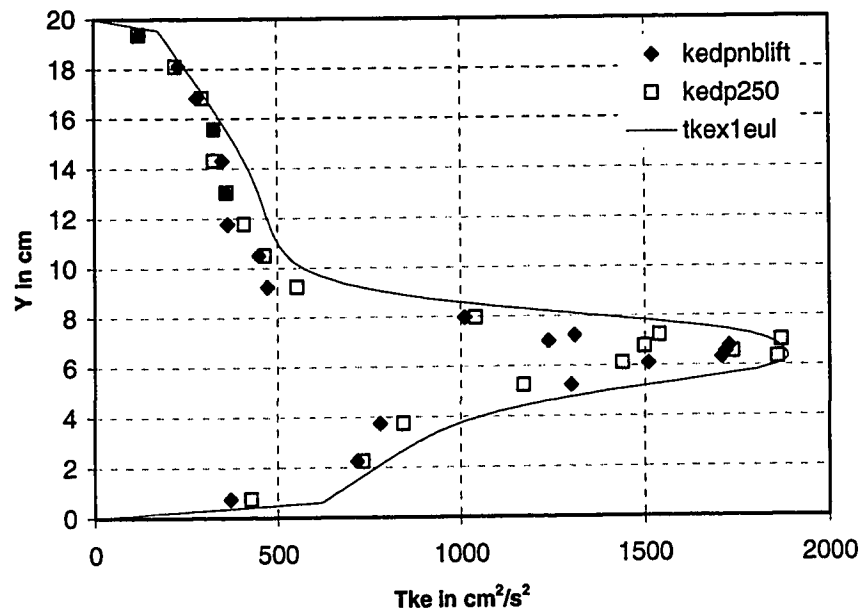


Figure 6-7(c). Sensitivity of Turbulent Kinetic Energy Obtained with Neutrally Buoyant Tracer with and without Lift Force

6.3.2 Sensitivity to Random Walk Model

The sensitivity of the recovery process to the turbulence model used (DRW or CRW) is shown in Figure 6-8 where the predictions of the horizontal velocity, based on two different turbulence models, are more or less the same from the engineering point of view ($E^{rel} = -1.6\%$) with the maximum difference between CRW and DRW $E^{max} = 22\%$. A similar trend is seen in Figure 6-8(b) for the comparison of predictions of turbulent kinetic energy variations ($E^{rel} = -.05\%$, $E^{max} = 19.2\%$). This indicates that the recovery process is not very sensitive to the turbulence model used. Some Lagrangian measures like the Return Time Distribution, circulation time distribution and mean return times (Roberts et. al., 1995) were also used to evaluate the sensitivity to the different numerical parameters. Figure 6-9(a) illustrates that the Return time distributions (RTD) are insensitive to the turbulence models used, which implies that the trajectories are not sensitive to the turbulence models used. The mean return times are also comparable. In Figure 6-9(b) the RTD's for the lighter and heavier particle are compared. There is a slight difference in the RTD's but the means appear

comparable indicating that the heavier and larger particle can be expected to follow the mean trajectories as well as the light particle.

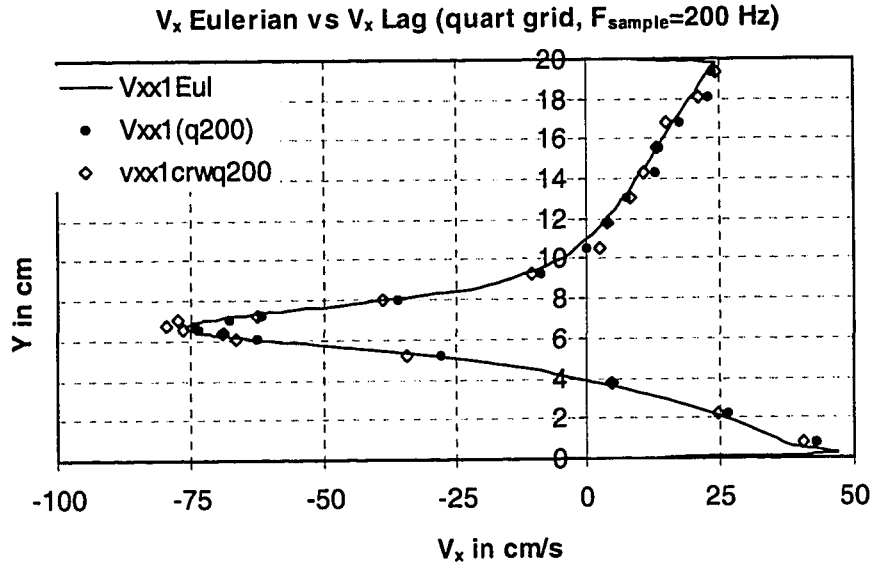


Figure 6-8(a). Velocity Estimates Obtained with DRW and CRW Turbulence Models

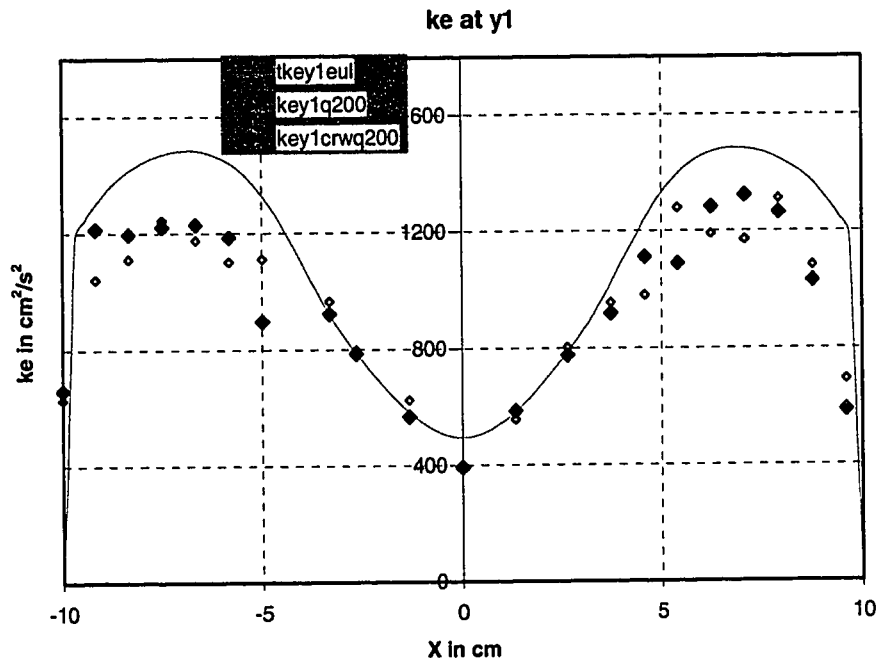


Figure 6-8(b). Turbulent Kinetic Energy Estimates Obtained with DRW and CRW Turbulence Models

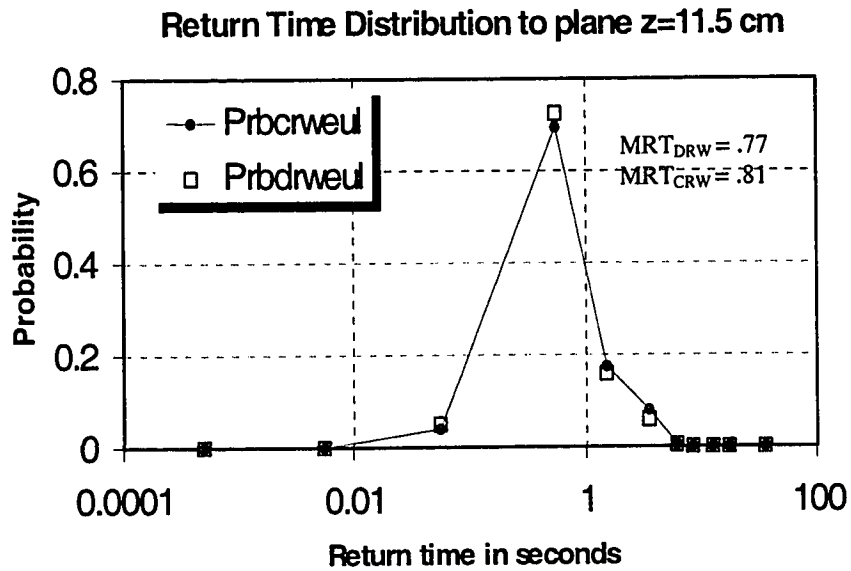


Figure 6-9(a). Sensitivity of Return Time Distributions to Turbulence Model (CRW or DRW)

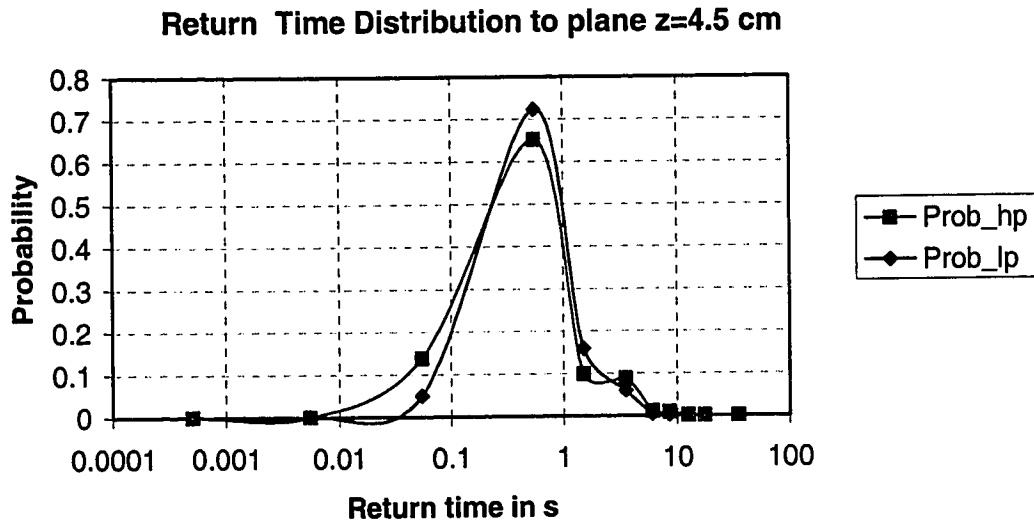


Figure 6-9(b). Sensitivity of Return Time Distributions to Particle Density

6.3.3 Effect of CARPT Grid

The effect of CARPT grid size on the Eulerian recovery process is intimately connected with the particle occurrence statistics per cell. With larger number of particle occurrences per cell one would expect better convergence of the ensemble averaged quantities given by equation (6.25) and (6.27). The particle occurrence per cell is expected to increase with increase in grid size but this lowers the spatial resolution of the ensemble-averaged quantities. Further, with higher data sampling rates one would expect to be able to capture the finer scales of particle motion, which would imply that one could expect better particle statistics with finer grids if data acquisition rates were sufficiently high. However, very high data sampling rates in practical implementation of CARPT result in a low signal to noise ratio and therefore greater position error is introduced. Hence, in this section we try to identify the smallest grid size and the minimum data sampling rate that will minimize the errors associated with the Eulerian recovery process.

Five different gridding schemes were used for recovering the Eulerian information from the Lagrangian trajectories. One grid was exactly the same as the grid used for Eulerian CFD simulations. The others were coarser or finer than the Eulerian grid. The details of these schemes are summarized in Table 6-2. The effect of CARPT grid size is shown in Figure 6-10. The use of a very fine grid results in considerable spatial fluctuations in the ensemble average velocity profiles due to a lower number of particle occurrences per cell. This results in non-converging ensemble averages in some cells (e.g. in a cell near the impeller the number of particle occurrences were as low as 250 for the finest grid as against at least 4000 occurrences observed in one of the coarser grids). It is apparent that a certain minimum fractional occurrence per cell must be maintained to ensure convergence of ensemble averages. For this system this minimum fractional occurrence (ratio of number of occurrences per cell to total occurrences in the entire domain) was found to be 100 occurrences per cell out of a total of 1 million occurrences in the entire domain (or 100 parts per million, p.p.m.). It was also found that the fractional occurrence distributions depended more on the velocity distribution in the domain of interest rather than on the total duration of the particle tracking simulation.

Table 6-2. Gridding Schemes Used for Recovering Eulerian Information from Lagrangian Data

Grid Type	No. of Blocks	Cells per X block	Cells per Y block
Original_grid	$N_x=3, N_y=3$	Block1 _x =30, Block2 _x =20, Block3 _x =30	Block1 _y =15, Block2 _y =24, Block3 _y = 41
Quart_grid	$N_x=3, N_y=3$	Block1 _x =8, Block2 _x =5, Block3 _x =8	Block1 _y =4, Block2 _y =6, Block3 _y = 10
Half_grid	$N_x=3, N_y=3$	Block1 _x =15, Block2 _x =10, Block3 _x =15	Block1 _y =7, Block2 _y =12, Block3 _y = 20
Double_grid	$N_x=3, N_y=3$	Block1 _x =30, Block2 _x =40, Block3 _x =30	Block1 _y =15, Block2 _y =48, Block3 _y = 41
Unif_grid	$N_x=3, N_y=3$	82	82

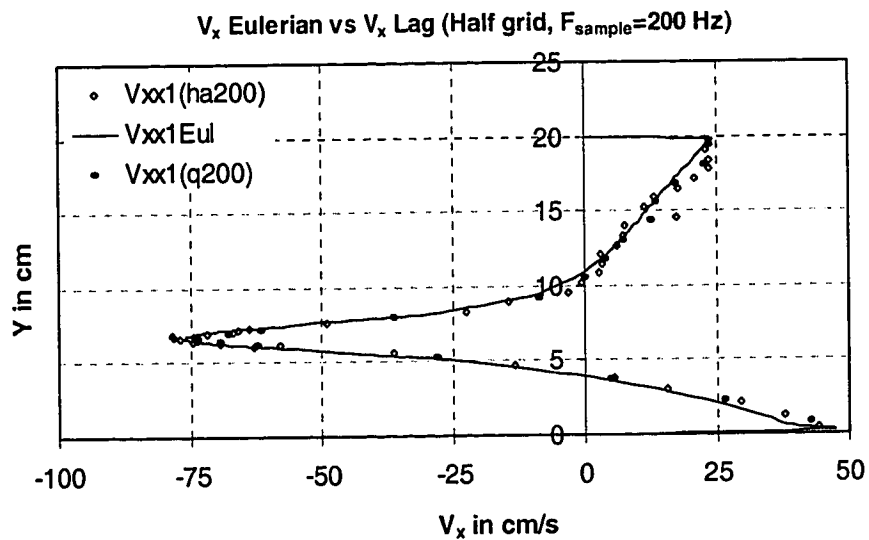


Figure 6-10(a). Comparison of Horizontal Velocities

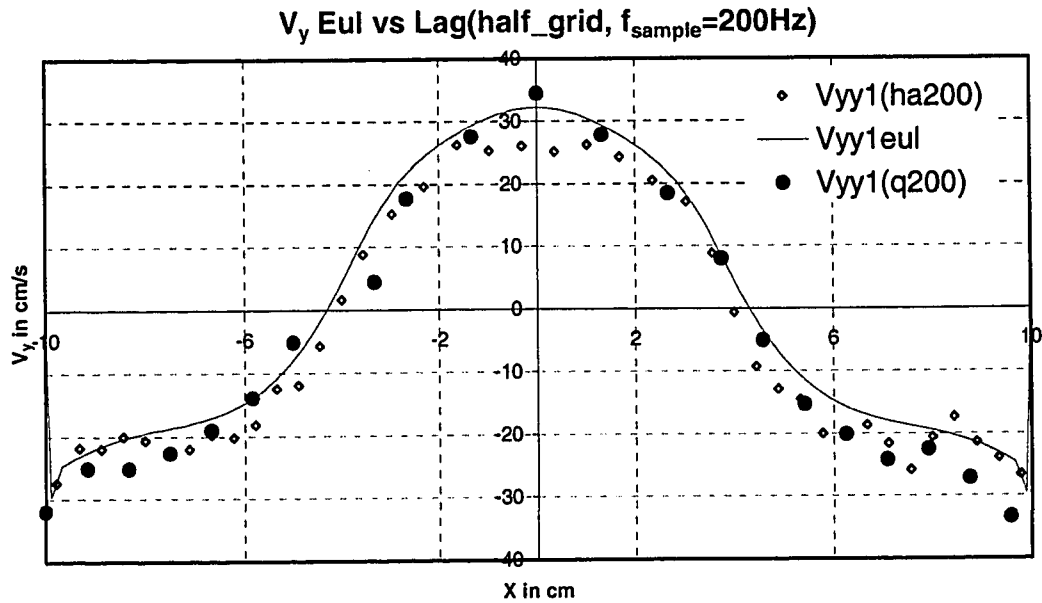


Figure 6-10(b). Comparison of Vertical Velocities

Figure 6-10. Comparison of Eulerian Velocity (Eul) with Lagrangian Estimates Obtained with Half (ha200) and Quarter (q200) Grids

This implies that performing longer experiments to obtain larger total occurrences (with at least 1 million total occurrences) may not really contribute to increasing the fractional occurrence in some cells. However, before the fractional occurrence criterion is used we must ensure that there are sufficient occurrences in each cell and in accomplishing this, the longer experiment definitely helps. It is also seen in Figure 6-11 that with increasing the sampling frequency for a fixed grid size the fractional particle occurrence distribution initially increases and then reaches a plateau beyond a certain minimum sampling frequency. For a finer grid (shown in Figure 6-11(b)) while a similar trend is observed, the fractional occurrence however is consistently below the minimum fractional occurrence (100 p.p.m.) for all frequencies. Hence, if the data acquisition rate is above this minimum data sampling rate then the fractional occurrence distribution will not be a function of the duration of the CARPT run or the data acquisition rate. This result can be generalized as follows:

$$\text{No. of occurrences per cell} = k(\Delta x_1)(\Delta x_2)(\Delta x_3) > N_{\text{critical}} (\text{function of application}) \quad (6-28)$$

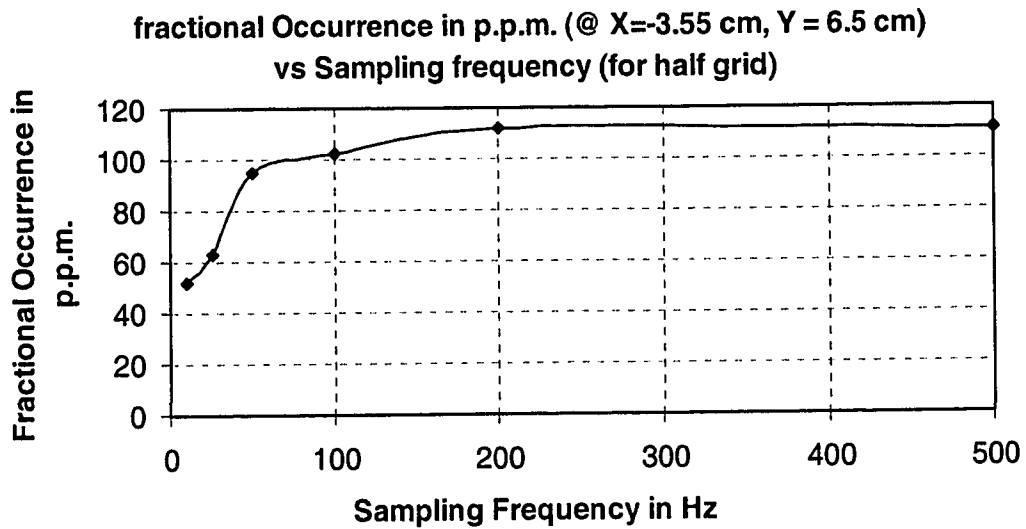


Figure 6-11(a). Variation of Fractional Occurrence with Sampling Frequency for half Grid

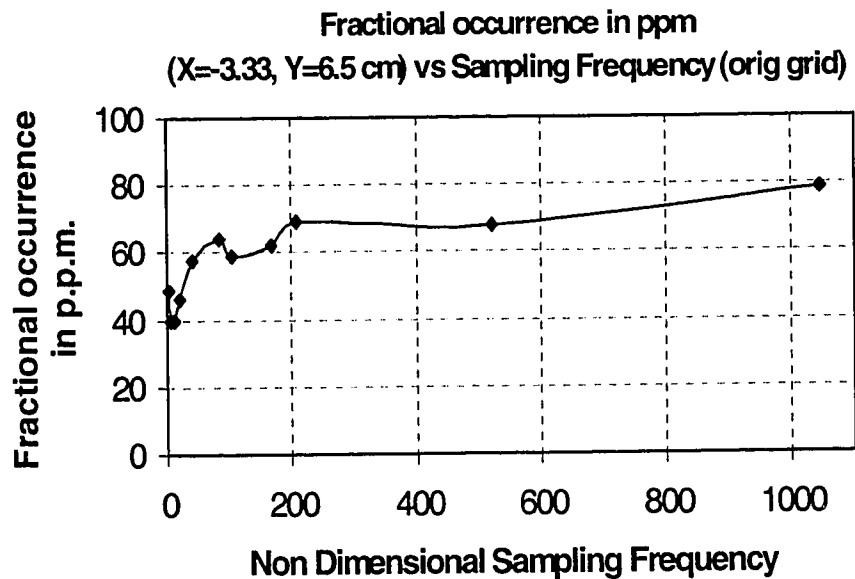


Figure 6-11(b). Variation of Fractional Occurrence with Sampling Frequency for Original Grid

The total occurrences in the reactor are:

$$\text{Total occurrences in the reactor} = kV_{\text{reactor}} \quad (6-29)$$

Therefore the fractional occurrence in a cell should be:

$$\text{Fractional Occurrence} = \frac{k(\Delta x_1)(\Delta x_2)(\Delta x_3)}{k V_{\text{reactor}}} \geq 100 \text{ p.p.m.} \quad (6-30)$$

If gridding were uniform in the three directions then from the above formulation we can find the minimum allowable grid size for estimating the Eulerian quantities from the Lagrangian trajectories as:

$$(\Delta x)_{\min} = (V_{\text{reactor}} * 100 \text{ p.p.m.})^{1/3} \quad (6-31)$$

In reality the gridding is non-uniform and there are constraints on spatial resolution in a certain direction depending on the physical situation. The above formulation still allows us to estimate the limiting uniform grid sizes. In all the above estimates we assume that a minimum of at least one million total occurrences of the particle is found in the reactor. With the coarser grids the mean velocity is recovered very well as shown in Figures 6-10(a) and 6-10(b). The errors associated with the Eulerian estimates have been quantified using the following formulae:

$$E(\langle G \rangle_{ij}) = \frac{\bar{G}_{\text{Eulerian}} - \langle G \rangle_{\text{Lagrangian}}}{\bar{G}_{\text{Eulerian}}} \times 100 \quad (6-32a)$$

$$\langle G \rangle_{ij} = \langle U(x, y) \rangle \text{ or } \langle V(x, y) \rangle \text{ or } \langle u'(x, y)u'(x, y) \rangle \quad (6-32b)$$

where equation (6.32a) quantifies the error associated with the estimate of an ensemble averaged quantity at one point. A relative mean error was defined as:

$$\bar{E}_j^{\text{rel}} = \frac{1}{N_x} \sum_{i=1}^{N_x} E(\langle G \rangle_{ij}) \quad \text{or} \quad \bar{E}_i^{\text{rel}} = \frac{1}{N_y} \sum_{j=1}^{N_y} E(\langle G \rangle_{ij}) \quad (6-32c)$$

respectively.

The maximum error is defined as:

$$E^{\max}(\langle G \rangle) = \max(E(\langle G \rangle)) \quad (6-32d)$$

It must be mentioned that in computing the mean errors and reporting the maximum errors, the points where the local base flow velocity is close to zero ($V_{\text{local}}/V_{\text{tip}} \sim O(10^{-2})$) were ignored. In these regions of low velocity the Eulerian estimates obtained from the Lagrangian trajectories are not reliable since the number of particle occurrences in these regions is very low. The inaccuracies in the Eulerian estimates in these regions are not a cause for concern since flow information in these regions is not vital in design except for identifying such regions. It has been shown

earlier (Rammohan et. al., 2001a) that CARPT can identify the location of such regions with reasonable accuracy.

Figure 6-10(a) shows the comparison of axial variation of the mean Eulerian horizontal velocity at $X_1 = -4.5$ cm with the Eulerian velocity extracted from particle tracking using grids half as fine ($V_{xx1ha200}$) and quarter as fine ($V_{xx1q200}$) as the original Eulerian grid. This figure demonstrates that the original Eulerian information for the mean velocity can be recovered very well from the Lagrangian trajectories and that the recovery is similar with the error from half coarse ($E^{rel} = -0.95\%$, $E^{max} = 26\%$) being slightly higher than the quarter coarse grid ($E^{rel} = -1\%$, $E^{max} = 16\%$). A similar trend is observed for the horizontal variation of the vertical velocity at $Y_1 = 4.5$ cm. The Eulerian mean velocities were obtained from the Lagrangian trajectories by resampling the trajectory information at 200 Hz (as against the 7000 samples generated per second of the simulation). The recovery of Eulerian information from Lagrangian trajectories was found to be insensitive to the sampling rates beyond 200 Hz as seen in Figures 6-12(a) and 6-12(b) with the half coarse grid and the original grid.

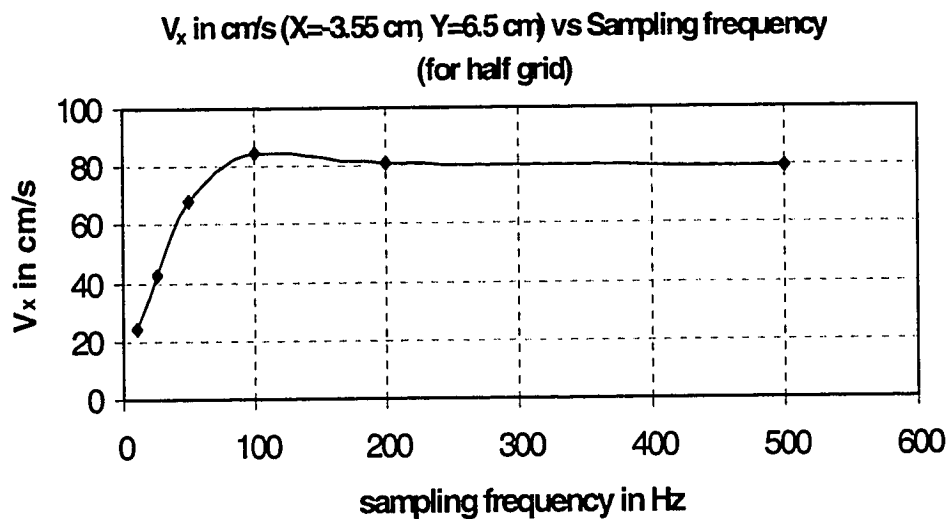


Figure 6-12(a). Variation of Horizontal Velocity with Sampling Frequency for Half Grid

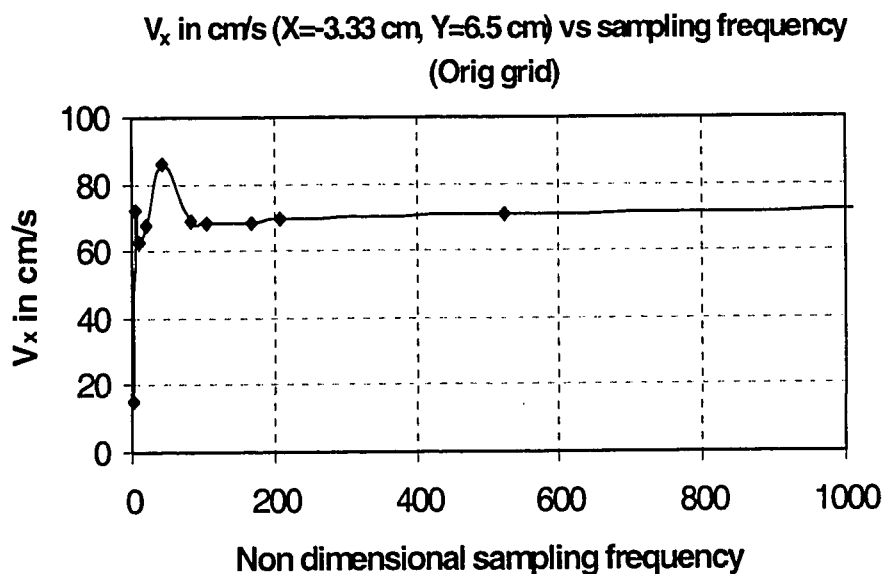


Figure 6-12(b). Variation of Horizontal Velocity with Sampling Frequency for Original Grid

The ability to recover the turbulent kinetic energy from the Lagrangian trajectories is shown in Figure 6-13. The axial variation of the turbulent kinetic energy at $X_1 = -4.5$ cm is somewhat captured with both the half fine ($E^{\text{rel}} = 4\%$, $E^{\text{max}} = 51\%$) as well as quarter fine grid ($E^{\text{rel}} = 4\%$, $E^{\text{max}} = 28\%$). A similar trend is observed for the horizontal variation of turbulent kinetic energy (half fine: $E^{\text{rel}} = 5\%$, $E^{\text{max}} = 49\%$; quarter fine grid: $E^{\text{rel}} = 12\%$, $E^{\text{max}} = 23\%$). The above comparison illustrates that a neutrally buoyant tracer particle of size $10 \mu\text{m}$ follows the motion of the fluid reasonably well. Furthermore, for effective estimation of the Eulerian information using the CARPT processing programs, the following criteria should be met: a) the appropriate grid size for estimating Eulerian quantities from Lagrangian trajectories should be selected based on the relationship proposed by equation (6.33), and b) the particle location must be sampled at least every 0.01 seconds (for the impeller tip speed of 1.0m/s) but more than 200 samples per second need not be acquired (where fractional occurrence is independent of sampling frequency, refer Figure 6-11).

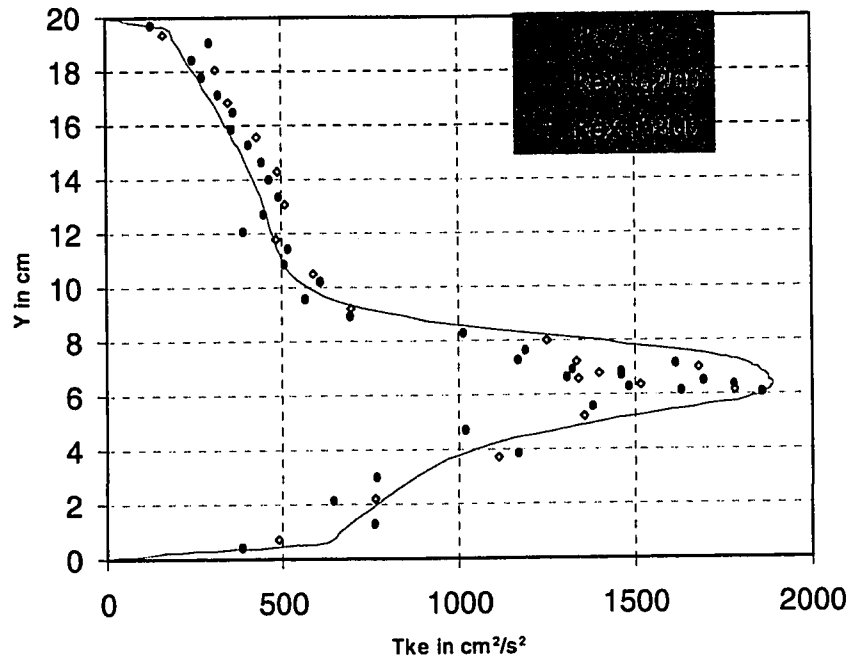


Figure 6-13(a). Comparison of Horizontal Variation of Turbulent Kinetic Energy Obtained with Quarter (q200) and Half (ha200) Grids at 200Hz

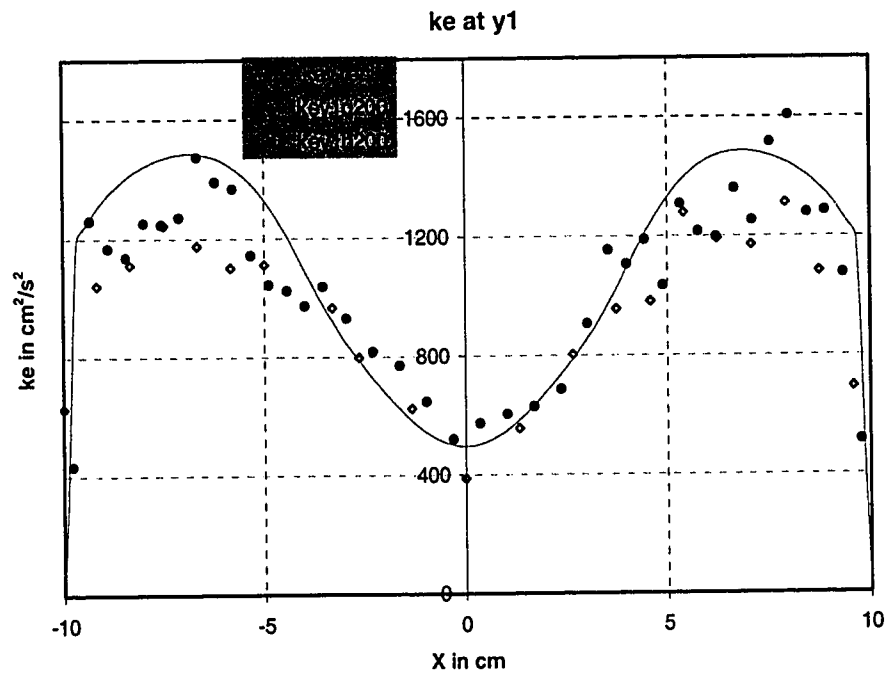


Figure 6-13(b). Comparison of Vertical Variation of Turbulent Kinetic Energy Obtained with Quarter (q200) and Half (ha200) Grids at 200Hz

This implies in general that the data must be sampled at least every $1/50^{\text{th}}$ of the process time scale or:

$$\frac{\tau_{\text{process}}}{\tau_{\text{sample}}} = \frac{\left(2 * \pi * r_{\text{impeller}} / V_{\text{tip}}\right)}{1 / f_{\text{sample}}} \gg 50 \quad (6-33)$$

Further studies are currently in progress to quantify in detail the relationship between the process time scale and the sampling time interval. These studies indicate that from a fluid dynamics consideration there is a certain minimum rate at which the particle trajectory information must be sampled. This study complements our earlier experimental findings (Chapter 5, Section 5.2, Rammohan et. al., 2001c) on the limits of the sampling frequency derived from a dynamic bias consideration. That study revealed that as the base flow velocity increases, the appropriate data sampling rate also increases, and recommended an optimum data sampling rate of 100 Hz for similar impeller tip speeds.

6.3.4 Effect of Particle Density and Size

The flow following capability of a larger (250 μm) and a much heavier ($\rho_p / \rho_f = 2.99$) tracer particle is shown in Figures 6-14 and 6-15. Figures 6-14(a) and 6-14(b) reveal that the larger and heavier particle can still follow the mean fluid motion reasonably well. The errors associated with the recovery for Figure 6-14(a) are, for half fine grid: $E^{\text{rel}} = 5.4\%$, $E^{\text{max}} = 67\%$ and for quarter fine grid: $E^{\text{rel}} = -8.8\%$, $E^{\text{max}} = 24\%$, respectively. The errors associated with the recovery for Figure 6-14(b) are, for half fine grid: $E^{\text{rel}} = 7.4\%$, $E^{\text{max}} = 71\%$ and for quarter fine grid: $E^{\text{rel}} = -18.6\%$, $E^{\text{max}} = 53\%$, respectively. The larger and heavier tracer filters the turbulent fluctuations of the fluid, as seen from Figure 6-15(a) (half fine grid: $E^{\text{rel}} = 7.8\%$, $E^{\text{max}} = 73\%$, quarter fine grid: $E^{\text{rel}} = 19.5\%$, $E^{\text{max}} = 100\%$) where the heavier particle misses almost 30% of the turbulent kinetic energy.

Figure 6-15(b) shows the ratio of the estimate of the computed turbulent kinetic energy from particle trajectories to the original turbulent kinetic energy at the impeller

tip for neutrally buoyant tracers of different diameters ranging from 150 μm to 2,300 μm .

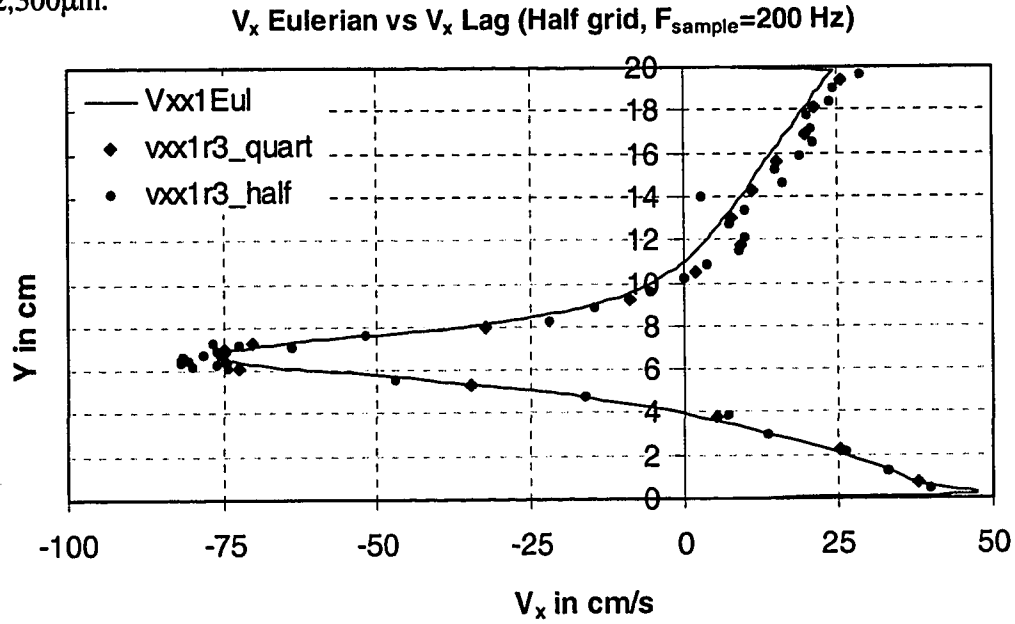


Figure 6-14(a). Horizontal Velocity Estimates Obtained with Dense and Large Particle on Quarter (r3_quart) and Half (r3_half) Grids

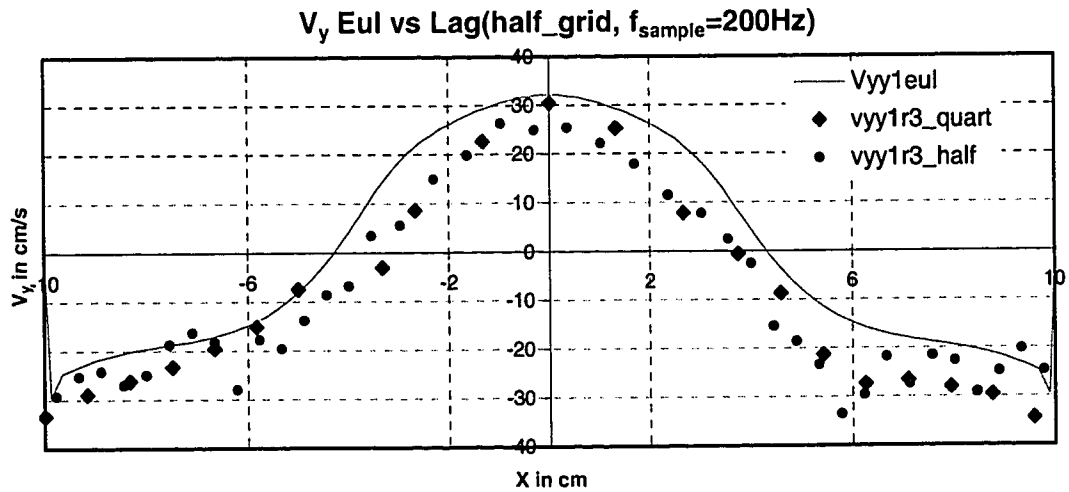


Figure 6-14(b). Vertical Velocity Estimates Obtained with Dense and Large Particle on Quarter (r3_quart) and Half (r3_half) Grids

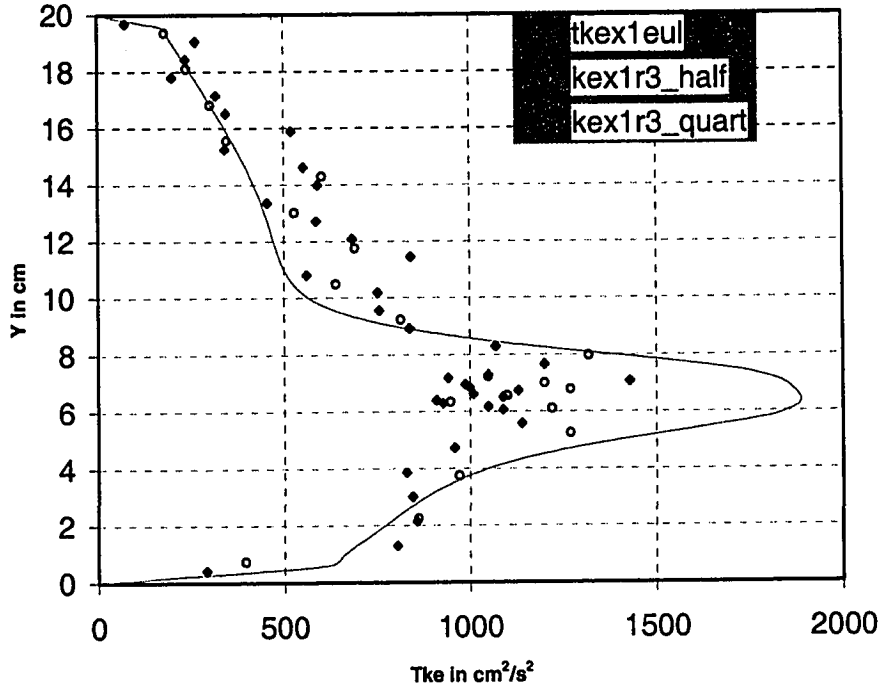


Figure 6-15(a). Sensitivity of Lagrangian Estimates to Density of Tracer (r3 = Heavier Tracer)

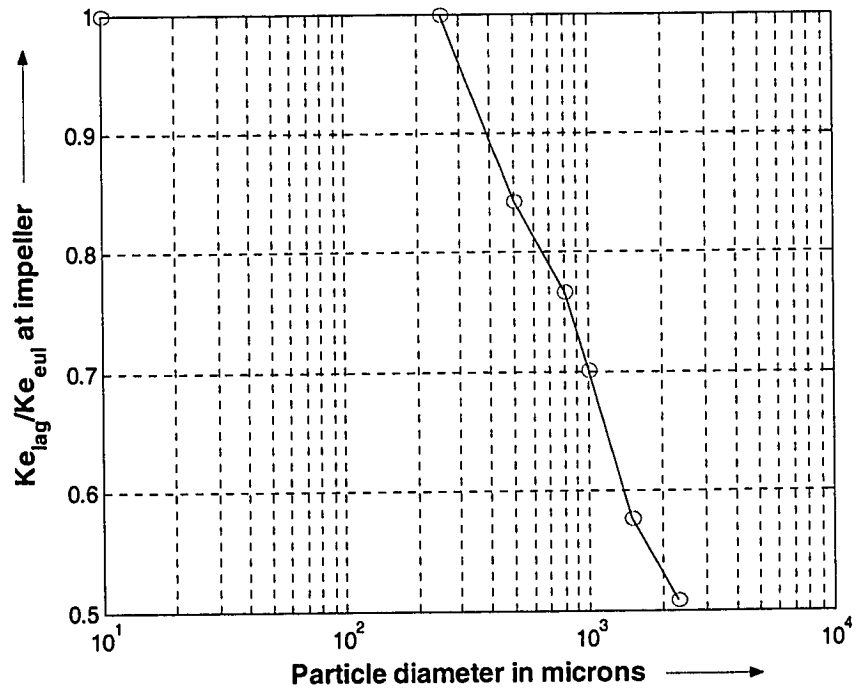


Figure 6-15(b). Sensitivity of Lagrangian Estimates to Size of Neutrally Buoyant Tracer

The figure indicates that the larger although neutrally buoyant tracers filter out almost 50% of the turbulent kinetic energy. This estimate is comparable to the experimentally observed loss of turbulence information in CARPT studies of the stirred tank with a 2.3 mm neutrally buoyant particle (Chapter 3 and Rammohan et. al., 2001b).

The relevant times scales to be examined related to particle ability to follow the flow at low particle Reynolds numbers are:

- a) The particle response time given by:

$$\tau_p = \frac{\rho_p d_p^2}{18\mu_f} \quad (6-34)$$

This represents the time needed for the fluid phase momentum to diffuse to the tracer particle.

- b) The particle relaxation time given by:

$$\tau'_{12} = \frac{4\rho_p d_p}{3\rho_f C_D |U_r|} \quad (6-35)$$

This represents the time taken by the particle to be entrained by the continuous phase.

- c) Fluid eddy life time:

$$\tau'_{12} = 0.15k/\varepsilon \quad (6-36)$$

This time scale represents the lifetime of a typical continuous phase eddy with which the tracer particle can be expected to interact.

For each tracer particle these time scales can be evaluated theoretically for free fall in the continuous phase. Using Morsi's and Alexander's correlation (1972) for evaluating the single particle non turbulent drag correlation, C_D , the slip velocity between the particle and fluid for the heavy particle was found to be 4.15 cm/s and for the smaller neutrally buoyant particle the slip velocity is close to zero. The relevant time scales for the two tracers are shown below in Table 6-3. The fact that the ratio of particle relaxation times to the eddy lifetime for both particles is $\ll 1$ indicates that both the light as well as the heavy particle can be expected to follow the fluid motion faithfully.

Table 6-3. Comparison of Time Scales of Light and Heavy Tracer

Time Scale	Light tracer	Heavy tracer
τ_p	.0115 s	6.17 μ s
τ_{12}^x	6.36 ms	6.17 μ s
τ'_{12}	.0115 s	.0115 s

However, the ratio of the particle relaxation time of the heavier particle to that of the lighter particle is three orders of magnitude higher. As the ratio of the particle relaxation time to the eddy life time increases beyond 1 the particle will be affected less and less by the continuous phase turbulence. Hence, this analysis allows us to anticipate the inability of the heavier and larger tracer to respond to all of the continuous phase turbulence.

6.3.4.1 Role of Particle Density

In the above section the combined effect of particle density and size were examined. In order to understand the influence of size and density separately, a comparison of Eulerian estimates obtained with a large, heavy tracer ($\rho_p/\rho_f \sim 2.99$, $d_p = 250\mu\text{m}$) and a large neutrally buoyant tracer ($\rho_p/\rho_f \sim 1.0$, $d_p = 250\mu\text{m}$) are presented in this section. Figure 6-16(a) and 6-16(b) show the comparison of horizontal and vertical velocities obtained with the heavy and neutrally buoyant tracers. The comparison between the horizontal velocities shows that density has little effect on the magnitude of the horizontal velocities ($E^{\text{rel}} = 7\%$, $E^{\text{max}} = 39\%$). The heavier particle is seen to have a larger vertical velocity (23%), in the regions of high base flow velocities, and smaller vertical velocity (25-30%), in the regions of low base flow velocity. The differences in the vertical velocity between the heavy and neutrally buoyant tracer are seen to be larger than the differences observed in the horizontal velocities ($E^{\text{rel}} = 29\%$, $E^{\text{max}} = 43\%$). There are huge differences in the estimates of turbulent kinetic energy obtained with the heavy and neutrally buoyant tracer as can be seen from Figure 6-16(c). The turbulent kinetic energy obtained with the neutrally buoyant tracer is

almost 100% larger (in the impeller region) than the estimate obtained with the heavier tracer ($E^{rel} = -0.8\%$, $E^{max} = 96\%$). This comparison clearly shows that density differences between tracer and fluid create a greater loss of turbulence information than an increase in the size of a neutrally buoyant tracer does.

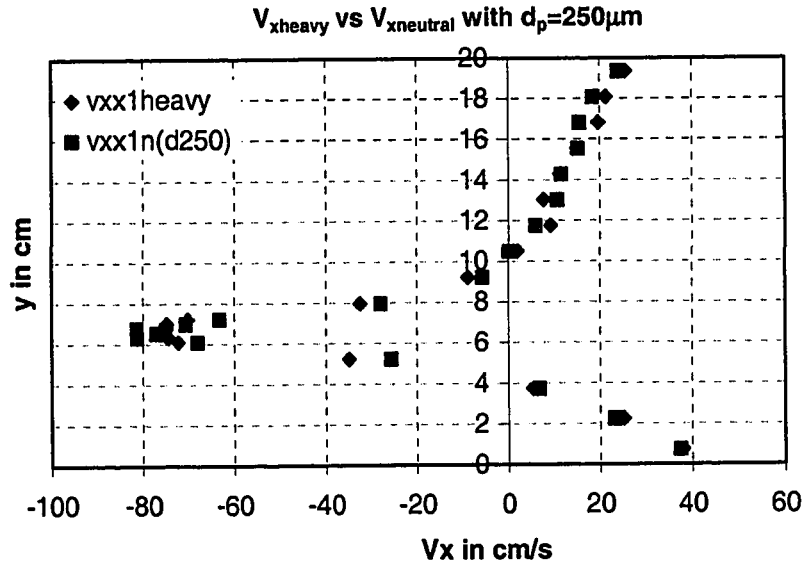


Figure 6-16(a). Effect of Particle Density on Lagrangian Estimate of Horizontal Velocity

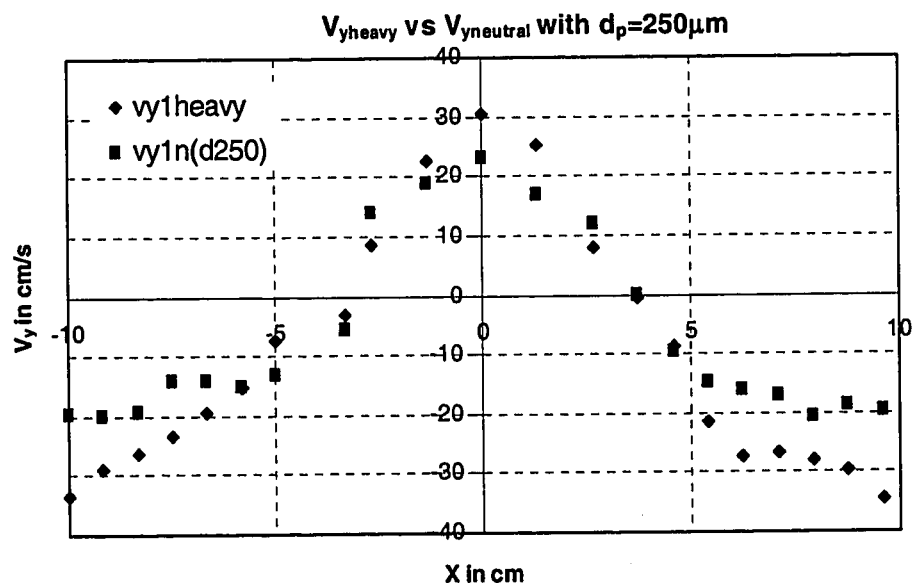


Figure 6-16(b). Effect of Particle Density on Lagrangian Estimate of Vertical Velocity

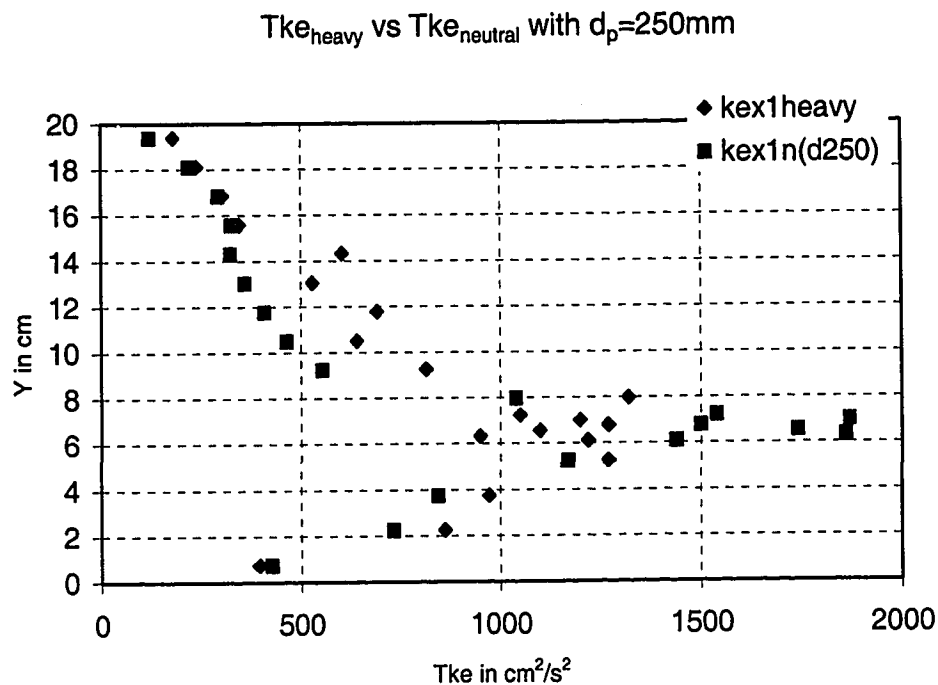


Figure 6-16(c). Effect of Particle Density on Lagrangian Estimate of Turbulent Kinetic Energy

6.4.0 Summary and Conclusions

The current study numerically simulates a typical CARPT experiment with the objective of evaluating the magnitude of the errors of type (2) and type (3) and their parametric sensitivity. The current work consists of four main components: a) Performing Eulerian simulations, b) Performing Lagrangian simulations, c) Quantifying the errors in estimating Eulerian information from reconstructed Lagrangian trajectories and d) Quantifying errors due to particle not following the flow faithfully.

A two – dimensional model problem mimicking the key features of flow generated by Rushton turbine in a stirred vessel was considered in the present work. Trajectories of particles of different density and size were then simulated using the converged flow field of liquid.

A sound basis for accounting for certain surface force terms and neglecting others in performing a particle tracking simulation was presented. The existing lift force models were found to underestimate the lateral force acting on a neutrally buoyant tracer. Inclusion of the lift forces for the heavy tracer results in an almost 100% increase in the estimates of turbulent kinetic energy in the impeller region. It was found that both particle Lagrangian trajectories and the Eulerian estimates obtained from them were insensitive to the two different turbulence models (DRW and CRW) used.

The following conclusions and recommendations are based on an understanding of error introduced by the CARPT processing programs:

- The effect of grid size on the Eulerian recovery process is intimately connected with the particle occurrence statistics and the rate at which the trajectory information is sampled. The influence of these two parameters on the Eulerian estimates could be decoupled by introducing a parameter called the fractional particle occurrence. The studies with different grids revealed that ensuring a certain minimum fractional particle occurrence (function of vessel type and flow) per cell is critical in estimating the Eulerian quantities from the Lagrangian trajectories. The analysis of the errors associated with the recovery process reveals that improper selection of grid parameters can cause errors to be as high as 100% and that with proper selection of the grid parameters the mean relative errors and the mean absolute errors can be as small as 1-10%.
- Further, the recovery process was found to be sensitive to the data acquisition rate for sampling rates below 100 Hz ($\tau_{process}/\tau_{sample} \sim 40$). The recovery was insensitive to the data sampling rates beyond sampling frequencies of 200 Hz ($\tau_{process}/\tau_{sample} \sim 80$) since the fractional occurrence reaches a plateau beyond these frequencies. This preliminary study suggests that the current CARPT technique, owing to current hardware limitations ($f_{sample} < 500$ Hz), may be limited to tracking the motion of flows whose process time scale is less than 0.1s or specifically to impeller tip speeds less than 4.2m/s (1200 r.p.m.).

The following conclusions and recommendations are based on an understanding of errors due to inability of the tracer to follow the base flow:

- A density mismatch introduces larger errors than the errors introduced by a finite size of tracer. A large neutrally buoyant tracer ($> 2300\mu\text{m}$) could miss as much as 50% of the base flow turbulent information. A neutrally buoyant tracer need not be smaller than $250\mu\text{m}$ to be able to capture the particular base flow field examined in the current study.
- Tracer particle density had little effect on various mean Lagrangian measures.

This study will be of considerable use when extended to simulating particle tracking in a three dimensional stirred tank, for then one would have a valuable numerical tool which would allow the selection of a CARPT tracer of optimum size, density ratio and data sampling rate which can follow the motion of a fluid of a certain velocity.

Chapter 7

Characterization of Gas – Liquid Flow Structures in Stirred Tank Reactors via Computer Automated Radioactive Particle Tracking (CARPT) and Computed Tomography (CT)

7.1 Introduction

Gas-liquid stirred reactors are used in a variety of industrial applications like oxidations, hydrogenations, aerobic fermentations and manufacture of several pure products (Shah, 1992). Performance of such reactors depends on three key parameters (Smith, 1985): scale, stirrer design and gas input rate. These parameters in turn affect the gas holdup, power demand, gas-liquid mass transfer coefficient, mixing characteristics and the residence time distribution. The impeller design and rotational speed determine the mechanism of breakage of gas into smaller bubbles, dispersion of bubbles throughout the liquid, retaining bubbles in the liquid for a sufficient time and providing turbulent eddies to feed liquid to and from the gas – liquid interfaces. Global parameters like overall gas hold-up, power demand and overall gas-liquid mass transfer coefficients are very strong functions of the local fluid dynamics of the gas and liquid phases in the stirred tank. However, several different combinations of the local fluid dynamics may result in similar global measurements. Hence, the practice of studying the variation of global parameters alone conceals detailed localized information. This local information may be crucial in the successful design of process equipment (eg., to avoid localized oxygen depletion Ranade and Van Den Akker, 1994; Gosman et al., 1992). The current literature on stirred tanks, although rich with information on the total power consumption, flooding phenomenon and overall gas holdup (Gezork et al., 2000; Nienow, 1996; Manikowski et.

al., 1994; Chapman et al., 1983;) is almost completely devoid of local measurements. Only a few studies, such as those of Lu and Ju (1987), Katsanevakis and Smith (1994), Morud and Hjertager (1996), Deen and Hjertager (1999), Wang, Dorward, Vlaev and Mann (2000); and Takahashi and Nienow, (1993); report the local quantities. A brief review of the pertinent experimental studies is provided in the following section.

7.2 Review of Previous Experimental Measurements

This review is intended to emphasize the fact that gas – liquid flows in stirred tanks exhibit a vastly complex, three dimensional and unsteady flow.

7.2.1 Qualitative Characterization of Flow through Photographic Studies

The principal mechanisms of the overall dispersion of gas into liquid, coalescence of gas bubbles and power requirements are largely determined by the behaviour of the gas – liquid mixture near the impeller blades. Van't Riet and Smith (1973) characterized the flow of gas – liquid mixtures near a Rushton turbine in a stirred tank reactor using two different types of photographic measurements. They used a video camera that was mounted to a table below the tank and rotated with the impeller speed and also obtained high speed photographs with stationary cameras taken through the side of the tank. The measurements in the moving frame were performed on a tank of 45 cm diameter while the stationary measurements were performed on a tank of 30 cm diameter. Gas was introduced from below the impeller through a ring sparger. Neutrally buoyant polystyrene beads (2.0mm) were added to the flow for better visualization. Gas flow rates were small enough not to disturb the main liquid phase flow features. The presence of centrifugal effects causes the migration of gas to the vortex core and tends to form a cavity (refer to Figure 7-1). A large proportion of gas was observed to be drawn into the vortex core. The size of cavities behind impeller depends on the overall gas flow rate in the impeller region and the agitator speed. At very low tip speeds (quantified in terms of Cavitation number and Froude number) the natural buoyancy forces are greater than the centrifugal

forces and hence no stable cavity is formed. Cavitation number, or gas flow number, is the ratio of gas sparging rate to rate at which liquid is pumped by the impeller given by:

$$Fl = \frac{Q_G}{ND^3} \quad (7-1)$$

The Froude number is the ratio of inertial forces (represented by the impeller rotational speed) to the gravitational force given by:

$$Fr = N_{Fr} = \frac{N^2 D}{g} \quad (7-2)$$

At higher impeller speeds some of the gas is drawn into the impeller region while the rest still escapes from the top surface. This results in formation of stable smooth cavities which persist over long periods (refer Figure 7-2).

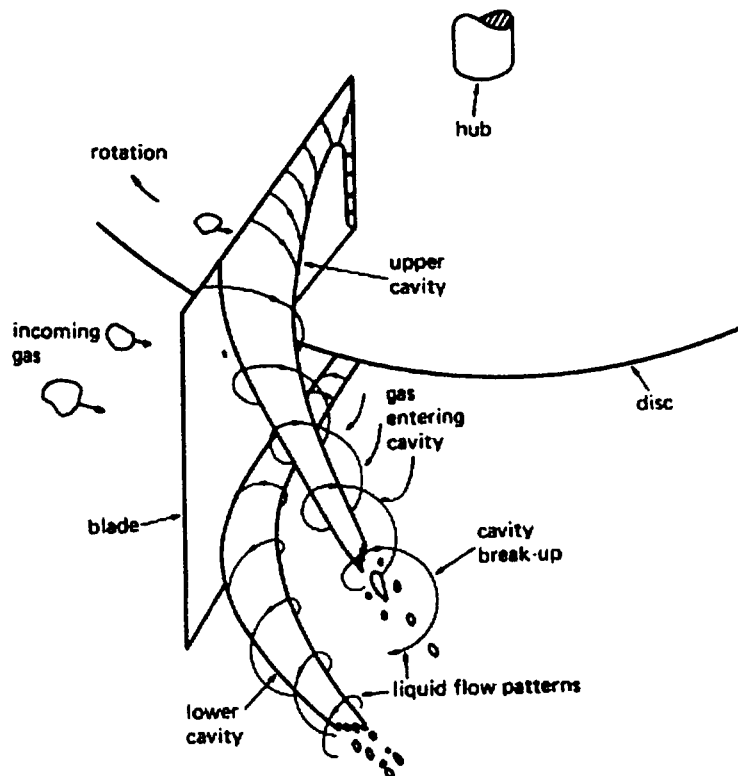


Figure 7-1. Mechanism of Cavity Formation

With increasing impeller speed the bubbles become much more distorted, their cylindrical form follows the vortex structure and their roughened surfaces reflect the increased turbulence (refer figure 7-1). The turbulence also causes breakage of the cavities into tiny bubbles which then escape into the liquid bulk. It is this mechanism of cavity formation and its subsequent breakage and escape into the bulk liquid which is responsible for the good dispersion of gas into the fluid bulk. At higher tip speeds there is gas phase recirculation in the tank. Larger bubbles entering the impeller region are rapidly extended into a roll form and broken up. The frequency with which bubbles are broken up by the cavity are far higher than breakup of larger bubbles just rising up with the impeller discharge stream. With increasing gas flow rates the diameter of the circulating core tends to increase, but there is a natural limit to this when the liquid film between the blade and the gas filled vortex breaks down. In the following section a detailed description of cavity structures and quantification of flow regime is provided.



Figure 7-2. Stable Cavity Formed at Higher Impeller Speeds and Gas Sparging Rates
(Reproduced from Bruijn et. al., 1974)

7.2.2 Classification of Cavity Structures

Gas filled cavity structures control the energy dissipation, spatial gas – phase distribution in the liquid bulk, flooding conditions and so on. The form and configuration of gas filled cavities depends on transport properties (Takahashi and Nienow, 1992), gas flow rate and impeller speed, and the number of blades (Warmoeskerken and Smith, 1982). A number of different researchers have worked on classifying the structure of gas cavities like Chapman et. al. (1983), Warmoeskerken et. al. (1981), Warmoeskerken and Smith, 1982, Ismail et. al. (1984), Takahashi and Nienow, (1992), Bombac et. al. (1997), etc. Here we provide a brief review of their findings. We begin by describing the findings of Chapman et. al. (1983).

The six bladed Rushton turbine is one of the popular gas dispersing impellers since the disc forces all the inflowing gas to pass through the high shear impeller region, ensuring sufficient break – up of the gas stream into bubbles and effective dispersion of the bubbles throughout the vessel. At low impeller speeds a large gas cavity covers the impeller. As the impeller speed increases the cavity shape modifies itself to fit the shape of the trailing vortex and at still higher speeds the breakaway points moved inwards along the blade forming vortex cavities. As a small amount of gas is introduced into the system, it migrates to the low pressure regions forming vortex cavities behind the impeller blades and therefore increasing the pressure in this area. The consequence of this is a reduced pressure difference over the blade and a slight drop in drag and power consumption. As gas flow rate is increased an increasing number of cavities are formed, streamlining the impeller and further reducing the drag. Eventually all six cavities reach a maximum size and the impeller pumping capacity is reduced to a minimum. Warmoeskerken et. al. (1981) proposed that three large cavities form simultaneously, causing a definite drop in the power consumption at a given gas rate, after which any further decrease can be explained by the reduction in the mean density of the pumped liquid.

Constant Gas Flow Rate with Increasing Impeller Speed:

At low speeds the tips of the blades are surrounded by liquid and the power number remains high because of the presence of two low pressure vortices at the back of each

blade. As impeller speed is increased, a large cavity forms over the upper half of the blade causing a reduction in power number. At a slightly higher speed the cavity covers the whole of the back face of the blade and a minimum occurs in the gassed power number. Further increases in the speed cause a rise in the power number as the size and number of large cavities fall and their shape tends towards those of vortex cavities. At high enough impeller speeds, recirculation of gas to the impeller becomes significant and the power number drops slightly again. The impeller speed required to achieve the resulting maximum is commonly designated N_R .

Ismail et. al. (1984) attempt to predict the appearance of gas cavities through power consumption measurements.

They classify the cavities into two types:

a) Cavities seen during Flooding

They find that at very low impeller speeds, the air stream formed large bubbles at the sparger holes or on the lower surface of the impeller disc, but was not dispersed by the impeller blades. Large bubbles thus formed, passed radially between the blades and left the disc from its edge. They ascribe the appearance of the first minimum on the Relative Power Demand (RPD) vs Impeller speed (N) curve to the formation of these large bubbles (refer to Section 7.2.4). At the rotational speed slightly above the first minimum, some of the bubbles enter into the rear part of the inner edge of the impeller blade. At this point, the RPD abruptly increases to the first maxima. As the sparging progresses, almost all the bubbles enter the rear part of the impeller blades at $n = n_{c1}$. Sparging and initial dispersion causes abrupt increase in gas holdup in the vessel. A convenient definition for flooding is the region where impeller speed is less than the impeller speed for complete circulation (i.e. $N < N_{c1}$, refer to Figure 7-3). They found that increase in impeller speeds beyond the critical speed resulted in significant dispersion of gas characterized by the appearance of :

b) Unstable Large Cavity:

They found that for some blades, the gas film was produced from the inside blade edge to the blade tip and was then elongated into the liquid to be dispersed into smaller bubbles. Large cavities were not observed on other blades at this time. The cluster of bubbles left

the blades at a midway point between the tip and the inner edge of the blade. The situation was not steady since the large cavity and cluster type cavity replaced each other with time on the same blade.

Bombac et. al. (1997) provide a quantitative characterization of the different cavity structures

- a) **Vortex Clinging Structure (VC):** The frequency analysis of structural function for vortex clinging structures shows principal frequencies corresponding only to the blade passage frequencies and its higher harmonics.
- b) **Clinging Cavities (1L):** Increasing gas flow rates results in clinging cavities. Further increase in gas flow rate results in the formation of the first large cavity. Analysis of cavity presence over longer periods suggested that a large cavity appeared on various blades randomly; it moved from blade to blade. In the frequency domain the random appearance of large cavities on various blades corresponds to the rise of significant subharmonics of the blade frequency (f_b) such as $f_b/6, f_b/3, f_b/2, 2f_b/3$ and $5f_b/6$.
- c) **Two Large Cavities (2L):** Cavities follow each other in the same sequence; one large cavity is followed by two vortex clinging cavities, and so on. Such a configuration is present only for a very short time and is followed by the appearance of two large cavities, but never on adjacent blades. In the frequency domain two significant subharmonics $f_b/3$ and $2f_b/3$ predominate.
- d) **Three large and Three Clinging Cavities (S33):** The beginning of the S33 structure can be seen by the appearance of a peak at $f_b/2$. The S33 structure is described (Bruijn et. al., 1974; van't Reit and Smith, 1973) as a combination of three large and three clinging cavities. The large cavities are present on the same blade.
- e) **Three Smaller and Three Larger Large Cavities (L33):** L33 is described (Nienow, 1990; Warmoeskerken and Smith, 1982) as a combination of three smaller and three larger large cavities. The large and small cavities are presently alternately on each of the blades. A rise in the coefficient of $f_b/2$ is seen till its value becomes almost equal to that of f_b .

f) **Ragged Cavity (RC)**: On increasing the gas flow rate further, according to Warmosekerken and Smith (1985), the stable L33 structure reverts to six symmetrical clinging cavities, and at higher impeller speeds the changeover passes through a regime with six large cavities of identical size, which are described as violently vibrating and referred to as the ragged cavity structure (Nienow, 1990). These cavities are each of different sizes with sporadic appearance of larger cavities. At higher gas flow rates, a longer absence of any cavity on a particular blade was also possible.

Hence for a fixed impeller speed increase in gas flow rate results in the following sequence of cavity structures appearing: Vortex Clinging (VC), One large cavity (1L), Two Large Cavities (2L), Three Large cavities and three small cavities (S33), Three larger large cavities and three smaller small cavities (L33) and finally ragged cavity structure (RC) before the transition to flooded condition occurs. The vast majority of industrial operations take place in the large cavity regime (Smith, 1991). Bombac et. al. have created a detailed map of Froude number vs Cavitation numbers (equation 7-1 and 7-2) clearly identifying which regions correspond to which of the above cavity structures (refer Figure 7-3).

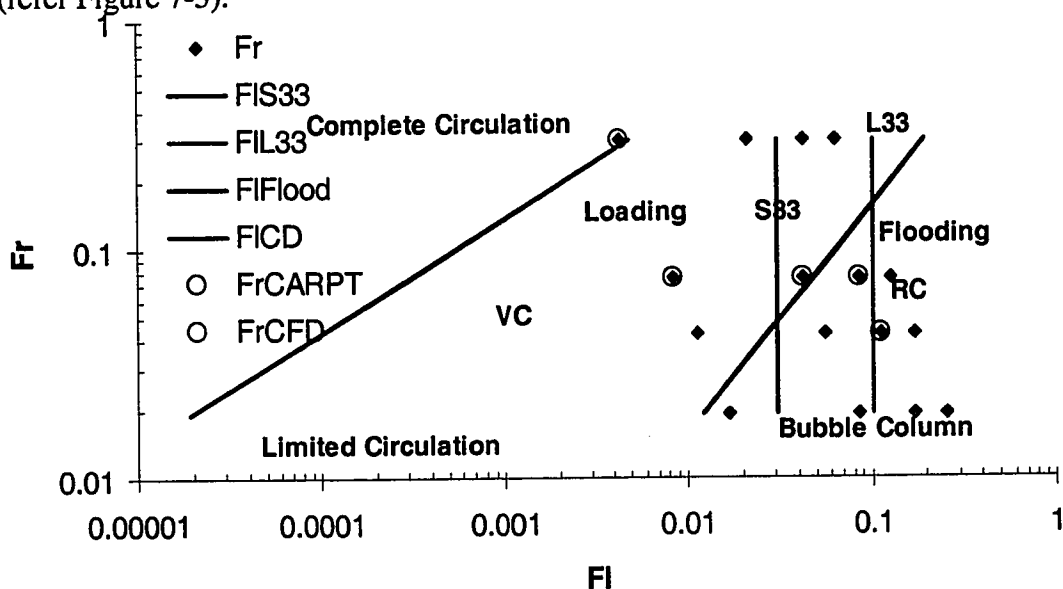


Figure 7-3. Flow Regime Map for CT+CARPT+CFD Data Obtained in Stirred Tank Reactor

7.2.3 Power Consumption Measurements

A number of researchers like Hughmark (1980), Midoux and Charpentier (1984), Michel and Miller (1962), Nagata (1975), Nienow et.al. (1977,1988), van't Riet and Tramper (1991), Rushton et.al. (1950), Smith et. al. (1977 and 1993), Warmoeskerken (1986), Warmoeskerken and Smith (1988), etc. report power uptake measurements in two phase flows in stirred tank reactors. According to Van't Riet et. al. (1976) the power consumption in an aerated vessel is largely controlled by the formation of gas cavities behind the stirrer blades. The sparger gas inflow rate is one of the variables which strongly influences the cavity shape. They report comparisons of power curves with and without recirculation which clearly show that the recirculated gas inflow to the cavity influences the power consumption. They make general observations like, agitators with larger number of blades have smaller cavities at a given gas inflow rate, increase in gas flow rate decreases the fraction of old gas leaving the impeller, and increasing the impeller speed increases the fraction of old gas leaving the impeller region.

Rushton et. al. (1950) were the first to apply dimensional analysis in order to predict the dependency of the liquid mixing mechanical power requirement for systems containing liquid only. For specified geometry, they showed that , the necessary power P_o can be obtained as:

$$N_p = \frac{P_o}{\rho_L N^3 D^5} = C_3 N_{Re}^x N_{Fr}^y \quad (7-3)$$

where N_p is the power number, $N_{Re} = \frac{ND^2}{\nu}$ is the Reynolds number and N_{Fr} is the Froude number defined in equation (7-2). In fully baffled tank $y=0$, and in the turbulent regime ($N_{Re} > 10^4$) the above equation reduces to:

$$N_p = C_4 \quad (7-4)$$

where C_4 is a constant specific to a particular impeller configuration. Correlations of N_p for various types of impellers have been provided by Rushton et. al. (1950), Bates et. al. (1962) and summarized by Nagata (1975) and Oldshue (1983).

According to Hasan and Robinson (1977) the reduction in mechanical power drawn by an impeller under sparged conditions does not depend merely on the change in the volume density of the tank contents resulting from the addition of dispersed gas bubbles but also is strongly influenced by the impeller and tank geometry, the impeller rotational speed, liquid phase physicochemical properties, and the gas sparging rate. Based on dimensional analysis they showed the Relative Power Demand (RPD) to depend on the following dimensionless variables:

$$RPD = \frac{P_g}{P_o} = C_1 N_{we}^m Fl^n \left(\frac{\rho_L}{\rho_D} \right)^8 \quad (7-5)$$

where $N_{we} = \frac{\rho D^3 N^2}{\sigma}$ the Weber number represents the ratio of inertial force to force due to surface tension. The concept of cavitation number (or aeration number) was first used by Ohyama and Endoh (1955) who measured the RPD for air – water dispersions using a variety of impeller types. Ohyama and Endoh (1955) performed all their measurements at constant impeller speed and varying gas flow rates. For this case they found that increasing the aeration number (i.e. gas flow rates) decreases the power consumption (refer Figure 7-4).

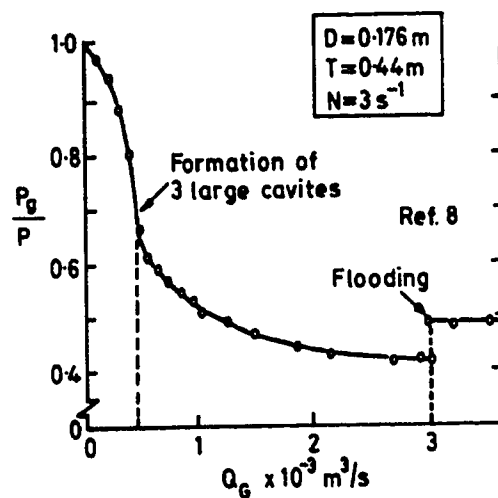


Figure 7-4. Change in RPD with Increasing Gas Sparging Rate at Fixed Impeller Speed

Michel and Miller (1962) and Vares (1975) found that the change in RPD with change in N_A is not consistent but is rather dependent on whether N_A is changed by altering gas sparging rate (Q_G) or impeller rotational speed (N). If Q_G is varied at constant N , continuously decreasing functions similar to those of Ohyama and Endoh (1955) are obtained with increasing Fl . However, if N is varied at constant Q_G , a separate curve is obtained for each gas flow rate, and these show that the RPD increases slightly with increasing Fl until an asymptotic limit is reached such that the RPD is constant. The limiting constant value of RPD depends on Q , decreasing as Q increases. Michel and Miller (1962) measured P_g . For various liquids (water, organics, aqueous solutions of organics) in a stirred tank with six bladed Rushton turbine Hassan and Robinson (1977) fitted a correlation of the form:

$$P_g = C_8 \left(P_o^2 N D^3 / Q^{0.56} \right)^{0.43} \quad (7-6)$$

They found that the correlation fitted the experimental data of Sachs (1950), Ohyama and Endoh (1955), Bimbinet (1959), and Michel and Miller (1962) within +/- 30% if the exponent 0.43 was changed to 0.45 and with $C_8 = 0.72$. Pharamond et. al. (1975) evaluated RPD for air – water dispersions and proposed a correlation of the form:

$$1.0 - \frac{P_g}{P_o} = 96(Q/V)D^{0.63} \quad (7-7)$$

Hassan and Robinson (1977) studied the variation of RPD with gas flow rate but not with rpm at constant gas flow rate. Hence, the correlation they proposed is limited because the variation of RPD with N at constant gas flow rate is very different.

Luong and Volesky have proposed the following correlation for Newtonian fluids:

$$\frac{P_g}{P_u} = 0.497 \left(\frac{Q}{ND^3} \right)^{-0.38} \left(\frac{N^2 D^3 \rho}{\sigma} \right)^{-1.18} \quad (7-8)$$

This correlation is restricted to systems with $\sigma = 55-72 \text{ dyn/cm}$ and an impeller to vessel ratio of 1/3. The equation is not applicable to systems like CCl_4 . Hence in order to correct for these limitations, Hughmark (1980) proposed a correlation, using various data sets, of the form:

$$\frac{P_g}{P_u} = 0.10 \left(\frac{Q}{NV} \right)^{-0.25} \left(\frac{N^2 D^4}{g D_{width} V^{2/3}} \right)^{-1/5} \quad (7-9)$$

where D_{width} is the impeller blade width and V is the liquid volume. The average absolute deviation between calculated and experimental values is 8.5%. The above correlation also fits the data of Bimibinet (1959) and the overall absolute deviation is 11.5%. Chapman et. al. (1983) propose a correlation of the following form:

$$Po_g = \frac{P_g}{\rho_L N^3 D^5} = Po(P_g/P) \propto P_g \quad (7-10)$$

The correlations of Michel and Miller (1962) and of Hughmark (1980) are often used in the literature. Midoux and Charpentier (1984) recommend Michel and Miller's (1962) correlations for estimating the gassed power uptake. However van't Riet and Tramper (1991) state that Michel and Miller's correlations are applicable only over a limited range of parameters.

Hughmark's correlation is considered to be quite good (Hughmark, 1980, Van't Riet and Tramper, 1991) since accurate power uptake measurements are difficult to perform. However, Warmoeskerken (1986) found both Michel and Miller's (1962) and Hughmark's (1980) correlations to overestimate the gassed power demand. Cui et. al. (1996) proposed a correlation for power uptake using 739 data points extracted from a number of different researchers. The variations of RPD $\left(\frac{P_g}{P_u} \right)$ vs flow numbers (from

Warmoeskerken, 1986) indicate that for the same flow number there is considerable variation in the RPD. Hence, the RPD depends on more parameters than the flow number alone. The expressions from Hughmark (1980) and Michel and Miller (1962) have a common drawback i.e. the RPD does not become 1 for ungassed conditions. Cui et. al. (1996) develop a correlation for 1.0-RPD as a function of gas volume flow rate, stirrer speed, impeller diameter, tank diameter. Here the basic assumption is RPD under gassed conditions will always be lesser than 1.0. Cui et. al. propose correlation of the form:

$$1 - \frac{P_g}{P_u} = f \left(\frac{Q_g N^{0.25}}{D^2} \right) \quad (7-11)$$

A plot of the LHS vs the RHS reveals almost one single curve (refer to figure 7-5). They also conclude that power uptake is not sensitive to T/D (tank diameter to impeller diameter) ratio. Cui et. al. (1996) have also shown that (refer figure 7-6) their correlation fits the data of a number of other researchers as well (Bruijn et. al., 1974; Hudcova et. al., 1989; Nagata, 1975; Nienow, 1977; Smith et. al., 1977; Warmoeskerken, 1986; Warmoeskerken and Smith, 1988). The variation shows that there are two distinct linear portions. The change in slope is attributed to a change in regime. The initial portion has a very steep slope while the latter portion has a smaller slope. The correlations obtained for these two portions are given below:

$$\frac{Q_g N^{0.25}}{D^2} \leq 0.055: \quad 1 - \frac{P_g}{P_u} = 9.9 \left(\frac{Q_g N^{0.25}}{D^2} \right) \quad (7-12a)$$

$$\frac{Q_g N^{0.25}}{D^2} > 0.055: \quad 1 - \frac{P_g}{P_u} = 0.52 + 0.62 \left(\frac{Q_g N^{0.25}}{D^2} \right) \quad (7-12b)$$

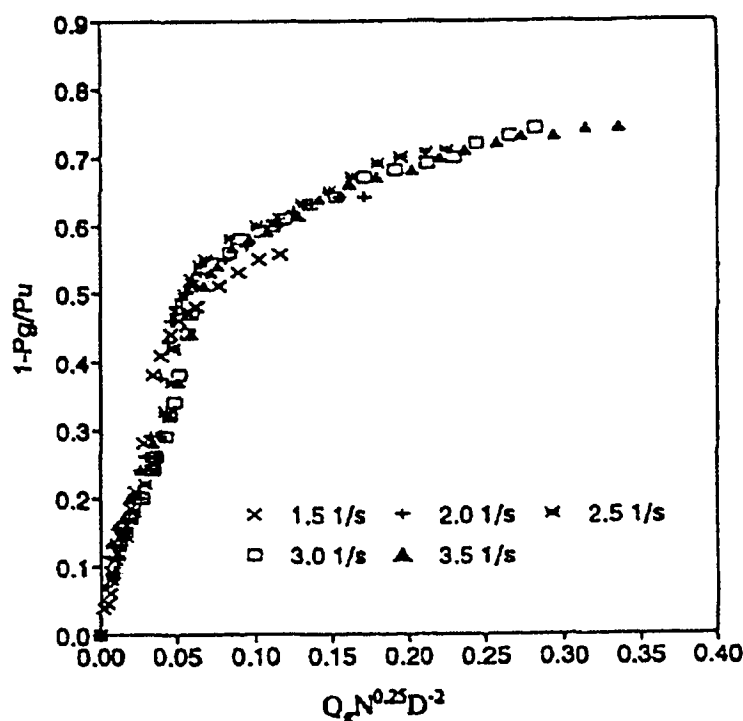


Figure 7-5. Reduction of Power Uptake by Single Impeller in a Gassed STR from Warmoeskerken, 1986 (T=1.2m, D=0.48 m, H=T)

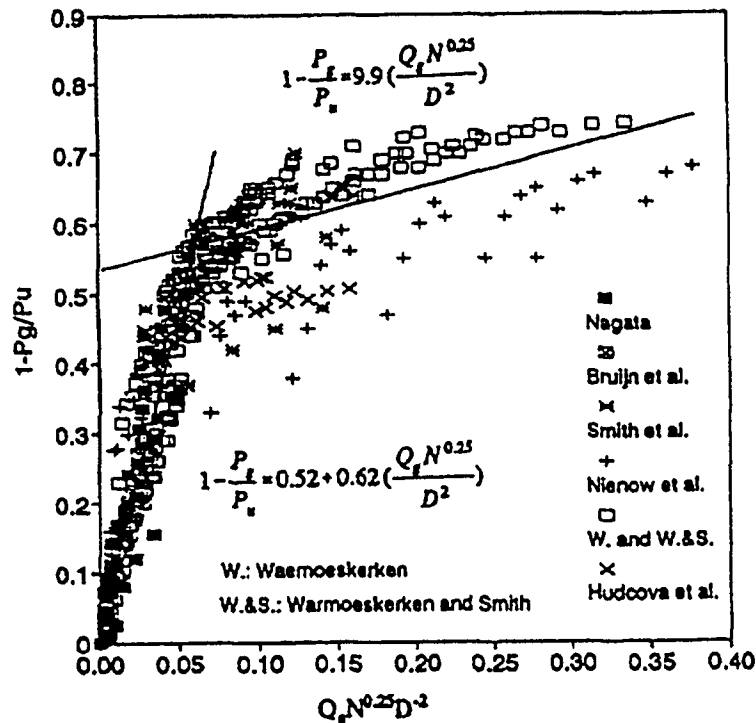


Figure 7-6. Comparison of Power Uptake Predicted by Cui et. al.'s Correlation with other Correlations

The relative errors for both parts are below 6%. The above correlation was developed only for the air – water system. Hence the sensitivity of the correlation to different combinations of working fluids is not known. Xu et. al. (1997) measure power consumption by a torque transducer mounted on the agitator shaft. They measure holdup by visual observation and the discharge flow number using tracer particles.

7.2.4 Overall Gas Holdup Measurements

A number of different researchers report the overall gas holdup measurements (refer to reviews by Pandit and Joshi; 1982; and Patwardhan) and found that as the impeller speed was increased the overall gas holdup increased. The overall holdup also increases with increase in gas flow rate. Flooding is observed at lower impeller speeds with higher gas inflow rates. At constant gas flow rates a bypass zone is observed for small agitator

speeds where the gas bubbles flow through the tank without recirculation. With increasing N the gas phase is effectively dispersed in the loading zone. With further increase in impeller speed the gas holdup reaches a maximum and then there is no further increase in the holdup with increase in impeller speed. This is the flooding zone. Loiseau et. al. (1977) have proposed two correlations for overall gas holdups (ϵ_g) one for foaming and the other for non-foaming solutions. The correlation for non – foaming solutions is:

$$\epsilon_g = .011u_s^{.36} s^{-.36} \mu^{-0.056} (\epsilon_A + \epsilon_D)^{0.27} \quad (7-13)$$

and for foaming solutions is:

$$\epsilon_g = .0051u_s^{.24} (\epsilon_A + \epsilon_D)^{.57} \quad (7-14)$$

The accuracy of (7-13) is 20% while that of (7-14) is 30%. ϵ_A is the mechanical agitation power in gas – liquid dispersion and ϵ_D is the sparged gas isothermal expansion power per unit volume of clear liquid [$\epsilon_D = \rho_G Q_G RT / M_G V_L \ln(p_s / p_o)$]. Midoux (1977) reported good agreement of (7-14) with experimental data if the LHS is replaced by $\epsilon_g / (1 - \epsilon_g)$. Hughmark (1980) has proposed a correlation for the gas holdup (ϵ_g) in a stirred tank reactor as:

$$\epsilon_g = 0.74 \left(\frac{Q}{NV} \right)^{0.5} \left(\frac{N^2 D^4}{g D_i V^{2/3}} \right)^{1/2} \left(\frac{D_p N^2 D^4}{\sigma V^{2/3}} \right)^{1/4} \quad (7-15)$$

The average error using this correlation was 8%. D_p is bubble diameter. He has also proposed a correlation for the interfacial area per unit volume of gas – liquid mixture as:

$$a = 1.38 \left(\frac{g\rho}{\sigma} \right)^{0.5} \left(\frac{Q}{NV} \right)^{1/3} \left(\frac{N^2 D^4}{g D_i V^{2/3}} \right)^{.592} \left(\frac{D_p N^2 D^4}{\sigma V^{2/3}} \right)^{.187} \quad (7-16)$$

7.2.5 Local Gas Holdup Measurements

One of the earliest methods of void fraction measurements by gas dispersion in a stirred tank was the vacuum sampling technique (Nienow et. al., 1977). Nagase and Yasui (1983) modified this method by incorporating a pair of resistivity probes for measuring

local holdups and local bubble sizes. Their experiments were performed in a tank of diameter 0.25 m ($D=T/2$) at one rpm (4.78rps, $Fr= 0.29$) and three gas flow rates ($4.92e-4$, $8.82e-4$ and $11.8e-4 \text{ m}^3\text{s}^{-1}$) corresponding to $Fl = 0.0527$, $.0945$ and 0.1264 . Based on the flow regime map developed by Bombac et. al. (1997, refer to Figure 7-3) these runs belong to the cavity types 2L, S33 and L33, respectively (refer to section 7.2.3 for discussion of these cavity types). For each of these conditions measurements are available at five different axial planes ($Z/T = 0.33$, 0.4 , 0.48 , 0.72 and 0.96) and six radial locations. For the 2L cavity structure at $Z=10 \text{ cm}$ ($Z/T = 0.33$, impeller plane) the holdup starts increasing as we move away from the shaft and peaks near the wall and starts going down very close to the wall. A similar trend is observed for the S33 and L33 conditions (refer to Figure 7-7a). The peak holdup value however increases from 2L to L33. At $Z = 12 \text{ cm}$ ($Z/T = 0.4$) for all three conditions the holdup starts rising from near the shaft and reaches a maximum value before the impeller region and remains more or less constant until $4/5$ of the tank radius (refer to Figure 7-7b). The maximum values once again are the highest for the L33 structure. At $z=18 \text{ cm}$ ($Z/T = 0.48$) the holdup has a high value near the shaft and then reach a peak value just beyond the radial position corresponding to the impeller tip and then starts falling to zero as it approaches the wall. At $z = 24 \text{ cm}$ ($Z/T = 0.72$) the holdup has two peaks, a small one near the shaft, and a larger one closer to the wall. There is a minimum between these two close to the radial position corresponding to the impeller. They report that the measurements near the impeller region are not accurate and they have not attempted to explain the appearance of the second maximum near the wall.

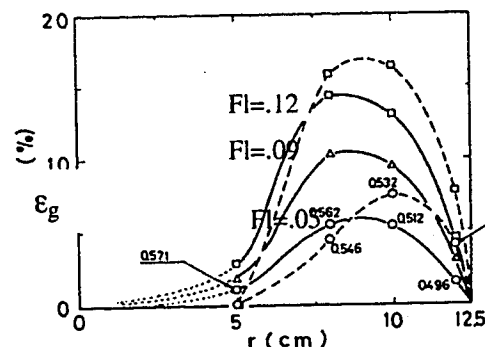


Figure 7-7(a). Radial Profile of Gas Holdup at Impeller Plane at $Fr = 0.29$ and $Fl = 0.05, 0.09$ and 0.12

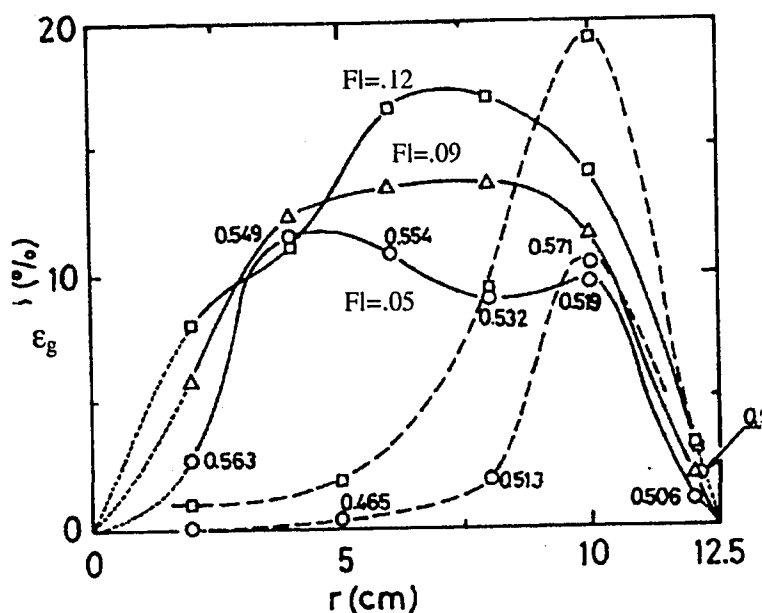


Figure 7-7(b). Radial Profile of Gas Holdup at $Z/T=0.4$ at $Fr=0.29$ and $Fl=0.05, 0.09$ and 0.12

Barigou and Greaves (1992) used two pairs of LED/photo detectors for holdup measurements. Impedance probes take advantage of the change of either resistivity or capacitance according to the phase considered. They found that increasing impeller speed increases gas holdup at every point and increases uniformity of holdup distribution. Increase in gas flow rate causes an almost uniform rise in gas holdup in the bulk, and reduced gas circulation in the lower region of the vessel. They report holdup measurements at 22 points in the midplane between baffles. Figueiredo and Calderbank (1979) used such probes to determine the bubble size distribution in an aerated stirred tank. Probe tips are normally of small diameters and enable detection of very small bubbles. Frijlink (1987) used optical probes (based on different refractive index of phases) for local void fraction measurements in gassed suspension reactors. Bombac et. al. (1997) and Zun et. al. (1995) used resistivity probes to measure local void phase holdup distribution. They define a structural function which as :

$$M_p(x,t) = \begin{cases} 1, & x \text{ is occupied by } p \\ 0, & x \text{ is not occupied by } p \end{cases} \quad (7-17)$$

where $p = \{L, G, S\}$.

The pulse length at constant impeller speed is proportional to the detected cavity size. The pulse length of a large cavity is a few times larger than the pulse length of a vortex or clinging cavity. Frequency analysis of the structural function M_p enables the presentation of the significant frequencies of an appearing gas phase. The local void fraction is given by

$$\alpha(x) = \lim_{\Delta t \rightarrow \infty} \frac{1}{\Delta t} \lim_{\delta \rightarrow 0} \int_t^{t+\Delta t} M_G(x, t) dt \quad (7-18)$$

where Δt denotes total sampling time and δ interfacial thickness. A discrimination procedure transforms the R-probe response into a binary signal. Bombac et. al. (1997) have provided detailed local void holdup profiles for three of the basic cavity structures i.e. the L33, S33 and VC structures (refer to Section 7.2.5). Under L33 conditions the liquid pumping capacity was weakened. The reduced pumping capacity resulted in a weak two – phase circulation in the liquid bulk especially below the impeller where 30% of liquid bulk remained undispersed. By increasing the impeller speed a transition from L33 to S33 occurred. This increased the liquid phase recirculation which also increased significantly the volume integrated holdup values. In S33 despite increase in the discharge flow a considerable part of the liquid bulk below the impeller remains undispersed.

7.2.6 Local Bubble Size Measurements

Kawecki et. al. (1967), Takahashi et. al. (1992), Parthasarthy and Ahmed (1990) measured the bubble size distributions in a stirred vessel by withdrawing the dispersion outside the tank into a small transparent column of square cross section and photographing them. Barigou and Greaves (1992) and Lu et. al. (1993) measured the Bubble Size distributions (BSD) using capillary suction tube and photoelectric capillary methods respectively. Their findings are summarized below:

- a) Average bubble size decreases with increase in impeller speed and increases with increase in gas flow rate in general.

- b) The BSD however, varies significantly with the position of the measurement location.
- c) In the impeller region the BSD is strongly dominated by the strength of the trailing vortex and the cavity structure behind the blade. In this region with increasing Flow numbers the bubble sizes increase and at a certain flow number there is an inflection in the curve (refer to Figure 7-8). This inflection location corresponds to a similar point on the RPD vs flow number curve (Refer Figure 7-8).
- d) In the upper circulation zone the BSD depends on the impeller dispersion ability. Increase in impeller speed is observed to promote coalescence and therefore an increase in the bubble size.
- e) In the lower circulation zone an increase in impeller speed initially causes an increase in the bubble size until a maximum is reached. Beyond this speed further increase in the impeller speed promotes redispersion of the bubbles by the impeller.

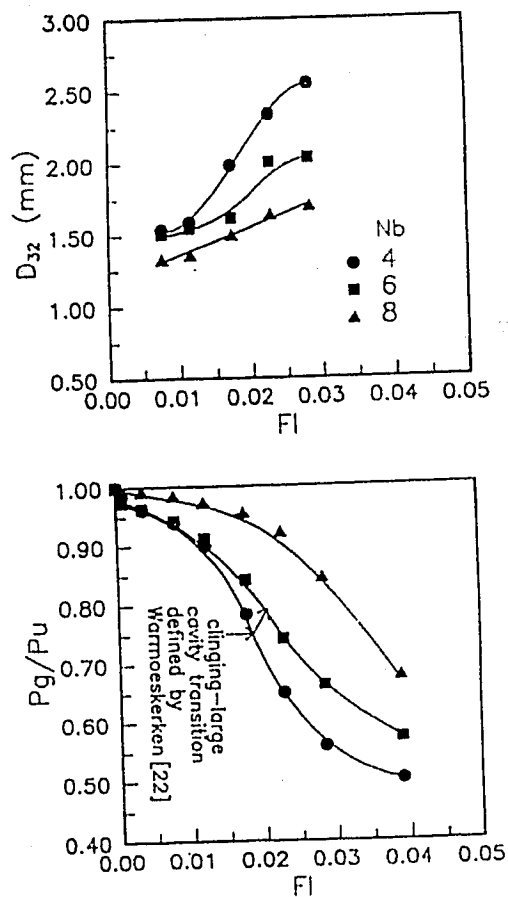


Figure 7-8. Bubble Size and RPD Variation with Fl at Impeller Tip (Lu et. al., 1993).

7.2.7 Liquid Velocity Measurements

Local liquid velocity measurements have been provided by Lu and Ju (1987) in a tank of diameter 0.28 m using Hot wire anemometry (HWA). The error associated with the velocity measurements are of the order of 5-25%. Morud and Hjertager (1996) and Deen and Hjertager (1999) perform Phase Doppler Anemometry (PDA) and PIV measurements in a 0.22m tank. However, their tank has a dished bottom and their impeller clearance is $1/2T$ while ours is $1/3T$. Further, the PIV measured liquid velocities are available at $Fl=0.029$ and $Fr=0.81$. We do not have data at these high Fr numbers in our study. Hence direct comparisons of the liquid velocity data (from CARPT) or the local holdup data (from CT) with values in the literature is not feasible. For further details of velocity measurements refer to Chapter 2 (Section 2.3).

Hence, for gas-liquid systems there is a clear need for accurate and reliable information of the fluid dynamics of the liquid and gas phase, especially at higher gas volume fractions. While a detailed qualitative picture exists, a clear need for a quantitative map of the flow structures emerges from the above analysis. Hence, in this work we address the issue of creation of a reliable database for the estimation of local gas holdup measurements using the technique of Gamma (γ) ray Computed Tomography (CT) and determining the detailed local liquid velocity structures using the technique of Computer Automated Radioactive Particle (CARPT). In the following sections the details of the Computed Tomography (CT) setup is provided. Details of the CARPT set up are provided in Chapter 3 and in our earlier studies (Rammohan et. al., 2001a; Rammohan et. al., 2001b and Rammohan et. al., 2001c).

7.3 Experimental Studies

7.3.1 Details of Computed Tomography

When a beam of electromagnetic radiation passes through matter, its intensity decreases because a fraction of the photons are absorbed or scattered by the intervening medium. This reduction in intensity is referred to as attenuation, and the extent of attenuation

depends on the density of the intervening medium. This property is the key to back-calculating the density of the intervening medium depending on the attenuation of a beam of radiation passing through it. This property is quantified by the Beer – Lambert's Law (Kak and Slaney, 1988) given by:

$$\frac{I}{I_0} = \exp \left[- \int_{l(x,y)=0} \mu_{eff}(x,y,z) dx \right] \quad (7-19)$$

where $\mu_{eff}(cm^{-1})$ is the effective point total attenuation coefficient in the domain, and is the product of $\tilde{\mu}(cm^2 g^{-1})$ and $\rho(g/cm^3)$. While $\tilde{\mu}$ is a material property, the density of the intervening medium is in general not uniform and there is a distribution of densities in the system. This is characterized by the distribution of densities in the path of the radiation. The tomography problem is an inverse problem of reconstructing the function $\mu_{eff}(x,y)$ based on measurements of the line averaged attenuation along various chords in the system of interest. In general, the function μ_{eff} can vary with time and typically does in multiphase systems that are inherently unstable. But the CT set up used for our studies due to constraints in collecting statistically significant photon counts, inertia and finite mechanical speed of operation, cost of detectors is limited to obtaining time averaged holdup measurements. In our CT set up the projection data is acquired over a sufficiently long time and the entire set of projections is assembled to reconstruct a density distribution that is representative of the time averaged volume fraction distribution over the entire period of acquisition. This process of measuring time- averaged attenuations is repeated all around the column and at various chords. From these measurements the time averaged effective attenuation coefficient $\langle \mu_{eff}(x,y) \rangle$ is obtained in every pixel by reconstructing the image from the entire set of projection measurements. The total mass attenuation coefficient can be represented as the sum of the individual phase mass attenuation coefficients weighted by the respective volume fractions. This is represented as:

$$\langle \mu_{eff}(x,y) \rangle = \mu_i \langle \varepsilon_i(x,y) \rangle + \mu_g \langle \varepsilon_g(x,y) \rangle$$

$$\langle \varepsilon_g(x, y) \rangle = \frac{\langle \mu_{eff}(x, y) \rangle - \mu_t}{\mu_g - \mu_t} \quad (7-20)$$

Evaluation of the time averaged phase holdup distribution function by equation (7-20) depends on the accurate reconstruction of the total mass attenuation coefficient $\langle \mu(x, y) \rangle$ distribution from the individual projection (attenuation) measurements. There are different algorithms available for this reconstruction as outlined by Kumar (1995). In the current study we use the Estimation – Maximization (EM) based algorithm developed in our group (Kumar, 1995). The EM algorithm ensures rapid convergence to a unique distribution of the attenuation coefficients. Its robustness has been tested in CREL with a number of different systems over the past few years. Some relevant details of the EM algorithm have been provided in the following section.

7.3.2 Data Analysis Algorithm

Basics of EM

The key to EM is the development of the log-likelihood function. The correct complete data likelihood takes advantage of the fact that the number of photons N_{ij} leaving pixel j depends only on the number M_{ij} entering the pixel, and the probability of passing through i.e. $l_{ij}\mu_j$ (refer to Figure 7-9).

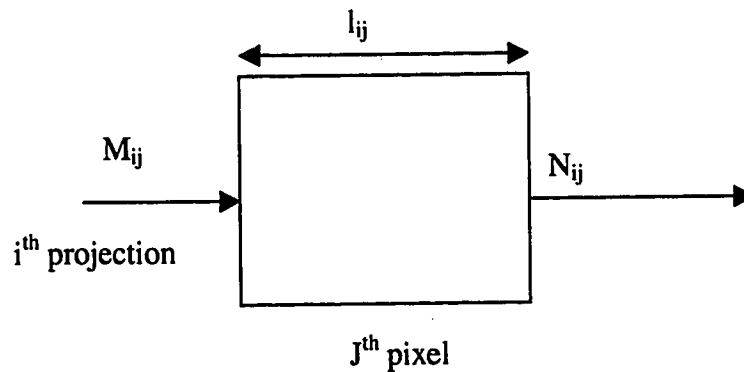


Figure 7-9. Schematic of CT Beam Passing through One Pixel

Thus, the probability that N_{ij} photons leave pixel j , given that M_{ij} photons entered that pixel, follows a binomial distribution with two outcomes: transmission and absorption.

The binomial density is given by:

$$p(N_{ij}) = {}^{M_{ij}}C_{N_{ij}} [\exp(-l_{ij}\mu_j)]^{N_{ij}} [1 - \exp(-l_{ij}\mu_j)]^{(M_{ij}-N_{ij})} \quad (7-21)$$

Since the emission process is Poisson distributed with the mean d_i , the probability density of the photons emitted from pixel 1 is:

$$p(N_{i1}) = \frac{d_i^{N_{i1}} \exp(-d_i)}{N_{i1}!} \quad (7-22)$$

Since each pixel is independent of the every other, the likelihood function for the entire complete data set is simply the product of the individual likelihood functions of each of the pixels along projection i :

$$f(X_i, \mu) = \frac{d_i^{N_{i1}} \exp(-d_i)}{N_{i1}!} \prod_{j=1}^{m-1} {}^{M_{ij}}C_{N_{ij}} [\exp(-l_{ij}\mu_j)]^{N_{ij}} [1 - \exp(-l_{ij}\mu_j)]^{(M_{ij}-N_{ij})} \quad (7-23)$$

The complete data log – likelihood (for projection i) is:

$$\begin{aligned} \ln f(X_i, \mu) = & \\ & -d_i + N_{i1} \ln d_i - \ln N_{i1}! + \sum_{j=1}^{m-1} \left\{ \ln({}^{M_{ij}}C_{N_{ij}}) \right. \\ & \left. + N_{ij} \ln[\exp(-l_{ij}\mu_j)] + (M_{ij} - N_{ij}) \ln[1 - \exp(-l_{ij}\mu_j)] \right\} \quad (7-24) \end{aligned}$$

When this is summed over all projections it yields:

$$\sum_i \ln f(X_i, \mu) = \sum_i \sum_{j=1}^{m-1} \{ N_{ij} \ln[\exp(-l_{ij}\mu_j)] + (M_{ij} - N_{ij}) \ln[1 - \exp(-l_{ij}\mu_j)] \} + R \quad (7-25)$$

where the term R includes all quantities that do not depend on the parameter μ_j . The maximization is carried out by computing the partial derivative with respect to μ_k and equating it to zero for each k . This yields:

$$\sum_i -N_{ik} l_{ik} + \sum_i (M_{ik} - N_{ik}) \frac{l_{ik}}{\exp(l_{ik} - 1)} = 0 \quad (7-26)$$

The above transcendental equation is solved using an approximation. Since in most practical applications $l_{ik}\mu_{ik}$ is small, the following relation is made use of:

$$\frac{1}{e^s - 1} = \frac{1}{s} - \frac{1}{2} + \frac{s}{12} + O(s^3) \quad (7-27)$$

Using the first two terms of the above expression with $s = l_{ik}\mu_{ik}$ in (7-27) we get

$$\mu_k^{n+1} = \frac{\sum_i (M_{ik} - N_{ik})}{\frac{1}{2} \sum_i (M_{ik} + N_{ik}) l_{ik}} \quad (7-28)$$

where μ_k^{n+1} indicates the estimate of μ in the k^{th} pixel for the $n + 1^{\text{th}}$ iteration. The above equations constitute the mathematical basis for the algorithm used for the image reconstruction in this research.

7.3.3 Details of the CT Scanner at CREL

In this work, the time averaged gas phase volume fraction measurements were performed with the computer tomography (CT) unit developed in-house in CREL by Kumar (1994). Figure 7-10 shows the schematic diagram of the setup. A detailed top view of the setup with the dimensions and angles that are used in the image reconstruction process are shown in Figure 7-11.

The support structure of the CREL CT setup consists of four threaded vertical guide rods on which a perfectly horizontal plate is positioned so as to allow its smooth vertical motion automated by gears. On this is fixed a “gantry” plate, and both plates have an aligned 2 feet diameter circular opening at the center to allow concentric positioning of the stirred tank. The gantry houses the 100mCi lead shielded Cs-137 source and an array of NaI(Tl) detectors which are positioned across the column diameter facing the source (7 detectors were used for the current study). The whole assembly (source plus detector array) rotates around the column during the data acquisition process, with the motion accurately timed and controlled by stepper motors. Thick lead shielding in front of the source is used to collimate the radiation into a fan beam whose angle can be varied to envelop the column of study. The detector array also has a lead collimator that can move, controlled by a stepper motor, in front of the detector (Figure 7-11). This novel

modification proposed by Kumar (1994) has been used to acquire 14 independent projection measurements per detector, which allows for a considerable improvement in spatial resolution at a minimal cost (as low as 2.0mm). In the current study the collimator slots have a width of 3.0 mm as against 6.0 mm used earlier (refer Figure 7-12). This reduction in collimator slot width enables us to use smaller pixel sizes (since smallest pixel size ~is equal to slot width). This also helps in better spatial resolution. During the data acquisition process, with the source switched on, the stepper motors control the motion of the rotating gantry in 99 positions spanning the 360° around the column. For each such “view”, the detector collimator moves 14 steps (and is then brought back to its original position) so as to acquire 14 independent projections for each detector per view. Thus, for the stirred tank reactor for which seven detectors are sufficient to span the fan beam, a total of 9702 projections were acquired ($14 \times 7 \times 99$). This with further spatial interpolation allows a final spatial resolution slightly less than 3.0 mm (the collimator slot width). The total scanning time, over which the holdup distribution is thus averaged, is a little over three hours.

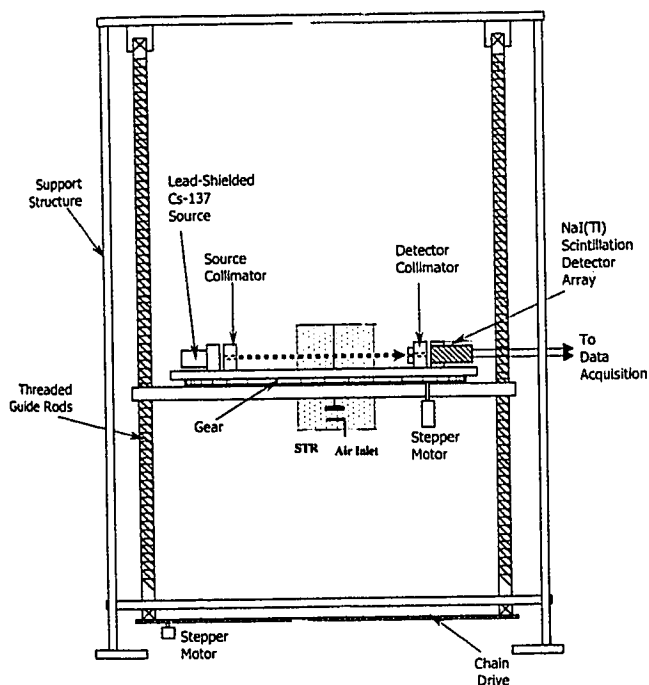


Figure 7-10. Schematic Diagram of the CREL Computer Tomography Scanner with the STR Installation (Front View)

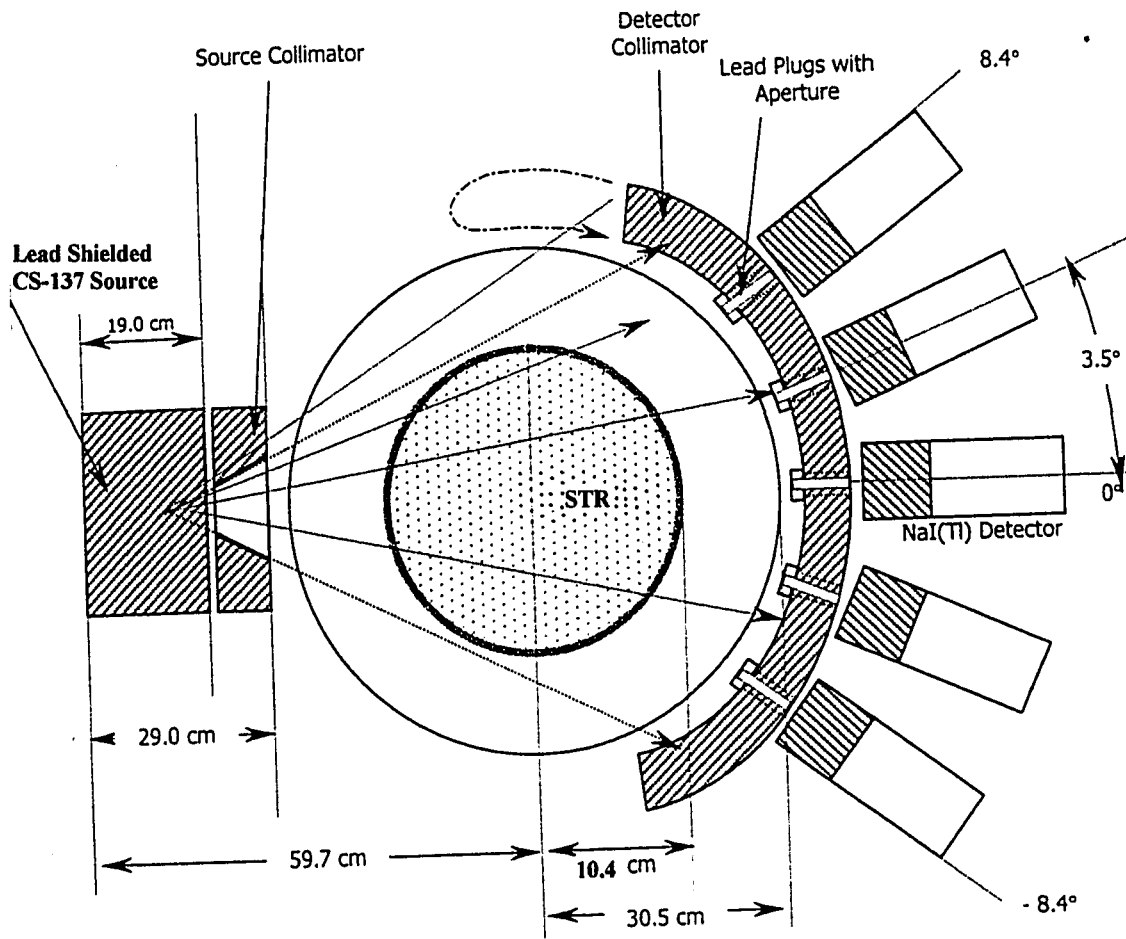


Figure 7-11. Schematic Top View of the CREL Computer Tomography (CT) Scanner with the Stirred Tank Installation, at One Specific Location of the Gantry Plate (Note that Dimensions and Angles are not to Scale and have been Exaggerated for Clarity)

The photon count data was acquired by using a threshold of 420mV which ensured that only the photo peak photons were collected and not the entire spectrum as was done earlier. The basis for doing this has been explained in Chapter 5. The adjusted spectra of the seven detectors is shown below in Figure 7-13.

Collimator in front of detector

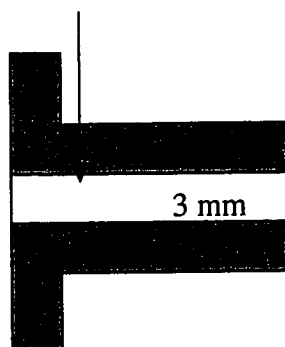
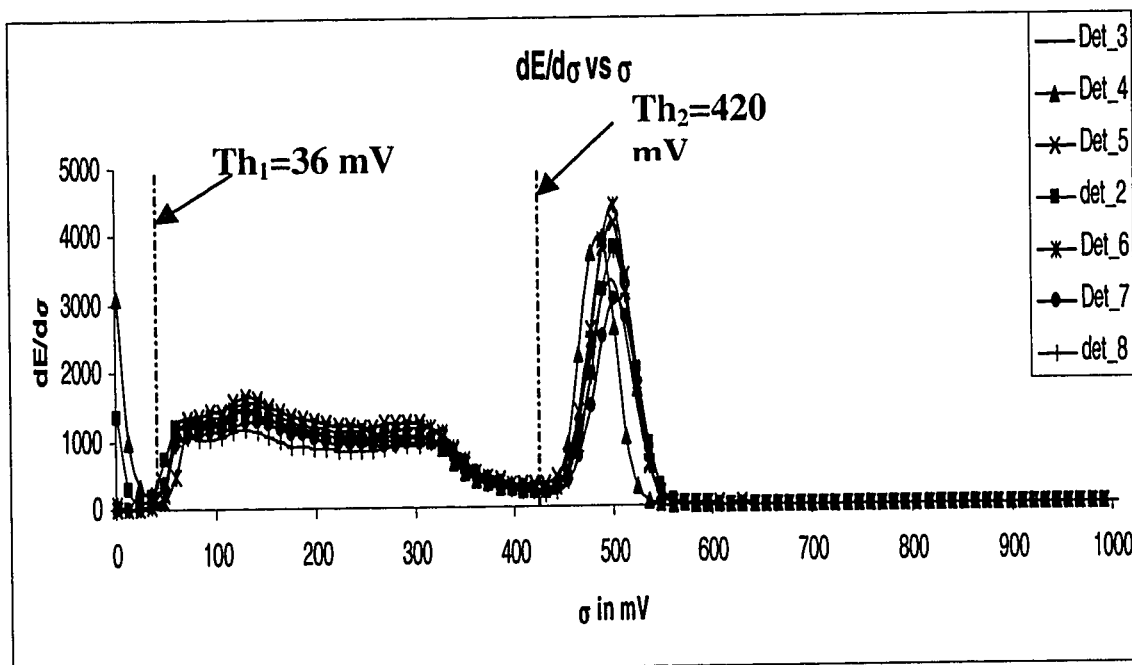


Figure 7-12. Details of New Collimator Used for Current Study

Figure 7-13. The Adjusted Photoenergy Spectrum of the Radiation Emitted by Cs¹³⁷ Received by the Seven Detectors

For image reconstruction the EM algorithm is used (refer to section 7.2.9), the implementation of which has been discussed in detail by Kumar (1994), and Kumar and

Dudukovic (1997). In order to ensure equivalent convergence of the different reconstruction cases (corresponding to changes in impeller speeds and gas flow rates) an internal convergence criterion has been defined as:

$$Res_{N+1} = \sum_{i=1}^{Npix} (\alpha_i^{N+1} - \alpha_i^N)^2 \quad (7-29)$$

where Res_{N+1} is the residual at the N+1 iteration, α_i^{N+1} is the value of the holdup in the i th pixel at the N+1 th iteration. This definition of the residual ensures that the difference in holdup in each pixel between the N+1 th iteration and Nth iteration reaches a certain minimum value predefined by the user. This criterion enables an automatic selection of the number of iterations required for the EM algorithm to converge. This simple criterion replaces the earlier procedure where the number of iterations for convergence was arbitrarily defined as 10-20 and ensures that the reconstructed images are all equally converged.

The CREL scanner currently has a spatial resolution of ~2-3 mm and a density resolution of 0.04 gm/cm^3 (Kumar, 1994). Radiation safety considerations limit the use of stronger source strengths, thus we need to acquire data for longer times which coupled with the other factors mentioned earlier limit the temporal resolution of the setup.

7.3.4 Sources of Errors in CT Measurements

A detailed analysis of the different sources of errors in CT measurements have been provided by Kumar (1995). Here a brief list of the errors and their importance is described. A detailed numerical analysis of one of the sources of errors is also provided.

The possible sources of errors in CT measurements are: statistical uncertainty in photon counts, system drift, Compton scattering effects, beam hardening effects, data sampling frequency in space, dynamic bias or void fluctuation effects, uncertainties due to the temporal structure of the flow and errors in the image reconstruction process. The issue of uncertainty in photon counts has been discussed in Chapter 5 and the error is kept to a minimum by sampling for a long enough time which ensures that the normalized variance

is negligible. System drift contribution was found to be minimal. The Compton scattering effects have no effect on the current study since only the photo-peak fraction of the total energy spectrum is acquired. Kumar (1994) indicates that emissions associated with single photopeak the beam hardening effects are negligible. The effect of frequency in space, dynamic bias and temporal structure of the flow can all be combined into one single “dynamic bias” error. This error is discussed in detail in Appendix A and a numerical model has been developed to quantify the maximum values of this error. The study revealed that this error is typically of the order of 1% for conditions of our interest.

7.3.5 Details of the Stirred Tank Set-up

We use the same stirred tank in which the single phase experiments were executed (refer to Chapter 3). To the existing set-up made modifications were made, which allow us to study gas–liquid flows. Lu and Ju (1987) used a ring sparger of diameter equal to $0.3T$ (T is tank diameter). The sparger consisted of a steel tube (dia = $0.02T$) and holes (dia= $0.007T$, spacing= $0.075T$, 4 #'s) are drilled on the tube. Our set-up follows their scaling relations. The details of our sparger are shown below in Figure 7-14:

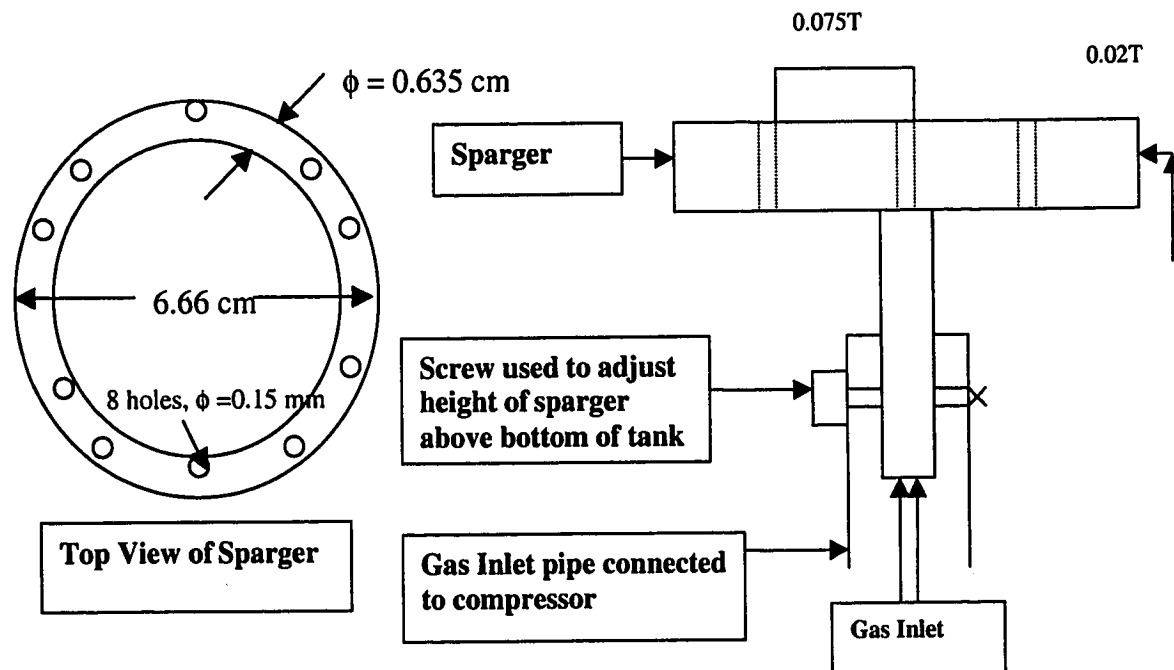


Figure 7-14. Details of Sparger Design

The sparger is made of clear plexi-glass. This configuration requires the least amount of modification to the existing system and is also the best from the point of view of having least interference from internals inside the reactor both for CARPT and CT. The sparger at the bottom causes much lesser disturbance to the CARPT and CT system than if we were to have a pipe running parallel to the axis and the ring sparger below the impeller. The details of the set-up with the sparger inside the tank is shown below in Figure 7-15.

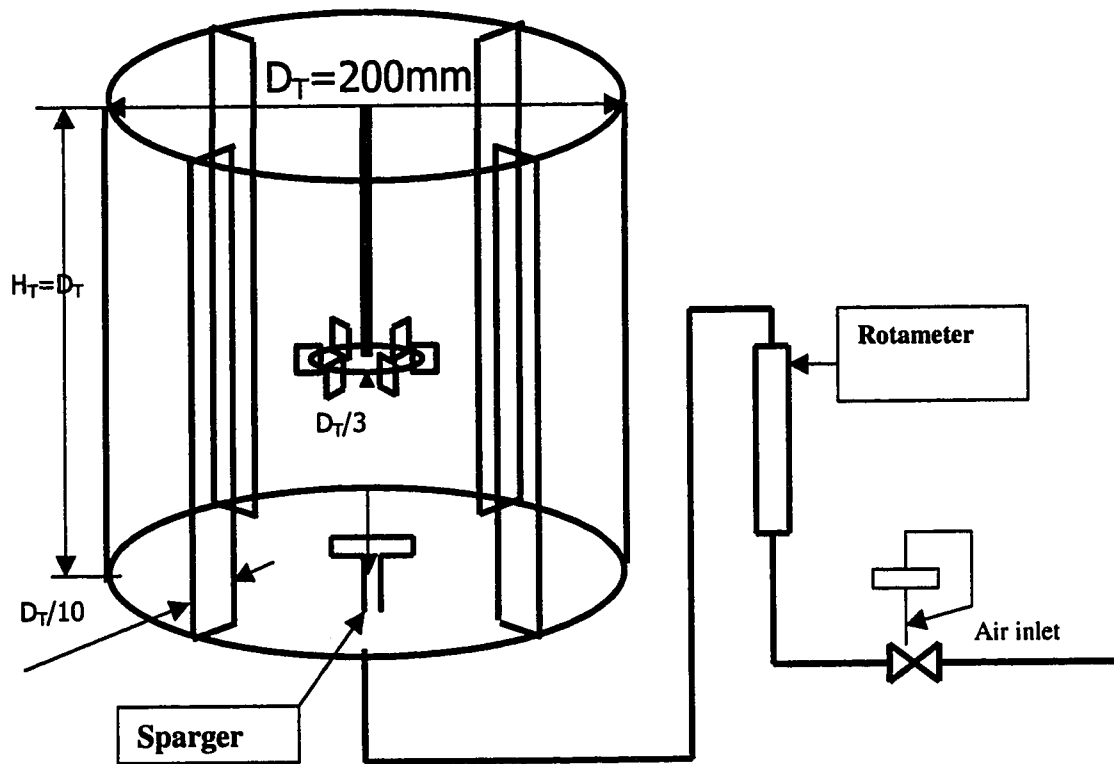


Figure 7-15. Details of the Stirred Tank Set-up Used for Gas –Liquid Studies

7.3.6 Experimental Conditions

Two dimensional time averaged gas holdup distributions in horizontal planes were measured at three different axial levels (5.0, 10 and 15 cm), at four different rpms (100, 150, 200 and 400) and at four different gas flow rates (0.5, 2.5, 5 and 7.5 l/min) which correspond to flow numbers in the range of 0.01-0.50. A flow regime map corresponding

to our data has been prepared along the lines of Bombac et. al. (1997) (refer to Figure 7-3). The map helps us to appreciate the flow regimes to which the different data points are expected to belong. From the map it can be seen that three data points belong to the vortex clinging cavity regime (VC), three belong to the S33 structure and a large number of the data belong to the regime between the Ragged cavity structure and the bubble column like regime. This is a limitation of the current data set that not much data is present in the fully established circulation regime which is typically of industrial interest. This limitation was largely due to the issue of dynamic bias of CARPT technique (refer Chapter 5, Section 5.2) at higher impeller speeds.

7.4 Results and Discussion

In order to test the ability of the CT set-up to capture the internals of the stirred tank reactor a scan of the empty vessel was performed with just the tank and then with the tank with internals i.e. baffles and impeller. The reconstructed holdup distribution of the glass internals in the tank is shown below in Figure 7-16.

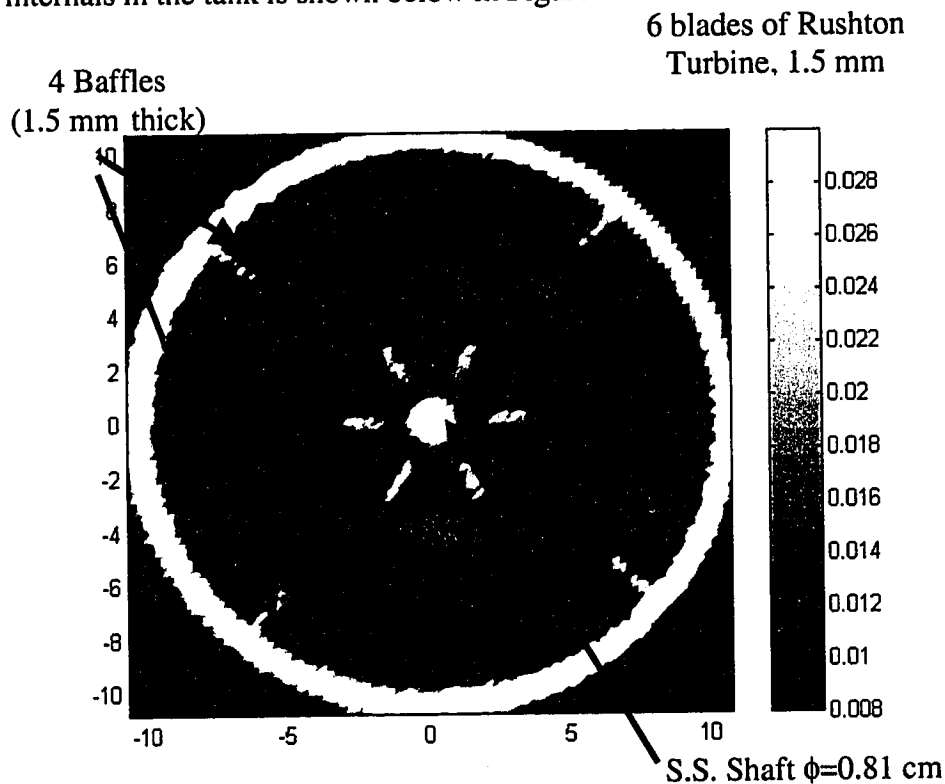


Figure 7-16. Reconstruction of Internals of the Stirred Tank Reactor

From the above Figure 7-16 it can be seen that CT can reconstruct the internals faithfully. This is very good considering the fact the blades and the baffles are as thin as 1.5 mm. The Figure 7-16 also shows that CT can clearly identify the four baffles and the six blades of the Rushton turbine. The presence of stainless steel shaft is also clearly seen as a hole of 0.81 cm diameter. Figure 7-16 also reveals that the impeller is centered perfectly in the tank.

A further test to check the ability of the CT setup was to take a scan of the axial plane above (1.67 cm) the sparger plane at very high gas flow rate ($Q_4=7.5$ l/min) and impeller speed of 100 rpm (N_1) corresponding to $Fl=0.253$ and $Fr=0.019$ (bubble column like regime from Figure 7-3). Under these conditions we expect to see jets of gas coming from the sparger holes. The CT scan obtained under these conditions has been processed to yield the gas holdup distribution which is shown below:

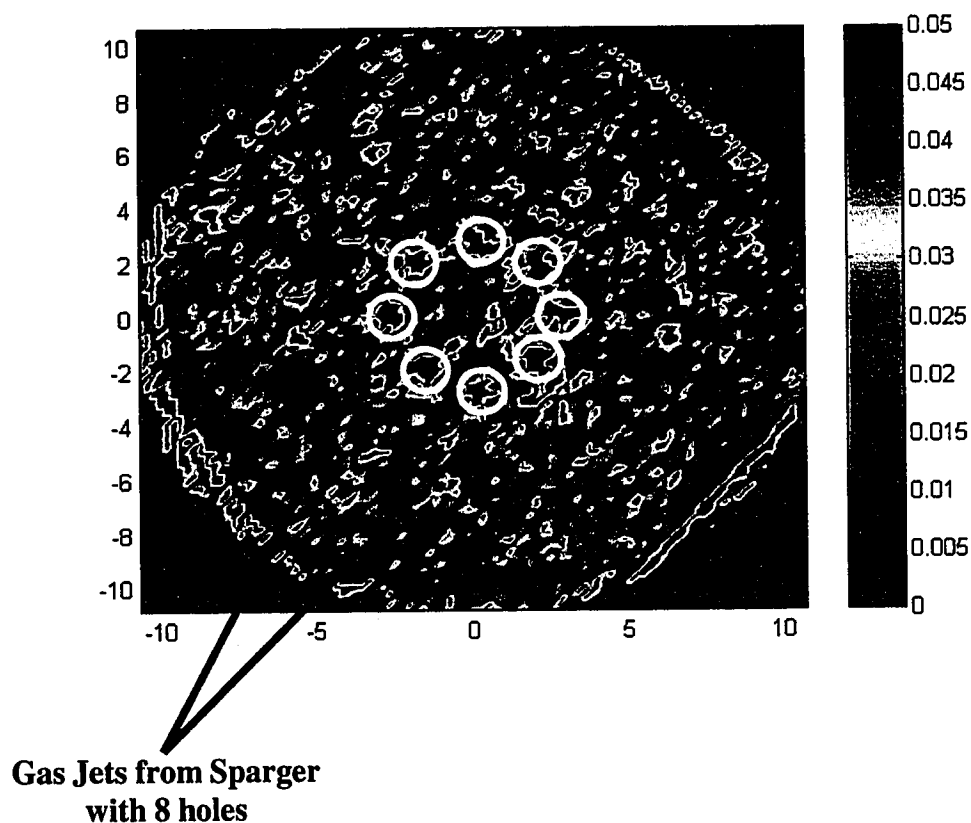


Figure 7-17. CT Scan of the Plane Just Above the Sparger ($Z=5.0$ cm, $Z/T=0.25$)

Figure 7-17 shows accumulation of gas in eight clear circles distributed axisymmetrically around the center. The diameter of these circles is approximately 1.0 cm. The radius of the circle along which these smaller circles lie is ~3.3 cm. The location of the gas pockets and the diameter of the circle along which they are distributed clearly shows that these pockets correspond to the eight jets of gas coming from the eight holes on the sparger. The radius of the sparger is 3.33 cm which confirms that these jets are indeed the gas from the sparger. The diameter of the holes on the sparger are of course much smaller, but it is to be expected that at such high velocities the diameter of the jet will increase rapidly with distance from the point of entry due to inertial effects.

The above tests suggest that the CT data collected in the stirred tank reactor can be expected to be reasonably accurate. In the following section further qualitative analysis of the CT data is provided.

7.4.1 Qualitative Analysis of Gas Holdup and Velocity Distributions

7.4.1.1 Analysis of Gas Holdup Distributions in the Stirred Tank Reactor

7.4.1.1.1 Analysis of Contours of Gas Holdups

There are fifty different data points from the CT experiments of which one select condition (of the three conditions at which CARPT data are available) is discussed below. The rest is shown in Appendix C. The figures that follow show the gas holdup distributions in the different axial planes in the stirred tank reactor. The figures are analyzed for the distribution pattern of gas and possible asymmetries in the distribution of gas. In the figures below the gas holdup distribution at three different axial planes at $Fl=1.112$ and $Fr=0.042$ (Ragged Cavity regime) is discussed. In general, for each condition the gas holdup at the highest axial plane i.e. $Z=15\text{cm}$ ($Z/T=0.75$) is lower than the holdup values found in the other two axial planes. At the lowest plane i.e. $Z=5\text{ cm}$ ($Z/T=0.25$) a ring of gas can be seen with a radius of around 3.3 cm (black circle marked region A in Figure 7-18a). This ring obviously corresponds to the region of gas jetting from the sparger. For a fixed gas flow rate an increase in impeller speed increases the

amount of gas found in this region A (due to greater gas dispersion) while an increase in gas flow rate for fixed impeller speed seems to result in the gas being concentrated more within the circle of radius 3.3 cm.

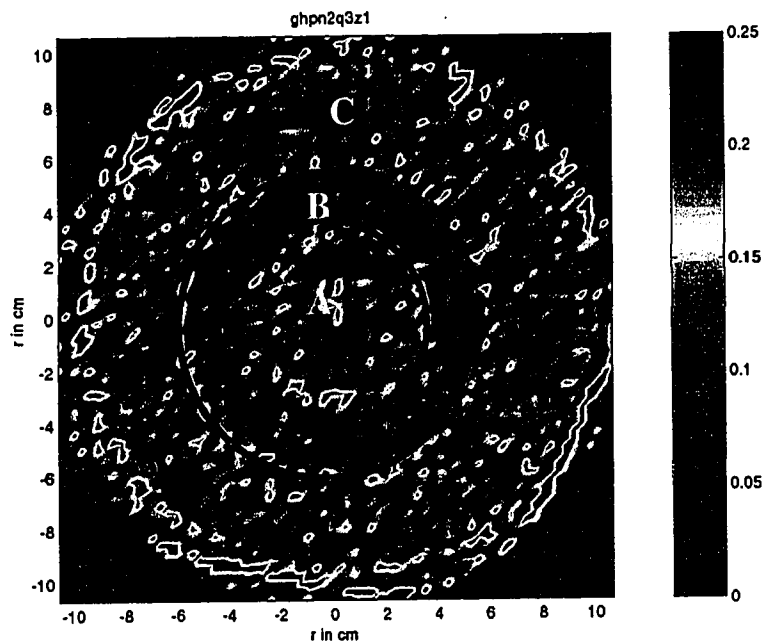


Figure 7-18(a). Gas Holdup Distribution at $Fl= .112$, $Fr= .042$ ($N=150$ rpm, $Q=5.0$ l/min) and $Z=5.0$ cm ($Z/T=0.25$)

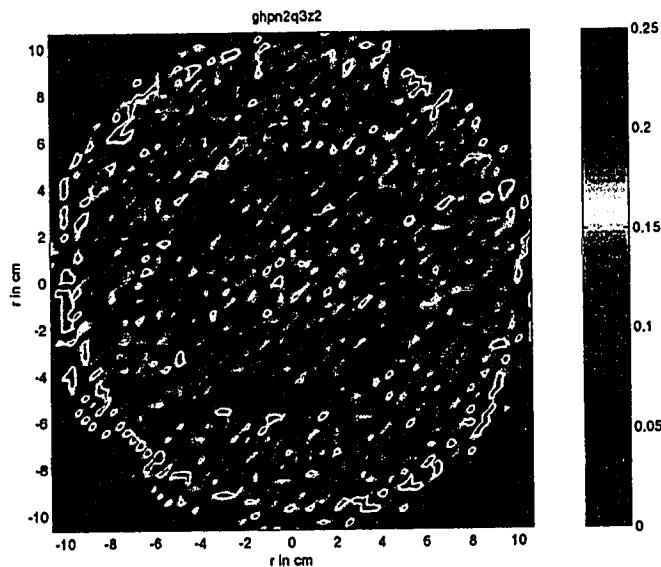


Figure 7-18(b). Gas Holdup Distribution at $Fl= .112$, $Fr= .042$ ($N=150$ rpm, $Q=5.0$ l/min) and $Z=10.0$ cm ($Z/T=0.5$)

The gas holdup in the outer ring seems (region marked C in Figure 7-18a) unchanged at the different conditions in the lowest axial plane. At the central plane $z=10$ cm ($Z/T=0.5$) two zones exist, a central ring and an annular ring. At this plane as expected the sparger effect is not felt. The central ring probably corresponds to the stream of gas either rising like in a bubble column or the gas being brought down by the liquid being drawn into the impeller region.

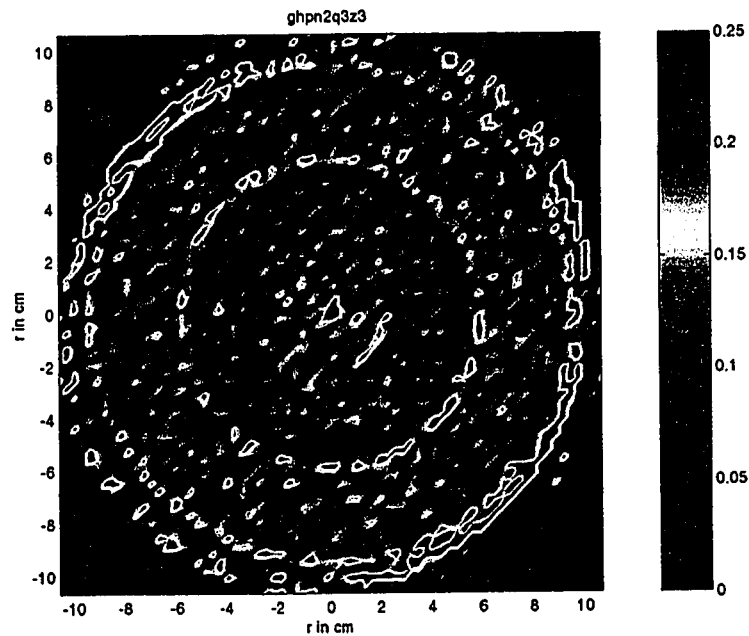


Figure 7-18(c). Gas Holdup Distribution at $Fl = .112$, $Fr = .042$ ($N=150$ rpm, $Q=5.0$ l/min) and $Z=15.0$ cm ($Z/T=0.75$)

The gas in the outer ring probably corresponds to the gas rising up either with its terminal velocity or being dragged up by the liquid. In the central plane, for a fixed impeller speed, increasing the gas flow rate seems to increase the gas holdup in the outer ring and a decrease in the gas holdup in the inner ring. This would suggest that the gas seen in the central region is more probably due to the gas being drawn into the impeller region by the liquid than the gas rising up like in a bubble column. At the highest axial plane $Z=15$ cm ($Z/T=0.75$) the behavior is similar to the central plane although at a fixed impeller speed the gas in the central portion remains the same but the amount of gas in the outer ring increases. In all the above cases the gas is seen to be distributed axisymmetrically. The

above analysis shows that CT data is capable of providing a wealth of information which can help in both visualizing the flow structures and as will be seen below in quantifying the flow field in the presence of gas.

7.4.1.1.2 Variation of Average Gas Holdups with Impeller Speeds and Gas Sparging Rates

In this section from the CT data global average of the gas holdup is computed and the variation is plotted with impeller speeds and gas sparging rates. The global average is obtained by axially averaging the value of gas holdup obtained earlier at the different elevations of $Z/T=0.25, 0.5$ and 0.75 respectively.

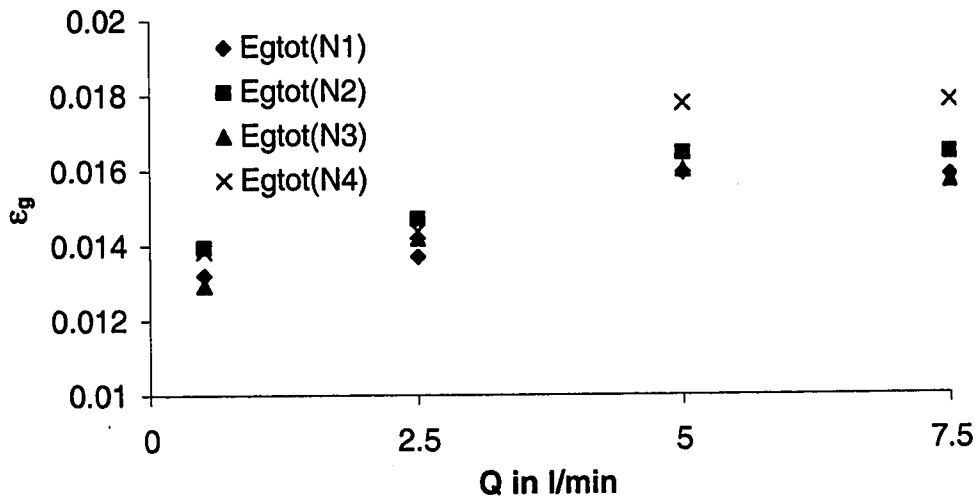


Figure 7-19(a). Variation of Overall Gas Holdup with Gas Sparging Rate at Different Impeller Speeds

The overall gas holdups for the conditions studied are seen to be very low with the maximum overall holdup being slightly less than 2.0%. It must be mentioned that since CT data was available only at three axial planes the measure of overall holdup is may not

be very accurate. Hence we present this data in the qualitative section to show that even with the limited data the global average obtained from CT follows the expected trends. Figure 7-19(a) shows that with increase in gas flow rate the overall gas holdup increases. At low gas sparging rates (i.e. less than 2.5 l/min) the overall gas holdups at different impeller speeds are pretty close to each other. It is beyond the gas sparging rate of 2.5 l/min that with increase in impeller speeds the gas holdups get higher. Even for this case the average holdups for impeller speeds between 100-200 rpm are very close to each other. It is only at 400 rpm that a distinct increase in the gas holdup can be seen for the higher gas sparging rates. This clearly shows that CT can capture the right trends for variation of overall holdups. In Figure 7-19(b) we plot the variation of overall gas holdup from CT with $F_{l, gas}$. Here we compare the measured variations of overall gas holdup with the values predicted by the correlations of Hassan and Robinson (1977), Matsumara et. al. (1977) and Barigou and Greaves (1987).

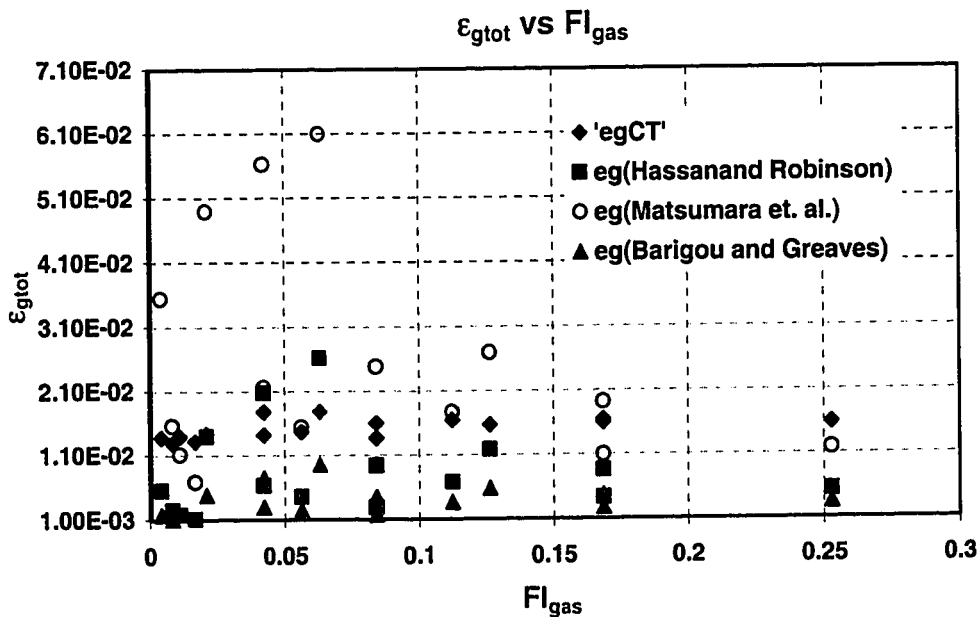


Figure 7-19(b). Comparison of Overall Holdup from CT with Predictions of Correlations

Both Hassan and Robinson (1977) and Matsumara et. al. (1977) performed experiments in tanks of dimensions comparable to that used in the current study while Barigou and

Greaves performed experiments in a tank five times the size of the tank used in this study. However, Barigou and Greaves (1987) account for variations in scale of the system. Figure 7-19(b) shows that the overall holdup obtained from CT is banded between the results Matsumara et. al. (1977) and the correlations of the other two researchers. At low Fl the predictions from Matsumara et. al. (1977) are much higher than those obtained with CT. The figure 7-19(b) suggests that CT predicts overall gas holdups which are comparable to those predicted by the correlations.

7.4.1.2 Analysis of Liquid Velocity Distributions obtained with CARPT

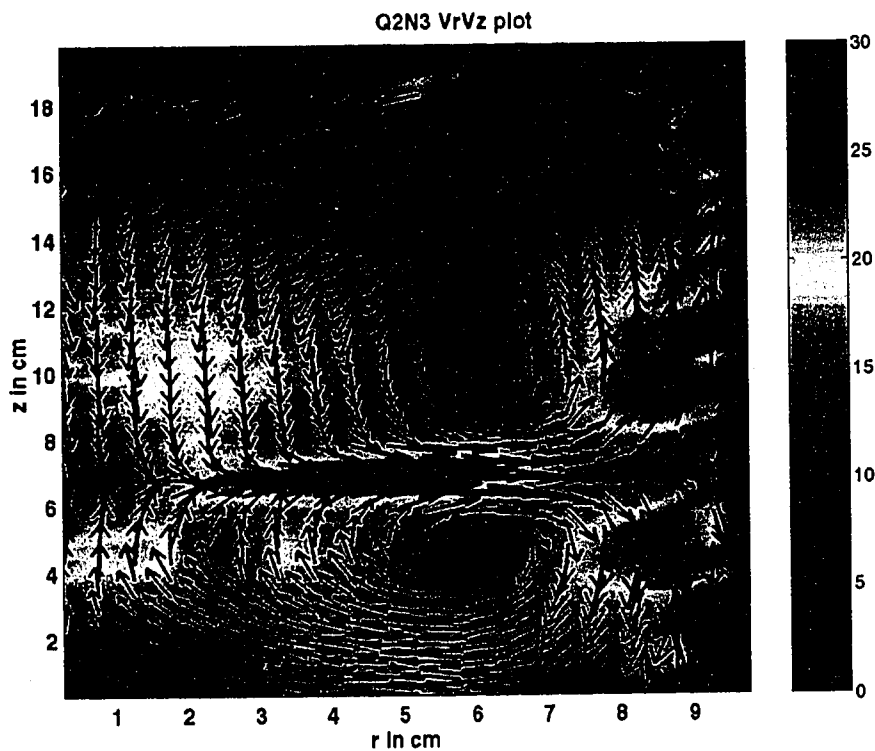


Figure 7-20. Azimuthally Averaged V_r - V_z Plot at $Fl=0.042$ and $Fr = 0.0755$ ($N=200$ rpm, $Q= 2.5$ l/min, S33 regime)

The azimuthally averaged velocity vector plot in the r - z plane at $Fl=0.042$ and $Fr=0.0755$ ($N=200$ rpm and $Q=2.5$ l/min) is shown in Figure 7-20. The plot shows the classical recirculating flow structure seen in the single phase flow in stirred tanks. The figure is

colored by contours of the magnitude of the velocity vectors in this plane. The impeller region is seen clearly by the radial jet emerging from the impeller. The radial jet, however, unlike in single phase flow does not extend all the way up to the wall. The jet seems to extend at least up to 8.0 cm which is $0.4T$ (T is tank diameter). The velocity vectors near the wall region and the top of the reactor are not seen clearly due to small tracer particle occurrences in those regions. The recirculating structures are characterized by two loops. The upper loop has a recirculating region of height ~ 4 cm from $H=8$ cm to $H=12$ cm with the center of the loop around 10 cm, i.e. height of the loop is $0.2T$ and extends from $0.4H$ to $0.6 H$. The upper recirculating structure extends radially from ~ 5 – 7 cm, i.e. $0.25T$ to $0.35 T$ with the center around 6 cm i.e. $0.3T$. The radial jet is not any more horizontal but is inclined at some angle to the horizontal pointing upwards. The lower recirculating loop has a smaller height but the radial location is similar to the upper loop. The height of the lower loop is ~ 2 cm i.e. $0.1T$ and is half the height of the upper loop.

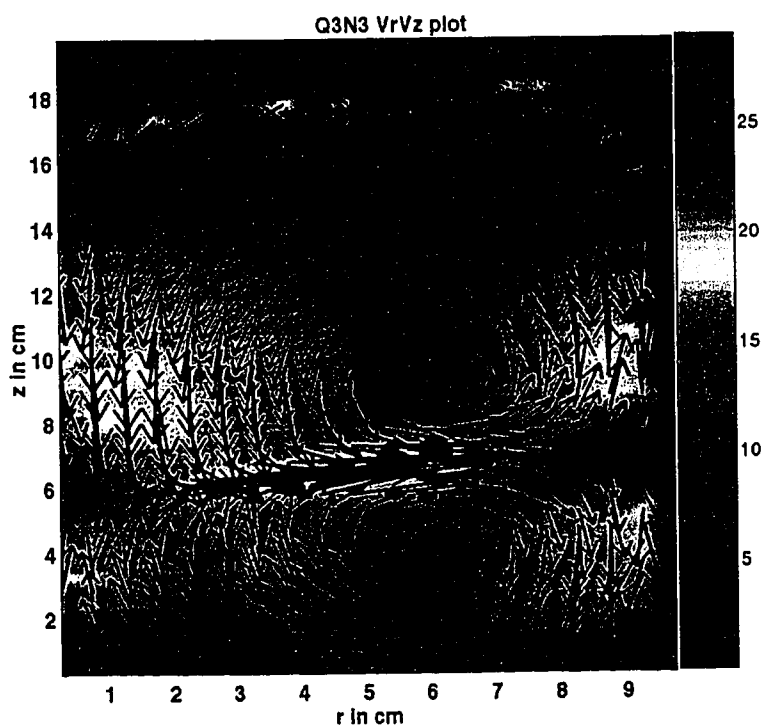


Figure 7-21. Azimuthally Averaged V_r - V_z Plot at $Fl = 0.084$ and $Fr = 0.0755$ ($N=200$ rpm, $Q= 5.0$ l/min, RC regime)

The azimuthally averaged projection of the velocity vector in the r-z plane at $Fl=0.084$ and $Fr= 0.0755$ ($N=200$ rpm, $Q= 5.0$ l/min) is shown in Figure 7-21. The plot shows the classical recirculating flow structure seen in the single phase flows in stirred tanks. The figure is colored by the magnitude as in Figure 7-20. The general characteristics of the flow under this condition is very similar to that seen in Figure 7-20. The length of the radial jet is seen to be slightly shorter than in Figure 7-20 with the jet extending up to 7.0 cm i.e. $0.35T$ while earlier it had extended upto $0.4T$. The upper recirculating loop is smaller in height than the one seen in Figure 7-20. The height is ~ 2.0 cm which at $0.1T$ is half the height of the earlier loop. The center of the upper loop has also moved down to 9.0 cm i.e. $0.45T$. The radial width of the upper and lower loops remain the same. The reduction in the size of the upper loop can be explained by the fact that the increase in the gas sparging rates lower the liquid velocity coming out from the impeller. Hence, when the liquid encounters the wall and starts rising up, due to the lower velocity it can not go as high as it could earlier. This causes the liquid to fall back earlier and therefore the recirculation into the impeller region is seen to begin much earlier. A similar reasoning explains the reduction in the length of the radial jet as well.

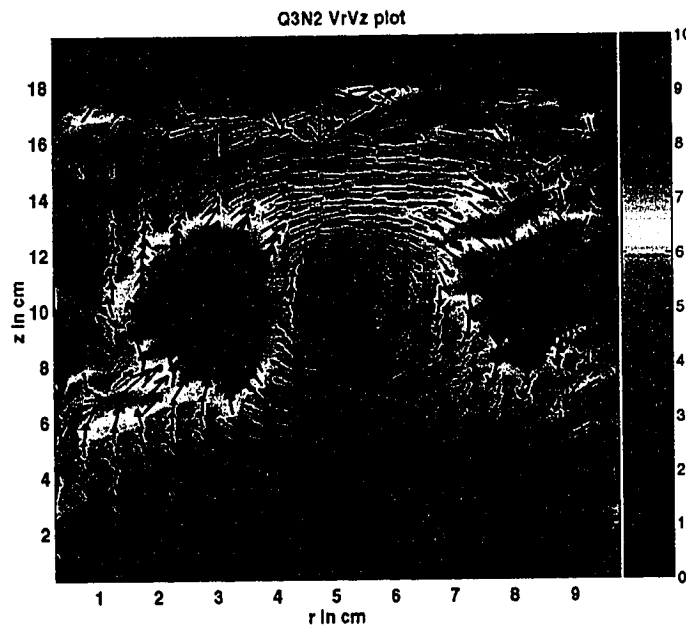


Figure 7-22. Azimuthally Averaged V_r - V_z Plot at $Fl = 0.112$ and $Fr = 0.042$ ($N=150$ rpm, $Q= 5.0$ l/min, RC regime)

From the flow regime map (Figure 7-3) it can be seen that two of the CARPT data points belong to the Ragged Cavity regime (Figures 7-21 and 7-22) with one (Q3N2) being closer to the bubble column like regime (Figure 7-22) and the third one is on the transition between Ragged cavity and S33 structure (Figure 7-20). This partially explains the velocity vector plot in the r-z plane we see in Figure 7-22. The figure shows that under these conditions of gas sparging rates ($Fl=0.112$ and $Fr=0.042$) the influence of the impeller is greatly diminished. None of the classic flow structure elements are seen except for the presence of a recirculating loop which is more characteristic of bubble column like flows. The direction of the liquid flow is totally opposite to that seen in the earlier two figures (7-20 and 7-21) as now at the impeller plane the liquid is flowing radially inward while near the top the liquid is flowing radially outward. This flow structure is akin to the flow structure expected in a bubble column. The upper loop has dimensions similar to the upper loop seen in Figure 7-20. The height is the same and the radial width is the same. However the radial location is shifted inward by 1.0 cm ($0.05T$).

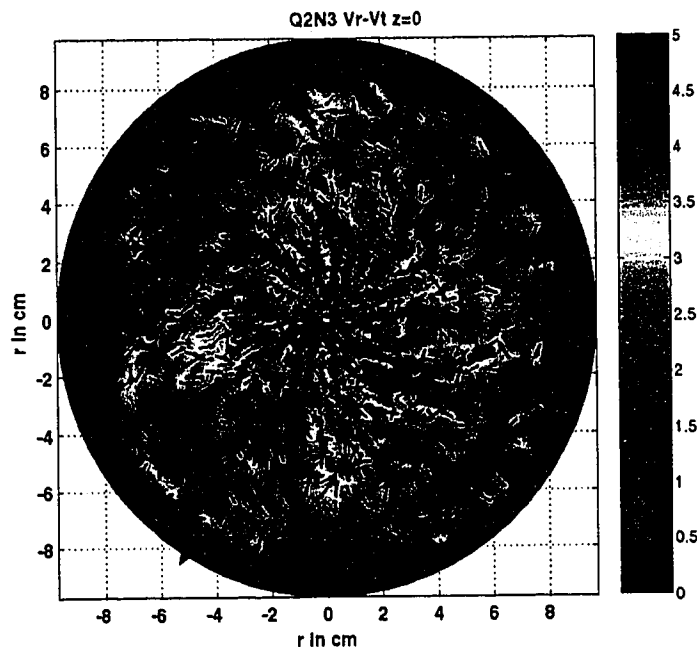


Figure 7-23. Azimuthally Averaged V_r - V_θ Plot at $Fl = 0.042$ and $Fr = 0.0755$ ($N=200$ rpm, $Q= 2.5$ l/min, S33 regime) at $Z=0$ cm ($Z/T=0$)

The velocity vector projection plotted in the axial plane corresponding to the bottom plane is shown above in Figure 7-23 at $Fl=0.042$ and $Fr=0.0755$ ($N=200$ rpm, $Q= 2.5$ l/min, S33 regime). The flow pattern is very different from the flow pattern seen for the single phase case (Refer Chapter 3) where a starfish like pattern was observed with clear zones of high liquid velocity surrounding zones of low velocity.

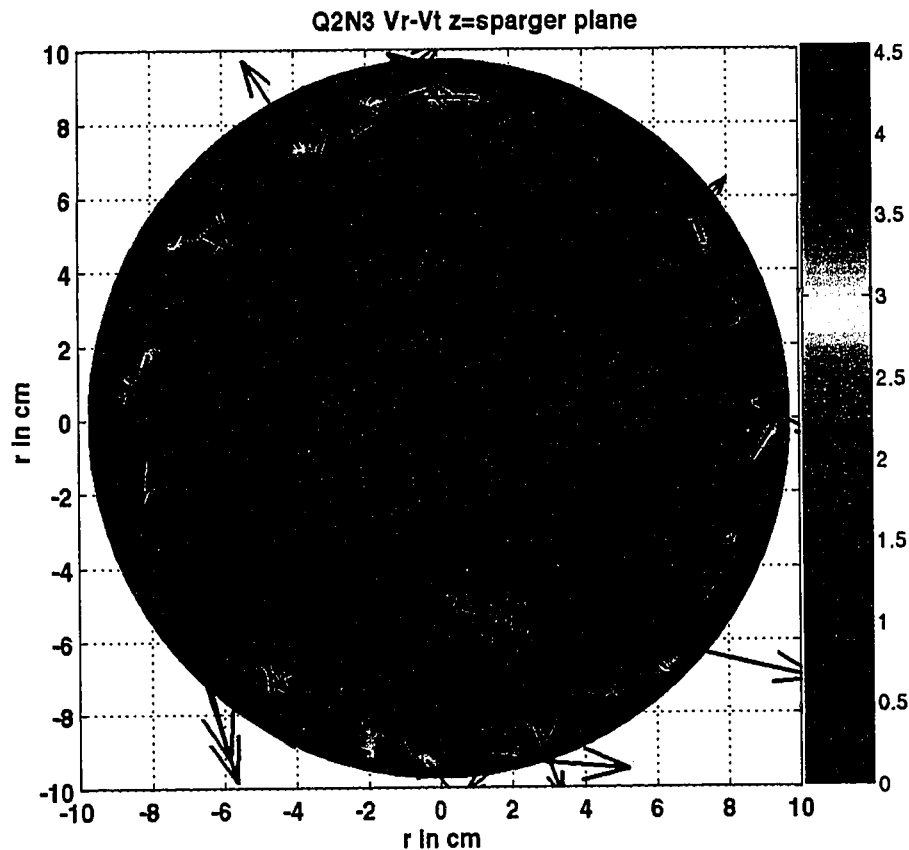


Figure 7-24. Azimuthally Averaged V_r - V_θ Plot at $Fl = 0.042$ and $Fr = 0.0755$ ($N=200$ rpm, $Q= 2.5$ l/min, S33 regime) at $Z=4.0$ cm ($Z/T=0.2$)

Figure 7-24 shows the distribution of the velocities in the axial plane just above the sparger. This plane shows a very interesting vortical structure of the liquid flow. There are four recirculating structures symmetrically distributed around the center. At the center is a region of high velocity. The central region is seen to have a radius of 2.0 cm. The outer boundary of the vortical structures are seen to lie along a circle of radius 4.0 cm clearly indicating that the vortical structures are due to the gas jets coming from the

sparger. In this plane the tangential flow is obviously stronger than the radial flow implying that the impeller influence is not very strong here except near the center. The very large velocity vectors very near the wall zone are artifacts of the technique which could not be filtered.

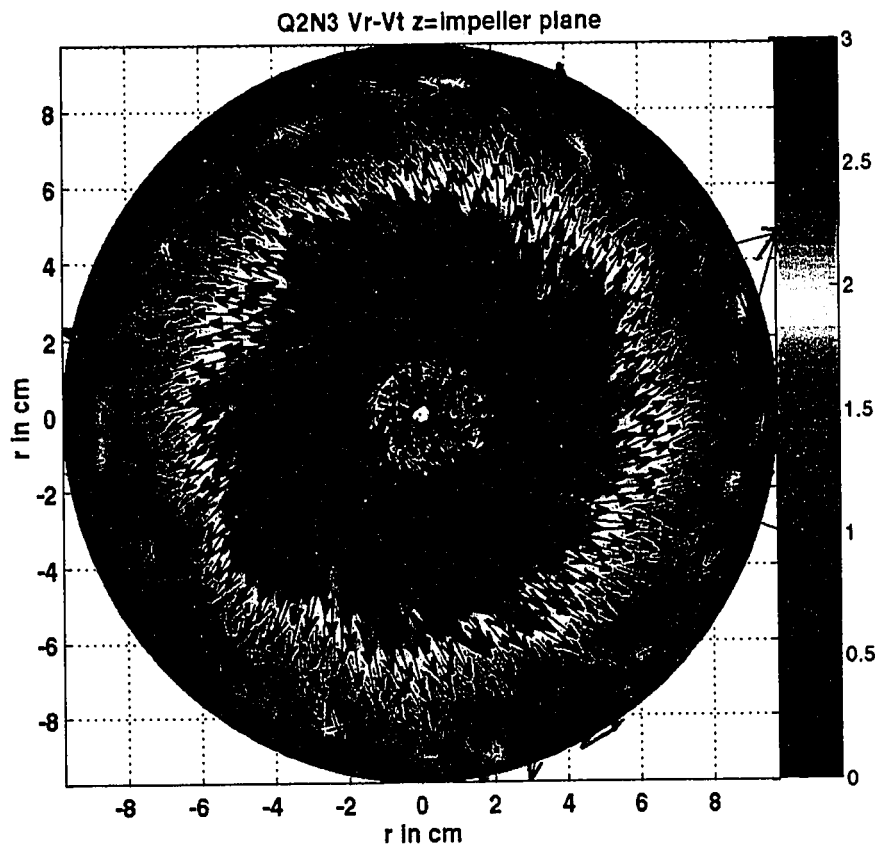


Figure 7-25. Azimuthally Averaged V_r - V_θ Plot at $Fl=0.042$ and $Fr=0.0755$ ($N=200$ rpm, $Q=2.5$ l/min, S33 regime) at $Z=6.66$ cm ($Z/T=0.33$)

The projection of the velocity vectors in the plane of the impeller is shown above in Figure 7-25. The vector plot shows the classical radial flow emerging from the impeller. The radial flow is seen to extend up to nearly 8.0 cm which matches with the length of the radial jet seen earlier in Figure 7-20.

This completes the qualitative analysis of the data obtained with CARPT and CT for gas – liquid flows in our stirred tank. In the following sections some quantitative analysis of the CARPT-CT data is presented.

7.4.2 Quantitative Characterization of Gas Holdup Distributions and Liquid Velocity Field

7.4.2.1 Azimuthally Averaged Radial Gas Holdup Distributions

Detailed radial variation of the azimuthally averaged gas holdup profile is shown below in Figures 7-33 to 7-35. The figures show the variation for different gas sparging rates and at different axial locations. From the figures it can be seen that the local holdups for the current study vary from 0-26%.

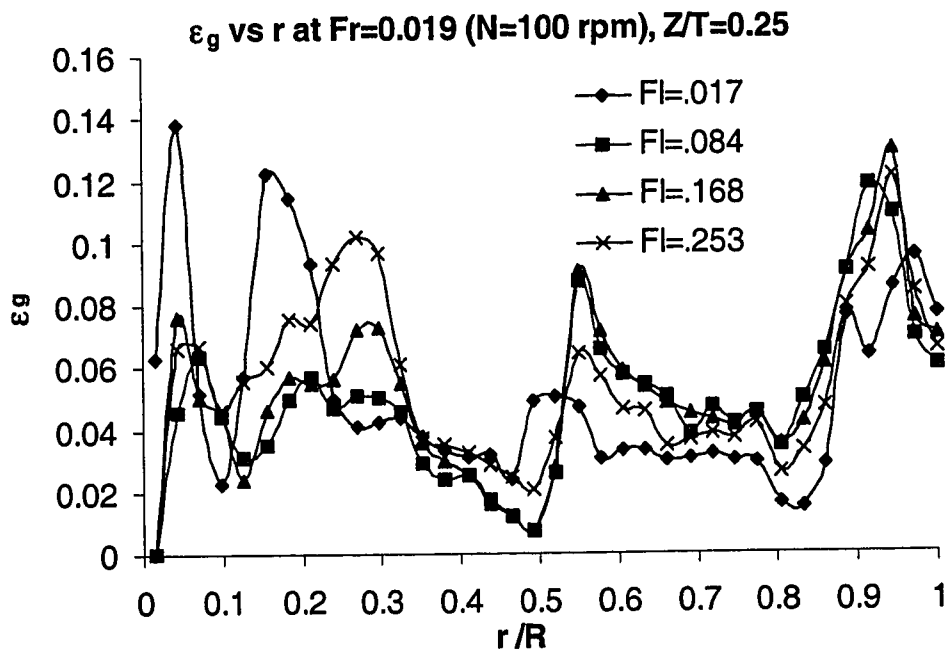


Figure 7-26(a). Influence of Gas Sparging Rates on the Radial Variation of Gas Holdup at $Fr=0.019$ ($N=100$ rpm), $Z/T=0.25$

Figure 7-26(a) which displays the gas holdup variation in a plane below the impeller indicates a distinct pick in the region corresponding to the impeller tip i.e. $\sim r/R=0.33$. At $Fl=0.017$ there is an accumulation of gas near the shaft region and the peak for this flow rate is seen near $r/R=0.2$ (where the impeller blades begin). The peak is seen to shift to the impeller tip with increase in Fl at fixed Fr . For all gas flow rates there is a second distinct peak in the bulk region near $r/R=0.6$. This peak probably corresponds to the region where the axial velocity changes direction. A third distinct peak is seen near the wall region where the gas holdup is rather high. In the impeller region an increase in gas sparging rate is seen to cause an increase in the gas holdup with a holdup of nearly 10% at $Fl=.253$. In the bulk region the gas holdup at all gas flow rates except the lowest are pretty close to each other.

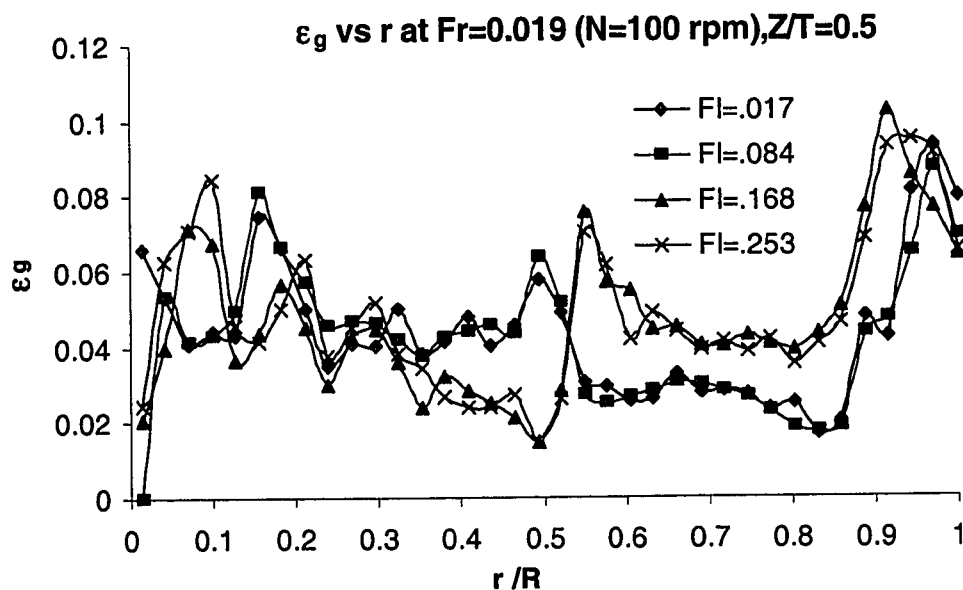


Figure 7-26(b). Influence of Gas Sparging Rates on the Radial Variation of Gas Holdup at $Fr=0.019$ ($N=100$ rpm), $Z/T=0.5$

Figure 7-26(b) shows the variation of gas holdup at $Z/T=0.5$ at $Fr=0.019$ ($N=100$ rpm). In this plane there is a tendency for gas to accumulate in the region around the shaft. The influence of the impeller is not really felt in this plane. The peak in the bulk region

around $r/R=0.6$ is seen once again. In the bulk region the holdups seem to follow two branches: an upper branch corresponding to the two high flow rates and a lower branch corresponding to the two low flow rates. The gas holdup is seen to peak in the region near the wall. The location of the peak in the bulk is slightly inward ($\sim 0.55r/R$) for the lower two flow rates while for the higher flow rates it is around 6.0 cm. The maximum holdup is around 10%.

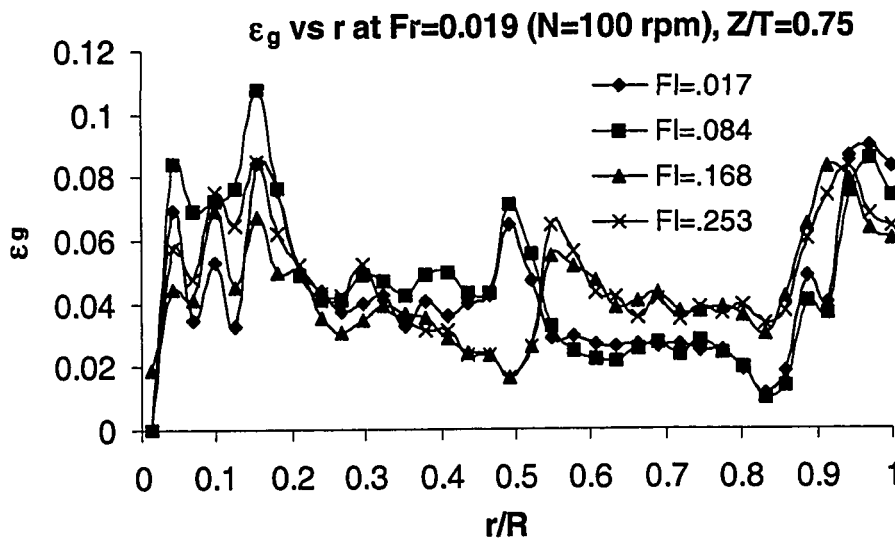


Figure 7-26(c). Influence of Gas Sparging Rates on the Radial Variation of Gas Holdup at $Fr = 0.019$ ($N = 100$ rpm), $Z/T = 0.75$

Figure 7-26(c) shows the variation of gas holdup at $Z/T=0.75$ at $Fr=0.019$ ($N=100$ rpm). The gas holdup near the center has increased compared to the earlier two axial planes. Unlike at $Z/T=0.25$ the holdup corresponding to $Fl=0.017$ is the lowest and the holdup near the center increases with gas sparging rate. Similar to the results at $Z/T=0.5$ a peak is seen in the bulk region and the location of the peak region shows a similar inward shift for the lower two flow rates (which are very close to each other). Hence, qualitatively in the two axial planes $Z/T=0.5$ and $.75$ a similar trend of gas holdup is observed with the only difference being a slightly higher value of gas holdup near the center in the $Z/T=0.75$ plane and the maximum value of gas holdup in this plane is $\sim 11\%$.

The above analysis shows that CT is capable of providing extensive local information regarding the gas holdup distributions in the stirred tank reactor. It is also seen that CT can capture both low and high values of gas holdup with ease. The CT obtained radial profiles also show the expected qualitative trends and the measures of global averages like the overall gas holdup show the right qualitative trends. There is at present no other source of such detailed local measurements which would enable a more detailed quantitative validation of the technique.

7.4.2.2 Liquid Velocity Distributions from CARPT

Figure 7-27 shows the radial variation of the radial liquid velocity profile at two different axial planes ($Z/T=0.19$ and 0.33). Figure 7-27(a) shows the radial variation at $Z=3.75$ cm ($Z/T=0.19$) which corresponds to the top surface of the sparger from which the gas jet is emerging. The radial velocity at Q2N3 ($Fl=0.042$, $Fr=0.0755$) is predominantly radially inward (hence the negative sign). The radial velocities in this plane are low with a maximum magnitude of -5.8 cm/s. The radial liquid velocity corresponding to Q2N3 is the maximum one since impeller speed is the highest and the gas flow rate is the lowest. For the same impeller speed increasing the gas flow rate results in lowering the magnitude of the radial velocity by almost 66%. For the same gas flow rate Q3 a reduction in impeller speed from N3 to N2 ($Fr=0.0755$ to $Fr=0.042$) makes the magnitude of the radial velocities extremely low with a maximum value of -1 cm/s. The radial liquid velocity at Q3N3 ($Fl=0.084$, $Fr=0.0755$) turns radially inward at radial location of 2.2 cm while for Q2N3 it remains radially inward almost until $r=0.75$ cm ($r/R=0.075$). This difference in the location of the change in direction is due to the higher liquid velocity at lower gas flow rate which causes the liquid to be drawn into the impeller with greater intensity than at higher gas flow rate. Figure 7-27(b) shows the radial variation in the plane of the impeller. The radial jet causes a region of high velocity in the bulk starting from the region near the start of the impeller blade up to almost $r=5-6$ cm ($r/R=.5$ to $.6$). The radial profile of the radial velocity in the impeller region looks quite different from the radial profile seen for the single phase case where the radial

velocity peaks close to the impeller tip and starts decreasing rapidly. Here the presence of gas is seen to cause the maximum value to be spread out radially. Further the maximum radial velocity for Q2N3 is only $0.387 V_{tip}$ and for Q3N3 is only $0.287 V_{tip}$ which is much lower than the $0.57 V_{tip}$ observed for the single phase case. Therefore sparging of gas causes drastic reduction in radial velocities.

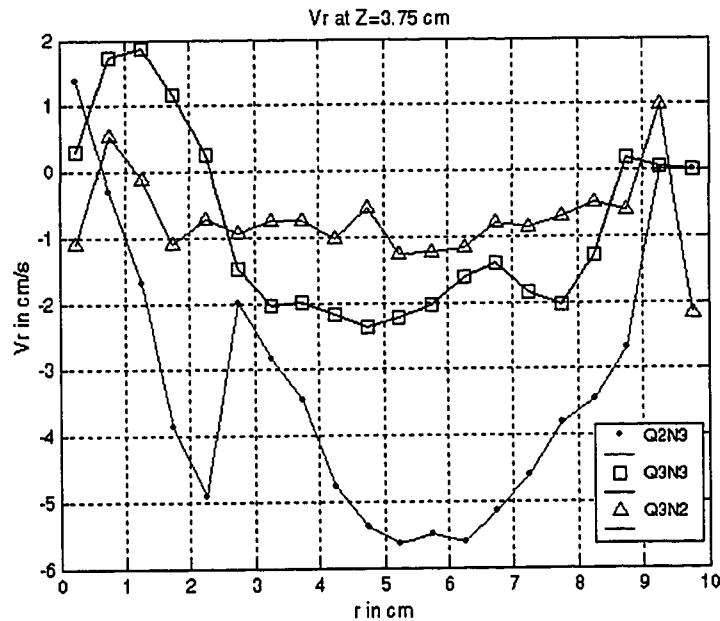


Figure 7-27(a). Radial Profile of Radial Liquid Velocity at Sparger Plane $Z=3.75$ cm

Increasing impeller speed is seen to clearly cause an increase in the radial velocities and for a fixed impeller speed decreasing the gas sparging rate causes an increase in the radial liquid velocity. Figure 7-28 shows the radial variation of the tangential velocity. At $Z=3.75$ cm (Figure 7-28(a)) the tangential velocity corresponding to Q2N3 is the highest near the center and progressively decreases away from the center. Interestingly the direction of the liquid rotation of the fluid changes sign in the bulk ($\sim r=6.0$ cm). The positive sign indicates that the direction of rotation coincides with the direction of rotation of the impeller. The change in direction of rotation occurs at $r=6.0$ cm both for the Q2N3 case and the Q3N3 case. This is clearly associated with the flow reversal observed at this radial location (refer to Figures 7-20 and 7-21). In the region near the

center the tangential velocity for Q2N3 is higher than the tangential velocity for Q3N3 by almost 50% and then it falls almost on top of the other in the bulk region.

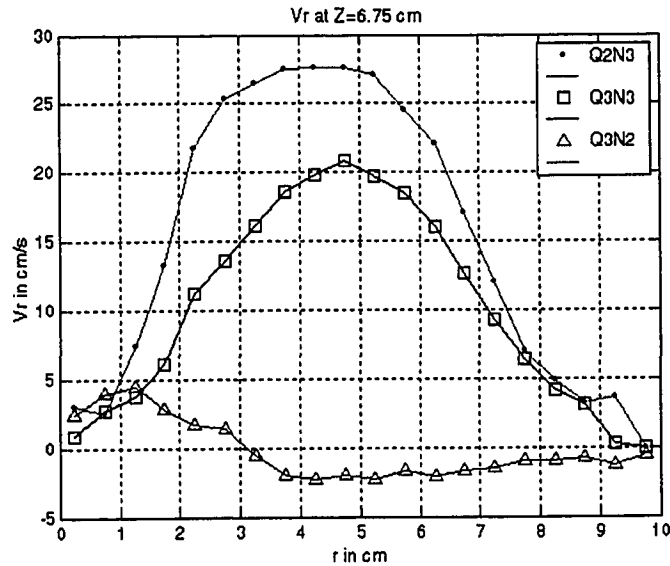


Figure 7-27(b). Radial Profile of Radial Liquid Velocity at Impeller Plane $Z=6.75$ cm

Interestingly the tangential velocities for the Q3N3 and the Q3N2 cases are very close to each other (less than 10%) in the central region.

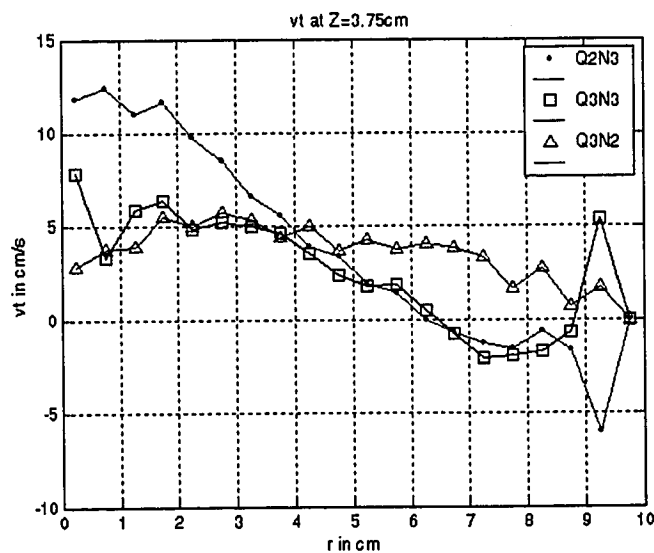


Figure 7-28(a). Radial Profile of Tangential Liquid Velocity at Sparger Plane $Z=3.75$ cm

Figure 7-28(b) shows the radial variation of the tangential velocity in the impeller plane. The Q3N2 case has a peak value of $0.6 V_{tip}$ while the Q3N3 case has a peak value of $0.286 V_{tip}$. The location of the peak value is $r=2.25$ cm ($r/R=.225$) for the Q3N2 case and $r=3.25$ cm ($r/R= .325$) for the Q3N3 case. The decrease in the tangential velocity away from the impeller is similar for the Q3N3 and Q3N2 case with the curves being almost parallel to each other beyond $r=5.0$ cm ($r/R=0.5$). Between $r=2.25$ ($r/R=0.225$) to $r=5.0$ cm ($r/R=0.5$) for the Q3N2 case the tangential velocity falls more rapidly than in the Q3N3 case. The Q3N2 case, as expected, does not have a peak near the impeller tip since this is the bubble column like flow regime (refer to Figure 7-23) where the impeller action is minimal. The Q3N2 case has a peak in the tangential velocity near the center ($r=1.25$ cm, $r/R=.125$) and then the velocity falls subsequently. Beyond $r=4.0$ cm ($r/R=0.4$) the bulk liquid is not subject to any rotation in this case.

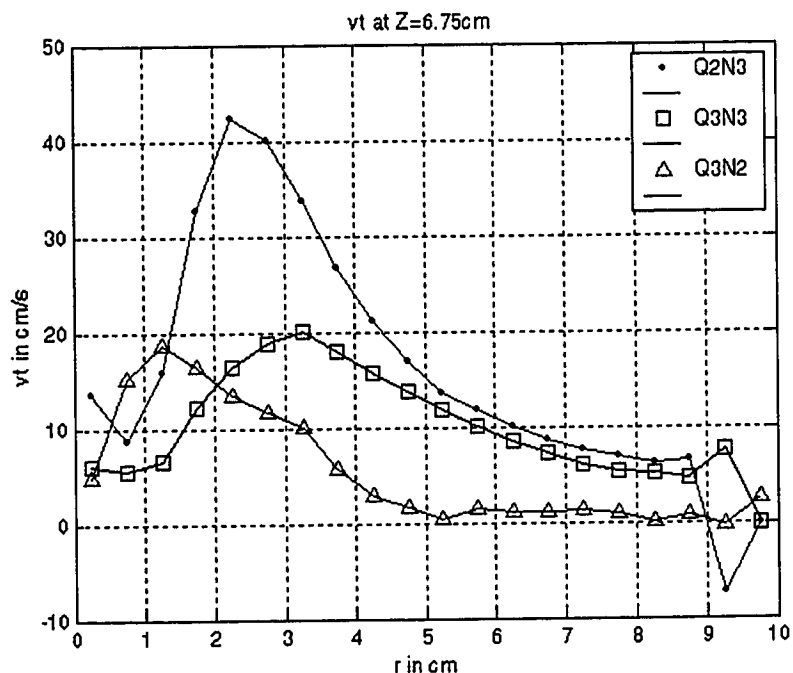


Figure 7-28(b). Radial Profile of Tangential Liquid Velocity at Impeller Plane $Z=6.75$ cm

The radial variation of the axial velocities is shown in Figure 7.29. These plots indicate that the axial velocities cross over from positive to negative velocities at $r=6.0$ cm

($r/R=0.6$) i.e. from flow upward to flow downward (in the planes below the impeller) and from flow downward to flow upward (in the planes above the impeller). This along with Figures 7-20 and 7-21 indicate that this radial location corresponds to the eye of the upper and lower circulating loops. Hence these regions are associated with very low velocity which causes the gas to accumulate in the eye of these recirculating loops. Figure 7-29(a) shows the radial variation of the axial velocity at $Z=3.75$ cm. The axial velocities at Q2N3 and Q3N3 are 2 to 2.6 times higher than the axial velocity at Q3N2 near the center. The axial velocities at Q2N3 are 1-40% higher than the axial velocities at Q3N3. Differences between Q2N3 and Q3N3 are more pronounced near the center and the walls. The differences are much lower in the bulk region. The axial velocities for the Q3N2 fall to zero around $r=3.0$ cm ($r/R=0.3$) indicating that there is almost no flow in this region. This is also seen clearly from the velocity vector plot shown in Figure 7-23.

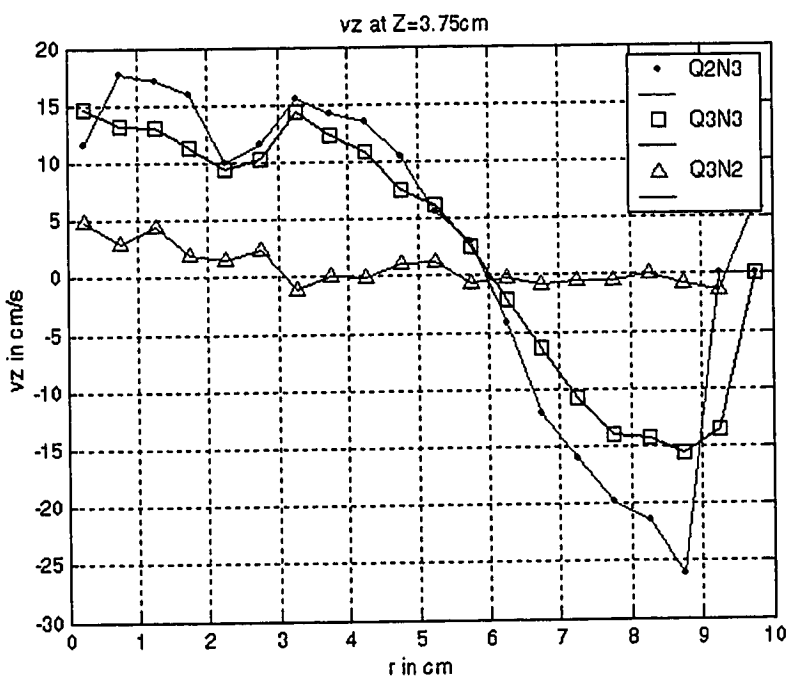


Figure 7-29(a). Radial Profile of Axial Liquid Velocity at Sparger Plane $Z=3.75$ cm

Figures 7-29(b) show the reversal of flow with the radial location where the reversal occurs at $r=6$ cm ($r/R=0.6$). At $Z=10$ cm the Q3N2 case shows a peak in the upward axial velocity near the center extending from $r=2$ to 3.75 cm ($r/R=0.2$ to 0.375) beyond which it

starts falling and becomes negative at $r=5.0$ cm ($r/R=0.5$). The axial velocity corresponding to Q2N3 is higher (5-20%) than the axial velocity of Q3N3. This completes the detailed analysis of the radial variation of the radial, tangential and axial velocities at select axial planes of interest in the stirred tank reactor. In the following section the axial variation of these velocity components is discussed in detail.

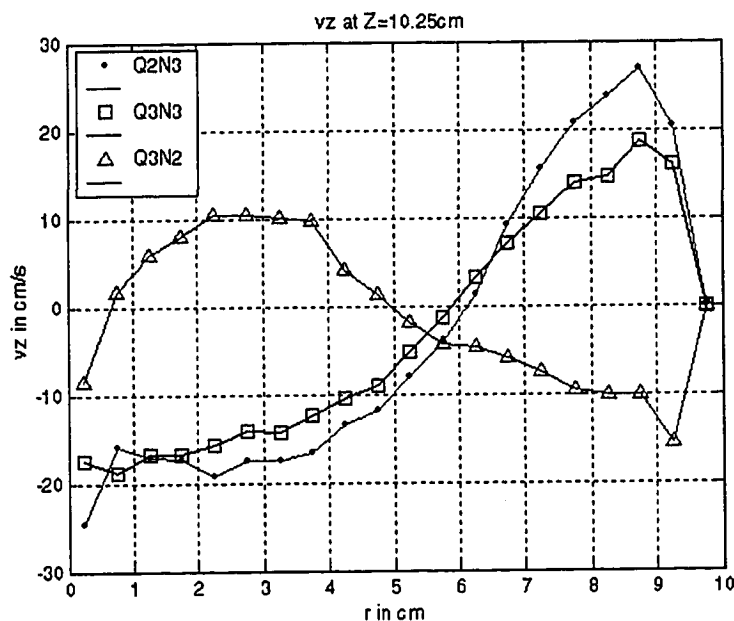


Figure 7-29(b). Radial Profile of Axial Liquid Velocity at $Z=10.25$ cm

Figure 7-30 shows the axial variation of the radial velocity at three different radial locations $r=2.25$ cm, 3.75 and 6.25 cm ($r/R=0.225$, 0.375 and 0.625) corresponding to regions near the start of impeller blade, impeller tip and point of flow reversal respectively. Figure 7-30(a), 7-30(b) and 7-30(c) show the influence of the impeller motion on the radial velocity. The maximum radial velocity is seen at $r=3.75$ cm ($r/R=0.375$) as expected. The radial velocity corresponding to Q2N3 is always higher (10-50%) than the velocities corresponding to Q3N3 case. As expected the Q3N2 cases shows no influence of the impeller. The axial profile of the tangential velocities (Figure 7-31) show a similar behavior as the radial velocities as seen from Figure 7-30, except for the fact that the impeller influence is not felt at $r=6.25$ cm ($r/R=0.625$). The other two inner radial locations show the impeller influence clearly and the maximum value of the

tangential velocity is seen at $r=2.25$ cm and not at $r=3.75$ cm. This behavior is to be expected and has been clearly established for the single phase case by Stoots and Calabrese (1995).

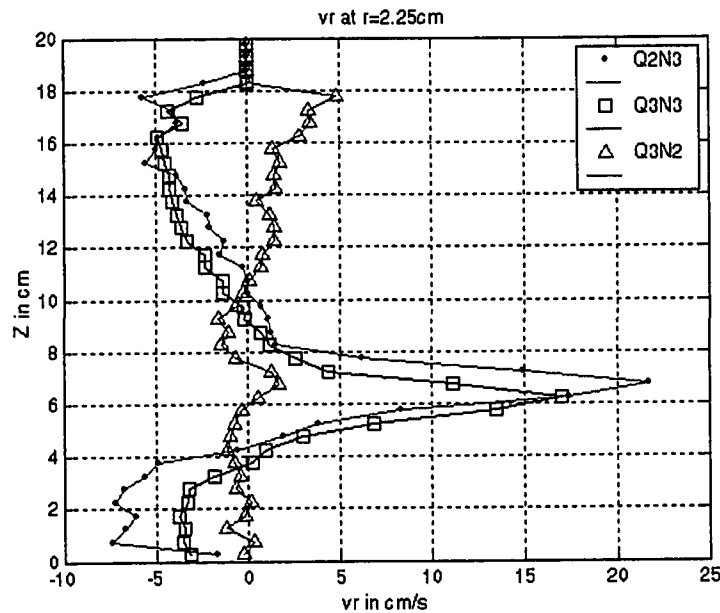


Figure 7-30(a). Axial Profile of Radial Liquid Velocity at $r = 2.0$ cm

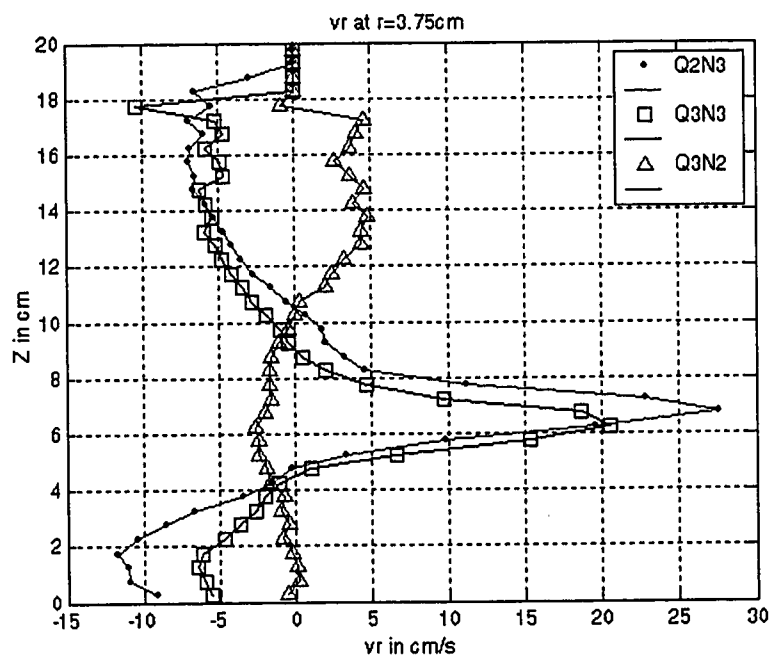


Figure 7-30(b). Axial Profile of Radial Liquid Velocity at $r = 3.75$ cm

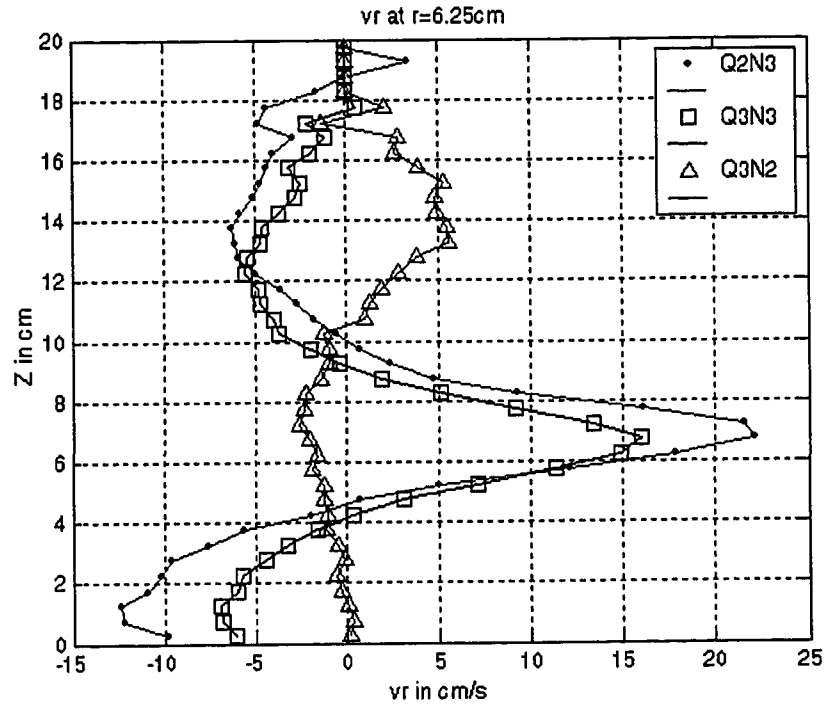


Figure 7-30(c). Axial Profile of Radial Liquid Velocity at $r = 6.25$ cm

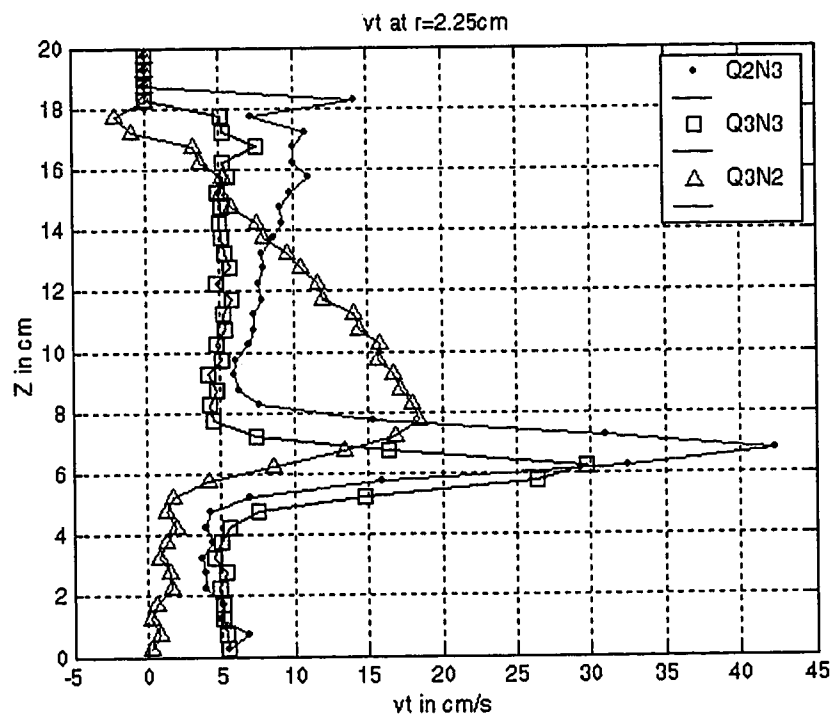


Figure 7-31(a). Axial Profile of Tangential Liquid Velocity at $r = 2.0$ cm

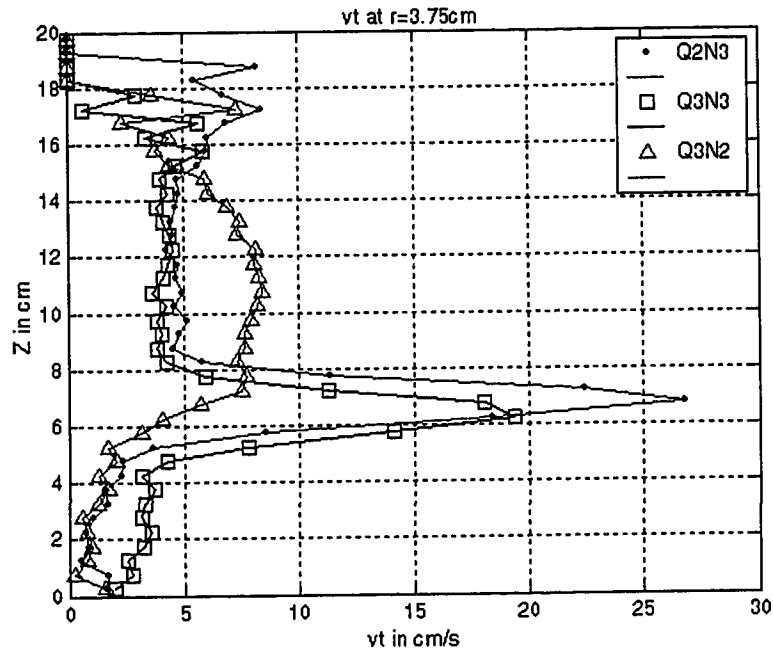


Figure 7-31(b). Axial Profile of Tangential Liquid Velocity at $r = 3.75$ cm

This completes the detailed analysis of the liquid velocity distributions in the stirred tank reactor in the presence of gas. The analysis reveals that together CARPT and CT data provide extensive qualitative and quantitative information regarding the nature of the gas – liquid flows. The analysis also shows that it is the combination of the two techniques which allows us to extract a more complete picture of the nature of the flow. The current limitation of lack of temporal resolution currently prevents CT from giving us information about the transient nature of the gas cavities near the impeller region.

Figure 7-32 shows the radial profile of the turbulent kinetic energy at the impeller plane. The turbulent kinetic energy for the three different conditions are comparable and the slopes are almost parallel to each other. The kinetic energy starts increasing from the center until near the wall and then it falls to zero rapidly near the wall region. The profile of the turbulent kinetic energy is similar to the profiles reported earlier (refer to Chapter 2) by Ranade and Van den Akker (1994). The non-dimensional maximum values for Q2N3 and Q3N3 are $0.74V_{ip}^2$ and $1.35V_{ip}^2$ for the Q3N2 case. The profile of the turbulent kinetic energies are the same at the different axial planes and hence the detailed

profiles have not been shown here. The radial profiles of turbulent kinetic energy in the presence of gas are very different from the profiles seen with single phase flows (Refer to chapter 4).

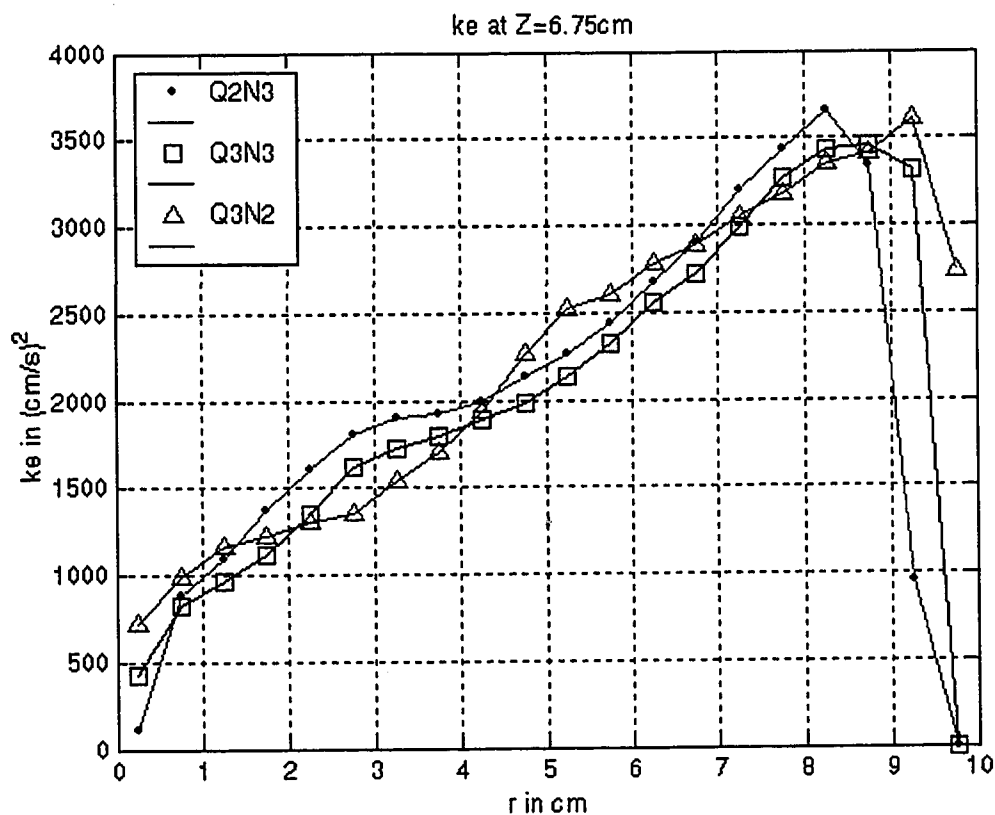


Figure 7-32. Radial Profile of Turbulent Kinetic Energy at the Impeller Plane

In single phase flows the maximum turbulent kinetic energy is typically seen near the impeller region while in the presence of gas the maximum is seen near the wall region.

7.5 Gas Liquid Flow Simulations via Snapshot Approach

Earlier efforts to model two phase flows in stirred tank reactors have been reviewed in Chapter 2 (section 2.4). The details of the snapshot approach are also provided in Chapter 2. The geometry and grid used for the two phase simulations are the same as those used for single phase simulations (refer to chapter 4). In the current study we use the two fluid

approach (Ishii, 1975 ; and Johansen, 1988). Drag is the only interphase term accounted for. Preliminary simulations were done with the default drag option in FLUENT and subsequently Tomiyama's drag correlation modified by Brucato et. al. (1998) correction factor to account for background turbulence was used. This correction factor enables the prediction of lower slip between gas and liquid which helps the gas to follow the liquid more closely. In the current work we use a bubble diameter of 3.0 mm. A standard single phase k- ϵ turbulence model (Lauder, 1983) has been used to model the primary phase turbulence. Secondary phase turbulence effects have been ignored. Boundary conditions for liquid are similar to those used for single phase simulation (refer to chapter 4). Gas was introduced through the sparger by activating the momentum source for the gas phase equations in the cells above the sparger. The gas velocity and holdup were specified such that there was an appropriate gas flow rate in the sparger region. The top surface of the reactor was modeled as an inlet (for details refer to Ranade, 2001). Gas liquid simulations were performed at a) N3Q1- impeller speed of 200 rpm, $Q=0.5$ L/min b) N3Q3 – impeller speed of 200 rpm, $Q=5$ L/min and c) N4Q1- impeller speed of 400 rpm, $Q=0.5$ L/min. The converged results of N3Q1 were used as initial guesses for both N3Q3 and N4Q1 case. Below we present some preliminary results.

7.5.1 Results and Discussions

Typical velocity vector plots of the gas and liquid phase are shown below in Figures 7-33a and 7-33b at conditions N3Q1 and N3Q3. Figure 7-33(a) shows that for the N3Q1 case the liquid velocity vectors resemble the single phase recirculating flow structure characterized by a radial jet in the impeller region and two recirculating loops above and below the impeller. According to Figure 7-3 this condition corresponds to the vortex clinging cavity regime and the Fr number is high enough for it to have more than limited recirculation but less than complete recirculation of the gas phase. However, a look at the gas phase velocity vectors suggests that there is negligible gas recirculating and most of the gas just rises up through the center of the column. This would suggest that the interfacial slip velocities between gas and liquid are high probably because the drag

coefficient is being underestimated. Figure 7-33(b) shows the liquid and gas phase velocity vectors corresponding to the N3Q3 (bubble column like regime, Figure 7-3, Chapter 7). This figure qualitatively looks similar to the Figure 7-22 (Chapter 7) but here the impeller is still seen to be effective. In Figures 7-34(a) and 7-34(b) the contours of turbulent kinetic energy and holdup are shown at N3Q1 and N3Q3, respectively.

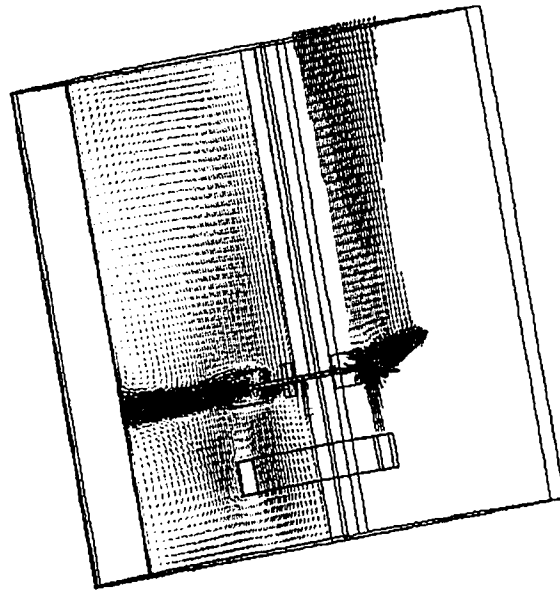


Figure 7-33(a). Predicted Flow Field for N3Q1 Case. Left: Vectors of Liquid Phase;
Right: Vectors of Gas Phase

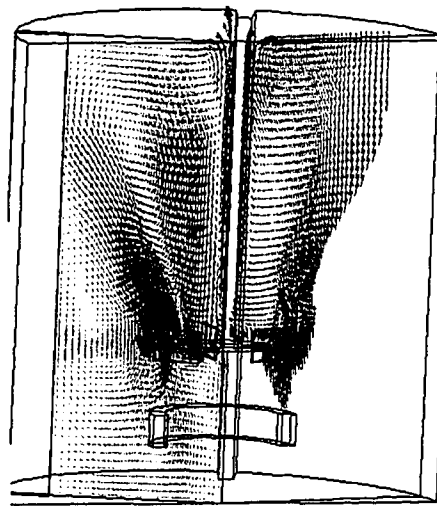


Figure 7-33(b). Predicted Flow Field for N3Q3 Case. Left: Vectors of Liquid Phase;
Right: Vectors of Gas Phase

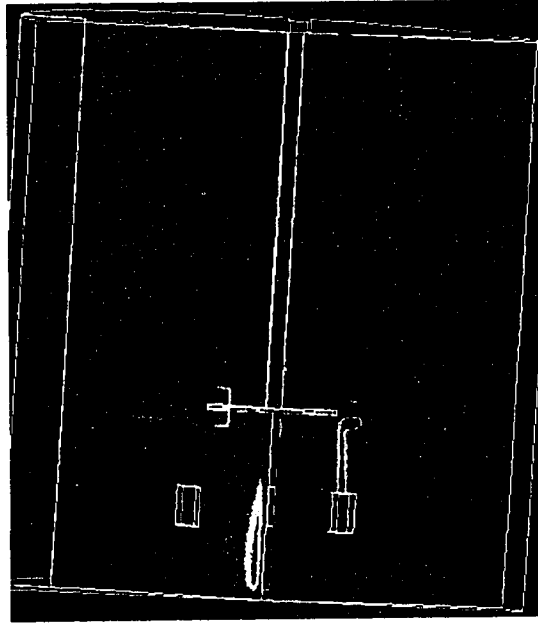


Figure 7-34(a). Predicted Flow Field at N3Q1. (Left: Contours of Turbulent Kinetic Energy; Right: Contours of Gas Holdup). Ten Uniform Contours Maximum Value = 0.1(Black) and Minimum Value = 0 (Blue)

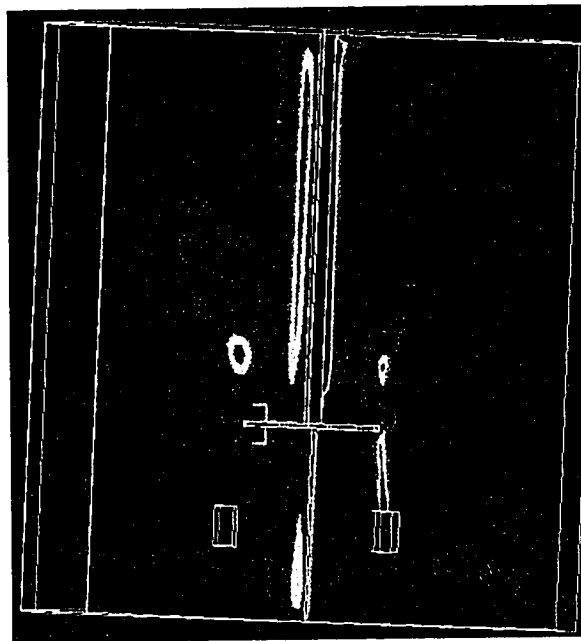


Figure 7-34(b). Predicted Flow Field at N3Q3. (Left: Contours of Turbulent Kinetic Energy; Right: Contours of Gas Holdup). Ten Uniform Contours Maximum Value = 0.6(Black) and Minimum Value = 0 (Blue)

The above figures suggest that the flow pattern predicted by CFD is itself vastly different from that obtained with CARPT. CFD predicted liquid velocities are different both in magnitude and in qualitative trends, from CARPT measured values which allows little scope for comparison. It was not possible to compare the gas holdup profiles from CFD with CT since CFD predicts very low values (0.0005 to 0.01) of the gas holdup and in regions away from the impeller predicts that negligible gas is present (unlike CT, refer to Figure 7-26).

The problems in the current simulation could be due to the following reasons:

- a) **Use of Incorrect Drag Formulation:** Lane et. al. (2000) indicated that using a lower value of drag correction factor may have worked for their case but also caution that it cannot be really generalized. Preliminary calculations performed with the default drag correlations in FLUENT suggested that the gas holdup pattern is extremely sensitive to the drag correlation used.
- b) **Account for Secondary Phase Turbulence:** The fact that the turbulent kinetic energy profiles are vastly different and the CFD predictions are orders of magnitude lower suggest that we may need to account for the influence of the secondary phase turbulence.
- c) **Role of Boundary Conditions:** In the current study we set the top liquid surface as an inlet and set the liquid velocity to be zero and that the gas rises at its terminal rise velocity of 20 cm/s. It is not clear if this is influencing the quality of the predictions. In the current study since we started with a very fine grid it was not possible to systematically inspect the role of boundary conditions and the role of drag by trying different combinations of these. A major problem faced in the current work was that the time taken for convergence for one condition was extremely long which allowed little opportunity to change conditions and rerun these cases.
- d) **Use of Single Bubble Size:** In the stirred tank reactor given the range of turbulence scales present, and the different forces present in different regions of the tank it is to be expected that there will be a distribution of bubble sizes. The

drag coefficients calculated in each region depend on the bubble size. Smaller bubble sizes cause the drag coefficients to be higher and therefore will predict smaller slip between gas and liquid. Therefore, using one single bubble size may also introduce considerable errors in the simulation unless of course a drag correlation independent of bubble size is used and shown to have reasonable predictions.

The current study clearly indicates a need to repeat the exercise using a much coarser grid than used for the current study and systematically examine the influence of various different parameters on the sensitivity of the predictions of this approach. The current work also clearly indicates that CFD in two phase stirred tanks is still in its early stages needing a lot more work in terms of development of physics based models.

7.6 Conclusions

A detailed analysis of data obtained by CARPT - CT in gas – liquid flows in stirred tank reactors is provided. A numerical model was developed to simulate a typical CT experiment to quantify the role of the error due to dynamic bias. This numerical model revealed that this error may not be significant for the conditions under which the current CT set up operates. The current study using the CT set-up achieved the following:

- The CT technique was able to capture the internals of the reactor like the baffles, the blades of the impeller and stainless steel shaft without having an prior information about their existence. This ability of the CT technique is valuable when applied to industrial reactors where it may not always be possible to get inside the reactor to check if all the internals are where they ought to be. CT even reveals the minute details such as whether the impeller is perfectly centered in our case.
- CT was able to capture the gas jets emerging from the sparger at an axial plane just above the sparger. The presence of eight circular jets on that plane also

clearly revealed the fact that all the eight sparger holes are functioning and don't suffer any malfunctioning due to blockage of the holes. This aspect would also be valuable when the technique is applied to industrial reactors where very often the sparger holes could get blocked by presence of contaminants.

- Volume averaged holdups obtained by CT reveal spatial variations which agree reasonably well with the variations reported in the literature. Comparison of overall holdup obtained by CT with the predictions by standard correlations available in the literature reveal that measured values are within the range of holdups predicted by the correlations. This ability of CT to provide the overall volume averaged holdup should be of considerable interest since currently crude techniques like gas disengagement, are still being employed to obtain the overall holdups. Morud and Hjertager (1996) report that errors with these techniques can be as high as 5-10%.
- CT was shown to provide detailed contours of the gas holdup distributions at different axial planes. These detailed contours have the potential to quickly help us in identifying regions of maldistribution if there are any. For the current system, at operating conditions used, the gas holdup distribution was shown to be very close to being uniform.
- It was also pointed out that the current temporal limitation of the CT technique limits the technique from capturing the time varying gas cavities in the impeller region.
- The effect of system parameters like impeller speed and gas sparging rate on the local gas holdups can be quantified from the CT measurements.
- The local gas holdup profiles were found to exhibit at least three local maxima a) near the impeller region b) in the bulk region around $r/R \sim 0.55$ to 0.6 and c) very close to the wall region. Earlier researchers like Nagasse and Yasui (1983) had also observed at least two maxima in the radial profile of the gas holdup. The maximum near the impeller region is obviously due to the phenomenon of cavity formation. With increase in Fl the location of the first maximum shifts radially outward from the shaft to the impeller tip region. The presence of the second

maximum could be explained when the liquid velocity profiles from CARPT at the same conditions were examined. The liquid velocity profiles reveal the existence of a circulating loop like structure most often both above and below the impeller or at least of one circulating loop. The eye of the loop (the region of low velocity) was found to be located at a radial position of $r/R \sim 0.55$ to 0.6 . This clearly indicated that this region of low velocity provides the necessary impetus for the gas to accumulate in the bulk.

- The identification of regions where gas tends to accumulate preferentially helps us in deciding what would be potentially good regions to sparge gas into. The fact that these locations shift with operating conditions would also help us in identifying operating conditions which will enable us to make the optimal use of existing spargers for such reactors.
- All this also reveals the enormous potential which the CT technique possesses for quickly evaluating if a certain new impeller design is actually capable of doing the job it is supposed to.

The CARPT technique was shown to capture in detail various aspects of both the liquid as well as gas flow structure in these reactors. The qualitative description of the liquid velocity vectors from CARPT are by themselves very informative for the reasons listed below:

- The velocity vector plots help us in identifying what is the regime of operation. The vector plots revealed CARPT's ability to capture both the classical recirculating flow structure observed in single phase flows and a different regime closer to a bubble column like flow. The vector plots in the axial planes revealed the role of circulating vortices which rotated in the same direction as the impeller in the central region and in the opposite direction in the region away from the impeller. This regime identification could be very important in deciding what kind of phenomenological models can be used to model such reactors.
- The velocity vector plots can capture the finer details of the liquid flow structure, like locations of eye of circulating loops, height and width of circulating loops

and how these parameters change with the impeller speed and gas sparging rates. These details are valuable inputs for reactor modeling of industrial reactors based on compartmentalization of the reactors. Currently, reliable CFD simulations of reactive flows is still too expensive computationally that a compartment based multi-scale model (Ranade, 2002) still seems to be the model of choice. Such models require a number of inputs like how many compartments should a reactor be broken into, where should these compartments be placed, what should their size be, what would be the liquid flow rates between these compartments and how do the gas holdups in these compartments vary with the operating parameters. CARPT and CT technique can provide just this kind of data.

- CARPT data was also shown to capture the sparger effects. This ability to pick up the effect or presence of internals by two different experimental techniques also serves as an internal validation of the two independent experimental techniques.
- The detailed velocity profiles from CARPT help us in quantifying the influence of the impeller speeds, the extent of its influence and how gas sparging rate affects the liquid velocities and their flow structure. The current study has provided for the first time detailed reliable local gas holdup data at a number of conditions and extensive liquid velocity and kinetic energy distributions in the stirred tank reactor.
- It is expected that this study will provide the much needed impetus for further development of CFD simulations of gas – liquid simulations of stirred tank reactor. Until, now there have been a handful of CFD simulations in this system and these are currently limited by the lack of reliable local holdup and velocity information.
- Attempts to simulate gas – liquid flows in stirred tanks with the Snapshot approach using currently available drag formulations produced results that are not in agreement with experimental evidence. Additional work is needed in improving closures.

Chapter 8

Summary, Conclusions and Recommendations

The objectives of this research have been three fold: 1) To investigate the single phase flow field in stirred tanks with CARPT and provide quantitative estimates of the capabilities of the technique, 2) To develop a data base using CARPT-CT in gas-liquid flows in stirred tanks at high gas holdups when other techniques fail, and 3) To critically evaluate the ability of commercially available CFD codes to predict the observed flow fields in single flows in stirred tanks.

To accomplish these objectives we began by systematically implementing the CARPT technique in single phase flows in stirred tanks. Stirred tank reactors unlike bubble column reactors or liquid – solid risers offer a number of challenges in implementing advanced techniques like CARPT and CT. Some of these challenges are:

- Presence of internals like the baffles, impeller, shaft, sparger etc. enhance the complexity of these flows. Solid wall collisions can cause serious damage to tracer particle, tracer particle could get trapped in dead zones behind these internals bringing the experiment to a halt, attrition of particle due to collisions with rotating impeller blades and careful choice of material of construction for internals and size is necessary to ensure minimum attenuation of the radioactive counts emitted by the CARPT tracer.
- Further in the stirred tank reactor there are regions of extremely low tracer residence times (near the impeller residence times are of the order of the CARPT sampling time) and regions of very high tracer residence times (dead zones at the bottom, 100 times the sampling time). Such vast differences in residence times have not been encountered in the systems in which the CARPT technique has previously been employed.

- The velocity gradients in this system are also very high typically of the order of 75s^{-1} to 300s^{-1} which is about 10-20 times the velocity gradients encountered in bubble column reactors or liquid solid risers.
- The turbulence levels in stirred tank reactors are at least 10-50 times higher than the turbulence levels encountered in these other systems explored at CREL. Further, in stirred tanks the changes in turbulence levels also occurs over every small length scales i.e. while regions close to the impeller experience fully turbulent flow, regions outside the influence of the impeller are usually in the transition regime between laminar and fully turbulent flows (at $\text{Re} < 10,000$).

Hence, the first part of the current study was to develop the appropriate tools to ensure that CARPT can be successfully implemented in this system. Single phase flows in stirred tanks have been studied extensively and offered an opportunity for us to critically evaluate the capabilities of the CARPT technique. The contributions of this first part of the thesis work are:

- CARPT was shown to capture the key features of the single phase flow like recirculating loops above and below the impeller, radial jet in the impeller plane. A detailed qualitative validation was also provided by comparisons with existing data from other experimental techniques like LDA, DPIV, etc.
- Detailed comparisons of quantitative features of flow like variations of radial pumping number, dimensionless mean radial and tangential velocity, dimensionless turbulent kinetic energy revealed that CARPT captures the right qualitative variation of these parameters. Quantitative comparisons indicated that size of CARPT tracer resulted in filtering of some of the fluid phase turbulence.
- CARPT enabled us to obtain valuable Lagrangian information like sojourn time distributions, return time distributions to the impeller region, Hurst exponents which provide valuable inputs to compartment based reactor models and serve as additional data to validate the ability of CFD codes to predict the system dynamics.

- This detailed validation allowed us to perform a needed evaluation of the capabilities and limitations of the CARPT technique.
- The investigation of CARPT capabilities indicate the following:
 - a) Errors introduced by CARPT data acquisition technique and existing CARPT position reconstruction algorithms were assessed. Acquisition of the total energy spectrum was found to introduce considerable spread in the calibration curves particularly in systems with internals and walls of high density (like Stainless Steel). Hence a new data acquisition strategy where only the photopeak fraction of the total energy spectrum was found to help in containing this error. A semi Monte Carlo like algorithm was developed which allows faster reconstruction of particle location (compared to the full Monte Carlo) but still retains the useful features of the full Monte Carlo model.
 - b) A Monte Carlo based model was developed to account for the ‘dynamic bias’ which is critical to ensuring the quality of CARPT data at high velocities. This model was partially validated by some carefully designed single phase experiments which showed that the dynamic bias error introduces a systematic offset in the CARPT measured velocity information. The offset was found to increase with increase in impeller speeds and offset decreases with increasing sampling frequency till a plateau is reached. At very high sampling frequencies the statistical nature of the experimental technique introduces more error causing the offset to increase. This experimental study provides an opportunity to develop an empirical correlation to correct the CARPT measurements as a function of system parameters like velocities and sampling frequency.
 - c) A CFD based two dimensional particle tracking simulation was performed which allowed us to evaluate the errors introduced by the CARPT processing algorithms and more importantly addressed the critical question of “ How closely is the CARPT tracer following the fluid?”. This two dimensional model brought to light several important issues in tracer selection and

established that density difference is more critical than size of tracer as far as flow followability of tracers is concerned. The study also enabled us to understand the loss of turbulent kinetic energy information obtained with 2.3 mm tracer in the stirred tank reactors, and revealed the importance of appropriate choice of grid size for converting the Lagrangian information into Eulerian information. This study enables a priori evaluation of CARPT tracers in different flow fields. The work also brought to light a fundamental issue which is the lack of engineering models to describe the lift force acting on a neutrally buoyant tracer.

- Further in this first part of the thesis the ability of commercial codes (FLUENT 4.5) to capture single phase flows was evaluated using two quasi steady models the Multiple Reference Frame (MRF) and the Snapshot approaches. These models were shown to capture the mean velocity fields reasonably accurately in very short periods of time without requiring any a priori inputs. This revealed the potential of these quasi steady models to be used as design tools for scale – up of single phase stirred tank reactors.
- In the second part of the thesis the techniques of CARPT and CT were extended to characterizing gas – liquid flows in stirred reactors. This enabled us to initiate the creation of a reliable data base of local gas holdup profiles over a range of Fl and Fr and extensive liquid velocity data.
- The resolution of the CT system was improved from 6.0 mm to 3.0 mm. The contribution of the dynamic bias error was shown to be negligible for conditions of current interest. Detailed gas holdup contours from CT revealed techniques ability to capture details of gas flow structure. Local gas holdup profiles at different axial planes obtained for the first time.
- Detailed Lagrangian information of the liquid velocity was obtained in such systems for the first time. Liquid velocity data obtained from CARPT allowed us to explain the gas holdup profiles from CT, gives information about flow regime, type of liquid flow structure associated with a certain regime and distribution of turbulent kinetic energies.

- The magnitude of the radial and tangential liquid velocities in the presence of gas was found to be lower (in the impeller region) than the corresponding single phase case. The presence of gas as expected lowered the radial pumping capacity of the impeller which resulted in shorter heights of recirculation loops above the impeller.
- Turbulent kinetic energy profiles in the presence of gas were very different from the single phase profiles with the turbulent kinetic energy increasing with radial distance from the impeller.
- Preliminary simulations were performed with the computational snapshot approach. These simulations revealed that simulating gas – liquid flows in stirred tanks is a lot more complex due to the interplay between several different forces and dominant role played by turbulence. The study echoed the need for physics based models for interfacial closures voiced by Lane et. al. (2000). The simulations were found to be extremely sensitive to the interfacial drag closures and lack of appropriate closures forms were found to result in very poor predictions of gas and liquid flow patterns and the gas distribution in these reactors.

In the following section we provide recommendations for future research.

8.1 Recommendations for Future Research

In this thesis under the broad framework related to gas – liquid flows in stirred tank reactors several different aspects have been investigated. These lead to several open research problems, which could form topics for further investigation. Some of these issues are listed below

- The issue of dynamic bias in CT has been probed using a numerical model. The value of this study would be greatly enhanced if these results could be supported by experimental verification of the dynamic bias error contribution like done for the single phase study in stirred tank reactor. Some preliminary work has already

been done to design some special experiments which simulate the passage of a bubble motion in a reactor with the bubble oscillating along a prescribed path with known frequencies. These carefully designed experiments need to be processed and their results used as a starting point for quantifying the dynamic bias errors in CT.

- Some preliminary simulations were done to quantify the dynamic bias in CARPT. A more detailed program needs to be undertaken to simulate the various experimental cases and establish the validity of the Monte Carlo model. This detailed program would endow us with a powerful tool which could then be used to assess the role of dynamic bias in other systems like the gas – solid riser where the issues of dynamic bias could be much more relevant. An important issue not addressed in the current study is to develop some kind of a correction factor to account for the dynamic bias error. This would allow us to extend the current studies in stirred tank reactors to much higher impeller speeds.
- Preliminary experiments were done with CARPT to experimentally quantify the flow followability of the CARPT tracer particle of various sizes. These experiments need to be repeated in a more carefully designed set of experiments using the results of the numerical particle tracking experiments as a starting point. This would enable us to develop an appropriate criterion for tracer particle selection for different types of flows.
- The studies with gas – liquid flows in stirred tank reactors need to be extended by performing similar experiments with different impeller types. For the current study the Rushton turbine was selected since a number of researchers have reported their observations for this kind of impeller. Now that the CARPT- CT data in two phase has been validated these techniques can now be used to explore previously uncharted regimes of flow. A very careful design of the experiments have to be done ensuring that there are other global measurements like using local gas holdup probes (which are currently being developed in the group), overall power measurements and level based overall gas holdup measurements are

performed. This will enable us to create a set of internally validated accurate data for industrial use.

- Some preliminary efforts were made at evaluating two-phase simulations in stirred tank reactors. This area needs to be explored in a much more detailed and systematic fashion. Two phase flows in stirred tank reactors are much more complex than two phase flows in systems like the bubble column reactor or riser reactor, etc. The complexity arises due to the phenomena of cavity formation in the impeller region due to an interaction between several different forces like the centrifugal force, pressure force, buoyancy etc. These interactions result in a wide variety of flow regimes in stirred tank reactors. To capture these different regimes a basic understanding of the physics behind the different forces is required to be able to formulate appropriate interphase momentum exchange coefficients. Moreover the contribution of turbulence in enhancing the drag coefficients is very significant in the stirred tank reactor. Currently only one or two studies make an effort to come up with modifications to the standard drag correlations to account for the turbulent drag. More fundamental studies are needed to understand the mechanism which enhances the drag coefficient and based on that develop a model.

Appendix A

Grid Independence of Computed Mean Quantities from CARPT

Three different grids were examined in this study. The details of the grids are given below in Table A-1.

Table A-1. Details of the Grids Examined in this Study

Grid Parameters	Grid I (GI)	Grid II (GII)	Grid III (GIII)
N_i	36	72	72
N_j	10	40	20
N_k	20	80	40
Δr (cm)	1.0	0.25	0.5
Δz (cm)	1.0	0.25	0.5
$\Delta \theta$ (degrees)	10°	5°	5°

In Table A-1, N_i is the number of compartments in the angular direction, N_j is the number of compartments in the radial direction and N_k is the number of compartments in the axial direction. For each grid compartment the radial and the axial variation of the radial velocity, the tangential velocity and the axial velocity were examined. The radial variation was examined at three different axial planes ($Z_1=D/5$, $Z_2=D/3$ and $Z_3=D/2$, where D is the tank diameter). The first and the third axial planes correspond to the axial locations of the eye of the lower and the upper recirculation loops, respectively (Rammohan et al., 2001). The second axial plane corresponds to the impeller midplane. Similarly, the axial variation was examined at three different radial locations ($r_1=D/6$, $r_2=D/3$ and $r_3=2D/5$). The first radial location lies at the impeller tip and the third radial

location corresponds to the radial co-ordinate of the eye of the two recirculation loops. The results are shown below in Figures A-1 to A-3. The results with finer grids GII and GIII seem to converge while the coarsest grid results are somewhat different.

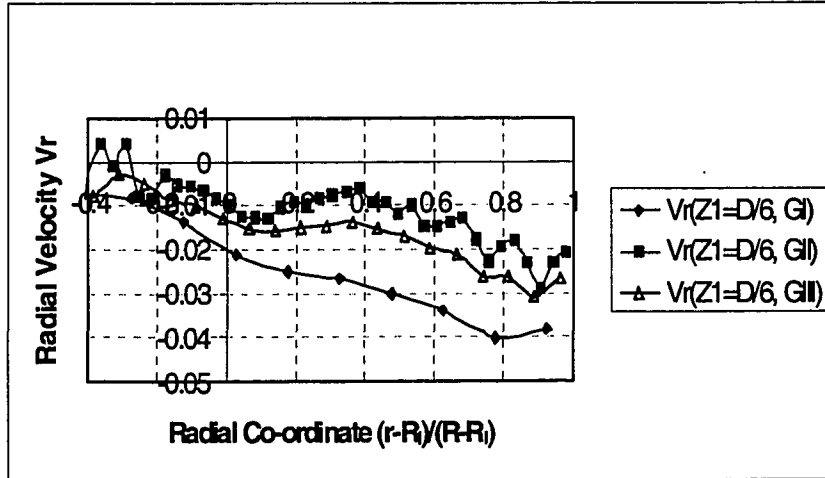


Figure A-1(a). Radial Profile of Radial Velocity at $Z_1 = D/5$

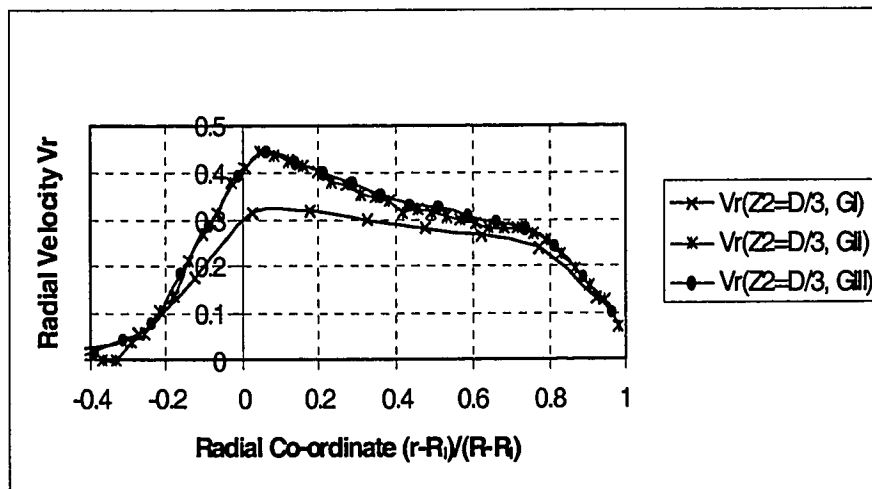


Figure A-1(b). Radial Profile of Radial Velocity at $Z_2 = D/3$

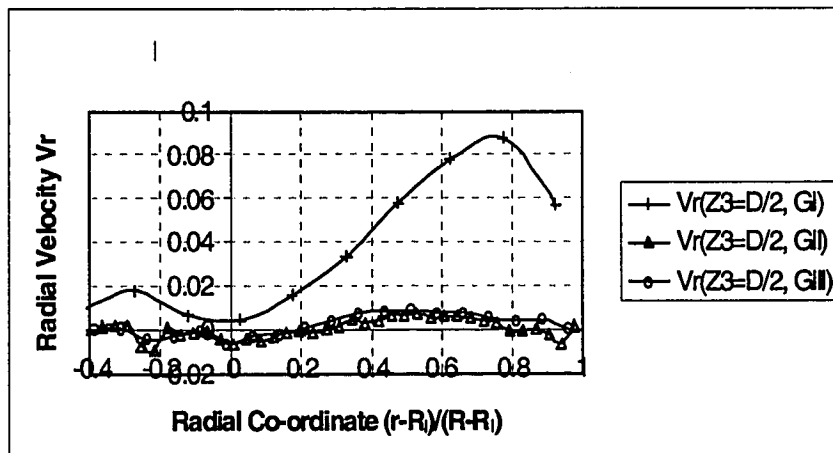


Figure A-1(c). Radial Profile of Radial Velocity at $Z_3 = D/2$

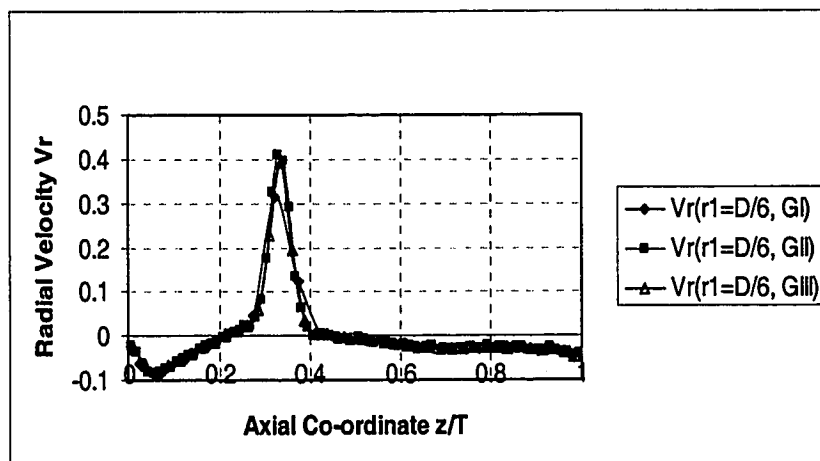


Figure A-1(d). Axial Profile of Radial Velocity at $r_1 = D/6$

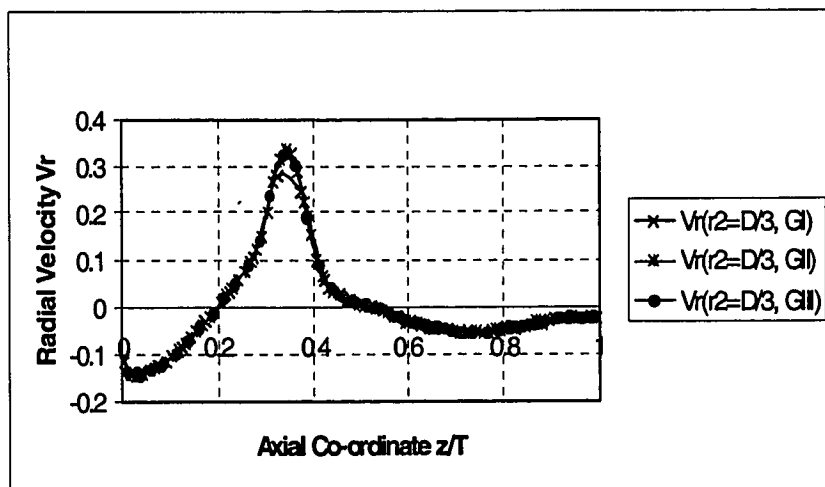


Figure A-1(e). Axial Profile of Radial Velocity at $r_2 = D/3$

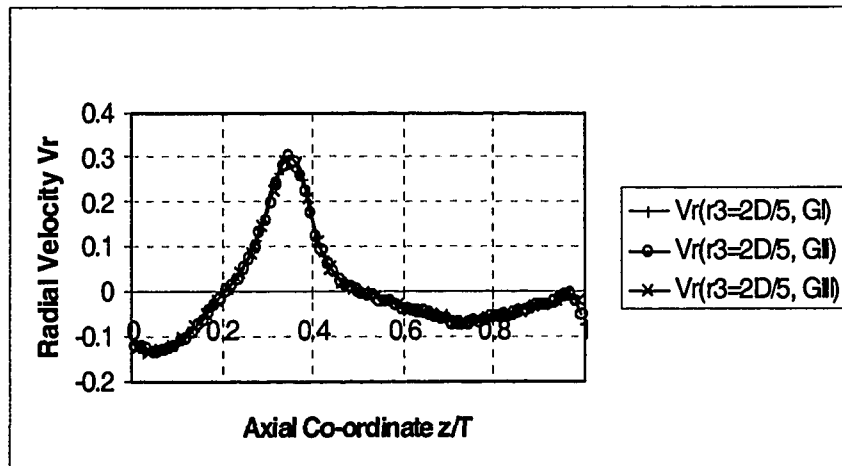


Figure A-1(f). Axial Profile of Radial Velocity at $r_3 = 2D/5$

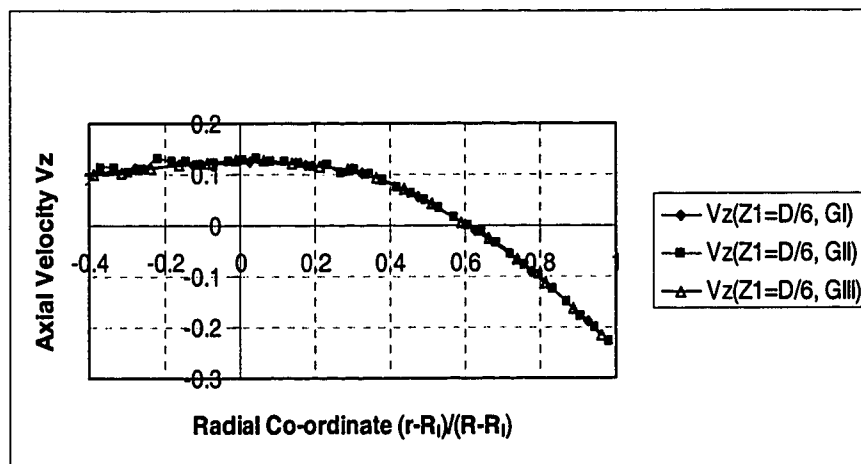


Figure A-2(a). Radial Profile of Axial Velocity at $Z_1 = D/5$

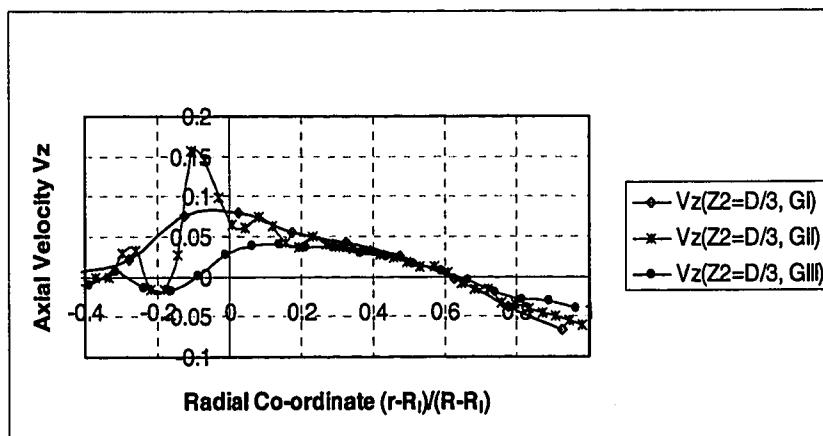


Figure A-2(b). Radial Profile of Axial Velocity at $Z_2 = D/3$

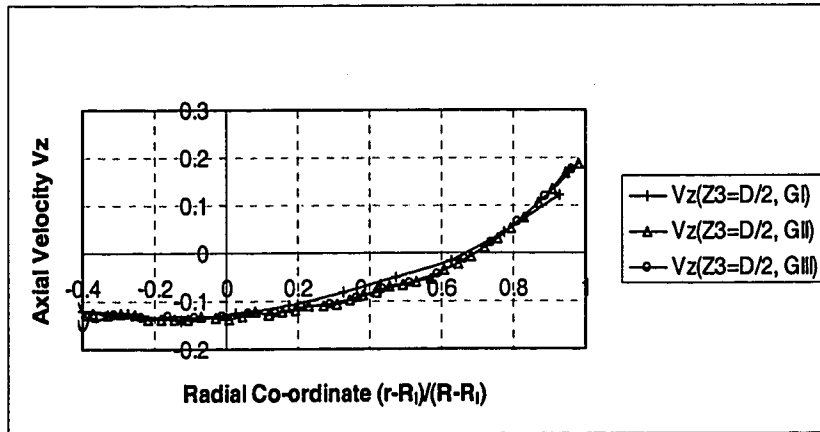


Figure A-2(c). Radial Profile of Radial Velocity at $Z_3 = D/2$

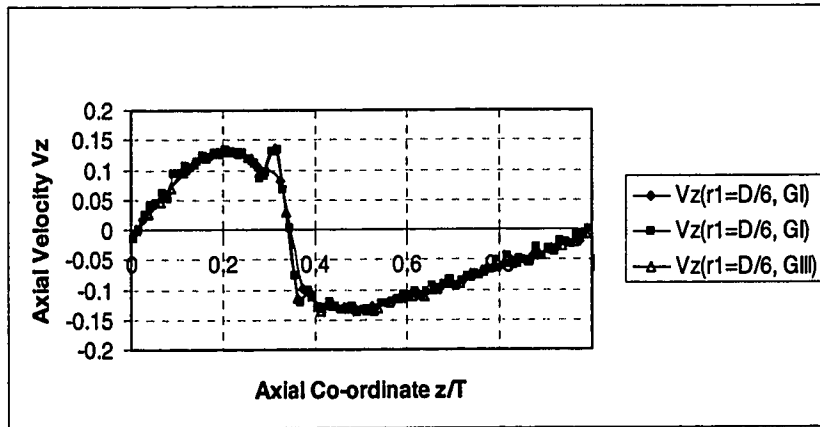


Figure A-2(d). Axial Profile of Axial Velocity at $r_1 = D/6$

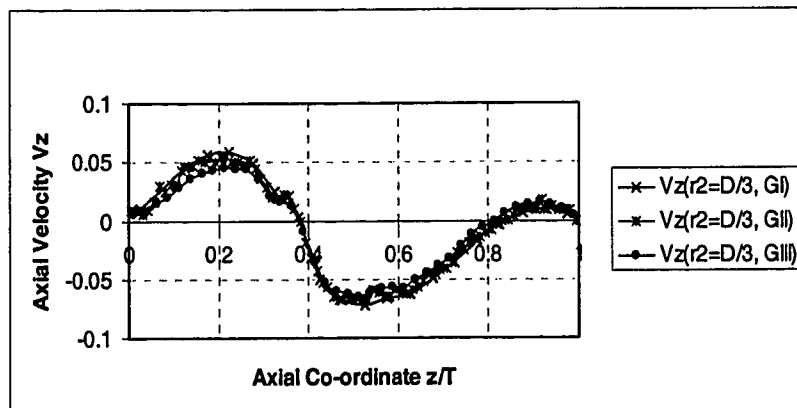


Figure A-2(e). Axial Profile of Axial Velocity at $r_2 = D/3$

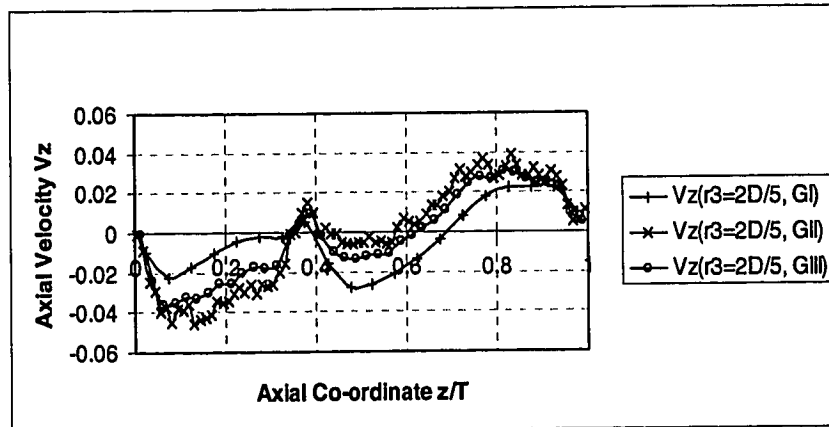


Figure A-2(f). Axial Profile of Axial Velocity at $r_3 = 2D/5$

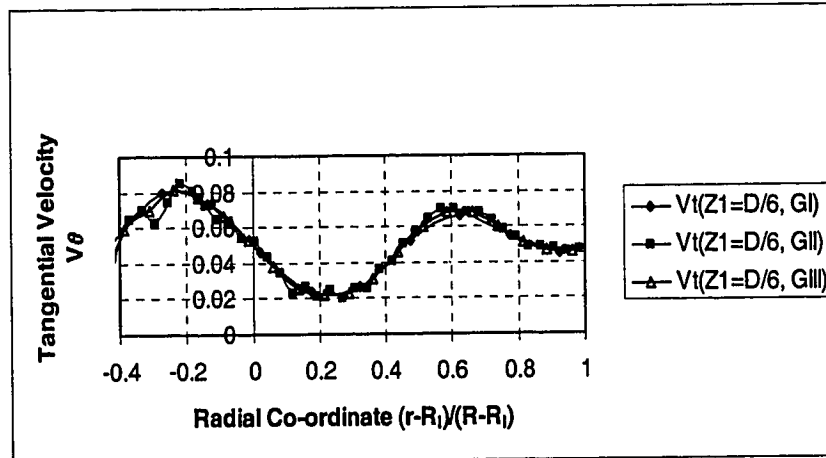


Figure A-3(a). Radial Profile of Tangential Velocity at $Z_1 = D/5$

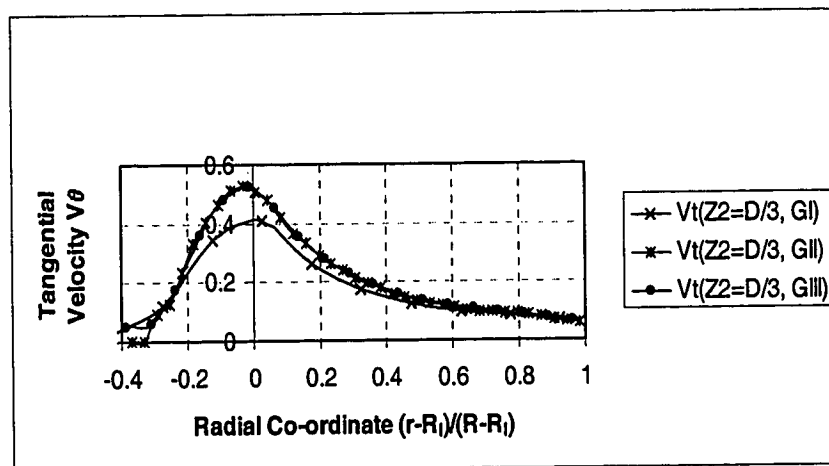


Figure A-3(b). Radial Profile of Tangential Velocity at $Z_2 = D/3$

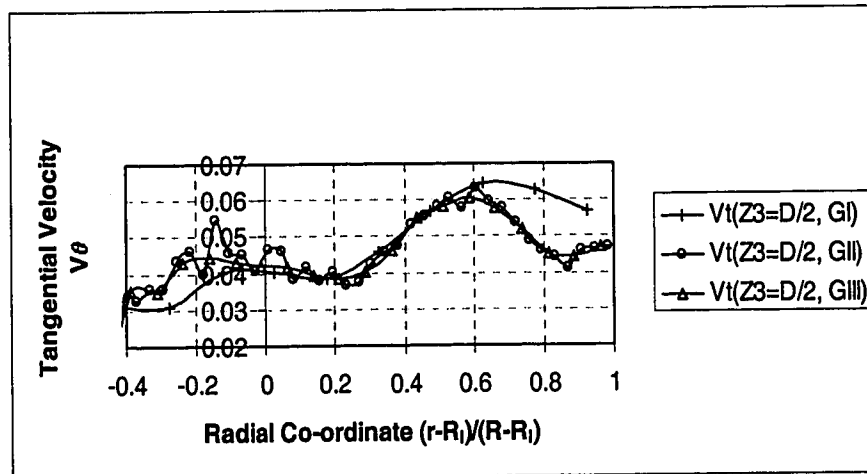


Figure A-3(c). Radial Profile of Tangential Velocity at $Z_3 = D/2$

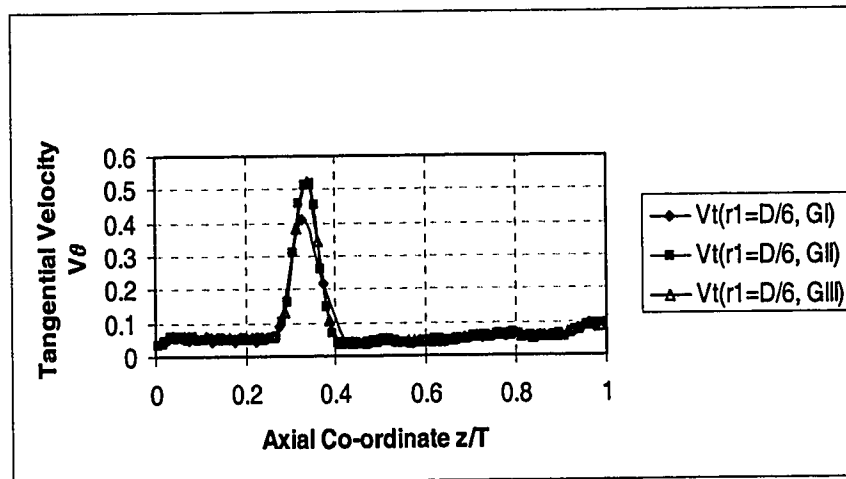


Figure A-3(d). Axial Profile of Tangential Velocity at $r_1 = D/6$

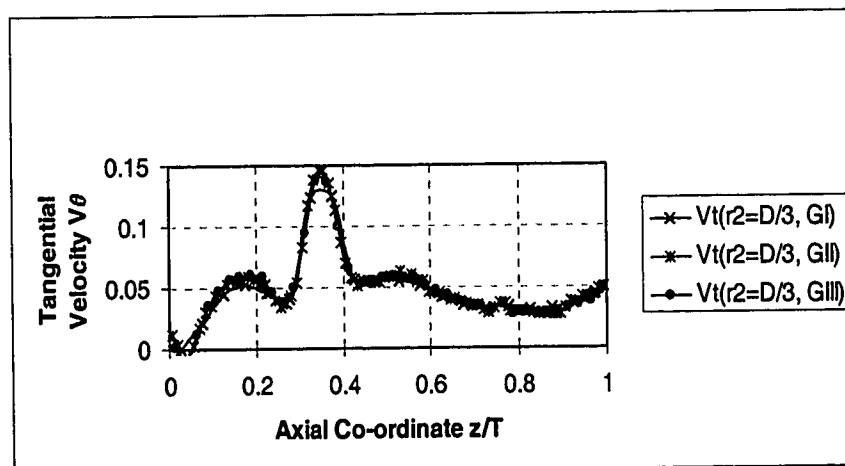


Figure A-3(e). Axial Profile of Tangential Velocity at $r_2 = D/3$

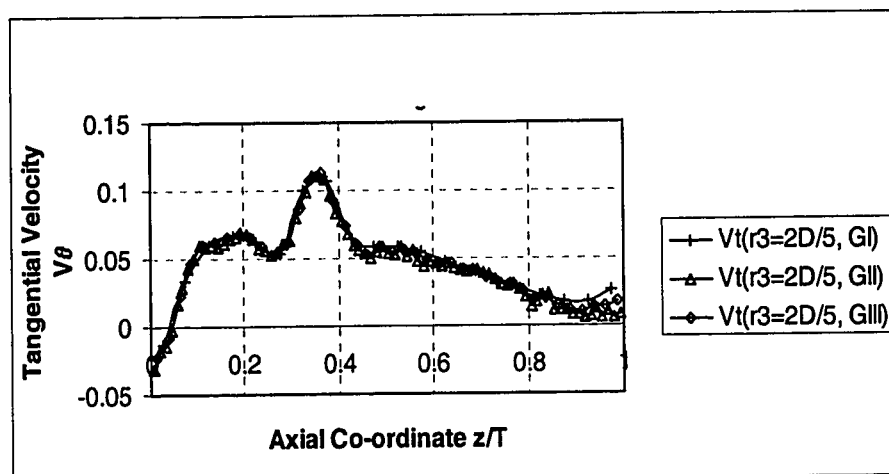


Figure A-3(f). Axial Profile of Tangential Velocity at $r_3 = 2D/5$

Due to current limited duration of CARPT runs there are inadequate statistics when one uses very fine grids (i.e. insufficient number of particle visits) and, therefore, at present we cannot tell whether current CARPT results are completely grid independent. However, the results presented so far are encouraging since for a number of variables the finer grids II and III produced results that are very close. Therefore we use grid III for interpretation of all the data in Chapter 4.

Appendix B

Dynamic Bias in CT

CT relies on the attenuation of a beam of (high-energy) photons that travels through a medium consisting of air and water. As the attenuation follows an exponential-law, errors in the estimated fraction of gas (air) along a line through the two-phase mixture arise as a consequence of fluctuations in time of the gas (air)-fraction. This is easily understood, as the ensemble average of the logarithm of the attenuation ratio is different from the logarithm of the ensemble average of the attenuation ratio i.e.

$$\left\langle \ln\left(\frac{I}{I_o}\right) \right\rangle \neq \ln\left\langle \frac{I}{I_o} \right\rangle \quad (\text{B-1})$$

:In CT, we use many different scanning lines for the γ -beam and try to reconstruct the 2-dimensional gas fraction field in a time averaged sense from these chordal measurements. Obviously, every measurement will be an average in time and thus 'spoiled' by the above inequality. The question addressed in this section is:

- What is the influence of fluctuations in the gas fraction in a part of the measuring plane?

This error is quantified by the 'dynamic bias' defined as:

$$\text{Dynamic Bias} = \frac{\overline{\alpha_a} - \overline{\alpha_c}}{\overline{\alpha_c}} \times 100 \quad (\text{B-2})$$

where $\overline{\alpha_a}$ is the true time average defined as:

$$\overline{\alpha_a} = \frac{1}{\tau} \int_0^{\tau} \alpha(t) dt \quad (\text{B-3})$$

and $\overline{\alpha_c}$ is the time average from CT obtained from:

$$T_{calc}(\tau) = \exp[-\lambda(l - \overline{\alpha_c})] \quad (\text{B-4})$$

where λ is the mean free path, $T_{calc}(\tau)$, is the projection measurement obtained from CT.

This study attempts to quantify the limits on the dynamic bias for different CT sampling

rates τ and bubbling frequency ($1/t_b$), propagation of dynamic bias error from pixel to pixel and sensitivity of the error to the gradients in the holdup distribution.

B.1 Approach

To answer these questions numerical data are generated and reconstructed. The advantage is that these data can be noise-free and the fluctuating gas fraction is known exactly.

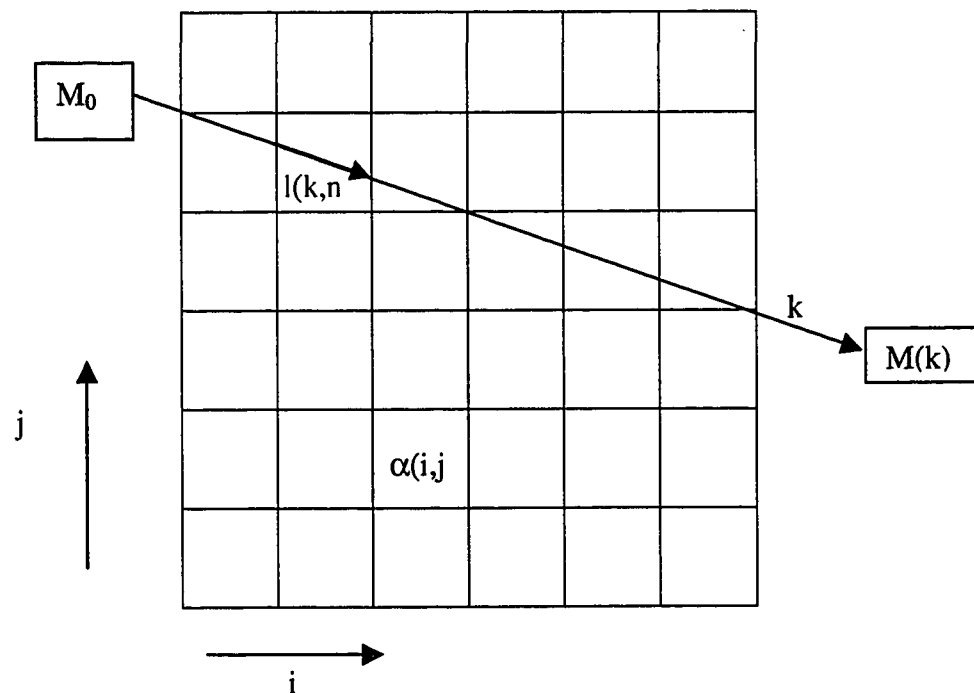


Figure B-1. Schematic of Radiation Received by Detector Traveling through Column Media

Figure B-1 shows the principle of this simulation. The gas fraction distribution is represented by a $N \times N$ grid (6*6 in the figure). In each grid cell there is a gas fraction, $\alpha(i,j)$ which in principle is a function of time. A measurement is performed by having a line-beam of γ 's cross the measuring area, i.e. the grid, in a specified direction. The beams are assumed to be generated corresponding to the fan beam geometry found in the CT set-up at CREL. The lines thereby pass through various grid cells and will be

attenuated by that cell according to the gas fraction in that cell and the path length $l(k,n)$ (in blue in the figure B-1.) through that cell. When leaving the grid, the number of counts received in the sampling time can thus be calculated (assuming $\mu_g \ll \mu_l$), according to:

$$M(k) = M_0 \exp\left(-\mu \sum_{\text{path } k} l(k,p) [1 - \alpha(i,j)]\right) \quad (\text{B-5})$$

where $p=1$ to $N*N$ pixels. For the reconstruction of $N*N$ pixels, at least $N*N$ independent measurements $M(k)$ are required. It is convenient to introduce the vector A (of length $N*N$) that contains all $\alpha(i,j)$ values, defined as:

$$A(k) = \alpha([i-1]*N + j) \quad (\text{B-6})$$

where $k=1,2,\dots,N*N$, $i=1,2,\dots,N$ and $j=1,2,\dots,N$. These $N*N$ measurements correspond to the total number of projections used in the CT measurements (for eg. 9702 projections).

B.2 Forward Problem

Now the 'forward problem' that simulates the measurement along $N*N$ independent lines, can be written as:

$$M(k) = M_0 \exp\left(-\mu \sum_n L(k,n) [1 - A(n)]\right) \quad (\text{B-7})$$

with the matrix L ($N*N, N*N$) containing on each row the length of the paths of a γ -beam through the individual cells. It will be clear that L contains many zeros. Hence the information contained in L is stored in a single dimension array with another single dimensional array containing the location of the non-zero elements of the original L array.

So, the task is now to: (i) prescribe $\alpha(i,j)$, (ii) set up L and (iii) carry out measurements over a given time interval, Δt . The latter is done by sub-dividing the actual interval Δt into smaller intervals of length δt , during which the fluctuating $\alpha(i,j)$ is kept constant. Obviously, this is just digitizing of $\alpha(i,j)$ in time. Summing all the contributions to the count rate of the intervals δt , gives the count rate in Δt . Depending on the choice of the

time scale of the gas fraction fluctuations (and the amplitude of that) this has a weak or strong effect on the reconstructed gas fraction distribution.

B.3 Backward Problem

The backward problem, i.e. the reconstruction of $\alpha(i,j)$ from $M(k)$ can be done by using the EM algorithm which needs the projection measurements and the information about the L matrix and the convergence criterion. In this way the combined effect of the fluctuations and the use of the algorithm can be investigated without the influence of measurement noise.

B.4 Implementation

The calculation of the L-matrix, generation of a fluctuating gas fraction and the calculation of the measured count rate is done in a FORTRAN code. The generation of L matrix for the fan – beam geometry uses the code FANMAT.f developed by Kumar (1994). This code uses a sub-sampling time of $\delta t=1e-3$ (value can be changed in the include-file). So 50 samples for one measurement ($N_{\text{samples}}=50$) would result in a sampling time of 50ms.

The gas fraction distribution is created (for each specific time-interval δt it is recalculated) by assuming that in each grid cell, the gas fraction fluctuates according to a block function, mimicking the passage of a bubble or group of bubbles. So, the ‘instantaneous’ gas fraction in a cell as a function of time looks like:

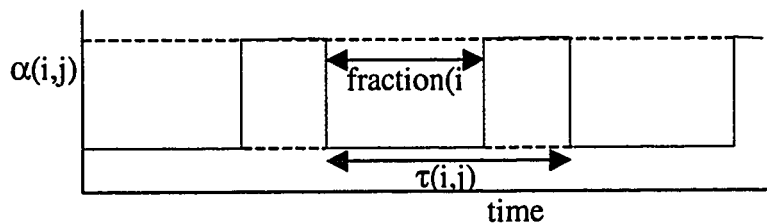


Figure B-2. Details of Simulated Gas Holdup Fraction

Four parameters are important here:

$\tau(i,j)$, the period of the fluctuation in cell (i,j). This time is coupled to the velocity profile of the bubbles and a characteristic length scale δs . In the example-program the velocity varies from relatively low at the walls to high in the center, for δs the arbitrary value $1e-2m$ is chosen.

$\text{fraction}(i,j)$, representing the fraction of time that the gas fraction is low. This value controls the true time-averaged gas fraction.

Two $\alpha(i,j)$ base levels: a low value and a high value. Obviously, also these influence the true time-averaged gas fraction. Once the instantaneous gas fraction distribution is calculated, an instantaneous count rate is calculated. Subsequently, the contribution to the true time averaged gas fraction and the number of counts are each added to the mean gas fraction and the total count rate for the entire measuring period. Then, the cycle is repeated. Finally the data are written to file: Once these data are generated, the EM algorithm recalculates the gas fraction profile according to equation (7-32). The calculated values are then compared with the original time averaged gas holdup distributions. These results are discussed below in the following section.

B.5 Results and Discussion of Dynamic Bias Error

B.5.1 Dynamic Bias in N*N Pixels

In this section the dynamic bias error has been evaluated for three different types of input gas fields and for two different pixel sizes (4 X 4 and 20 X 20) for each input. The inputs differ in the ratio of time scale of holdup fluctuation to CT sampling time i.e. $\Delta t/\tau$ either $\ll 1$, ~ 1 or $\gg 1$.

Error with Input of Type 1

The details of the holdup variation corresponding to input of type 1 is shown below in Figure B-3. The holdup variation in each of the 4 X 4 pixels is the same and they are all

synchronized. This results in the following true and reconstructed time averages: This comparison shows that there are slight differences between the reconstructed and the true time average field. The errors however are seen to vary between -0.8% to -2.4% . The errors in the center for this case seem very slightly higher than the errors near the wall. For the same type of input when 20×20 pixels are used the errors increase slightly but they are still seen to be between -0.8% to -4% .

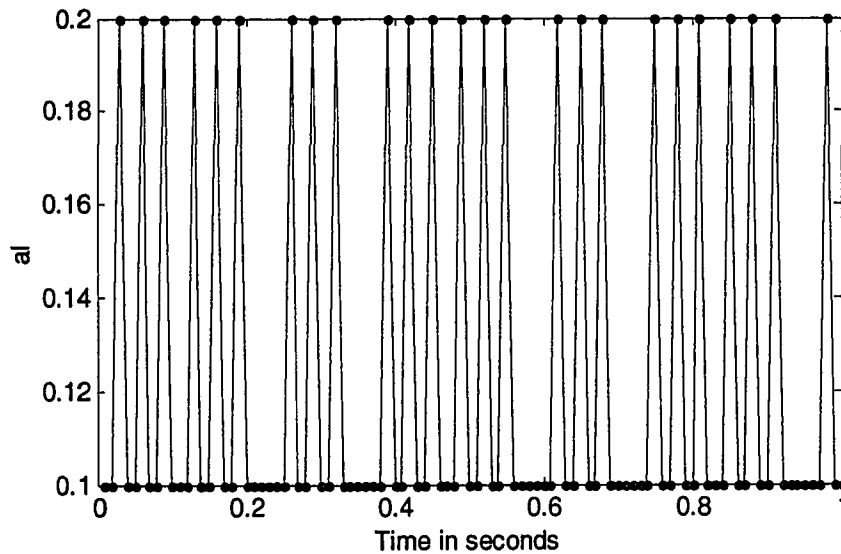


Figure B-3. The Parameters are $\Delta t = 0.01s$; $\tau = 0.0327s$, $A_{av} = 0.125$, $N_{sample} = 100$

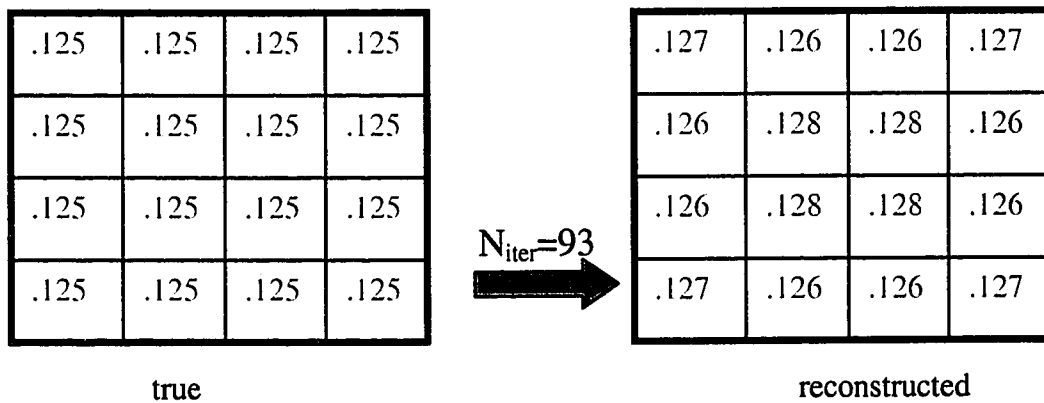


Figure B-4. Comparison of True Time Average with Reconstructed Time Average for Input of Type 1 on a 4×4 Pixel

The details of inputs of type 2 and type3 are shown below in Figures B-5 and B-6 respectively. For both these inputs the errors are between -0.8 to -2% for the 4×4 pixel

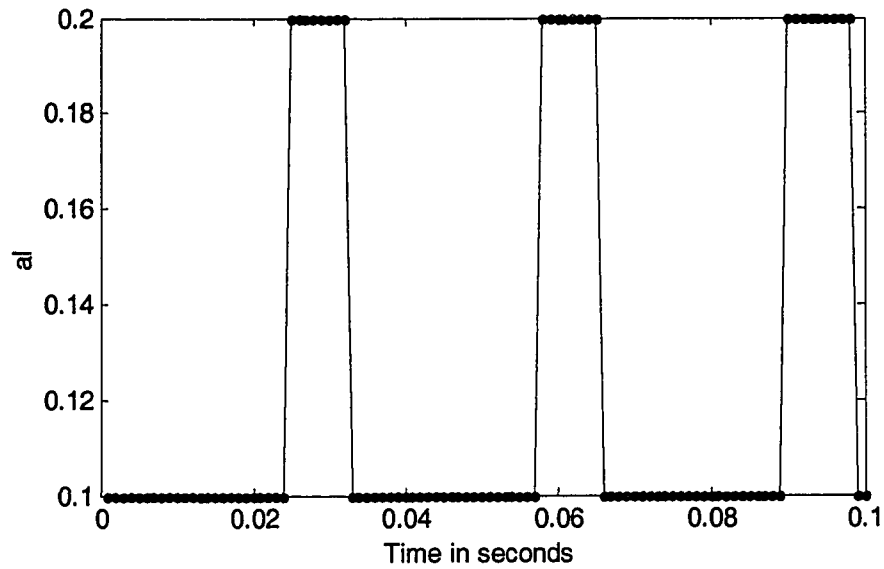


Figure B-5. The Parameters are $\Delta t = 1e-3$ s; $\tau = 0.0327$ s, $Al_{av} = 0.125$, $N_{sample}=100$

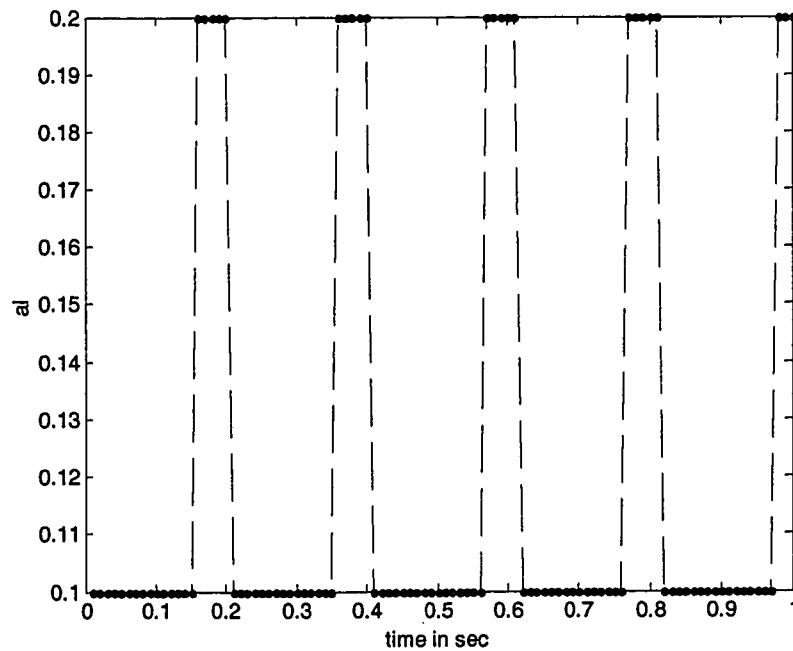


Figure B-6. The Parameters are $\Delta t = 1e-2$ s; $\tau = 0.00327$ s, $Al_{av} = 0.123$, $N_{sample}=100$

B.6 Conclusions on the Dynamic Bias in CT

For all current simulations it was assumed that the CT sampling times are long enough for source emissions to be considered constant (for details refer to Wyman and Harris,

1985). Dynamic Bias (DB) effect was studied in N pixels. DB in N pixels has been studied numerically. The EM algorithm was used for the numerical procedure after ensuring that the E.M. algorithm does not introduce any errors of its own. Effect of three types of holdup profiles were studied on two different grid sizes (4 X 4 and 20X 20). For the smaller grid size for all 4 input types the reconstruction overestimated the holdup and errors were of the order -2.5 to -0.8 %. Smaller sampling times reduce the DB but very small intervals are expected to increase error due to source fluctuation. If sampling time is smaller than bubbling time scale then less error is introduced. With larger number of pixels DB increases. For input types 1-3 (CT sampling time comparable to bubble time scale, less than bubble time scale and greater than bubble time scale) error was in the range of -4 to -0.8 %, slightly larger than the errors with smaller pixel. Based on the obtained estimates of the dynamic bias errors in the current holdup measurements by our CT are quite reliable.

Appendix C

Gas Holdup Variation in STR from Computer Tomography

C.1 Analysis of Contours of Gas Holdups

Corresponding to the different flow regimes there are fifty different data points from the CT experiments of which nine select conditions (corresponding to the three conditions at which CARPT data are available) are analyzed. Three of these are reported in Chapter 7 and the remaining six conditions are reported below. The figures below show the gas holdup distributions in the different axial planes in the stirred tank reactor. The figures are analyzed for the distribution pattern of gas and possible asymmetries in the distribution of gas.

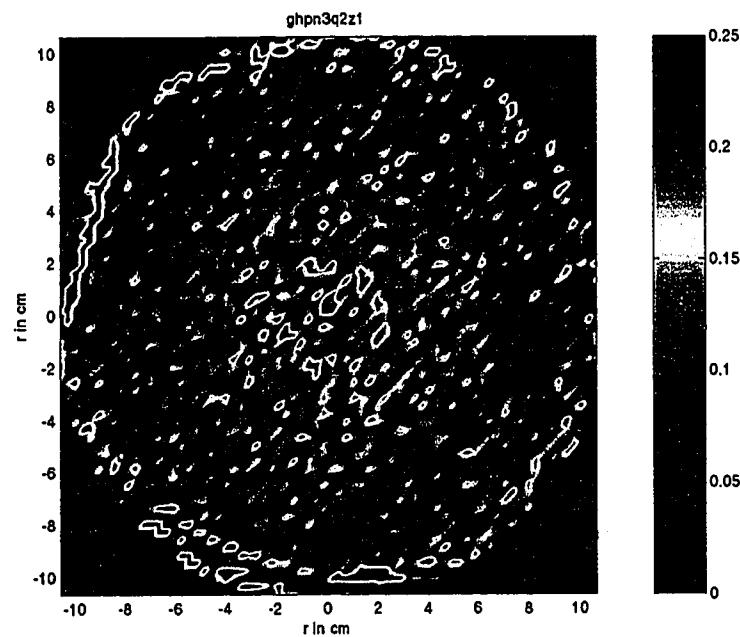


Figure C-1(a). Gas Holdup Distribution at $Fl = 0.042$ and $Fr = 0.0755$ ($N = 200$ rpm, $Q = 2.5$ l/min) and $Z = 5.0$ cm

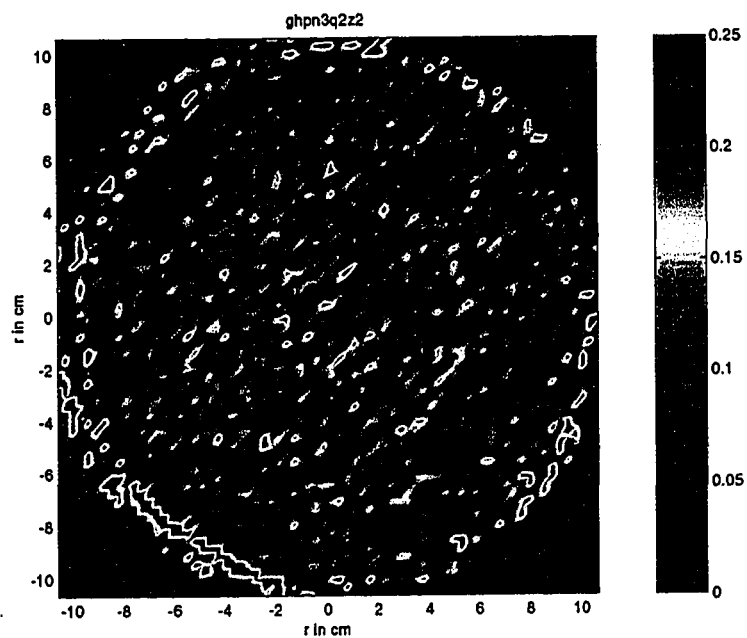


Figure C-1(b). Gas Holdup distribution at $Fl = 0.042$ and $Fr = 0.0755$ ($N = 200$ rpm, $Q = 2.5$ l/min) and $Z = 10.0$ cm

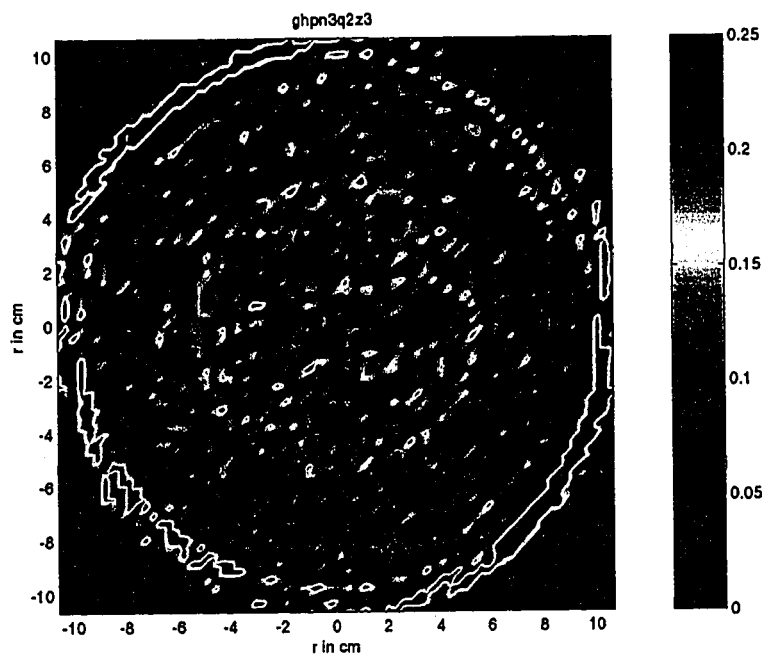


Figure C-1(c). Gas Holdup distribution at $Fl = 0.042$ and $Fr = 0.0755$ ($N = 200$ rpm, $Q = 2.5$ l/min) and $Z = 15.0$ cm

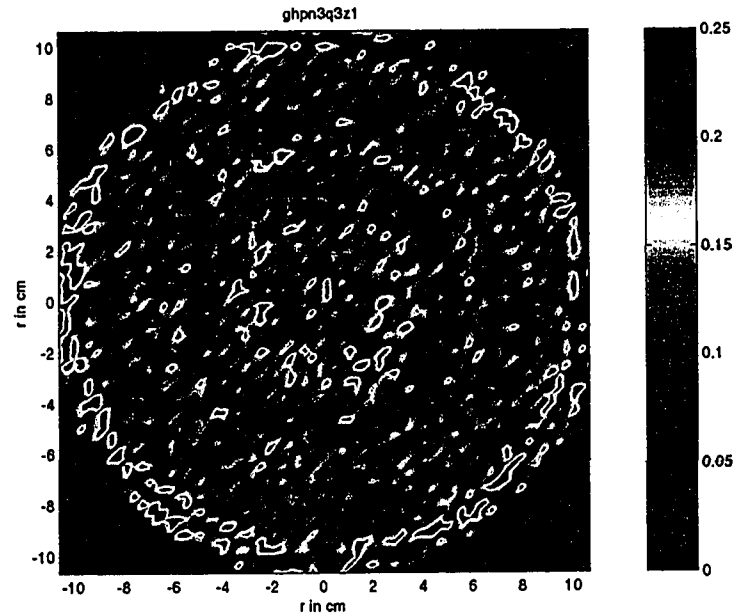


Figure C-2(a). Gas Holdup distribution at $Fl = 0.0842$ and $Fr = 0.0755$ ($N = 200$ rpm, $Q = 5.0$ l/min) and $Z = 5.0$ cm

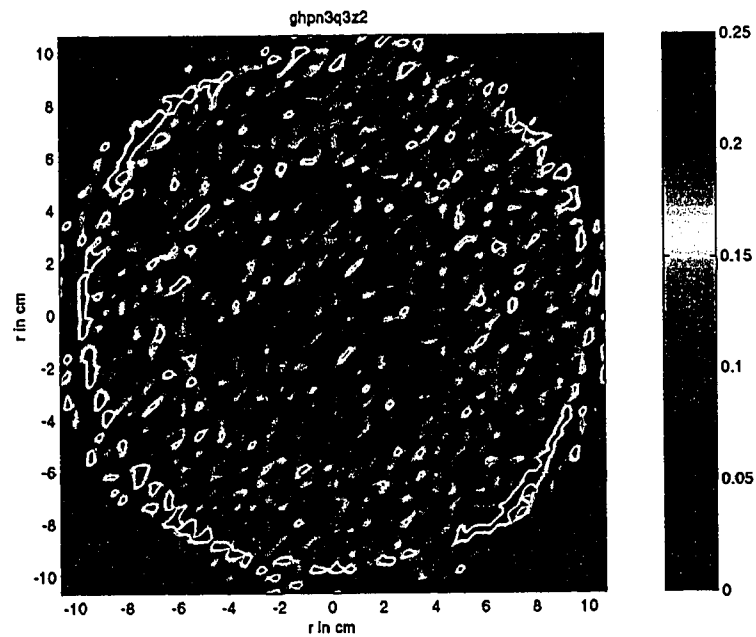


Figure C-2(b). Gas Holdup distribution at $Fl = 0.0842$ and $Fr = 0.0755$ ($N = 200$ rpm, $Q = 5.0$ l/min) and $Z = 10.0$ cm

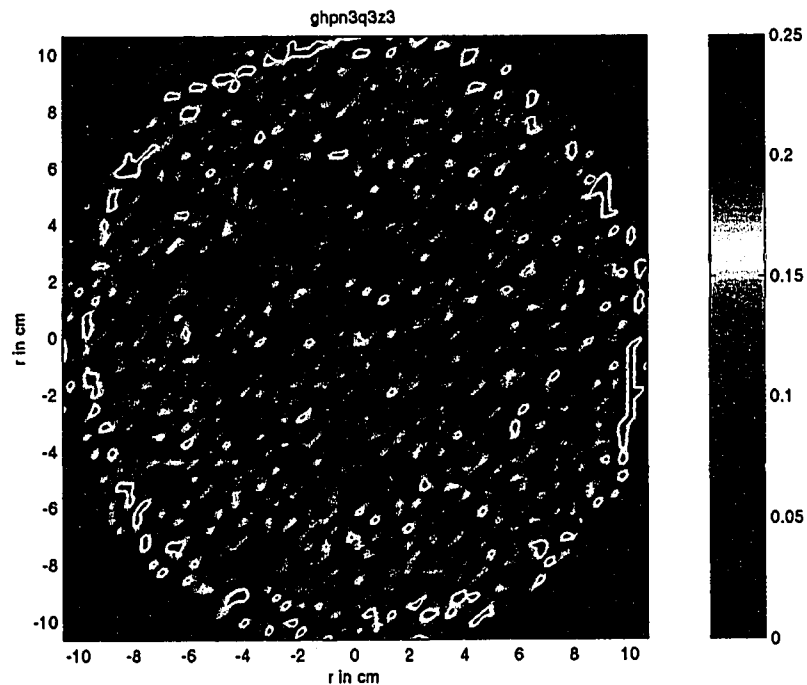


Figure C-2(c). Gas Holdup Distribution $Fl = 0.0842$ and $Fr = 0.0755$ ($N = 200$ rpm, $Q = 5.0$ l/min) and $Z = 15.0$ cm

In the above figures the gas holdup distribution at three different axial planes for different gas sparging rates and impeller speeds have been shown. In general for each condition the amount of gas at the highest axial plane i.e. $Z=15$ cm seems to be lower than the gas found in the other axial planes. At the lowest plane i.e. $Z=5$ cm a ring of gas can be seen with a radius of around 3.3 cm. This ring obviously corresponds to the region of gas jetting from the sparger. For a fixed gas flow rate increase in impeller speed seems to increase the amount of gas found in this region (due to greater gas dispersion) while an increase in gas flow rate for fixed impeller speed seems to result in the gas being concentrated more within the circle of radius 3.3 cm. This is seen clearly from both Figure C-2(a) where a circular band of very low to negligible gas hold seems to circle the central portion of diameter 3.3 cm. The gas holdup in the outer ring seems unchanged at

the different conditions at the lowest axial plane. At the central plane $z=10$ cm two zones seem to exist a central ring and an annular ring. At this plane as expected the sparger effect is not felt. The central ring probably corresponds to the stream of gas either entraining like in a bubble column or the gas being brought down by the liquid being drawn into the impeller region. The gas in the outer ring probably corresponds to the gas rising up either with its terminal velocity or being dragged up by the liquid. In the central plane for a fixed impeller speed increasing the gas flow rate seems to increase the gas holdup in the outer ring and a decrease in the gas holdup in the inner ring. This would suggest that the gas seen in the central region is probably more due to the gas being drawn into the impeller region by the liquid than the gas rising up like in a bubble column. This can be seen to be the case from figures C-1(b) and C-2(b). In C-1(b) gas in central ring is more due to lower gas flow rate the impeller effect is more pronounced and therefore more gas is being drawn into the impeller region. While in C-2(b) there is lesser gas in the central region which probably corresponds to the gas just rising up like in a bubble column and due to the increase in gas flow rate more of gas is seen in the outer ring. At the highest axial plane $Z=15$ cm the behavior is similar to the central plane though at a fixed impeller speed the gas in the central portion remains the same but the amount of gas in the outer ring increases. In all the above cases the gas is seen to be distributed axisymmetrically.

References

- Ambegaonkar, A.S., Dhruv, A.S., and Tavlarides, L.L., 'Fluid-particle hydrodynamics in agitated vessels', *Can J Chem Engg*, **55(4)**, pp. 414-421 (1977).
- Baldyga, J. and Bourne, J.R., 'A fluid mechanical approach to turbulent mixing and chemical reaction', *Chem. Eng. Commun.*, **28(4-6)**, pp 231-281 (1984).
- Barigou, M., and Greaves, M., Gas holdup and interfacial area distributions in a mechanically agitated gas – liquid contactor, *Transactions of Institutions of Chemical Engineers*, **74A**, pp.397 – 405 (1996).
- Bartels, C., Breuer, M., and Durst, F., 'Comparison between Direct Numerical Simulation and k- ϵ prediction of the flow in a vessel stirred by a Rushton turbine', *10th European Conference on Mixing*, p.p. 239 – 246 (2000).
- Batchelor, G.K., 'The Theory of Homogeneous Turbulence', Cambridge Univ. Press, England (1953).
- Bimbinet, J.J., M.S.Thesis, Purdue University, Lafayette, Ind. (1959).
- Bombac, A., Zun, I., and Filipic, B., Gas filled cavity structures and local void fraction distribution in aerated stirred vessel, *A.I.Ch.E. Journal*, **43**, 11, pp. 2921-2931 (1997).
- Bruijn, W., van't Riet, K., and Smith, J.M., 'Power consumption with aerated Rushton turbines', *Transactions of Institution of Chemical Engineers*, **52**, pp.88 (1974).
- Calderbank, P.H., 'Physical rate processes in industrial fermentation', *Transactions of Institution of Chemical Engineers*, **36**, pp.443 (1958).

Chaouki, J., Larachi, F. and Dudukovic', M.P., 'Non Invasive Monitoring of multiphase flows', Elsevier, Amsterdam (1997a).

Chaouki, Jamal; Larachi, Faical; Dudukovic, Milorad P., 'Noninvasive Tomographic and Velocimetric Monitoring of Multiphase Flows'. *Ind. Eng. Chem. Res.*, **36(11)**, pp. 4476-4503 (1997b).

Chapman, C.M., Nienow, A.W., Cooke, M. and Middleton, J.C., 'Particle –Gas-Liquid mixing in stirred vessels Part II: Gas-Liquid Mixing', *Chemical Engineering Research and Design*, **61**, pp. 82-95 (1983).

Chapman, F.S., and Holland, F.A., 'Liquid mixing and processing in stirred tanks', pp. 11-14, New York Reinhold publns (1966).

Chen, J., Rados, N., Al-Dahhan, M. H., Dudukovic, M.P., Nguyen, D., Parimi, K., 'Particle motion in packed/ ebullated beds by CT and CARPT' , *A.I.Ch.E. Journal*, **47(5)**, pp. 994-1004 (2001).

Chen, J.; Kemoun, A.; Al-Dahhan, M. H.; Dudukovic, M. P.; Lee, D. J.; Fan, L.S., 'Comparative hydrodynamics study in a bubble column using computer-automated radioactive particle tracking (CARPT)/computed tomography (CT) and particle image velocimetry (PIV)', *Chemical Engineering Science* , **54(13-14)**, pp. 2199-2207 (1999).

Chen, K.Y., Hajduk, J.C. and Johnson, J.W., *Chem Eng Commn*, **72**, pp.141 (1988).

Chen, Y.S. and Kim, S.W., 'Computation of turbulent flows using an extended k- ϵ turbulence closure model', NASA CR-179204 (1987).

Clark, M.W., Vermeulen, T., UCRI-10996, University of California, Berkeley (1963).

Cooper, R.G. and Wolf, D., *Can J Chem Eng*, **46**, pp.34 (1968).

Costes, J. and Couderc, J.P., 'Study by LDA of the turbulent flow induced by a Rushton turbine flow induced by a Rushton turbine in a stirred tank influence of the size of the units –I . Mean flow and turbulence', *Chemical Engineering Science*, **43(10)**, pp.2751-2764 (1988).

Costes, J. and Couderc, J.P., 'Study by LDA of the turbulent flow induced by a Rushton turbine flow induced by a Rushton turbine in a stirred tank influence of the size of the units –II . Spectral analysis and scales of turbulence', *Chemical Engineering Science*, **43(10)**, pp.2765-2772 (1988).

Crowe, C., Sommerfeld, M., and Tsuji, Y., 'Particle fluid interaction', in '*Multiphase flows with Droplets and particles*', CRC press, pp. 88 (1998).

Cui, Y.Q., van der lans, R.G.J.M., and Luyben, K.Ch.A.M., 'Local power uptake in gas – liquid systems with single and multiple Rushton turbines', *Chemical Engineering Science*, **51**, 11, pp. 2631 – 2636 (1996).

Cutter, L.A., 'Flow and Turblence in a stirred tank', *AIChEJ*, **4**, pp.485 (1967).

Dandy, D.S., and Dwyer, H.A., 'A sphere in a shear flow at finite Reynolds number: effect of shear on particle lift, drag and heat transfer', *J. Fluid Mech.*, **216**, pp. 381 – 410 (1990).

Daskopoulos, Ph. and Harris, C.K., 'Three dimensional CFD simulations of turbulent flow in baffled stirred tanks: an assessment of the current position', *Fluid Mixing 5*, IchemE Symposium Series, No. **140**, pp.1-13 (1996).

Deen, N.G. and Hjertager, B.H., 'Multiphase Particle Image Velocimetry Measurements in an Aerated Stirred Tank', Paper prepared for presentation at the 1999 Annual Meeting

of AIChE, Dallas, Tx, Oct 31-Nov5, Session 06005 : Solid- Liquid & Gas- Liquid Mixing, Unpublished (1999).

De Figueiredo, M.M.L., and Calderbank, P.H., The scale – up of aerated mixing vessels for specified oxygen dissolution rates, *Chemical Engineering Science*, **34**, pp.1333 (1979).

Degaleesan, S., 'Fluid dynamic measurements and modeling of liquid mixing in bubble columns', D.Sc., St.Louis, Missouri (1997).

Degaleesan, S., and Dudukovic', M.P., 'Measurement of turbulent dispersion coefficients in bubble columns using CARPT', Mixing X, Banff, Canada, June (1995).

Derksen, J.J., Kooman, J.L. and van den Akker, H.E.A., 'Large Eddy simulation of stirred tank flow by means of a lattice Boltzmann scheme', PVP-Vol 377-2, Computational Technologies for Fluid/ Thermal/ Structural/ Chemical systems with industrial applications, Volume II, ASME, San Diego, July 26-30 (1998).

Derksen, J.J. and van den Akker, H.E.A., 'Large Eddy simulations on the flow driven by a Rushton turbine', *AIChE J*, **45(2)**, pp. 209-221 (1999).

Devnathan, N., 'Investigation of Liquid Hydrodynamics in Bubble columns via Computer Automated Radioactive Particle Tracking (CARPT)', D.Sc., St.Louis, Missouri, (1991).

Devanathan, N., Moslemian, D., Dudukovic', M.P., 'Flow mapping in bubble columns using CARPT', *Chemical Engineering Science*, **45(8)**, pp. 2285-91 (1990).

Dohi, N.Y., Matsuda, Y.N., Itano, K., Shimizu and Y.Kawase, 'Mixing Characteristics in Slurry Stirred Tank Reactors with Multiple Impellers', *Chem Engg Commn*, **171**, pp.211-229 (1999).

Drbohlav, J., Fort,I., Maca, K. and Placek, J., *Coll Czech Chem Commn*, **43**, pp.3148 (1978).

Dyster, K.N., Koutsakos, E., Jaworski, Z., and Nienow, A.W., 'An LDA study of the radial discharge velocities generated by a Rushton turbine: Newtonian Fluids, $Re > 5$ ', *Transactions of Institution of Chemical Engineers*, **71A**, pp.11-23 (1993).

Fangary, Y.S., Barigou, M., Seville, J.P.K., and Parker, D. J., 'Fluid trajectories in a stirred vessel of non Newtonian liquid using Positron Emission Particle Tracking', *Chemical Engineering Science*, **55(24)**, pp. 5969 – 5979 (2000).

Fasano, J.B. and Bakker, A., 'Analysis of the flow field in agitated tanks using particle image velocimetry', Presented at the Mixing XIV, June 20-25 (1993).

Fort, I., Obeid, A. and Brezina, V., 'Studies on mixing LVIII Flow of liquid in a cylindrical vessel with a turbine impeller and radial baffles', *Czech Chem Commn*, **47(1)**, pp. 226.-239 (1982).

Frijlink, J.J., Physical aspects of gassed suspension reactors, Doctoral thesis, TU Delft, The Netherlands (1987).

Gavze, S. 'The accelerated motion of rigid bodies in non-steady stokes flow', *International journal of multiphase flow*, **16**, pp.153 – 166 (1990).

Goldstein, R.J. 'Fluid mechanics measurements', Washington D.C., *Taylor and Francis*. (1996).

Gosman, A.D., Lekakou, C., Politis, S., Issa, R.I. and Looney, M.K., 'Multidimensional modeling of turbulent two phase flows in stirred vessels', *AIChE J*, **38 (12)**, pp. 1946-1956 (1992).

Gosman, A.D., and Ioannides, E., 'Aspects of computer simulation of liquid fueled combustors', 19th Aerospace meeting, St.Louis, MO, *AIAA*, paper 81 – 03223 (1981).

Gunkel, A.A. and Weber, M.E., 'Flow phenomena in stirred tanks- I, Impeller stream', *AIChE J*, **21(5)**, pp. 931-949 (1975).

Hasal, P., Montes, J.L., Boisson, H.C. and Fort, I., 'Macro Instabilities of velocity field in stirred vessel : detection and analysis', *Chem Engng Sci*, **55 (2)**, pp. 391-401 (2000).

Hinze, J.O., *A.I.Ch.E. Journal*, **1, 1**, pp.289 (1955).

Ho, B.P., and Leal, L.G. 'Inertial migration of rigid spheres in two dimensional unidirectional flows', *J. Fluid Mech.*, **65(2)**, pp. 365 – 400 (1974).

Holland, F.A. and Chapman, F.S., 'Liquid mixing & processing in stirred tanks', New York, Reinhold publns, pp. 11 –14 (1966).

Hudcova, V., Machton, V., and Nienow, A.W., 'gas liquid dispersion with dual Rushton turbine impellers', *Biotechnology and Bioengineering*, **34**, pp.617-628 (1989).

Hughmark, G. A., 'Power requirements and interfacial area in gas liquid turbine agitated systems', *Industrial Engineering Chemistry Process Design and Development*, **19**, pp.641-646 (1980).

Hurst, E.H., 'Methods of using long term storage in reservoirs:I', *Proceedings of Institution of Civil Engineers*, **5**, pp. 519-525 (1956).

Katsanevakis, A.N. and Smith, J.M., 'Power Input and mean flow changes in two phase agitation', *IChem E Symp Ser*, **146**, pp. 187-198 (1999).

Katsanevakis, A.N. and Smith, J.M., 'Velocity and turbulence measurements in two phase boiling stirred tanks', *IChem E Symp Ser*, **136**, pp. 603-610 (1994).

Kawecki, W.T., Reith, T., van Heuven, J.W., and Beek, W.J., *Chemical Engineering Science*, **22**, 11, pp.1519 (1967).

Kemoun, A., Lusseyran, F., Mallet, J., Mahoust, M., 'Experimental scanning for simplifying the model of a stirred tank flow', *Experiments in Fluids*, **25**, pp. 23-36 (1998).

Kemoun, A., 'Experimental Characterization of the structures in a stirred tank reactor', PhD thesis, Institut National polytechnique de Lorraine, Nancy, France (1995).

Kemoun, A., ' Mise En Oeuvre Du Banc " ESMERALDA" Etude des Systemes de Melange en Reacteur Agite par Anemometrie Doppler a Laser', MS thesis submitted to L'Institut National Polytechnique De Lorraine, Nancy, France (1991).

Kumar, S.B., and Dudukovic', M.P., 'Computer assisted gamma and X-ray tomography: Application to multiphase flow' in 'Non-Invasive monitoring of multiphase flows', Eds.: Elsevier, Amsterdam, The Netherlands (1997).

Kumar, S.B., Moslemian, D., and Dudukovic', M.P., 'A gamma ray tomographic scanner for imaging void fraction distribution in bubble columns', *Flow Meas. Instr.*, **6(1)**, pp. 61-73 (1995).

Lamberto, D.J., Muzzio, F.J., Swanson, P.D. and Tonkovich, A.L., 'Using time dependent rpm to enhance mixing in stirred vessels', *Chem Engng Sci*, **51(5)**, pp.733-741 (1996).

Larachi, F.G., G.Kennedy and J.Chaouki, 'A gamma ray detection system for three dimensional Particle Tracking in Multiphase Reactors', *Nuclear Instruments and Methods in Physics Research*, **A338**, pp 568 –576 (1994).

Lauder, B.E., and Spalding, D.B., 'The numerical computation of turbulent flows', *Computer methods in applied mechanics and engineering*, **3**, pp. 269 –289 (1974).

Loiseau, B., Midoux, N., and Charpentier, J.C., 'Some hydrodynamics and power input data in mechanically agitated gas – liquid contactors', *A.I.Ch.E. Journal*, **23**, 6, pp.931-935 (1977).

Lovalenti, P.M., and Brady, J.F., 'The temporal behavior of the hydrodynamic force on a body in response to an abrupt change in velocity at small but finite Reynolds number', *J. Fluid Mech.*, **293**, pp. 35-46 (1995).

Lee, K.C. and Yianneskis, M., 'The Extent of Periodicity of the Flow in Vessels Stirred by Rushton Impellers', *AIChE Symp Ser*, **90**, **299**, pp 5-18 (1994).

Lu, W.M., Hsu, R.C., Chien, W.C., and Lin, L.C., Measurement of local bubble diameters and analysis of gas dispersion in an aerated vessel with disk turbine impeller, *Journal of Chemical Engineering Japan*, **25**, 5, pp. 551-557 (1993).

Lu, W.M. and Ju, S.J., 'Local gas holdup, mean liquid velocity and turbulence in an aerated stirred tank using hot film anemometry', *The Chemical Engineering Journal*, **35(1)**, pp. 9-17 (1987).

Luo, J.Y., Issa, R.I. and Gosman, A.D., 'Prediction of impeller induced flows in mixing vessels using multiple frames of reference', *I ChemE Symp. Ser.*, **136**, pp. 549-556 (1994).

Luong, H.T., and Volesky, B., *AIChE Journal*, **25**, pp.893.

Mahouast, M., 'Etude Du Melange En Cuve Agitee Par Analyse Des Champs Turbulent Et De Concentration VLD Mono Et Bidimensionnelle Conductimetrie', Docteur De L'INPL, Submitted to L'Institut National Polytechnique De Lorraine, Nancy, France (1987).

Mandelbrot, B.B., and Wallis, J.R., 'Robustness of the Rescaled Range R/S in the Measurement of Noncyclic Long Run Statistical Dependence', *Water Resources Research*, **5**, pp.967-988 (1969).

Mann, R.; Williams, R. A.; Dyakowski, T.; Dickin, F. J. and Edwards, R. B., 'Development of mixing models using electrical resistance tomography', *Chemical Engineering Science*, **52(13)**, pp. 2073-2085 (1997).

Manikowski, M., Bodemeier, S., Lubbert, A., Bujalski, W., and Nienow, A.W., 'Measurements of gas and liquid flows in stirred tank reactors with multiple agitators', *The Canadian Journal of Chemical Engineering*, **72**, pp.769-781 (1994).

Mclaughlin, J.B., 'Inertial migration of a small sphere in linear shear flows', *J. Fluid Mech.*, **224**, pp. 261 – 274 (1991).

Mei, R., Adrian, R. J., and Hanratty, T.J., 'Particle dispersion in isotropic turbulence under Stokes drag and Basset force with gravitational settling', *J. Fluid Mech.*, **225**, pp. 481-95 (1991).

Mei, R. 'An approximate expression for the shear lift force on a spherical particle at finite Reynolds number', *International Journal of Multiphase Flows*, **18**, pp. 145 – 147 (1992).

Michaelides, E.E., 'Review – The transient equation of motion for particles, bubbles, and droplets', *Journal of Fluids Engineering*, **119**, pp. 233 – 247 (1997).

Michel, B.J., and Miller, S.A., 'Power requirements of gas – liquid agitated systems', *A.I.Ch.E. Journal*, **8**, pp.262-266 (1962).

Middleton, J.C., 'Gas-Liquid dispersion and mixing', in 'Mixing in the Process Industries', Edited by Harnby, N., Edwards, M.F., and Nienow, A.W., pp.322-354, Butterworths Series in Chemical Engineering (1985).

Midoux, N., and Charpentier, J.C., 'Mechanically agitated gas – liquid reactors part I: Hydrodynamics', *International Chemical Engineering*, **24**, pp. 249 – 287 (1984).

Midoux, N., 'Hydrodynamique, transfert e maitere et optimization energetique des reacteurs gaz – liquide a cuve agitee', These, Universite de Nancy, France (1977).

Moens, L., J. De Donder, X.L. Lin, F. De Corte, A. De Wispelaere, A. Simonits and J. Hoste, 'Calculation of the absolute peak efficiency of the gamma ray detectors for different counting geometries', *Nuclear Instrumentation and methods*, **187**, pp.451 – 472 (1981).

Morsi, S.A., and Alexander, A.J. 'An investigation of particle trajectories in two phase flow system', *J. Fluid Mech.*, **55(2)**, pp. 193 – 208 (1972).

Morud, K.E. and Hjertager, B.H., 'LDA measurements and CFD modeling of gas –liquid flow in a stirred vessel', *Chem Engng Sci*, **51(2)**, pp.233-249 (1996).

Moslemian, D.; Devanathan, N. and Dudukovic, M.P., 'Radioactive particle tracking technique for investigation of phase recirculation and turbulence in multiphase systems', *Rev. Sci. Instrum.*, **63(10, Pt. 1)**, pp. 4361-72 (1992).

Mujumdar, A.S., Huang, B., Wolf, D., Weber, M.E. and Douglas, W.J.M., 'Turbulence parameters in a stirred tank', *Can J Chem Engng*, **48**, pp. 475 (1970).

Myers, K.J., Ward, R.W. and Bakker, A., 'A DPIV investigation of flow field instabilities of axial flow impellers', *Journal of fluids engineering*, **119 (3)**, pp. 623 –632 (1997).

Nagase, Y. and Yasui, H., Fluid motion and mixing in a gas – liquid contactor with turbine agitators, *Chemical Engineering Journal*, **27**, pp.37 (1983).

Nagata, S., 'Mixing principle and applications', Kodansha Ltd, A Halsted press, Tokyo (1975).

Ng., K., Fentiman, N.J., Lee, C.K. and Yianneskis, 'Assessment of sliding mesh CFD predictions and LDA measurements of the flow in a tank stirred by a Rushton impeller', *Trans I Chem E*, **76(A)**, pp. 737-747 (1998).

Nienow, A.W., 'Gas-Liquid Mixing Studies: A comparison of Rushton turbines with some modern impellers', *Trans IChemE*, **74(A)**, pp. 417-423 (1996).

Nienow, A.W., Gas dispersion performance in fermentor operation, *Chemical Engineering Progress*, pp.61 (1990).

Nienow, A.W., Huoxing, L., Haozhung, W., Allsford, K.V., Cronin, D., and Hudcova, V., 'The use of large ring spargers to improve the performance of fermenters agitated by single and multiple standard rushton turbines', *2nd International Conference on*

Bioreactor fluid dynamics, Ed. King R., held at Cambridge, England:21 –23. September (1988).

Nienow, A.W., Wisdom, D.J., and Middleton, J.C., The effect of scale and geometry on flooding, recirculation, and power in gassed stirred vessels, *Proceedings of the European Conference on Mixing, Paper F1*, Cambridge (1977).

Oshinowo, L and Marshall, L., 'Comparison of turbulence models in CFD predictions of flow patterns and power draw in stirred tanks', Presented at Mixing XVII, August 15-20th, Banff, Alberta, Canada (1999).

Ottino, J.M., 'The kinematics of mixing : stretching, chaos, and transport', *Published Cambridge ; New York : Cambridge University Press* (1989).

Oyama, Y., and Endoh, K., *Chemical Engineering Japan*, **10**,pp.2 (1955).

Parthasarathy, R., and Ahmed,N., 'Breakup behaviour of bubbles in an aerated stirred vessel', *AIChE Symposium Series*, **293**, 89, pp.97 – 104 .

Patankar, N.A., Huang, P.Y., Ko, T., and Joseph, D.D., 'Lift off of a single particle in Newtonian and viscoelastic fluids by direct numerical simulation', *J. Fluid Mech.*, **438**, pp. 67 – 100 (2001).

Pope, S.B., 'Lagrangian modeling of turbulent flows', *Annual Review of Fluid Mechanics*, **26**, pp. 23 – 63 (1994).

Pericleous, K.A. and Patel, M.K., 'The modeling of tangential and axial agitators in chemical reactors', *Physico Chem Hydrodyn.*, **8(2)**, pp. 105-123 (1987).

Perng, C.Y. and Murthy, J.Y., 'A moving deforming mesh technique for simulation of flow in mixing tanks', *AIChE Symp Ser*, **89,293**, pp. 37-41 (1993).

Pharamond, J.C., Roustan, M., and Roques, H., Determination de la puissance consommee dans une cuvee aeree et agitee, *Chemical Engineering Science*, **30**, 907 (1975).

Placek, J., Tavlarides, L.L., Smith, G.W. and Fort, I., 'Turbulent flow in stirred tanks II: A two scale model of turbulence', *AIChE J* **32(11)**, pp. 1771 (1986).

Rammohan, A.R., Kemoun, A., Al-Dahhan, M.H., and Dudukovic, M.P., 'A Lagrangian description of Flows in stirred tank reactor via Computer Automated Radioactive Particle Tracking', *Chemical Engineering Science*, **56(8)**, pp.2629-2639 (2001a).

Rammohan, A.R., Kemoun, A., Al-Dahhan, M.H., and Dudukovic, M.P., 'Characterization of Single Phase Flows in Stirred Tanks Via Computer Automated Radioactive Particle Tracking (CARPT)', *Transactions of Institution of Chemical Engineers, Part A*, **79:A8**, pp.831-844 (2001b).

Rammohan, A.R., Kemoun, A., Al-Dahhan, M.H., Dudukovic, M.P., and Larachi, F., 'CARPT Dynamic Bias Studies: Evaluation of Accuracy of Position and Velocity Measurements', *Tracers and Tracing methods*, **15(79)**, pp. 59 – 67 (2001c).

Rammohan, A.R., 'Characterization of Flow pattern in a stirred tank reactor', *Doctoral Proposal* submitted to Washington University, St.Louis, MO, USA (2000a).

Rammohan, A.R., 23rd Quarterly Report to submitted to the Department of Energy (2000b).

Ranade, V.V. and Joshi, J.B., 'Flow generated by a disc turbine', *Trans IchemE*, **68(A)**, pp. 19-50 (1990).

Ranade, V. V., Perrard, M., Le Sauze, N., Xuereb, C., Bertrand, J., 'Trailing vortices of Rushton turbine: PIV measurements and CFD simulations with snapshot approach.', *Chem. Eng. Res. Des.*, **79(A1)**, pp.3-12 (2001).

Ranade, V.V. and Van den Akker, H.E.A., 'A computational snapshot of gas –liquid flow in baffled stirred reactors', *Chem Engng Sci*, **49(24B)**, pp. 5175-5192 (1994).

Revstedt, J.; Fuchs, L. and Tragardh, C., 'Large eddy simulations of the turbulent flow in a stirred reactor', *Chem. Engng. Sci.*, **53(24)**, pp4041-4053 (1998).

Revill, B.K. and Irvine, 'Measurement of Local Gas Phase Fraction in a Stirred Tank', ICI plc, private communication (1987)

Roberts, R.M., Gray, M.R., Thompson, B., and Kresta, S.M., 'The effect of impeller and tank geometry on circulation time distributions in stirred tanks', *Transactions of Institution of Chemical Engineers*, **73A**, pp. 78-86 (1995).

Rousar, I. and Van den Akker, H.E.A., 'LDA measurements of liquid velocities in sparged agitated turbines with single and multiple Rushton turbines', *Institution of Chemical Engineers Symposium Series*, **136**, pp. 89-96 (1994).

Roussinova, V. and Kresta, S.M., 'Analysis of Macro Instabilities (MI) of flow field within stirred tank reactor (STR) agitated with Pitched Blade Turbine (PBT)', Presented at Mixing XVII, August 15-20th, Banff, Alberta, Canada (1999).

Roy, S., Larachi, F., Al-Dahhan, M.H., and Dudukovic, M.P., 'Resolution and sensitivity in computer-automated radioactive particle tracking (CARPT)', *Proc. SPIE-Int. Soc. Opt. Eng*, pp.122 – 133 (2001).

Roy, S.; Chen, J.; Degaleesan, S.; Gupta, P.; Al-Dahhan, M. H.; Dudukovic, M. P., 'Non-invasive flow monitoring in opaque multiphase reactors via CARPT and CAT.', *FED (Am. Soc. Mech. Eng.)* (1998), **245**, pp. 50-68 (1998).

Roy, S. and Dudukovic, M. P., 'Flow Mapping and Modeling of Liquid-Solid Risers', *Ind. Eng. Chem. Res.*, **40(23)**, pp.5440-5454 (2001).

Roy, S., 'Quantification of two phase flows in liquid-solid risers' , D.Sc., St.Louis, Missouri (2000).

Roy, S., Larachi, F., M. P. Dudukovic, Dodson, R. and Al-Dahhan, M.H., 'Implementation of computer automated radioactive particle tracking (CARPT) on a gas-solid riser:experiment design and analysis', CREL Internal Report (1999).

Roy, S., Chen, J., Kumar, S.B., Al Dahhan, M.H., and Dudukovic', M.P., 'Tomographic and Particle Tracking studies in a Liquid – Solid Riser', *Industrial and Engineering Chemistry Research*, **36(11)**, pp 4666-4669 (1997).

Rubinow, S., I., and Keller, J.B., 'The transverse force on a spinning sphere moving in a viscous fluid', *J. Fluid Mech.*, **11**, pp. 447 – 459 (1961).

Rushton, J.H., Costich, E.W., and Everett, H.J., 'Power characteristics of mixing impellers', *Chemical Engineering Progress*, **46**, pp.395 (1950).

Rutherford, K., Mahmoudi, S.M.S., Lee, K.C. and Yianneskis, M., 'The influence of Rushton impeller blade and disk thickness on the mixing characteristics of stirred vessels', *Trans I Chem E*, **74(A)**, pp. 369-378 (1996).

Sangani, A.S., Zhang, D.Z., and Prosperetti, A., 'The added mass, Basset and viscous drag coefficients in non – dilute bubbly liquids undergoing small amplitude oscillatory motion', *Physics of Fluids*, **A3**, pp. 2955 – 2970 (1991).

Schaefer, M., and Hofken, M., 'Experimental study of trailing vortices around impeller blades', Presented at Mixing XVII, August 15-20th, Banff, Alberta, Canada (1999).

Schaefer, M., Hofken, M., and Durst, F., 'Detailed LDV measurements for visualization of the flow field within a stirred tank reactor equipped with a Rushton turbine', *Transactions of Institution of Chemical Engineers*, **75(A)**, pp. 729 – 736 (1997).

Segre, G., and Silberberg, 'A. Behaviour of macroscopic rigid spheres in Poiseuille Flow, Part 2 - Experimental results and interpretation', *J. Fluid Mech.*, **14**, pp. 136 – 157 (1962).

Shah, Y.T., 'Design Parameters for Mechanically Agitated Reactors', in *Advances in Chemical Engineering*, Edited by Wei, J., Anderson, J.L., and Bischoff, K.B. **17**, pp.1-196, Academic Press Inc (1992).

Smith, J.M., Dispersion of Gases in Liquids: The Hydrodynamics of Gas Dispersion in Low Viscosity Liquids, in *Mixing of Liquids By Mechanical Agitation*, Edited by Ulbrecht, J.J., and Patteson, G.K., pp.139-202, Gordon and Breach Science Publishers (1985).

Smith, J.M., van't Riet, K., and Middleton, J.C., 'Scale – up of agitated gas – liquid reactors for mass transfer', F4, *Second European Conference on Mixing*, F6, Cambridge, England, 30th March – April 1st (1977).

Sommerfeld, M., 'Numerical simulation of the particle dispersion in turbulent flow. The importance of particle lift forces and particle/wall collision models', *American Society of*

Mechanical Engineers, Fluids Engineering Division (Publication) FED, v **91**, p.p 11-18 (1990).

Stoots, C.M. and Calabrese, R.V., 'Mean velocity field relative to a Rushton turbine blade', *A.I.Ch.E. J.*, **41(1)**, pp. 1-11 (1995).

Takahashi, K., and Nienow, A.W., 'Bubble sizes and coalescence rates in an aerated vessel agitated by a Rushton turbine', *Journal of Chemical Engineering*, **26(5)**, pp. 536-543 (1992).

Tsoufanidis, N., 'Measurement and detection of radiation', McGraw Hill, New York (1983).

Van der Molen, K. and van Maanen, H.R.E., 'Laser Doppler measurements of the turbulence flow in stirred vessels to establish scaling rules', *Chem Engng Sci*, **33(9)**, 1161-1168 (1978).

Van't Riet, K., and Tramper, J., 'Basic bioreactor design', Marcel Dekker, Inc. New York (1991).

Van't Riet, K., Boom, J.M., and Smith, J.M., 'Power consumption, impeller coalescence and recirculation in aerated vessels', *Transactions of Institution of Chemical Engineers*, **54**, pp.124 – 131 (1976).

Van't Riet, K. and Smith, J.M., 'The trailing vortex system produced by Rushton turbine agitators', *Chem Engng Sci*, **30 (9)**, pp. 1093-1105 (1975).

Warmoeskerken, M.M.C.G., and Smith, J.M., 'Impeller loading in multi turbine vessels', 2nd International Conference on Bioreactor fluid dynamics, Ed. King R. held at Cambridge, England, 21 – 23 September (1988).

Warmoeskerken, M.M.C.G., 'Gas liquid dispersing characteristics of turbine agitators', PhD. Thesis at TU Delft (1986).

Warmoeskerken and Smith, Flooding of disk turbines in gas – liquid dispersions: A new description of the phenomenon, *Chemical Engineering Science*, **40**, 11, pp.2063 (1985).

Warmoeskerken, M.M.C.G., and Smith, J.M., Description of the power curves of turbine stirred gas – liquid dispersions, Proceedings of the European Conference on Mixing, Paper G1, Noordwijkerhout, The Netherlands (1982).

Westerweel, J., 'Efficient detection of spurious vectors in particle image velocimetry data', *Exp. Fluids*, **16**, pp. 236-247 (1994).

Wittmer, S., Falk, L., Pitiot, P., Vivier, A., 'Characterization of Stirred vessel hydrodynamics by three dimensional trajectography', *Canadian Journal of Chemical Engineering*, **A7(6)**, pp. 600 – 610 (1998).

Wu, H. and Patterson, G.K., 'LDA measurements of turbulent flow parameters in a stirred mixer', *Chem Engng Sci*, **44 (10)**, pp.2207-2221 (1989).

Yang, Y.B., Devnathan, N., and Dudukovic, M.P., 'Liquid backmixing in bubble columns', *Chemical Engineering Science*, **47(9-11)**, pp.2859-2864 (1992).

Yakhot, V. and Orszag, S.A., 'Renormalization group analysis of turbulence', *Journal of Scientific Computing*, **3**; pp.35 (1986).

Yianneskis, M., Popilek, Z. and Whitelaw, J.H., 'Steady and unsteady flow characteristics of stirred reactors', *J. Fluid Mechanics*, **175**, pp. 537-555 (1987).

Yianneskis, M. and Whitelaw, J.H., 'On the structure of the trailing vortices around Rushton turbine blades', *Trans I Chem E*, **71 (A)**, pp.543-550 (1993).

Zhou, G. and Kresta, S.M., 'Distribution of energy between convective and turbulent flow for three frequently used impellers', *Trans I Chem E*, **74 (A)**, pp.379-389 (1996).

Zun, I., Filipic, B., Perpar, M., and Bombac, A., Phase discrimination in void fraction measurements via genetic algorithms, *Reviews in Scientific Instrumentation*, **66 (10)**, pp. 5055 (1995).



9803 1200 211 900

Vita Aravind Rammohan

Date of Birth: September 15th, 1974
Place of Birth: Chennai, India
Degrees: B.Chem Engg, May 1996,
U.D.C.T., Mumbai, India.
M.S. Chemical Engineering, May 2000,
Washington University, St.Louis, MO.
D.Sc. Chemical Engineering, (expected) December 2002
Washington University, St.Louis, MO.

Publications

- "A Lagrangian description of flows in stirred tanks via Computer Automated Radioactive Particle Tracking (CARPT)", Rammohan, A. R., Kemoun, A., Al-Dahhan, M. H. and Dudukovic', M. P., 2001, *Chemical Engineering Science*, **56(8)**, pp. 2629-2639.
- "Characterization of single phase flows in stirred tank reactors via Computer Automated Radioactive Particle Tracking (CARPT)", Rammohan, A. R., Kemoun, A., Al-Dahhan, M. H. and Dudukovic', M. P., 2001, *Chemical Engineering Research and Design*, **79**, A8.
- "CARPT dynamic bias studies: Evaluation of accuracy of position and velocity measurements", Rammohan, A. R., Kemoun, A., Al-Dahhan, M. H., Dudukovic, M. P., and Larachi, F., 2001, *Tracers and Tracing methods*, Leclerc, J. P., Ed., **15 (79)**, pp. 59 – 67.
- "Eulerian flow field estimation from particle trajectories: Some numerical experiments", Rammohan, A. R., Dudukovic', M. P., and Ranade, V. V., 2001, submitted to *I & EC research*
- "Characterization of gas - liquid flow structures in stirred tank reactors via Computer Automated Particle Tracking (CARPT) and Computed Tomography (CT) - Part I", Rammohan, A. R., Kemoun, A., Al-Dahhan, M. H., and Dudukovic, M. P., *A.I.Ch.E Journal* (in progress).

Conference Proceedings/Posters

- "Characterization of single-phase flow in a stirred tank using Computer Automated Radioactive Particle Tracking (CARPT)", Rammohan, A. R.; Kemoun, A.; Al-Dahhan, M. H. and Dudukovic, M. P., paper 166e, Presented at *AIChE 1999 Annual Meeting*, October 31-November 5, 1999, Dallas, Texas.

- “Characterization of single-phase flow in a stirred tank using Computer Automated Radioactive Particle Tracking (CARPT)”, Rammohan, A. R.; Kemoun, A.; Al-Dahhan, M. H. and Dudukovic, M. P., MIXING XVII, Presented at *17th North American Mixing Conference*, August 1999, Alberta Canada.
- “Motion of neutrally buoyant particles in stirred vessels: Computer Automated Radioactive Particle Tracking (CARPT) experiments and CFD simulations”, Ranade, V. V.; Rammohan, A. R.; Kemoun, A.; Al-Dahhan, M. H. and Dudukovic, M. P., MIXING XVII, Presented at *17th North American Mixing Conference*, August 1999, Alberta Canada.
- “Characterization of single-phase flow in a stirred tank using Computer Automated Radioactive Particle Tracking (CARPT)”, Rammohan, A. R., Kemoun, A., Al-Dahhan, M. H., and Dudukovic, M. P., Presented at *Fourth International Symposium on Mixing in Industrial Processes*, 14th - 16th May, 2001, Toulouse, France.
- “Gas liquid flow in stirred tank reactors”, Rammohan, A. R., Kemoun, A., Al-Dahhan, M. H., and Dudukovic, M. P., paper 174d, Presented at A.I.Ch.E 2002 Annual Meeting, Indianapolis, Indiana.
- “Eulerian flow field estimation from particle trajectories: numerical experiments”, Rammohan, A.R., Dudukovic, M.P. and Ranade, V.V., paper 175h, Presented at A.I.Ch.E. 2002 Annual Meeting, Indianapolis, Indiana.

December 2002